

# Behaviour of Mesoporous Silica (MCM-41) Supported Catalysts in Degradation Reactions

by

Colin P. Guthrie

A thesis  
presented to the University of Waterloo  
in fulfillment of the  
thesis requirement for the degree of  
Doctor of Philosophy  
in  
Earth Sciences

Waterloo, Ontario, Canada, 2012

© Colin P. Guthrie 2012

## **AUTHOR'S DECLARATION**

I hereby declare that I am the sole author of this thesis. This is a true copy of the thesis, including any required final revisions, as accepted by my examiners.

I understand that my thesis may be made electronically available to the public.

## ABSTRACT

A research project was carried out to investigate several aspects of Mobil's composition of matter #41 (MCM-41) pertaining to its potential application in water treatment technologies. The goal of the work was to lead to a recommendation of whether further work investigating this particular, potential application is warranted at the present time.

A dissolution experiment indicated that Pd/MCM-41 is more stable in contact with deionized water at  $25 \pm 0.1^\circ\text{C}$  than purely siliceous MCM-41. Stability increases with increasing mass percent loading of Pd in the Pd/MCM-41 material. The increased stability was attributed to a reduction in Pd/MCM-41 surface areas relative to the parent MCM-41 material. The reduction in surface area is likely the result of partial or complete blocking of the MCM-41 mesopores by Pd centres. Ni/MCM-41 was less stable in contact with deionized water than MCM-41 and Pd/MCM-41. Both Ni and Pd impregnated MCM-41 exhibited enhanced stability relative to purely siliceous MCM-41 in 0.01 M *NaCl* solution. The stability enhancement was more pronounced for Pd/MCM-41. A long term dissolution experiment showed that MCM-41 retained its characteristic hexagonal mesopore structure and high surface area after 1,174 days of contact with deionized water.

The ability of Pd/MCM-41 to absorb hydrogen was investigated in a series of experiments in pressure cells at  $25 \pm 0.1^\circ\text{C}$  and approximately 101.3 kPa. The Pd in Pd/MCM-41 was able to absorb  $0.85 \pm 0.18$  moles of hydrogen per mole of Pd present. This was a higher level of absorption than found in most other, published Pd-hydrogen investigations. It is proposed that enhanced uptake of hydrogen by Pd/MCM-41 may be the result of a higher proportion of surface and subsurface sites in the samples relative to other supported Pd materials.

Batch and column trichloroethylene (TCE) degradation experiments indicated that Pd/MCM-41 has substantial longevity while degrading at least 91% of inflow TCE concentrations in hydrogen-saturated deionized water over 5,036 pore volumes. The average inflow TCE concentration was  $4.94 \times 10^{-2} \pm 4.87 \times 10^{-3}$  mmol/l with maximum and minimum concentrations of  $7.24 \times 10^{-2}$  mmol/l and  $2.63 \times 10^{-2}$  mmol/l, respectively. The dominant breakdown product of TCE degradation in the presence of Pd/MCM-41 was ethane. Minimal concentrations of intermediate degradation products were detected, if at all. This result suggests that TCE

completely degrades to ethane before desorbing from the Pd/MCM-41 surface. It was shown that Pd/MCM-41 was more effective and had better longevity at treating inflow TCE compared to a lower cost substitute, Pd/sand. Unlike Pd/MCM-41, Ni/MCM-41 did not induce degradation of TCE. Column experiments using Ni-Pd/MCM-41 materials indicated that while the material does induce degradation of TCE, the Pd cannot be substituted for Ni on a 1:1 basis while still obtaining similar degradation results as Pd/MCM-41. Pd/MCM-41 was not able to substantially reduce initial concentrations of hexamethylphosphoramide (HMPA) in a batch experiment. A small reduction in the initial HMPA concentration was attributed to adsorption onto the Pd/MCM-41 surfaces rather than degradation of the compound.

Several of the above-mentioned results suggest that MCM-41 and Pd/MCM-41 show great potential for being incorporated into water treatment technologies. Both the long term stability of the material in contact with deionized water and the longevity of a Pd/MCM-41 column in treating inflow TCE are very promising results with respect to applications in water treatment technologies. It is recommended that future work be pursued with this goal in mind.

## ACKNOWLEDGEMENTS

I thank my advisor Eric Reardon for his mentorship throughout this project and during my years as a graduate student. I also thank my committee members Hartwig Peemoeller, Carol Ptacek, and Neil Thomson for their questions, suggestions, and input on this project.

Special thanks to the many colleagues I have worked with during my research: my original lab-mates Mark Hall and Randy Fagan; Wayne Noble, Brian Ellis, and Ralph Dickhout for their guidance on analytical aspects of this work; John Vogan, Claude Lemaire, Jaspreet Walia, Ian Lam, and Josh Crone for their collaboration on several projects; Firaz Mansour and Jamal Hassan for the conversations and helpful tips as I synthesized my first batches of MCM-41.

I extend my gratitude to Sue Fisher for patiently answering a million questions as I navigated the requirements towards completing my degree.

Thank you to my family for their love and support.

And to Tanya, I couldn't have finished this without you and it definitely wouldn't have been as much fun.

Funding for this project was provided by NSERC (Natural Sciences and Engineering Research Council of Canada), ETECH (Ontario Centre of Excellence), and Envirometal Technologies Inc.

## TABLE OF CONTENTS

AUTHOR'S DECLARATION .....	ii
ABSTRACT.....	iii
ACKNOWLEDGEMENTS.....	v
TABLE OF CONTENTS.....	vi
LIST OF FIGURES .....	viii
LIST OF TABLES.....	xi
1. INTRODUCTION .....	1
1.1 Background.....	1
1.2 Research Objectives.....	5
2. SYNTHESIS AND CHARACTERIZATION OF EXPERIMENTAL MATERIALS .....	6
2.1 Background.....	6
2.2 Experimental Methods.....	13
2.2.1 Reagents.....	13
2.2.2 Synthesis of MCM-41.....	13
2.2.3 Metal-impregnated MCM-41.....	16
2.2.4 Pd-impregnated silica sand.....	18
2.3 Results and Discussion .....	19
2.3.1 MCM-41 .....	19
2.3.2 Metal Impregnated MCM-41.....	29
2.3.3 Metal Impregnated Silica Sand.....	44
2.4 Conclusions.....	46
3. STABILITY OF MCM-41-SUPPORTED METAL AND LONG TERM STABILITY OF MCM-41 .....	48
3.1 Background.....	48
3.2 Experimental Methods.....	50
3.2.1 Solubility experiment.....	50
3.3 Results and Discussion .....	52
3.3.1 Solubility Experiment.....	52
3.3.2 Dissolution Rate Modeling.....	65

3.3.3 Long term dissolution experiment .....	69
3.4 Conclusions.....	72
4. HYDROGEN UPTAKE BY Pd/MCM-41 .....	73
4.1 Background.....	73
4.2 Experimental Methods.....	74
4.2.1 Reagents.....	74
4.2.2 Hydrogen Absorption.....	74
4.3 Results and Discussion .....	76
4.3.1 Hydrogen Absorption Experiments .....	76
4.4 Conclusions.....	83
5. DEGRADATION OF CONTAMINANTS BY METAL IMPREGNATED MCM-41 .....	84
5.1 Background.....	84
5.2 Experimental Methods.....	87
5.2.1 Reagents.....	87
5.2.2 TCE Degradation Batch Experiment .....	87
5.2.3 TCE Degradation Column Experiment.....	90
5.2.4 HMPA Degradation Batch Experiment .....	98
5.3 Results and Discussion .....	101
5.3.1 TCE Degradation Batch Experiment .....	101
5.3.2 TCE Degradation Column Experiment.....	109
5.3.3 HMPA Degradation Batch Experiment .....	132
5.4 Conclusions.....	134
6. SUMMARY OF CONCLUSIONS AND FUTURE WORK RECOMMENDATIONS.....	137
6.1 Summary of Conclusions.....	137
6.2 Future Work Recommendations .....	139
REFERENCES .....	140
APPENDIX A.....	152
APPENDIX B .....	177
APPENDIX C .....	182
APPENDIX D.....	189
APPENDIX E .....	209

## LIST OF FIGURES

Figure 1: Representation of the Pd/MCM-41 catalyst and zero-valent iron technology.....	2
Figure 2: Example SEM images of different MCM-41 particles prepared for this research.....	3
Figure 3: Graphical representation of (1) liquid crystal phase initiated pathway for the synthesis of MCM-41.....	8
Figure 4: An illustration of the three types of surface silica and silanol groups in MCM-41 .....	10
Figure 5: Example low angle XRD plot for calcined MCM-41 produced from an individual synthesis batch .....	20
Figure 6: Low angle XRD results for combined batch ‘Combo 2’ .....	21
Figure 7: Comparison between (A) single synthesis batch calcined MCM-41 in aluminum sample holder (sample MCM-2B), and (B) calcined combined batch of MCM-41 analyzed in an epoxy sample holder (Combo 2).....	24
Figure 8: Full adsorption-desorption isotherm results for a combined batch of MCM-41.....	26
Figure 9: SEM image of calcined MCM-41 particles.....	28
Figure 10: TEM image of calcined MCM-41 showing porosity .....	29
Figure 11: Low angle XRD results for a palladized MCM-41 sample.....	31
Figure 12: High angle XRD results for five metal impregnated MCM-41 samples prepared using different metals (Pd, Ni, Ni-Pd) .....	33
Figure 13: High angle XRD results for 2.30% Pd/MCM-41 .....	35
Figure 14: Full adsorption-desorption isotherm results for Pd/MCM-41.....	37
Figure 15: SEM images collected at two magnifications for Pd impregnated MCM-41. ....	38
Figure 16: TEM image of Pd impregnated MCM-41 sample.....	40
Figure 17: Results of EDAX analysis for a Pd impregnated MCM-41 sample.....	41
Figure 18: Schematic of sample bottles in an isotherm bath .....	51
Figure 19: Results of dissolution experiments comparing solubility of Pd/MCM-41 at two different mass percent loadings .....	54
Figure 20: Results of dissolution experiments comparing solubility of Pd/MCM-41 at two different mass percent loadings.. .....	54

Figure 21: Results of dissolution experiments comparing solubility of Ni/MCM-41 at two different mass percent loadings. ....	56
Figure 22: Results of dissolution experiments comparing solubility of Ni/MCM-41 at two different mass percent loadings. ....	56
Figure 23: Results of dissolution experiments comparing solubility of Ni/MCM-41 at two different mass percent loadings. ....	58
Figure 24: Results of dissolution experiments comparing solubility of Ni/MCM-41 at two different mass percent loadings.. ....	58
Figure 25: Comparison of as-synthesized Pd/MCM-41 and materials recovered after 50 d in deionized water. ....	61
Figure 26: Comparison of as-synthesized Ni/MCM-41 and materials recovered after 40 d in deionized water. ....	63
Figure 27: Results of dissolution experiments comparing purely siliceous MCM-41 (Combo 2), 0.12% Pd/MCM-41, and 0.12% Ni/MCM-41 in a 0.01 M <i>NaCl</i> solution. ....	65
Figure 28: Phreeqci simulation of dissolution kinetics for 1.16% Pd/MCM-41 .....	68
Figure 29: Comparison of simulated and experimental dissolution results for: (A) 0.12% Pd/MCM-41 at a solid to liquid ratio of 1/200, (B) 0.12% Pd/MCM-41 at a solid to liquid ratio of 1/100, (C) 1.16% Pd/MCM-41 at a solid to liquid ratio of 1/200, and (D) 1.16% Pd/MCM-41 at a solid to liquid ratio of 1/100. ....	69
Figure 30: Comparative low angle XRD plots for as-synthesized MCM-41 as well as material recovered after 280 d and 1,174 d contact with deionized water. ....	71
Figure 31: Schematic showing setup of pressure cells. ....	75
Figure 32: Typical hydrogen absorption results for pure silica MCM-41. ....	77
Figure 33: Typical pressure versus hydrogen absorption curve for a Pd/MCM-41 .....	78
Figure 34: Typical pressure versus hydrogen absorption isotherms for Pd black. ....	79
Figure 35: Results of hydrogen absorption by Pd/MCM-41 samples at different mass percent loadings of Pd. ....	81
Figure 36: Representation of (A) trichloroethylene and (B) hexamethylphosphoramide molecular structures .....	86
Figure 37: Schematic showing typical reactive sample setup for: first phase of TCE degradation batch experiment and second phase including hydrogen headspace. ....	89
Figure 38: Schematic of TCE degradation columns. ....	92

Figure 39: Schematic of columns with computer-controlled pump and valve system.....	96
Figure 40: Representation of typical reactive sample for HMPA degradation batch experiment including a 6 ml hydrogen headspace.....	100
Figure 41: Results of TCE degradation batch experiment comparing sand and MCM-41 supported Pd.....	103
Figure 42: Results of a carbon balance performed on batch TCE degradation experiment using 1.00% Pd/sand.....	105
Figure 43: Results of a carbon balance on expanded y-axis performed on batch TCE degradation experiment using 1.00% Pd/sand.....	106
Figure 44: Results of a carbon balance performed on batch TCE degradation experiment using 1.00% Pd/sand.....	107
Figure 45: Results of a carbon balance on expanded y-axis performed on batch TCE degradation experiment using 1.00% Pd/sand.....	107
Figure 46: Results from TCE degradation columns including control, Pd/sand, and Pd/MCM-41 samples plotted as a function of total pore volumes.....	111
Figure 47: Results from TCE degradation columns including control, Pd/sand, and Pd/MCM-41 samples plotted as a function of total time.....	112
Figure 48: Long term normalized TCE concentration results versus pore volumes for 0.99% Pd/MCM-41 column.....	113
Figure 49: Long term normalized TCE concentration results versus total time for 0.99% Pd/MCM-41 column.....	114
Figure 50: Comparison of low angle XRD results for 0.99% Pd/MCM-41 when freshly synthesized and recovered from column following termination of TCE degradation column experiment.....	118
Figure 51: High angle XRD analysis of 0.99% Pd/MCM-41 recovered from column experiment.....	120
Figure 52: Normalized TCE concentration versus pore volume results for Ni/MCM-41 and Ni-Pd/MCM-41 samples.....	121
Figure 53: Normalized TCE concentration (C/Co) versus time profile for column #1.....	129
Figure 54: Normalized TCE concentration (C/Co) versus time profile for column #3.....	130
Figure 55: Normalized HMPA concentration versus time results for degradation batch experiments.....	133

## LIST OF TABLES

Table 1: Summary of physical characteristics of calcined MCM-41 determined from XRD analysis.....	22
Table 2: BET nitrogen adsorption surface area results for calcined MCM-41 samples.....	25
Table 3: Summary and calculation of percent mass loadings of metal on MCM-41. ....	30
Table 4: Summary of calculated cell parameter values for metal impregnated MCM-41 samples. Percent change in primary mesopore diameter (Wd) relative to the parent material (Combo 2) is noted.....	32
Table 5: Comparison of common species between metal sources in five metal impregnated MCM-41 samples.....	34
Table 6: Summary of BET nitrogen adsorption surface area analysis results for metal impregnated MCM-41 samples.....	36
Table 7: Comparison of percent loadings by mass of metal on MCM-41 determined via EDAX, ICP and AAS with calculated loadings.....	43
Table 8: BET surface area, calculated surface area, and mass percent loadings of Pd on sand in Pd/sand materials. ....	46
Table 9: Summary of conductivity measurements taken during the various dissolution experiments.....	60
Table 10: Comparison of physical characteristics calculated using low angle XRD results for as-synthesized and recovered Pd/MCM-41 and Ni/MCM-41 materials.....	62
Table 11: Summary of values calculated for dissolution rate constant calculations for Pd/MCM-41 materials. ....	67
Table 12: Comparison of MCM-41 characteristics determined by low angle XRD after 280 and 1,174 days in deionized water.....	72
Table 13: Comparison of published hydrogen uptake by palladium values.....	82
Table 14: Summary of column porous material properties. First set of column experiments.....	93
Table 15: Summary of column fill properties. Second set of column experiments.....	98
Table 16: Method detection limits (MDL) for TCE and its intermediate and final degradation products.....	102
Table 17: First-order reaction rate calculations for first set of batch TCE degradation experiments using 1.00% Pd/sand. ....	104
Table 18: Results of a carbon balance performed on 1.10% Pd/MCM-41 samples during the TCE degradation batch experiment. ....	107
Table 19: Results of batch TCE degradation experiment comparing 1.00% Pd/sand and 1.10% Pd/MCM-41 in <b>Na2B4O7 · xH2O</b> in hydrogen saturated deionized water with 2 ml <b>H2(g)</b> headspace. ....	109

Table 20: Results of pH measurements taken during control and 0.99% Pd/MCM-41 column experiments.....	116
Table 21: Conductivity results for 0.99% Pd/MCM-41 column.....	117
Table 22: Comparison of low angle XRD characterization results for as-prepared and recovered 0.99% Pd/MCM-41.....	119
Table 23: Results of pH measurements taken during 1.02% Ni/MCM-41 and 1.01% Ni-Pd/MCM-41 column experiments.....	122
Table 24: Conductivity results for 1.02% Ni/MCM-41 and 1.01% Pd/MCM-41 columns.....	123
Table 25: Comparison of normalized TCE concentration results for column experiments containing 0.12% Pd/MCM-41 or 0.13% Ni-Pd/MCM-41.....	124
Table 26: Results of pH measurements taken during 0.12% Pd/MCM-41 and 0.13% Ni-Pd/MCM-41 column experiments.....	125
Table 27: Conductivity results for 0.12% Pd/MCM-41 and 0.13% Ni-Pd/MCM-41 columns..	126
Table 28: Summary of first and zero-order rate laws fit to degradation profiles of columns #1 and #3.....	132

## CHAPTER 1

### 1. INTRODUCTION

#### 1.1 Background

The overarching goal of this research was to explore a possible application of Mobil's Composition of Matter #41 (MCM-41) as a support for transition metal catalysts in the catalytically-enhanced degradation of aqueous contaminants in groundwater. Conclusions of this work serve as a preliminary step towards using an MCM-41-supported metal catalyst in conjunction with zero-valent iron in groundwater treatment technologies. Although a great deal of research has been published since MCM-41 was first developed in 1992, many aspects regarding this particular application have not yet been fully explored. In particular, stability of MCM-41 catalysts in water, interaction of hydrogen with MCM-41-supported Pd, and the comparative benefit of using MCM-41 as a support material in degradation reactions compared to other possible, lower cost supports have not been fully described in the current literature. This work investigates these aspects of MCM-41-supported catalysts at the lab scale. Individual experiments were conceived and designed based on a set of research objectives which are discussed below in Section 1.2. A summary and consideration of the conclusions made from these experiments led to a recommendation of whether further research into using MCM-41-supported transition metal catalysts in groundwater remediation is a viable application of the material.

The study includes two target contaminants: trichloroethylene (TCE) and hexamethylphosphoramide (HMPA). An illustration of how an MCM-41-supported transition metal could be used in degrading TCE is presented in Figure 1. In the envisaged application, the supported Pd would catalyze the degradation of chlorinated volatile organic compounds (cVOCs) in the presence of hydrogen furnished via anaerobic corrosion of zero-valent iron particles. Successful integration of a supported metal catalyst into zero-valent iron-based treatment systems such as permeable reactive barriers (PRBs) could represent an enhanced treatment method for groundwater contaminated with cVOCs; potentially reducing reaction times, mass of required zero-valent iron, and increasing the extent of cVOC degradation. Treatment technologies include *in situ* methods such as the aforementioned PRBs composed of

zero valent iron; pump-and-treat, where contaminated groundwater is pumped above ground, treated, and then returned to the hydrologic cycle; and biodegradation, where microbial action converts harmful contaminants into products of lesser toxicity (Mackay & Cherry, 1989; Gillham & Ohannesin, 1994; Gavaskar, 1999; Kao & Lei, 2000; Appelo & Postma, 2007; Moreno *et al.*, 2011). Treatment of contaminated sites may use combinations of different technologies, depending on the site and contaminant-specific characteristics. MCM-41-supported metal catalysts could potentially be incorporated into any existing technology.

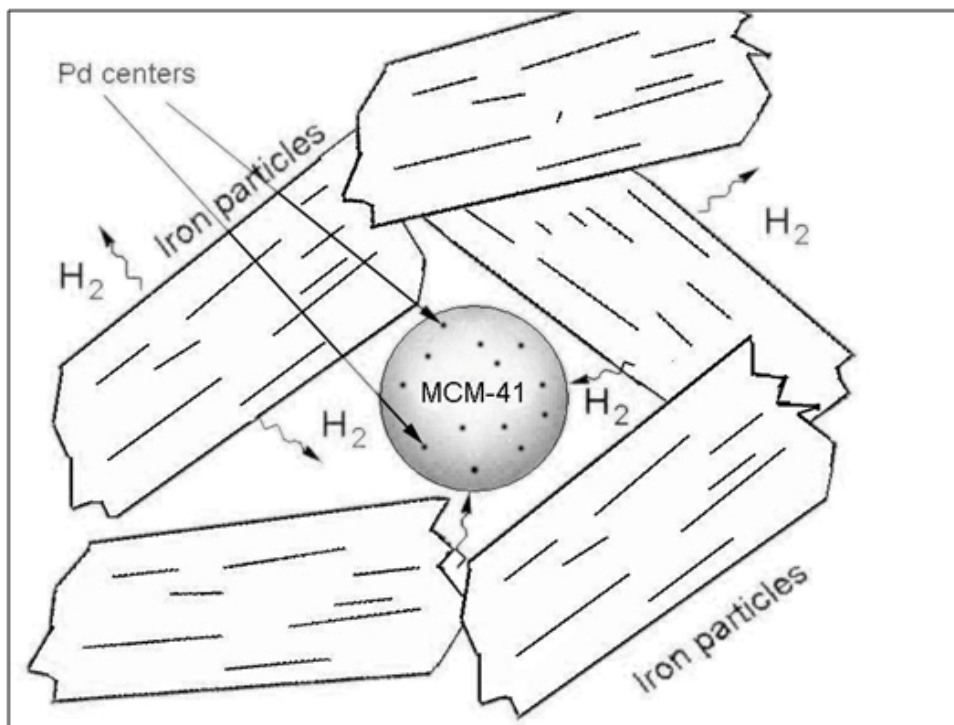


Figure 1: Representation of the Pd/MCM-41 catalyst and zero-valent iron technology (After Reardon, E. J. (2005) Presentation at the Waterloo/Dupont Iron Technology in Groundwater Remediation Meeting, Waterloo, March 30<sup>th</sup>, 2005).

MCM-41 was selected as a solid support material for transition metal catalysts due to its possessing several interesting characteristics including: customizable pore size, exceptionally high-surface areas, and a relatively straightforward synthesis procedure. An image of MCM-41 taken using a scanning electron microscope (SEM) is presented in Figure 2. Details concerning the unique properties of MCM-41 are discussed in greater detail in Section 2.1, Chapter 2. Three varieties of transition metal catalysts were used in this research: Pd, Ni, and bimetallic Ni-Pd. The selection of MCM-41-supported Pd was made due to its demonstrated ability to catalyze hydrogenation and dehalogenation reactions in the presence of hydrogen (Okumara *et al.*, 2003).

Ni catalysts were included to explore the possibility of a lower cost substitute for the relatively costly Pd sources needed in producing Pd catalysts. Bimetallic Ni-Pd catalysts were included to determine if the presence of Pd in a Ni-supported MCM-41 could enhance Ni's ability to utilize hydrogen gas to dechlorinate cVOCs through a hydrogen spillover mechanism.

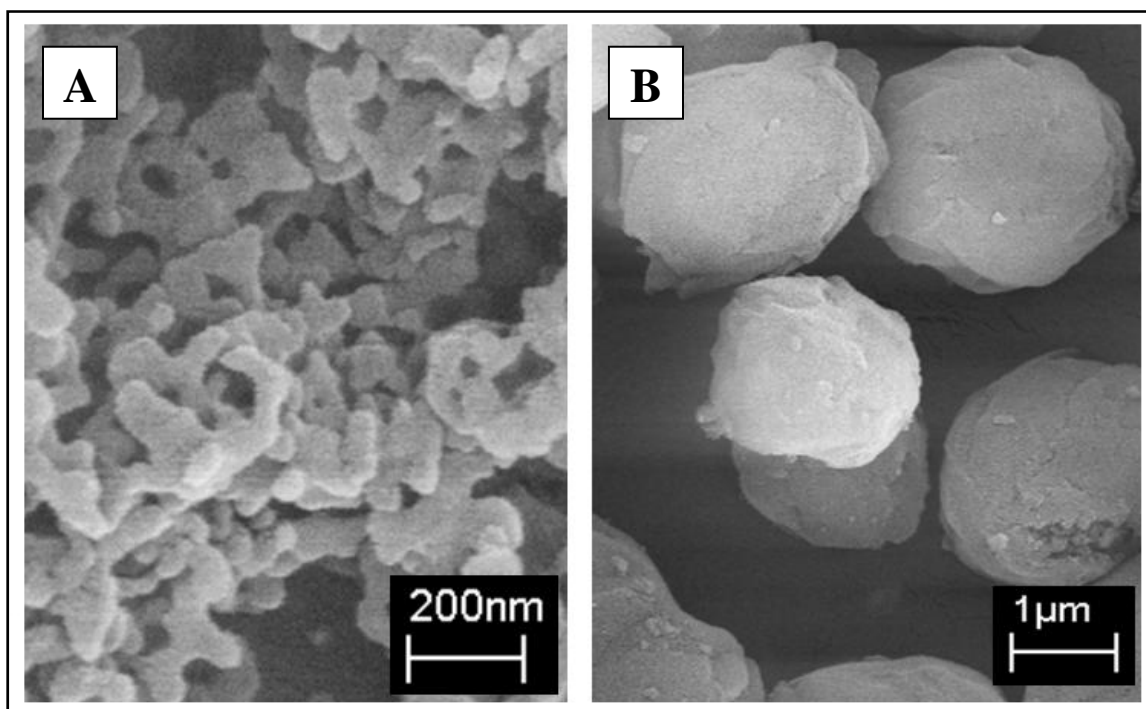


Figure 2: Example SEM images of different MCM-41 particles prepared for this research. (A) Typical, ‘wormy’ morphology of calcined MCM-41. (B) Morphology of spherical MCM-41 prepared following a different procedure from that of (A).

The four chapters which follow in this document will each develop and describe a set of experiments which explore a unique aspect of using MCM-41-supported transition metal catalysts in water treatment technologies. The first of these chapters (Chapter 2) provides an introduction to the MCM-41 material itself, its many potential applications in different fields, the method of its synthesis, and its use as a catalyst support. Experimental sections of Chapter 2 will detail the synthesis and characterization of MCM-41, MCM-41-supported Pd, and other supported transition metal materials used in later chapters. Chapter 3 will describe the experimental procedures, results, and conclusions of a series of experiments investigating the stability of MCM-41 and transition metal-impregnated MCM-41. It also includes the results of an experiment investigating the long term stability of as-synthesized, calcined MCM-41 over 1,174 days in deionized water. Understanding the stability in water of any material used in water

treatment technologies is an important aspect of its characterization. Chapter 4 will detail an experiment performed to determine the ability of the Pd in Pd/MCM-41 to absorb and release hydrogen gas at  $25\pm 0.1^\circ\text{C}$  and approximately 101.3 kPa. It was necessary to investigate aspects of hydrogen absorption by Pd/MCM-41 because hydrogen is intimately involved in the degradation reactions of both TCE and HMPA. Chapter 5 will detail a series of batch and column experiments investigating TCE degradation in the presence of Pd/MCM-41, Ni/MCM-41, Ni-Pd/MCM-41, and Ottawa silica sand-supported Pd in hydrogen-saturated deionized water. Chapter 5 will also include the results of a batch experiment investigating potential degradation of HMPA by Pd/MCM-41 in hydrogen-saturated deionized water. Finally, Chapter 6 will summarize the overall conclusions of this research and recommend possible future research directions suggested by the results of the current work. A recommendation of whether or not future research work exploring the use of MCM-41-supported transition metal catalysts in water remediation technologies is warranted will also be discussed in Chapter 6.

## 1.2 Research Objectives

The objective of the current research is to assess the ability of MCM-41 as a transition metal catalyst support material in degradation reactions involving chlorinated volatile organic compounds. Positive results will indicate that further work towards scaling up of the MCM-41-supported catalyst technology to field or industrial-scale experiments is warranted. Negative results will indicate that further steps are not necessary at the current time. This objective will be approached by completing the following goals:

- Determine the size, location, concentration, and distribution of transition metal particles in prepared samples of metal-impregnated MCM-41.
- Confirm the stability of metal-impregnated MCM-41 materials in deionized water as it compares to purely siliceous MCM-41.
- Investigate the absorption and release of hydrogen by dry samples of Pd/MCM-41 as compared to bulk Pd (Pd-black).
- Complete a series of batch and column experiments to demonstrate the ability of Pd/MCM-41, Ni/MCM-41, Ni-Pd/MCM-41 to induce degradation of trichloroethylene in deionized water in the presence of hydrogen. Compare these results to those obtained using Pd-impregnated silica sand to ascertain the benefit of using MCM-41 as a support material.
- Complete a batch experiment to assess the ability of Pd/MCM-41 to induce degradation of hexamethylphosphoramide in deionized water in the presence of hydrogen.

## CHAPTER 2

### 2. SYNTHESIS AND CHARACTERIZATION OF EXPERIMENTAL MATERIALS

#### 2.1 Background

In the following document, the characteristics of three varieties of supported transition metal catalysts and their ability to induce degradation of chlorinated volatile organic compounds (cVOCs) will be examined. A properly chosen support material can aid in both obtaining and maintaining well-dispersed reactive metal centers of relatively small diameter and high surface area, while avoiding coalescence of the metal particles during their use as a reactant (Koh *et al.*, 1997; Huang *et al.*, 2006; Park & Lee, 2010; Prasanth *et al.*, 2010). MCM-41 is one such support material of interest.

MCM-41 is a silica-based, mesoporous material and member of the M41S family of materials first developed by scientists at the Mobil Corporation in 1992 (Beck *et al.*, 1992; Sayari, 1996). The M41S family contains three major forms of the material, each differentiated based on the geometry of the assembled pores. These three forms include the hexagonal MCM-41, cubic-phased MCM-48, and a lamellar phase. Of the M41S materials, MCM-41 has attracted considerable interest from researchers working in many different fields due to its possessing several interesting characteristics: exceptionally high surface areas ( $> 1,000 \text{ m}^2/\text{g}$ ) and a pore size that can be adjusted between 1.5 and 10 nm, depending on the synthesis procedure and reagents used in its synthesis (Beck *et al.*, 1992; Cheng *et al.*, 1997; Blin *et al.*, 2001; Kumar *et al.*, 2001; Jana *et al.*, 2004). Therefore, MCM-41 falls within the current IUPAC definition of mesoporosity: pore diameters which fall between those of microporous ( $< 2 \text{ nm}$ ) and macroporous ( $> 50 \text{ nm}$ ) materials (Rouquerol *et al.*, 1994).

The high surface area of MCM-41 is of particular interest in the field of catalysis as the larger the available surface area of the support, the larger the possible surface area of the metal catalyst exposed to target reagents. Dispersing small masses of transition metals over a support with surface areas in the range of those of MCM-41 presents the possibility of attaining nano-sized catalyst centres. Certain properties of nanometre-scale metal particles including solubility, reactivity, surface area, concentration of surface sites, and density of defects differ markedly

from their larger-sized, or bulk counterparts (Wang & Zhang, 1997; Chen & Elimelech, 2006; Theng & Yuan, 2008). These properties suggest that an MCM-41-supported transition metal may possess advantages with respect to reactivity when compared to catalysts composed of free metal particles, or those where metal particles are dispersed over support materials of relatively low surface area.

Many different applications for MCM-41 have been developed and described in the literature in the two decades since its initial synthesis and description. MCM-41 has been used in catalysis, separation processes, composite materials, adsorbents, and drug carriers (Landmesser *et al.*, 1997; Zhao *et al.*, 1997; Sayari *et al.*, 2005; Azaïs *et al.*, 2006). In the last ten years, researchers investigating applications for MCM-41 in the environmental sciences have found many potential uses for it in treating aqueous pollutants. These uses include as an immobilizer of metals, a reactant, and adsorbent for organic pollutants as well as for phosphate, nitrate, and cationic dyes (Ghiaci *et al.*, 2004; Algarra *et al.*, 2005; Serna-Guerrero & Sayari, 2007; Saad *et al.*, 2008; Shevchenko *et al.*, 2008; Idris *et al.*, 2011; Zanjanchi *et al.*, 2011; Jutidamrongphan *et al.*, 2012; Trouvé *et al.*, 2012). Many of these applications require some degree of modification of the MCM-41 material, either through adjusting the pore size, adding cationic species during its hydrothermal synthesis, or via post-synthesis techniques such as adding functional groups, metals, metal oxides, or other reactive substances to its surfaces and within its pores. In this sense, MCM-41 provides a versatile platform for modification and adaptation for use in many different applications.

Following its initial development and description, many different synthesis procedures for MCM-41 have been published in the literature. However, all successful procedures share three common ingredients: a solvent, a template, and a source of silica (Araujo *et al.*, 2005). MCM-41 is formed via a liquid crystal template mechanism where silica tetrahedrons form around rod-like arrangements of hexagonally organized organic surfactant micelles (Beck *et al.*, 1992; Mastalir *et al.*, 2007). The micellar organic template is then removed in the final steps of the synthesis procedure through copious washing with deionized water and a calcination step. In their seminal paper on MCM-41, Beck *et al.* (1992) presented a graphic representation of this process (Figure 3). The hydrophobic, organic template molecules migrate through solution and aggregate together, taking on several possible forms which seek to minimize the energy of interaction

between the apolar liquid crystal molecules and the polar water molecules (Hassan, 2006). The different aggregated forms of the organic template molecules are dependent on the initial concentration of the organic precursors in solution. They will take a spherical form at low concentrations of the organic templating agent. At higher concentrations, the micelles will arrange into a rod-like form, which, in the case of MCM-41, are further organized into a hexagonal arrangement. If the concentration of the organic precursor is increased still further, the final arrangement will take on a lamellar, or sheet-like form.

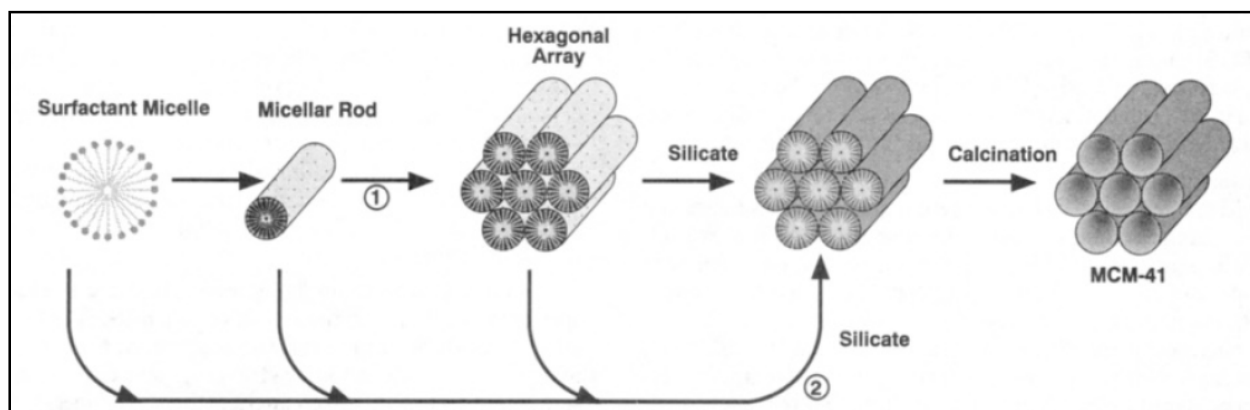


Figure 3: Graphical representation of (1) liquid crystal phase initiated pathway for the synthesis of MCM-41 (from Beck *et al.*, 1992).

The physical characteristics of the final material are also strongly influenced by the carbon chain length of the surfactant molecules making up the liquid crystal template, the molar ratio of the surfactant with respect to silica, and aspects of the synthesis procedure used in producing the material (Beck *et al.*, 1992). The pore diameter of the final material is closely related to the carbon chain length of the alkyl ammonium surfactant and so pore sizes of different samples prepared using the same surfactant molecule should be similar. However, tailoring of the MCM-41 pore diameter can be accomplished by including additional or auxiliary organic reagents; altering the proportions of organic surfactants in the reaction gel; increasing crystallization times or temperatures during synthesis; or, via post-synthesis treatments with additional reagents such as *N,N*-dimethyldecylamine (Corma *et al.*, 1997; Jana *et al.*, 2004; Araujo *et al.*, 2005; Sayari *et al.*, 2005).

Much of the research surrounding MCM-41 has been concerned with developing applications related to its high surface area. Therefore, an understanding of the surfaces of MCM-41 is

worthwhile in any work seeking to take advantage of this unique aspect of the material. Being a silica-based material, the bulk chemical composition of MCM-41 is  $SiO_2$ . The surfaces of the particles and inner pores of MCM-41 are dominated by groups which may take three forms, denoted  $Q^4$ ,  $Q^3$ , and  $Q^2$  (Landmesser *et al.*, 1997; Zhao *et al.*, 1997; Hassan, 2006). An illustration of these different groups is provided in Figure 4. The  $Q^4$  group consists of a Si atom in four-fold association with surrounding oxygen atoms, each of which is associated with another Si. This form of group is principally located in the pore walls of MCM-41 (Hassan, 2006). The  $Q^3$  group is composed of a single hydroxyl group associated with one Si. Such groups can exist singly, or be associated with neighboring silanol groups via hydrogen bonding. This type of group is the most common on the MCM-41 surface, representing up to 60% of total surface silica groups (Zhao *et al.*, 1997; Trebosc *et al.*, 2005; Hassan, 2006). The *geminal* group is denoted as  $Q^2$  and composed of two hydroxyl groups associated with a single Si. At up to 5% of the total surface groups, the *geminal* type makes up a relatively small proportion of surface groups (Zhao *et al.*, 1997; Hassan, 2006). The total combined surface density of all three groups on the surfaces and within the pores of MCM-41 is between 2.5 and 3 groups/nm<sup>2</sup> (Zhao *et al.*, 1997). Upon introducing H<sub>2</sub>O to MCM-41, either through exposure to ambient humidity or mixing with water, all silanol groups become weakly associated with H<sub>2</sub>O molecules via hydrogen bonding (Trebosc *et al.*, 2005).

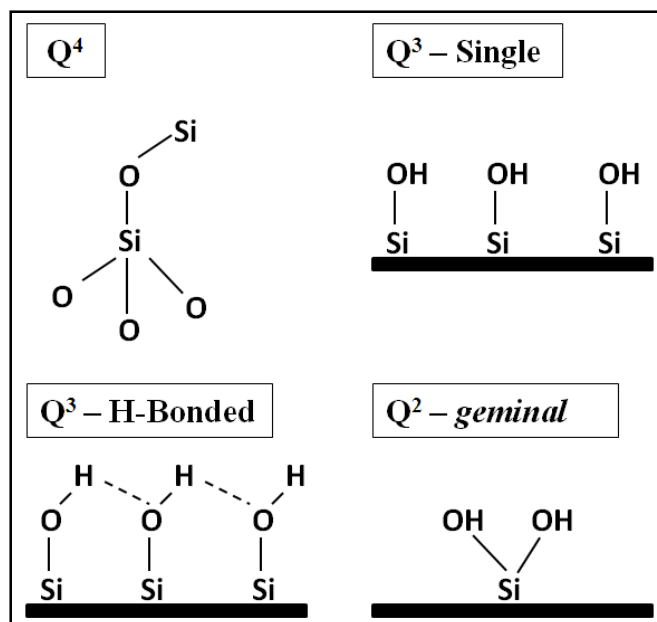


Figure 4: An illustration of the three types of surface silica and silanol groups in MCM-41 (after Zhao *et al.*, 1997; Hassan, 2006)

The MCM-41 surface is weakly acidic, but can be altered to form Brønsted acid sites via incorporation of cationic metals such as  $Al^{3+}$  during its hydrothermal synthesis (Sayari, 1996; Matsumoto *et al.*, 1999). Additionally, other reactive metals and their oxides such as Pd, Ni, Fe, Cu can be grafted to the surfaces and within the pores of MCM-41 following a post-synthesis treatment (Koh *et al.*, 1997; Lensveld, 2001; Decyk, 2006). Additional metals including Al, Co, Ti, V, Nb, Mo, and Mn may be incorporated within the MCM-41 structure during its hydrothermal synthesis (Zhang *et al.*, 1996; Matsumoto *et al.*, 1999; Lim *et al.*, 2003; Ziolk *et al.*, 2004). In these cases, a reagent containing the desired metal is included in the initial reaction gel during the early stages of MCM-41 synthesis. The metal atom then substitutes for  $Si^{4+}$  in the MCM-41 structure. This substitution may be accompanied by a corresponding decrease in the order of the material's hexagonal pore arrangement. This decreased order is the result of size differences between the metal cation and the  $Si^{4+}$  atom it replaces as well as from an increase in the uptake of charge-compensating cations such as  $Na^+$  and  $H^+$  into the MCM-41 structure to satisfy any charge imbalance between the metal and  $Si^{4+}$  (Shen & Kawi, 2002).

A brief description of the different materials that were used in the current research is provided in the following paragraphs. Detailed descriptions of the synthesis and characterization of these materials are included in the experimental and results sections of this chapter. Appendix A

contains characterization results of experimental materials not included in this chapter. Each material used in the experiments described in chapters 3 through 5 is carefully identified so that pertinent details about its synthesis and characterization can be easily found in this chapter or Appendix A.

A small number of experiments performed during the course of this research used an MCM-41 sample which was made up of calcined materials generated via three, separate synthesis batches. In the sections that follow, this material is referred to as ‘Combo 1’ as shorthand for ‘Combined Batch #1’. Combining batches was necessary as each synthesis batch could only produce small quantities of MCM-41. The largest final masses of MCM-41 produced from a single batch were generally 6 to 7 g. The majority of the experimental research work made use of a second, combined batch referred to as ‘Combo 2’. This combined batch is composed of the calcined materials produced from four separate synthesis batches. Two smaller-scale experiments described in later chapters used calcined MCM-41 samples produced from single synthesis batches. Effort was made to use a single MCM-41 material (Combo 2) for as many aspects of this research as possible. However, this was not always feasible considering the period of time over which this project took place and the large quantities of MCM-41 material required to complete the experiments. The synthesis and characterization results for these samples are included in this chapter with additional characterization results presented in Appendix A.

Pd, Ni, and bimetallic Ni-Pd impregnated MCM-41 materials were prepared using the as-synthesized, calcined MCM-41 batches mentioned in the above paragraph and are referred to as Pd/MCM-41, Ni/MCM-41, and Ni-Pd/MCM-41, respectively. The synthesis and characterization procedures for these metal-impregnated materials are described in detail in this chapter and Appendix A.

Finally, several experiments made use of Pd impregnated silica sand. These low surface area materials were used in some experiments and compared with results obtained using Pd/MCM-41. These results were included to illustrate the potential benefit afforded by the unique properties of MCM-41. As in the case of the MCM-41 samples described above, the synthesis and characterization results of these samples are included in this chapter and Appendix A.

A brief discussion regarding the safe handling of MCM-41 is pertinent before proceeding to a description of its synthesis. The relative newness of MCM-41 and lack of detailed data regarding the potential health risks of human exposure to the material mean that caution must be exercised during its use. Dry, calcined MCM-41 powder is easily dispersed into the air through handling of containers, accidental spillage, or through static charging of particles during transfer to and from glass or HDPE bottles. These air-dispersed particles, in addition to those accumulated through direct contact, present a potential health risk via exposure routes such as inhalation, contact with eyes, or indirect routes such as hand-to-mouth. These types of exposures to MCM-41 particles may increase the risk of adverse health effects given chronic exposure over time. Care should be taken to minimize the quantity of MCM-41 particles dispersed into the air while handling the material and appropriate personal protective equipment should be employed. The fineness of the material along with its chemical composition ( $SiO_2$ ) suggests that it should be handled following similar precautions as with other fine, powdered silica materials such as fumed silica. Additionally, proper care must be taken while synthesizing MCM-41 from its various precursors. Reagents including fumed silica and tetramethylammonium hydroxide pentahydrate are especially hazardous when handled without due care.

## 2.2 Experimental Methods

### 2.2.1 Reagents

Tetramethylammonium hydroxide pentahydrate (TMAOH,  $C_4H_{13}NO$ , 97%, CAS#10424-65-4, St Louis, MO) and fumed silica ( $SiO_2$ , 99.8%, CAS#112945-52-5, St. Louis, MO) were obtained from Sigma-Aldrich. Hexadecyltrimethylammonium bromide (CTABr,  $C_{19}H_{42}BrN$ , technical, CAS#57-09-0, Fair Lawn, NJ) was obtained from Fisher Scientific. Ammonium chloride ( $NH_4Cl$ , ACS reagent grade, CAS#12125-02-9, UK) was obtained from BDH. Palladium ( $Pd(NH_3)_4Cl_2 \cdot H_2O$ , 99.9%, CAS#13933-31-8, Ward Hill, MA) and two nickel sources ( $CNiO_3$ , 99%, CAS#3333-67-3, Ward Hill, MA;  $NiCl_2 \cdot 6H_2O$ , 99.3%, CAS#7791-20-0, Ward Hill, MA) were obtained from Alfa Aesar. A third nickel source ( $Ni(NO_3)_2 \cdot 6H_2O$ , 99.5%, CAS#13138-45-9, Phillipsburg, NJ) was obtained from J.T. Baker. Deionized water was used in all experimental work, unless noted otherwise.

### 2.2.2 Synthesis of MCM-41

The synthesis procedure followed for producing MCM-41 was adapted from methods described in the literature (Cheng *et al.*, 1997; Mansour *et al.*, 2002). The following procedure consistently yielded well-formed samples of MCM-41 possessing its characteristic physical features including hexagonally arranged silica mesopores and high surface areas per unit mass.

Briefly, tetramethylammonium hydroxide (TMAOH) and cetyltrimethylammonium bromide (CTABr) were dissolved in Nanopure<sup>®</sup> deionized water under gentle stirring at 300 K. Fumed silica powder was added once the initially opaque solution turned clear. The resulting mixture was stirred and heated for 3 h. The final relative molar composition of the gel was 1  $SiO_2$ , 0.19 TMAOH, 0.27 CTABr, 40  $H_2O$ . The required masses of reagents were calculated on a basis of 250 g of deionized water. This particular mass basis of deionized water was selected because it produced the largest possible volume of reaction gel that could still be enclosed in the autoclave described below. The resulting high viscosity, opaque white reaction gel was covered with Parafilm and aged for 24 h at room temperature.

The aged reaction gel was transferred to a stainless steel autoclave sealed with a Viton Teflon O-ring and heated for 68 h at 400 K. It was found that maintaining high pressure in the autoclave during this heating stage was crucial in obtaining well-formed samples of MCM-41. Failure to maintain a high-pressure seal in the autoclave at this stage would allow loss of vapour from the autoclave, producing a distinct odour of ammonia or 'spoiled fish' in the lab. In these cases, the resulting material was a grayish white, solid cake. Samples of this brittle material that were crushed and analyzed indicated an amorphous, non-mesoporous final material of low surface area. Successful completion of the hydrothermal stage of synthesis produced an opaque white, high-viscosity, paste-like gel. It was found necessary to replace the Viton Teflon O-ring in the autoclave each time an MCM-41 batch was synthesized to ensure a proper seal.

At the end of the heating stage, the reaction was arrested by quenching the autoclave under cold water for 30 min. Rapid cooling under cold water would create a vacuum within the autoclave, which rendered it difficult or impossible to open. Allowing the autoclave and its contents to re-equilibrate with ambient temperatures for 30 min ensured that the top could be removed safely and easily. The contents of the autoclave were transferred to plastic centrifuge bottles and washed with deionized water, centrifuged, and decanted. This process was repeated up to 12 times or until the conductance of the supernatant rinsate was less than 10  $\mu\text{S}/\text{cm}$ . Finally, the solid material was calcined under air for 8 h at 923 K to ensure complete decomposition and removal of the organic template as  $\text{CO}_{2(g)}$ ,  $\text{NO}_{2(g)}$ , and  $\text{H}_2\text{O}_{(g)}$  (Hassan, 2006).

The mesoporosity and hexagonal arrangement of the pores were verified by low angle X-ray diffraction analysis (XRD) between 1 and  $8^\circ 2\theta$  with a  $0.025^\circ 2\theta$  step size and 0.50 s step time. A Bruker AXS D8 Advance X-ray diffractometer with 1.5418 Å X-ray source was used for the analysis. Samples were also analyzed between  $35^\circ 2\theta$  and  $100^\circ 2\theta$  using the same diffractometer with a  $0.050^\circ 2\theta$  step size and 0.20 s step time. XRD data for some samples was collected over a wider range, between  $0.3^\circ 2\theta$  and  $112^\circ 2\theta$  using an Inel XRG 3000 diffractometer. However, diffraction data from below  $35^\circ 2\theta$  and above  $100^\circ 2\theta$  appeared to be beyond the limits of the instrument's capability and provided no useful data about the samples. Therefore, high angle XRD data is generally presented between the range of  $35^\circ 2\theta$  and  $100^\circ 2\theta$ . When necessary, peaks were indexed to possible crystal phases using *Visual XRD* (Copyright 2000, Batiste & Reardon) and *Eva* (Copyright 1996-2007, Bruker AXS) software packages.

Surface area was determined using a Micromeritics Gemini VII Surface Area Analyzer following the Brunauer-Emmet-Teller isotherm (BET) nitrogen adsorption surface area technique (Brunauer *et al.*, 1938). All samples were conditioned overnight at 473 K under a flow of N<sub>2(g)</sub> prior to surface area analysis. For simple surface area measurements, an 11 point adsorption isotherm between relative pressures (P/P<sub>o</sub>) of 0.03 and 0.50 was recorded. Relative pressures are reported as the unit-less ratio of a given pressure value 'P' to the initial pressure 'P<sub>o</sub>'. P<sub>o</sub> is equal to atmospheric pressure and was measured at the beginning of an analysis run. A full adsorption-desorption isotherm was recorded between 0.30 and 1.00 relative pressure for one sample of purely siliceous, calcined MCM-41. Full adsorption-desorption isotherms were collected using a Quantachrome Instruments Autosorb-1 surface area analyzer. These samples were degassed under vacuum at 473 K for a minimum of 2 h prior to analysis.

Full adsorption-desorption isotherms are unnecessary in calculating the surface area of a material because the BET method is based only on the linear portion of the adsorption isotherm. The linear portion of the isotherm occurs between relative pressures of 0.03 and 0.50 for MCM-41. Therefore, it was deemed unnecessary to collect full adsorption-desorption isotherms for all materials used in this research when simple calculations of sample surface area were sufficient. This decision was made based on the substantial time, cost, and difficulty in instrument scheduling necessary to collect the detailed, full adsorption-desorption isotherms. The results obtained for the one, calcined MCM-41 sample was considered as representative of similar, remaining samples prepared following similar synthesis procedures.

The morphology of a representative sample of MCM-41 was determined using a Leo 1530 Field Emission Scanning Electron Microscope (SEM). Samples were sputter coated with carbon before analysis. Carbon coating was selected over gold to avoid interference with other metals in the case of metal-impregnated MCM-41 samples. Gold and palladium produce similar signals when analyzed via energy dispersive X-ray analysis in the course of SEM imaging.

The pore structure of one sample of calcined MCM-41 sample was examined using a Philips CM20 high resolution transmission electron microscope (TEM).

### 2.2.3 Metal-impregnated MCM-41

Palladium impregnated MCM-41 (Pd/MCM-41) at various mass percent palladium loadings was prepared following a previously published procedure by Koh *et al.*, (1997) which included an ammonium exchange step. Mass percent loadings were calculated as mass of metal relative to the final sample mass. The Pd source ( $Pd(NH_3)_4Cl_2 \cdot H_2O$ ) dissociates in solution, forming  $Pd^{2+}$ . The  $Pd^{2+}$  cations in solution were deposited as palladium metal clusters on the MCM-41 surface and within pores when the sample was dried. An ammonium exchange performed on the MCM-41 sample prior to the addition of the palladium source facilitated the reduction of  $Pd^{2+}$  to palladium metal via reaction with  $NH_4^+$ . The ammonium exchange involved adding desired masses of calcined MCM-41 to 100 ml of 2 M  $NH_4Cl$  solution. The mixture was stirred for 15 min and transferred to plastic centrifuge bottles, where it was rinsed with deionized water, centrifuged, and decanted up to 12 times, or until the conductance of the supernatant rinsate was less than 10 uS/cm. Solid MCM-41 was recovered by centrifugation and dried overnight at 353 K.

Different mass percent loadings of Pd on MCM-41 were achieved by dissolving appropriate mass of  $Pd(NH_3)_4Cl_2 \cdot H_2O$  into a small volume of deionized water ( $\leq 5$  ml), which was added dropwise to the dried MCM-41 following an incipient wetness technique (Haber *et al.*, 1995). The material was then dried overnight at 353 K under air. Finally, the material was calcined under air for 3 h at 593 K.

A brief survey of the literature suggests that wet impregnation of MCM-41 with a metal dissolved in deionized water solution is effective in depositing the metal within the material's pores following a drying and calcination step. In a neutron diffraction study of water interaction with MCM-41, Tun *et al.* (2002) concluded that when MCM-41 is mixed with excess water, the water will completely fill the mesopores along their entire length with no voids or air bubbles within the pores. Entry of water into MCM-41's pores is aided by the hydrophilic silanol groups lining the interior pore surfaces of the material. Evaporation of the water from the wetted material will remove most of the water from the pores (Landmesser *et al.*, 1997). The last stage of water evaporation leaves a thin film of water on the inside surfaces of the pores followed by its complete removal (Tun *et al.*, 2002). Therefore, a solution of Pd dissolved in water should

penetrate completely into the pores of MCM-41. Subsequent evaporation of deionized water from the MCM-41 pores would leave deposits of the metal-containing compound. As a further precaution, MCM-41 samples wetted with the Pd source solution were placed under light vacuum for 30 min to ensure that the solution was drawn fully into the mesopores.

Nickel-impregnated MCM-41 (Ni/MCM-41) samples were prepared following a similar procedure as for Pd/MCM-41. Two sets of Ni/MCM-41 materials were prepared for this research using either nickel carbonate or nickel (II) chloride as the nickel source.

A series of bimetallic Ni and Pd impregnated MCM-41 (Ni-Pd/MCM-41) samples were prepared for this research following similar procedures as for the Pd/MCM-41 and Ni/MCM-41 materials described above. In these cases, appropriate masses of Ni and Pd source materials were dissolved simultaneously in a 2 M ammonium chloride solution and added dropwise to the MCM-41 samples via a similar incipient wetness method as described above. The ammonium chloride solution was used to duplicate the ammonium exchange conditions in the method described by Koh *et al.* (1997). In the case of bimetallic MCM-41 samples, the percent loading refers to the total mass of metal present relative to total sample mass. All such samples were prepared to contain 50% Ni and 50% Pd by mass and following a similar procedure as the other metal-impregnated samples described above. Therefore, the materials are denoted as X% Ni-Pd/MCM-41, where  $X = \frac{X}{2}Ni + \frac{X}{2}Pd$ .

Metal impregnated MCM-41 samples were characterized via low and high angle XRD following a similar procedure as described in Section 2.2.2. Diffraction peaks were identified using Visual XRD and EVA software when appropriate. Surface area of materials was determined via an 11-point BET nitrogen adsorption surface area analysis using the Micromeritics Gemini VII surface area analyzer. Data for constructing full adsorption-desorption isotherms between relative pressures of 0.03 and 1 were collected for a set of five Pd/MCM-41 samples over a range of Pd loadings using the Quantachrome Instruments Autosorb-1 surface area analyzer. The same set of samples was imaged and analyzed for the presence of Pd via an energy-dispersive X-ray spectroscope (EDAX) equipped Leo 1530 Field Emission Scanning Electron Microscope (SEM). Metal impregnated materials studied via EDAX were prepared by sputter-coating powdered samples with carbon. The use of carbon coating rather than gold eliminates the possibility of

peak interference between Au and Pd in EDAX results. The surface morphology of two other palladized samples was examined via scanning electron microscope (SEM). The pore size, pore structure, and Pd location in these two samples were also investigated by transmission electron microscope (TEM). A series of Pd and Ni-Pd-impregnated MCM-41 samples were analyzed for total Pd concentration by fire assay with inductively coupled plasma (ICP). A second set of Ni in addition to the same Ni-Pd-impregnated samples were analyzed for total Ni concentration by  $HNO_3 - HF - HClO_4 - HCl$  digestion and atomic absorption spectroscopy (AAS). Samples were prepared by mixing approximately 65 mg of metal impregnated samples with approximately 30 g of 50-70 mesh Ottawa silica sand. This dilution of the metal impregnated samples was necessary to stay within the acceptable range of concentrations for the analysis techniques. Analysis results were multiplied by the calculated dilution factor for each sample to obtain the real concentration values. Control samples containing only 50-70 mesh Ottawa silica sand were also analyzed to eliminate the possibility of any Pd and Ni contamination present in the diluent sand.

#### **2.2.4 Pd-impregnated silica sand**

One experiment performed for the current research also made limited use of palladized silica sand materials (Pd/sand). These materials were used to ascertain the comparative benefit of using MCM-41 as a transition metal support.

Pd/sand samples were prepared by adding masses of 50-70 mesh Ottawa silica sand to a 500 ml beaker containing 400 ml of a 10% by volume nitric acid solution at ambient temperatures. The sand was vigorously stirred in the acid solution for 30 min using a magnetic stir bar. The purpose of the acid washing step was to remove any residual iron or other residual reactive metal contaminants that may have been present on the surfaces of the sand particles. After stirring, the sand was allowed to settle in the beaker for 5 min and the supernatant acid solution was decanted and discarded. The recovered sand was rinsed repeatedly with deionized water until the supernatant pH trended towards a constant value of approximately 5. The recovered sand was dried under air overnight at 353 K. This acid washed sand was then used in preparing the Pd/sand samples following similar procedures and using the same Pd source as for the Pd/MCM-41 described above in Section 2.2.3.

Surface area of Pd/sand samples was determined from an 11 point adsorption isotherm between relative pressures of 0.03 and 0.5 using the Micromeritics Gemini VII and following the BET nitrogen adsorption surface area analysis technique. Samples were analyzed for total Pd concentration by fire assay with inductively coupled plasma (ICP).

## **2.3 Results and Discussion**

### **2.3.1 MCM-41**

The final, calcined MCM-41 material presents as a loose, white powder. The relatively low density of the powdered material lends it a characteristically fluffy texture when handled. In this sense, it is similar to fumed silica. Final materials were stored in tightly sealed HDPE bottles. Sample bottles intended for long periods of storage were kept loose-capped under light vacuum in a desiccation vessel. The following sections discuss in detail the results of physical characterization for selected calcined MCM-41 samples. Detailed characterization data for the remaining MCM-41 materials used in this research may be found in Appendix A.

#### **2.3.1.1 Low Angle X-Ray Diffraction**

An example of a low angle XRD pattern for a calcined MCM-41 sample prepared by a single synthesis batch is presented in Figure 5. A complete set of small angle XRD patterns for all MCM-41 samples prepared as single batches is presented in Appendix A. The small angle XRD pattern for a well-formed example of MCM-41 displays a minimum of three prominent peaks between 1 and 8° 2 $\theta$ . These first three peaks are labelled (100), (110), and (200) according to the Miller indices of a hexagonal unit cell. Although the indices for a hexagonal unit cell can be described using four integers in the form (*hkil*), the convention in the MCM-41 literature is to omit the *i* value as it is simply based on the *h* and *k* values ( $i = -(h + k)$ ). The XRD plot in Figure 5 exhibits all three of these characteristic, prominent peaks, indicating that the sample is composed of hexagonally arranged mesopores (Mansour *et al.*, 2002). The fourth peak, labelled 210 is sometimes seen along with a fifth peak (300) in exceptionally well-formed samples of MCM-41.

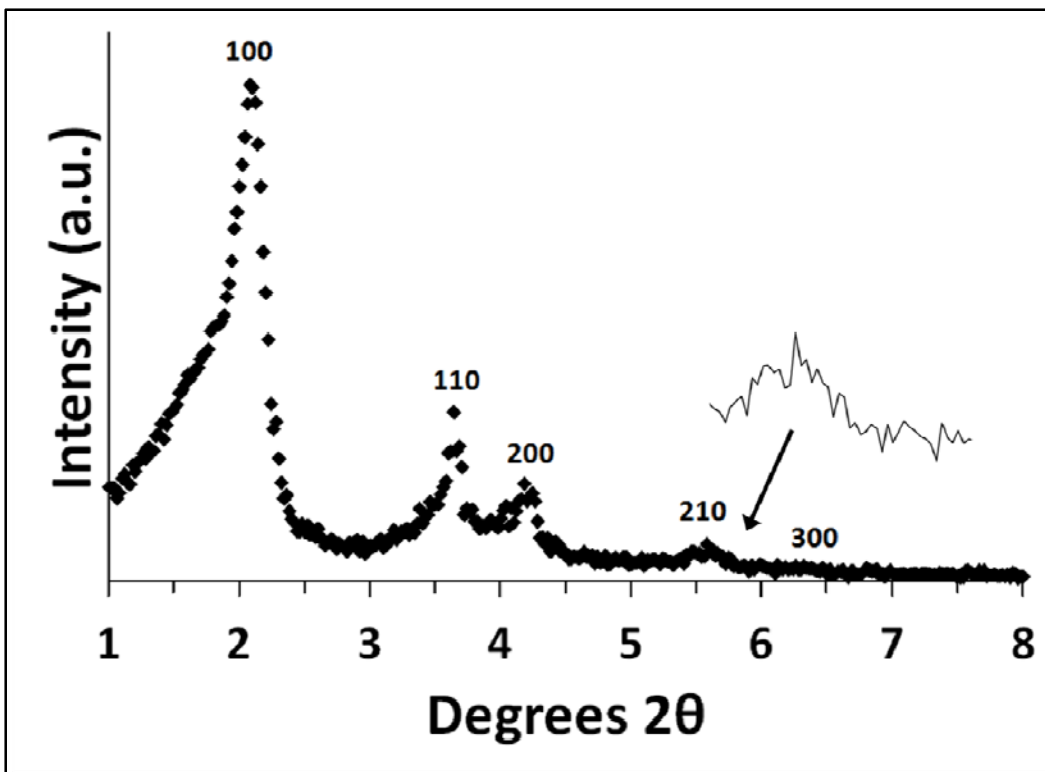


Figure 5: Example low angle XRD plot for calcined MCM-41 produced from an individual synthesis batch (sample MCM-2D).

An example of low angle XRD results for a combined batch is presented in Figure 6. Several differences may be noted between the low angle XRD results for a combined and an individually synthesized MCM-41 batch by comparing Figure 5 and Figure 6. In Figure 6, the peaks labelled as 110 and 200 are not as sharp as those of Figure 5. Additionally, the distinct peak labelled 210 in Figure 5 is somewhat less distinct in Figure 6, although it is still easily discernible in the inset plot. It is proposed that the reason for these differences is an averaging of the physical characteristics of each of the four individually synthesized batches when combined to make Combo 2. A wider distribution of characteristics such as pore diameter and arrangement of mesopores would produce wider peaks compared to samples with narrow distributions of these characteristics. Regardless, low angle XRD results for the four individual batches each demonstrate sharp, distinct peaks, with some samples exhibiting the (300) peak only seen in exceptionally well-formed samples (Mansour *et al.*, 2002). Therefore, low angle XRD results for the individual batches composing Combo 2 indicate well-formed MCM-41 samples and thus it may be concluded that Combo 2 itself is composed of well-formed MCM-41.

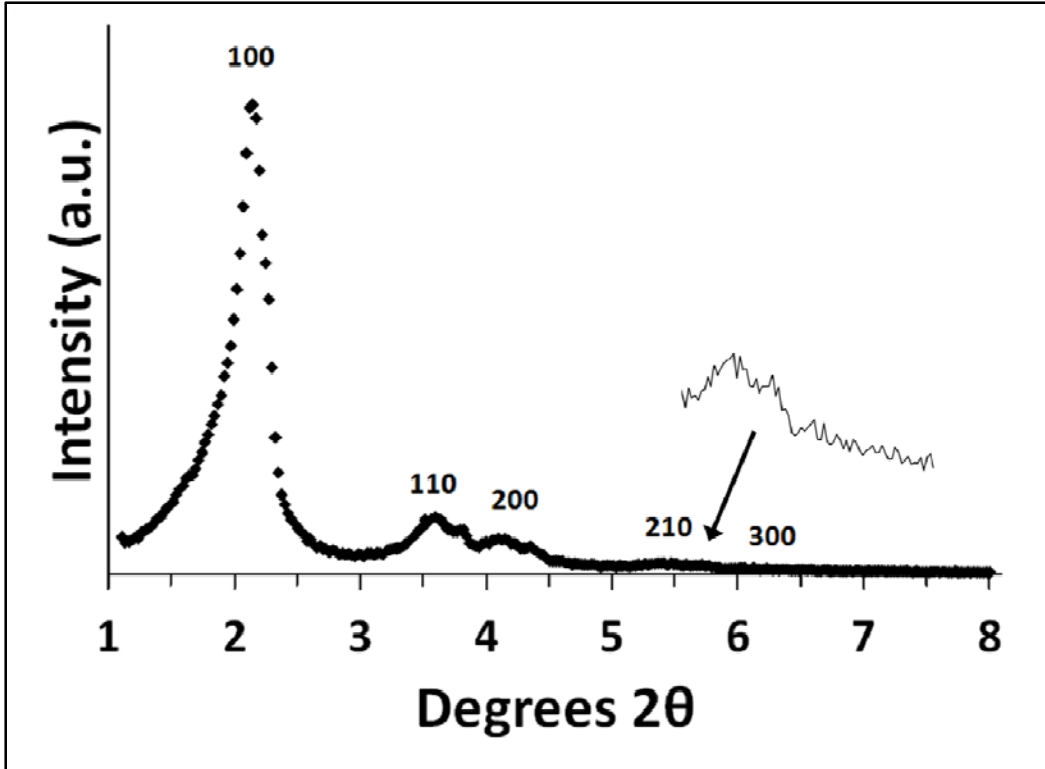


Figure 6: Low angle XRD results for combined batch ‘Combo 2’, an MCM-41 sample composed of materials produced from four separate synthesis batches.

Low angle XRD results were used in calculating the cell parameter “a” based on the  $2\theta$  position of the maximum intensity peak (100) and Bragg’s Law:

$$2d_{100}\sin\theta = n\lambda$$

$$a = (2/\sqrt{3}) * d_{100}$$

where ‘n’ is an integer equal to 1 and the wavelength parameter  $\lambda$  is equal to 1.5418 Å. The repeating structure of MCM-41 results from the arrangement of the mesopores. Therefore, cell parameter values correspond to the pore centre-to-centre distance and include the radii of two, adjacent pores and the thickness of the pore wall separating them (Beck *et al.*, 1992). The cell parameter value can provide a simple estimate of the relative size of pore diameters when comparing samples of MCM-41. The primary mesopore diameter ( $W_d$ ) can be calculated using the following equation:

$$W_d = cd\left(\frac{\rho V_p}{1 + \rho V_p}\right)^{1/2}$$

where the constant ‘c’ is equal to 1.213 for pores that are circular in cross-section (Kruk & Jaroniec, 1999; Kruk *et al.*, 2000), d is the d-spacing of the (100) peak, and  $\rho$  is the pore wall density, assumed equal to 2.2 cm<sup>3</sup>/g for amorphous silicas (Kruk *et al.*, 1997). The parameter  $V_p$  is the primary mesopore volume and is equal to 0.91 cm<sup>3</sup>/g based on the carbon chain length of the organic surfactant (Kruk *et al.* 1997). The organic surfactant used in synthesizing all MCM-41 samples for this research was CTABr (C<sub>19</sub>H<sub>42</sub>BrN), which has a chain length of 16. Pore wall thickness (Wt, below) is calculated by subtracting the primary mesopore diameter from the cell parameter. The results of these calculations for all calcined MCM-41 samples used in this research are summarized in Table 1. All average values presented in Table 1 were calculated using individual synthesis batch materials. Results for Combo 1 and Combo 2 are omitted from calculation of averages. The  $\pm$  values were calculated as the 95% confidence interval of the average values. This is true for all  $\pm$  values reported in the following document. The average primary mesopore diameter of 4.31  $\pm$  0.08 nm is within the definition of mesoporosity (between 2 and 50 nm) as well as the accepted range for calcined MCM-41 (between 1.5 and 10 nm).

**Table 1: Summary of physical characteristics of calcined MCM-41 determined from XRD analysis.**

Sample	2 $\theta$ (100)	d100	a (nm)	Wd (nm)	Wt (nm)
<b>Combo 1</b>	2.09	42.4	4.89	4.20	0.70
MCM - 1A	2.04	43.3	5.01	4.29	0.71
MCM - 1B	2.08	42.5	4.91	4.21	0.70
MCM - 1C	2.04	43.3	5.01	4.29	0.71
<b>Combo 2</b>	2.13	41.6	4.80	4.12	0.68
MCM - 2A	2.06	42.8	4.95	4.24	0.70
MCM - 2B	1.98	44.6	5.15	4.42	0.73
MCM - 2C	1.96	45.1	5.21	4.47	0.74
MCM - 2D	2.07	42.7	4.93	4.23	0.70
<b>Individual Batches</b>					
MCM - 3	1.97	44.8	5.17	4.43	0.73
MCM - 4	2.07	42.6	4.92	4.22	0.70

<b>Average</b>	<b>2.03</b>	<b>43.4</b>	<b>5.03</b>	<b>4.31</b>	<b>0.71</b>
$\pm$	0.04	0.8	0.09	0.08	0.01

### 2.3.1.2 High Angle X-Ray Diffraction

An example of a high angle XRD pattern for calcined MCM-41 produced from a single synthesis batch is presented below in Figure 7 (A). This sample was analyzed in an aluminum

sample holder. The XRD pattern for a combined batch of MCM-41 material is presented in Figure 7 (B). Combo 2 was analyzed in an epoxy sample holder. Other high angle XRD plots for calcined MCM-41 samples used in this research are presented in Appendix A. An apparent increase in the proportion of noise in the result for Combo 2 relative to MCM-2B results from the expanded x-axis in Figure 7 (B). It is clear from inspecting Figure 7 (A) that all distinct peaks are found between d-spacings of 1.0 and 2.5. The trace for MCM-2B using the aluminum sample holder shows a large shoulder at a d-spacing of 4.0 and six sharp peaks between d-spacings of 1.0 and 2.5. The large shoulder at d-spacing 4.0 indicates the amorphous nature of the sample. This result is to be expected given that the MCM-41 pore walls are composed of amorphous  $SiO_2$ . This shoulder is observed at a similar d-spacing in all large angle XRD results for calcined MCM-41 samples.

The six distinct peaks were identified using Visual XRD software. Three of the six, at d-spacings of 1.229, 2.057, and 2.358, were identified as aluminum. The remaining three peaks, at d-spacings of 0.934, 1.177, and 1.450 could not be attributed to any crystalline solid using Visual XRD. However, as MCM-2B was analyzed using an aluminum sample holder and Combo 2 was analyzed using an epoxy holder, it is clear that all six peaks in the MCM-2B sample can be attributed to the presence of the aluminum sample holder. Once the effect of the aluminum sample holder was noted, all future XRD analyses were performed using an epoxy sample holder. The six peaks were absent in any analysis performed using the epoxy sample holder. Samples analyzed using the aluminum sample holder were not re-analyzed using the epoxy holder. XRD analysis of calcined MCM-41 at high angles ( $> 8^\circ 2\theta$ ) confirms only that the material is amorphous. Therefore, high angle XRD analysis of purely siliceous, calcined MCM-41 samples is of little utility unless the presence of other crystalline phases is expected.

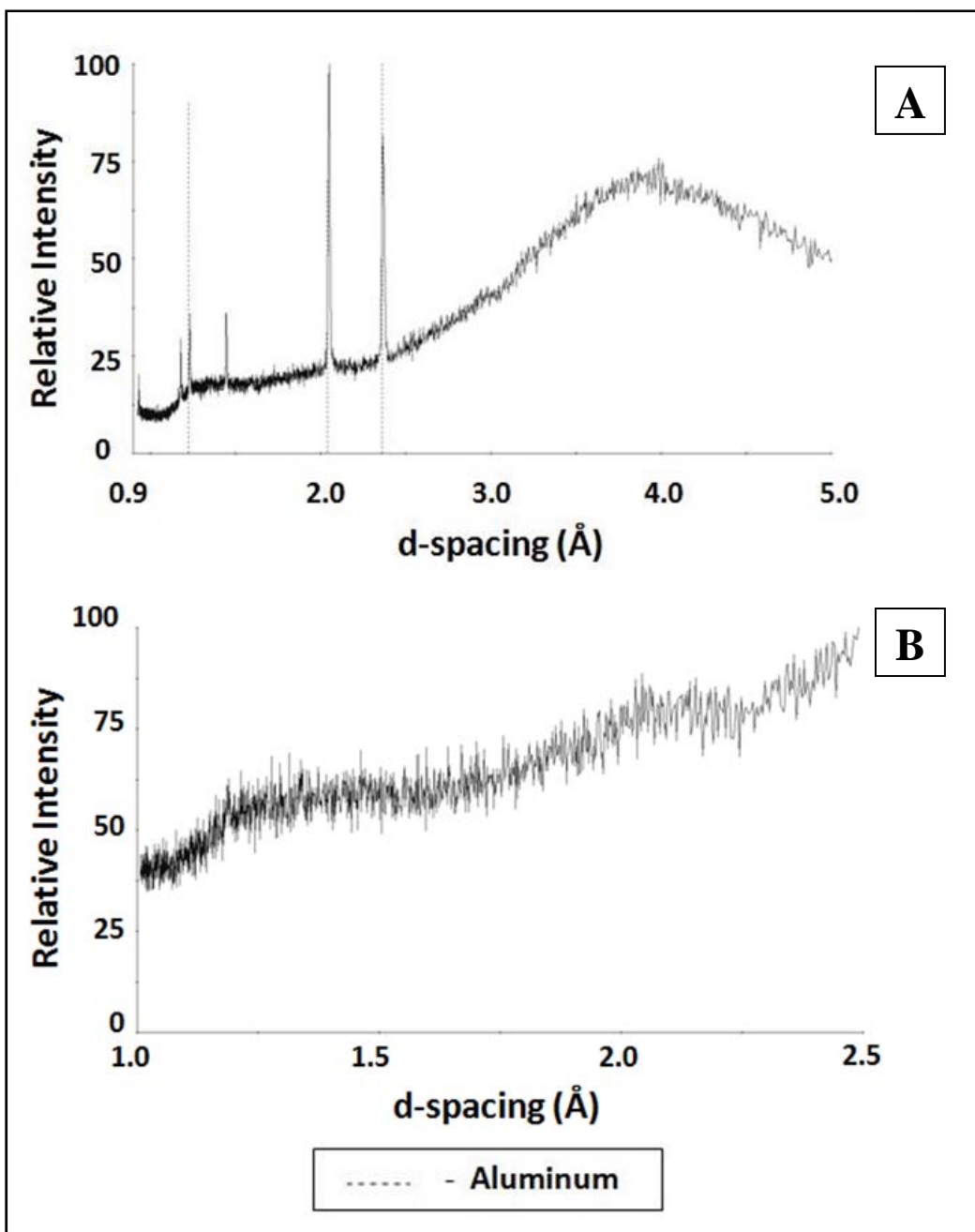


Figure 7: Comparison between (A) single synthesis batch calcined MCM-41 in aluminum sample holder (sample MCM-2B), and (B) calcined combined batch of MCM-41 analyzed in an epoxy sample holder (Combo 2). Peaks in (A) were indexed to aluminum using Visual XRD.

### 2.3.1.3 BET Nitrogen Adsorption Surface Area Analysis

BET surface area data collected using the Micromeritics Gemini VII instrument for all materials are summarized and presented in Table 2. Results of the BET nitrogen adsorption surface area analyses and plots of the 11 point adsorption isotherms for all MCM-41 materials

are presented in Appendix A. The average BET surface area of all MCM-41 samples was  $983 \pm 50 \text{ m}^2/\text{g}$ . This result is within the expected range for well-formed sample of calcined MCM-41. Calculation of the average surface area did not include results from the combined batches Combo 1 and Combo 2. The surface area of batch MCM-3 was relatively low compared to other MCM-41 samples. However, it still possessed high surface areas with low angle XRD results confirming the characteristic hexagonal mesoporosity of an MCM-41 material (Appendix A).

**Table 2: BET nitrogen adsorption surface area results for calcined MCM-41 samples.**

Sample	SA ( $\text{m}^2/\text{g}$ )
<b>Combo 1</b>	1016
MCM - 1A	1049
MCM - 1B	1072
MCM - 1C	983
<b>Combo 2</b>	1000
MCM - 2A	1036
MCM - 2B	978
MCM - 2C	948
MCM - 2D	1000
<b>Individual Batches</b>	
MCM - 3	874
MCM - 4	911

<b>Average</b>	<b>983</b>
$\pm$	50

Data for plotting the full adsorption-desorption isotherms for Combo 2 was collected using the Quantachrome Autosorb-1 instrument over relative pressures of 0.05 to 1.00 (Figure 8). The BET surface area was calculated using the linear portion of the adsorption isotherm between relative pressures of 0.05 and 0.3. The sharp vertical step of the isotherms between relative pressures of 0.25 and 0.50 indicates a narrow distribution of pore diameters in the sample. The BET surface area result for this analysis was  $1,670 \text{ m}^2/\text{g}$ . This value is 50% higher than the result determined via the Micromeritics Gemini VII. The analysis carried out using the Autosorb-1 instrument was problematic. Evidence of this is shown by the small vertical translation of the desorption isotherm from the adsorption isotherm. The first and last volume adsorbed versus relative pressure points at a relative pressure of 0.05 should be superimposed. In addition, the total volume of adsorbed  $N_2$  per gram of sample is unusually high, resulting in the high surface area result. This result was attributed to an instrument malfunction in the opinions of both the

author and the technician charged with maintaining the instrument. The malfunction most likely resulted from a pressure leak in the instrument manifold. The vertical translation cannot be reliably corrected. This malfunction is the most likely reason for the large discrepancy in reported surface areas between the two instruments. It is proposed that the results included in Table 2 more closely approximate the real surface area of the MCM-41 sample. The identification of a narrow pore size distribution based on the vertical step is independent of the vertical translation between the isotherms. Therefore, full isotherm results presented in Figure 8 can still yield useful information about the MCM-41 sample and are thus included in this document, regardless of the possible instrument malfunction.

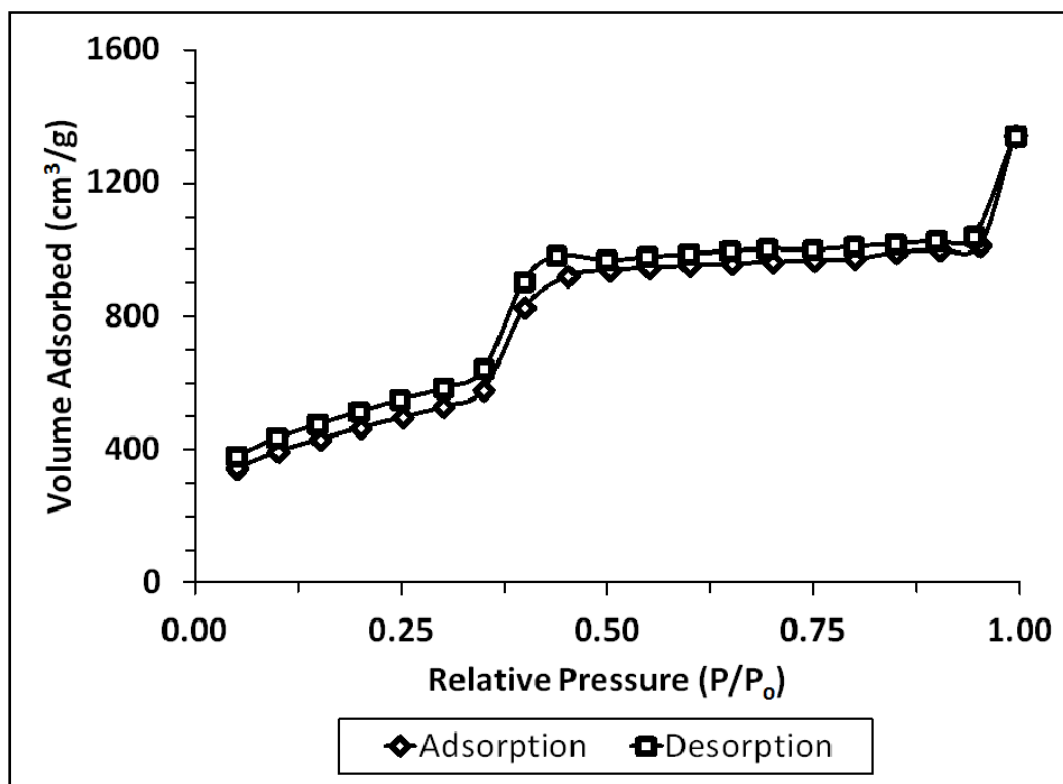


Figure 8: Full adsorption-desorption isotherm results for a combined batch of MCM-41 (Combo 2).

The average pore radius for Combo 2 calculated from results obtained using the Autosorb-1 instrument was 1.3 nm. It is proposed that the value of 1,000 m<sup>2</sup>/g presented in Table 2 more closely approximates the real surface area of the sample. Consistency of surface area results shown in Table 2, which are all within an acceptable range for MCM-41, also supports the proposition that these values can be assumed as the more accurate of the two data sets.

#### 2.3.1.4 SEM and TEM

A scanning electron microscope (SEM) image demonstrating the morphology of a typical calcined MCM-41 sample is shown in Figure 9. The left image, at lower magnification, shows a relatively homogeneous distribution of particle size and morphology. Estimated diameter of a particle in the image at lower magnification is 5 to 10  $\mu\text{m}$ . The right image shows the same sample at higher magnification. At this scale, the particles show a somewhat greater range of size and morphology. The sample appears to be composed of oblong particles with a variety of different particle geometries and orientations. Estimated particle length along the longer axes is in the range of 10 to 15  $\mu\text{m}$ . Estimated particle width across the shorter axes is in the range of 5 to 10  $\mu\text{m}$ . It appears that there may be many smaller particles present in the range of 2 to 5  $\mu\text{m}$  along their largest dimension. However, it is not possible to determine if these are in fact separate particles or are protrusions connected to the larger particles. Distinguishing individual particles in the image at the higher magnification is further complicated by layering of the particles on the sample holder. The sample morphology seen at the higher magnification in Figure 9 is similar to that of the MCM-41 sample shown in Figure 2 (A). Both of these samples were prepared using similar reagents and synthesis procedures. This type of MCM-41 morphology has been described as ‘wormy’ in the literature (Gaydhankar *et al.*, 2005).

While Beck *et al.* (1992) reported stand-alone, hexagonal particles of MCM-41, there has been a wide variety of possible particle morphologies for MCM-41 samples demonstrated in the literature. Particle geometries may range between spheres and elongated rods and may be stand-alone particles or aggregations of individual particles (Mokaya, 2002). Materials with a range of different morphologies may still be considered as MCM-41 as long as they retain the characteristic hexagonal mesoporosity and high surface areas of the material.

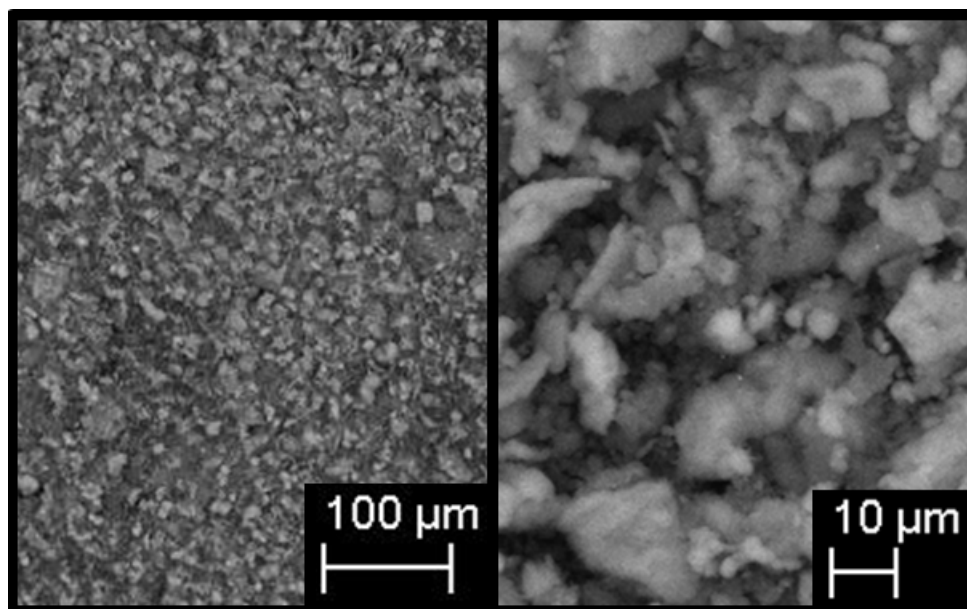


Figure 9: SEM image of calcined MCM-41 particles (Combo 2).

A transmission electron microscope (TEM) image of a calcined MCM-41 sample is presented in Figure 10. This sample was not used in experiments described in later chapters, but was produced from a batch synthesized using the same reagents and procedures described in Section 2.2.2. The image serves to illustrate several key features of MCM-41 as they are revealed by TEM. The arrow denotes a sharp transition to a light gray, un-mottled pattern in the upper left quadrant which is distinct from the darker, mottled pattern in the rest of the image. This distinct transition is proposed to represent an MCM-41 particle boundary. The regularity and ‘spotting’ of the colour pattern in the other three quadrants is a consequence of the hexagonally-arranged mesopores of the sample. By this interpretation, the cell parameter ‘a’ is represented by the separation between centres of the lighter, grayish-white spots. The separation between 50 centres was measured and the average value was found to be  $4.6 \pm 0.3$  nm. This result is in good agreement with the average cell parameter value determined via X-ray diffraction in Table 1 ( $a = 5.03 \pm 0.09$  nm). By assuming an average pore wall thickness (Wt) of 0.71 nm as shown in Table 1, the average pore diameter can be calculated from the TEM results. This value was found to be  $3.9 \pm 0.3$  nm. This result is within the acceptable range for a sample of calcined MCM-41.

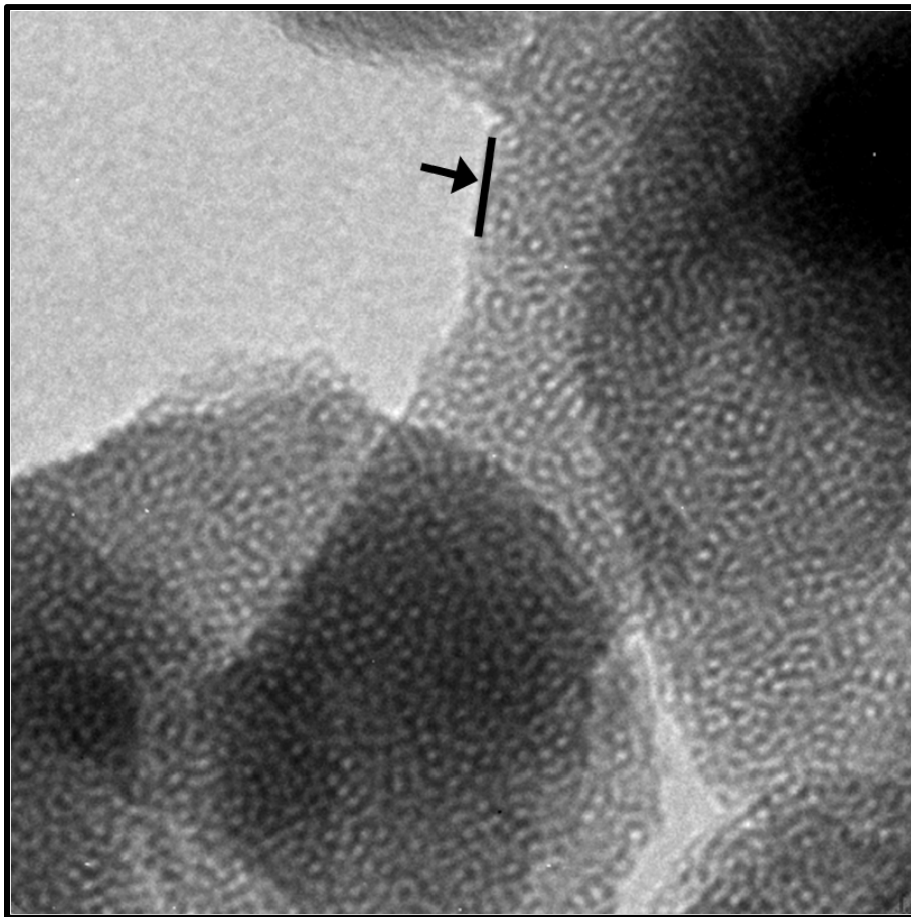


Figure 10: TEM image of calcined MCM-41 showing porosity. Width of image is 200 nm. Arrow indicates a proposed boundary of an MCM-41 particle.

### 2.3.2 Metal Impregnated MCM-41

Three varieties of metal impregnated MCM-41 materials were produced at different mass percent loadings of metal relative to the final sample mass. The three varieties included Pd, Ni, and Ni-Pd as described in Section 2.2.3. A list of these different samples, their parent MCM-41 material, the metal source used in their synthesis, and the calculated mass percent loadings of the metal are included below in Table 3. Mass percent loadings were calculated as the mass of metal added during synthesis relative to the final sample mass. These samples will be referred to by their calculated mass percent loading of metal. For example, 0.12% Pd/MCM-41 refers to an MCM-41 sample impregnated with 0.12% by mass Pd, while 0.13% Ni-Pd/MCM-41 refers to a sample impregnated with approximately equal masses of each metal such that the total mass of both metals combined is equal to 0.13% of the final sample mass.

**Table 3: Summary and calculation of percent mass loadings of metal on MCM-41.**

Metal	Metal Source	Parent Material	MCM-41 (g)	Metal Source (mg)	Metal (mg)	Yield (g)	% Loading
Pd	$Pd(NH_3)_4Cl_2 \cdot H_2O$	Combo 2	5.5627	14.396	5.61	4.7485	0.12
			1.0007	20.686	8.07	0.9973	0.81
			1.0099	26.154	10.20	1.0256	0.99
			0.9918	28.287	11.03	1.0017	1.10
			5.8384	151.253	58.99	5.0794	1.16
			0.9833	44.900	17.51	0.9938	1.76
			0.9999	59.016	23.02	1.0014	2.30
		Combo 1	17.202	442	172	13.984	1.23
			8.573	660	257	7.423	3.47
			MCM-4	8.537	200	78.0	7.745
Ni	$NiCl_2 \cdot 6H_2O$	Combo 2	1.3195	6.420	1.59	1.1570	0.14
			1.0005	40.926	10.11	0.9889	1.02
			0.5016	23.842	5.89	0.5251	1.12
			1.3018	61.860	15.28	1.1545	1.32
	$CNiO_3$	Combo 2	5.869	14.260	7.05	6.0350	0.12
			5.2740	125.174	61.89	5.5141	1.12
Ni-Pd	$NiCl_2 \cdot 6H_2O$ & $Pd(NH_3)_4Cl_2 \cdot H_2O$	Combo 2	2.0000	Pd: 3.104	1.21	1.9222	0.13
				Ni: 4.869	1.20		(Ni/Pd = 0.99)
			1.0070	Pd: 13.037	5.08	1.0055	1.01
		Ni: 20.505	5.06		(Ni/Pd = 1.00)		
	$Ni(NO_3)_2 \cdot 6H_2O$ & $Pd(NH_3)_4Cl_2 \cdot H_2O$	Combo 2	1.0116	Pd: 15.0865	5.88	0.9753	1.22
				Ni: 29.6793	5.99		(Ni/Pd = 1.02)

### 2.3.2.1 Low Angle X-ray Diffraction

An example result of low angle X-ray diffraction (XRD) analysis for a sample of Pd impregnated MCM-41 is presented in Figure 11. The full set of low angle XRD results for metal-impregnated samples used in the present study are included in Appendix A. Samples denoted 1.23%, 3.47%, and 1.01% Pd/MCM-41 were prepared during early stages of this work and were not analyzed via XRD. However, these samples were prepared following the same procedure as other Pd/MCM-41 materials and are expected to share similar characteristics as revealed by XRD analyses. Low angle XRD analysis was performed on the parent material for these samples.

The plot in Figure 11 may be compared to the low angle XRD results for the parent material (Combo 2) presented in Figure 6. Immediately apparent is the broadening of the initially sharp and distinct peaks with a substantial loss in intensity relative to background noise of the (110) and (200) peaks. The (210) peak identified in the parent material is no longer discernible in Figure 11. This loss in intensity, broadening, and loss of certain peaks was typical of metal impregnated samples produced for the current research. Although some metal impregnated

materials retain the (100) and (200) peaks to a certain extent, there was always a clear loss in intensity relative to the calcined, parent MCM-41 material (Appendix A).

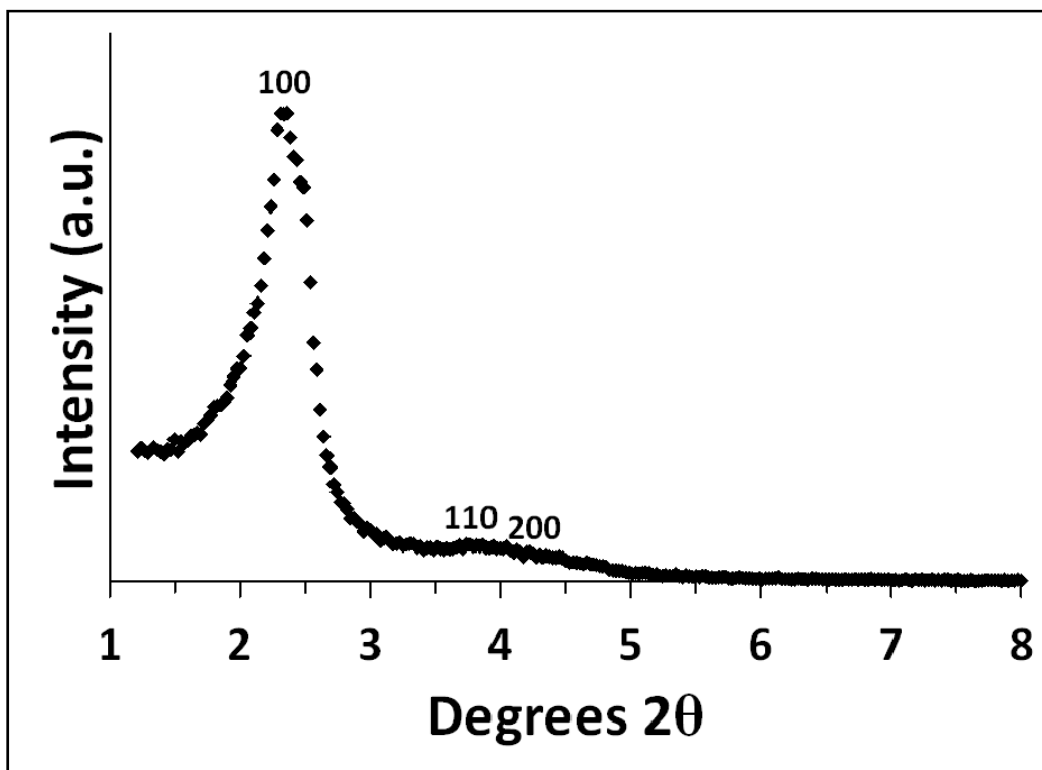


Figure 11: Low angle XRD results for a palladized MCM-41 sample (0.81% Pd/MCM-41).

The  $2\theta$  positions of the (100) peak for all metal impregnated samples summarized below in Table 4 have increased, resulting in a corresponding decrease in the value of the cell parameter ‘a’. Cell parameters were calculated for the samples following the method described in Section 2.3.1. As a result of decreased cell parameter values, the primary mesopore diameter ( $W_d$ ) for all samples also decreased an average of  $7.4 \pm 1.4\%$  relative to the parent material. Results tabulated in Table 4 demonstrate that this apparent decrease in pore diameter is typical of all metal impregnated MCM-41 samples prepared for the current research.

**Table 4: Summary of calculated cell parameter values for metal impregnated MCM-41 samples. Percent change in primary mesopore diameter (Wd) relative to the parent material (Combo 2) is noted.**

Metal	Metal Source	% Loading	2 $\theta$ (100)	d100	a (nm)	Wd (nm)	Wt (nm)	% $\Delta$ Wd
Pd	$Pd(NH_3)_4Cl_2 \cdot H_2O$	0.12%	2.19	40.3	4.66	3.99	0.66	-3.01
		0.81%	2.35	37.7	4.35	3.73	0.62	-9.80
		0.99%	2.36	37.4	4.32	3.70	0.61	-10.6
		1.10%	2.28	38.8	4.48	3.84	0.64	-6.86
		1.16%	2.19	40.3	4.66	3.99	0.66	-3.01
		1.76%	2.27	38.9	4.49	3.85	0.64	-6.59
		2.30%	2.35	37.6	4.34	3.72	0.62	-10.1
Ni	$NiCl_2 \cdot 6H_2O$	0.14%	2.30	38.5	4.44	3.81	0.63	-7.69
		1.02%	2.32	38.1	4.40	3.77	0.62	-8.73
		1.12%	2.28	38.7	4.47	3.83	0.64	-7.12
		1.32%	2.29	38.6	4.46	3.82	0.63	-7.38
	$CNiO_3$	0.12%	2.22	39.9	4.60	3.95	0.65	-4.15
		1.12%	2.22	39.9	4.60	3.95	0.65	-4.15
Ni-Pd	$NiCl_2 \cdot 6H_2O$ & $Pd(NH_3)_4Cl_2 \cdot H_2O$	0.13%	2.35	37.6	4.34	3.72	0.62	-10.1
		1.01%	2.34	37.8	4.36	3.74	0.62	-9.54
	$Ni(NO_3)_2 \cdot 6H_2O$ & $Pd(NH_3)_4Cl_2 \cdot H_2O$	1.22%	2.33	37.9	4.37	3.75	0.62	-9.24

### 2.3.2.2 High Angle X-ray Diffraction

The results of high angle X-ray diffraction (XRD) analyses for five different metal impregnated samples prepared using different metals and metal sources are presented on a single chart in Figure 12. Other high angle XRD results for metal impregnated samples used in this research are included in Appendix A. From top to bottom, the five traces in Figure 12 represent results for the following samples:

1. 1.12% Ni/MCM-41 prepared using  $CNiO_3$
2. 1.22% Ni-Pd/MCM-41 prepared using  $Ni(NO_3)_2 \cdot 6H_2O$  and  $Pd(NH_3)_4Cl_2 \cdot H_2O$
3. 1.01% Ni-Pd/MCM-41 prepared using  $NiCl_2 \cdot 6H_2O$  and  $Pd(NH_3)_4Cl_2 \cdot H_2O$
4. 1.32% Ni/MCM-41 prepared using  $NiCl_2 \cdot 6H_2O$
5. 2.30% Pd/MCM-41 prepared using  $Pd(NH_3)_4Cl_2 \cdot H_2O$

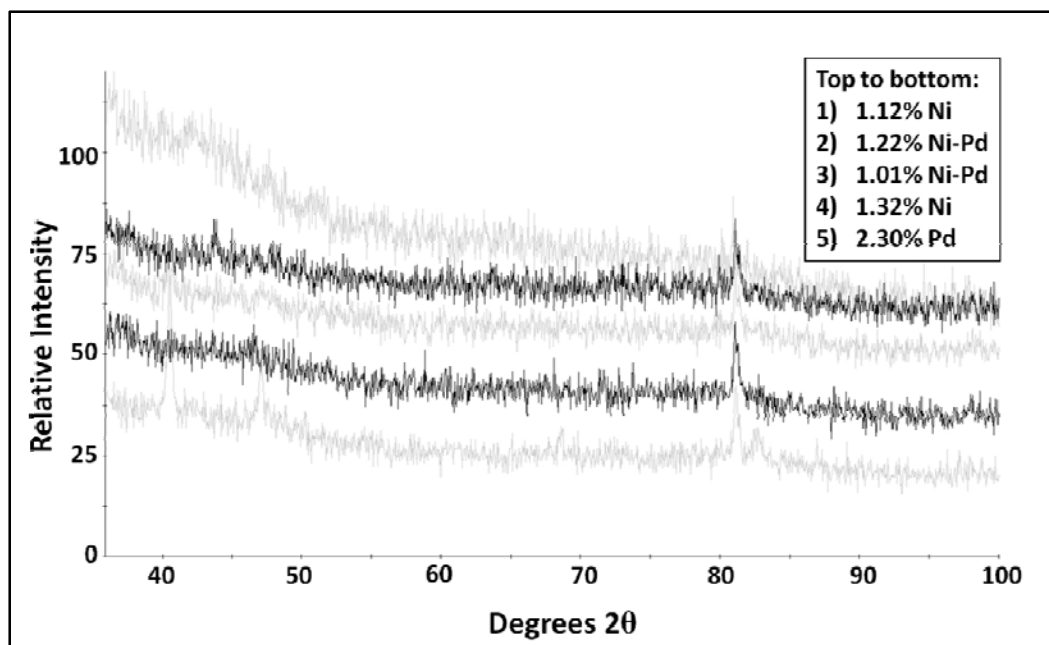


Figure 12: High angle XRD results for five metal impregnated MCM-41 samples prepared using different metals (Pd, Ni, Ni-Pd) and different metal sources.

The plots in Figure 12 are included to demonstrate that all five types of metal impregnated MCM-41 samples share a common peak at approximately  $80.7^{\circ}2\theta$ . Despite attempts to match this peak to a known crystalline phase using both Visual XRD and Eva software, it remains unidentified. Neither piece of software returned a reasonable match for any combination of possible elements present in the sample including different contaminants such as Al. The different species present in the metal sources used in preparing the five samples are summarized in Table 5. The lack of any common species between these five samples suggests that this peak is not associated with a crystalline phase originating from the metal source reagents. The peak could be attributed to the parent MCM-41 material (Combo 2), however, a possible peak at  $80.7^{\circ}2\theta$  (d-spacing = 0.12 nm) is not discernible given the background noise of the plot in Figure 7 (B). It is unlikely that this peak resulted from a malfunction of the instrument or was influenced by the epoxy sample holder used during analysis of metal impregnated samples. Therefore, the peak is assumed to be an artifact of the instrument or equipment used in the analysis.

**Table 5: Comparison of common species between metal sources in five metal impregnated MCM-41 samples.**

Sample	Species Present in Metal Source				
	Pd	Ni	N	Cl	C
1. 1.12% Ni/MCM-41		x			x
2. 1.22% Ni-Pd/MCM-41	x	x	x	x	
3. 1.01% Ni-Pd/MCM-41	x	x	x	x	
4. 1.32% Ni/MCM-41		x		x	
5. 2.30 % Pd/MCM-41	x		x	x	

Most metal impregnated MCM-41 samples had loadings of metal that were too low to produce a distinct XRD peak corresponding to the metal in high angle analysis results. The use of bulk sample XRD analysis for identification and quantification of metal species at such low concentrations is not possible. No attempt was made to quantify metal concentrations in metal impregnated MCM-41 samples based on XRD results. However, results for 2.30% Pd/MCM-41 provide an example of high angle XRD results at a higher mass percent metal loading where metal-indexed peaks were positively identified. A plot of high angle XRD results for the 2.30% Pd/MCM-41 sample is provided in Figure 13. Peaks were identified as palladium metal using Eva software. No palladium oxides or other palladium compounds were detected. As discussed above, the distinct peak between 80 and 81° 2θ is tentatively assigned to some aspect of the parent material (Combo 2).

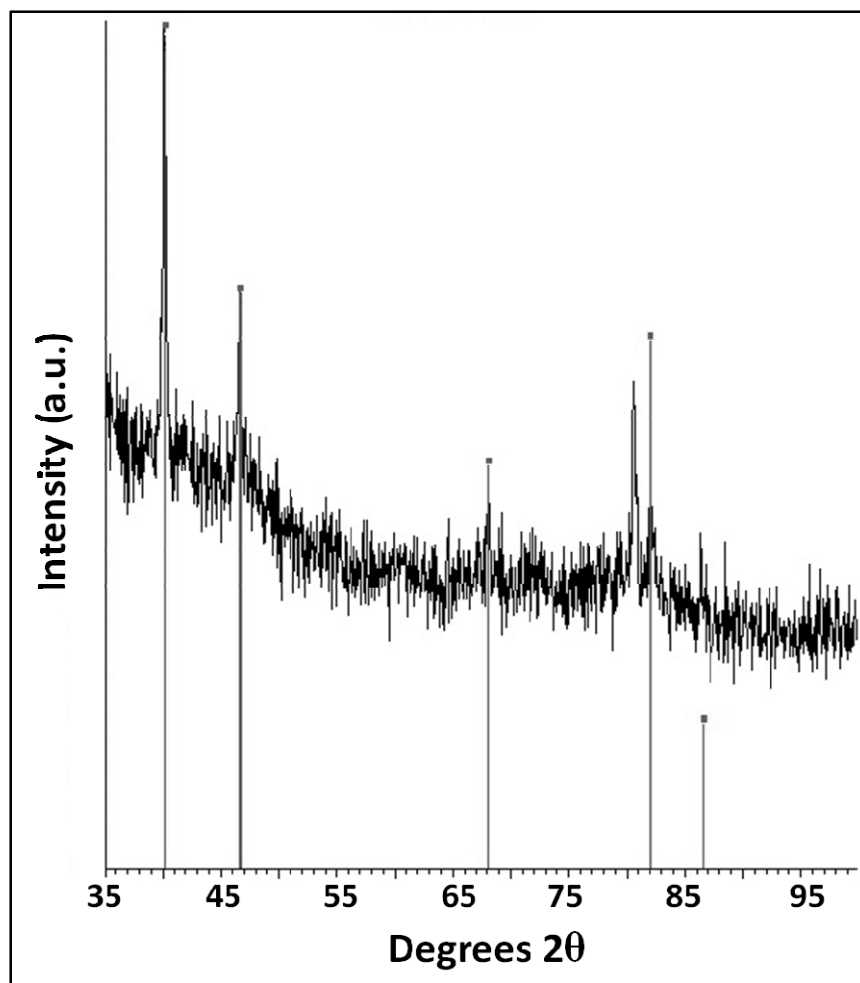


Figure 13: High angle XRD results for 2.30% Pd/MCM-41. Indicated peaks were identified as Pd metal using Eva software.

### 2.3.2.3 BET Nitrogen Adsorption Surface Area Analysis

Results of BET surface area analysis using the Micromeritics Gemini VII instrument for all metal impregnated MCM-41 samples used in this study are summarized in Table 6. The full set of adsorption isotherm results of the 11 point surface area analysis between 0.05 and 0.3 relative pressures are included in Appendix A. The average BET surface area for all metal impregnated samples prepared for this research was  $789 \pm 65 \text{ m}^2/\text{g}$ . This result is within the range of reported values for metal impregnated MCM-41 given that the parent material for these samples had a surface area of  $1,000 \text{ m}^2/\text{g}$  (Sener *et al.*, 2006). Decreased surface area in metal impregnated MCM-41 samples is attributed to partial filling of mesopores and partial or complete blocking of pore entrances by metal centres deposited on the parent material's surfaces.

There is no indication of a connection between increasing mass percent loadings of metal and decreasing surface areas relative to the calcined, parent MCM-41.

**Table 6: Summary of BET nitrogen adsorption surface area analysis results for metal impregnated MCM-41 samples.**

Metal	Metal Source	% Loading	SA (m <sup>2</sup> /g)	± (m <sup>2</sup> /g)
Pd	<i>Pd(NH<sub>3</sub>)<sub>4</sub>Cl<sub>2</sub> · H<sub>2</sub>O</i>	0.12%	522	3
		0.81%	869	26
		0.99%	792	6
		1.10%	788	17
		1.16%	521	6
		1.76%	761	16
		2.30%	849	25
Ni	<i>NiCl<sub>2</sub> · 6H<sub>2</sub>O</i>	0.14%	796	23
		1.02%	892	5
		1.12%	918	7
		1.32%	763	22
	<i>CNiO<sub>3</sub></i>	0.12%	923	3
		1.12%	918	7
Ni-Pd	<i>NiCl<sub>2</sub> · 6H<sub>2</sub>O</i> & <i>Pd(NH<sub>3</sub>)<sub>4</sub>Cl<sub>2</sub> · H<sub>2</sub>O</i>	0.13%	754	2
		1.01%	817	6
	<i>Ni(NO<sub>3</sub>)<sub>2</sub> · 6H<sub>2</sub>O</i> & <i>Pd(NH<sub>3</sub>)<sub>4</sub>Cl<sub>2</sub> · H<sub>2</sub>O</i>	1.22%	742	21

Five metal impregnated samples with a range of different mass percent loadings of Pd were analyzed for BET surface area using the Quantachrome Autosorb-1 instrument. Data was collected over the full relative pressure range from 0.05 to 1.00. An example of a full adsorption-desorption isotherm for 0.81% Pd/MCM-41 is presented in Figure 14. This isotherm is considered typical of Pd impregnated MCM-41 samples. The remaining four, full adsorption-desorption isotherms are included in Appendix A. The isotherm in Figure 14 may be compared to that of the parent MCM-41 material presented in Figure 8. There are two notable differences between the two isotherm results. First, the maximum adsorbed volume is lower in the case of the Pd impregnated material. This result is consistent with the lower surface area values indicated by both instruments. Second, the slope of the vertical step in volume of N<sub>2</sub> adsorbed between relative pressures of 0.30 and 0.50 is less than that of the parent material. This result suggests that there is a wider distribution of pore diameters in the Pd impregnated sample relative to the parent material. This result is likely the result of a non-homogeneous deposition of

Pd in the MCM-41 pores during the incipient wetness impregnation technique. There is no evidence that the incipient wetness method would yield a material with a continuous, thin film of Pd throughout all of the MCM-41 pores, rather, Pd deposited by the incipient wetness method is concentrated in metal centres as discussed below in Section 2.3.2.4. Therefore, full adsorption-desorption BET results indicate an apparently wider distribution of pore diameters in Pd impregnated materials due to partial and complete blocking of pores by Pd centres.

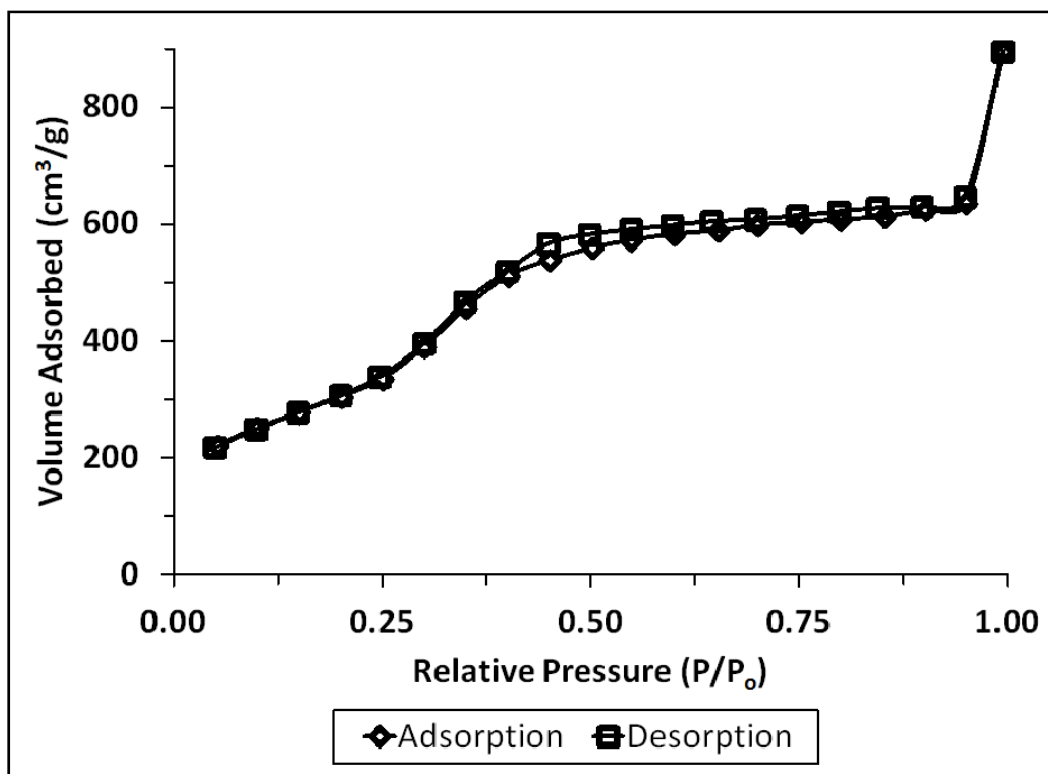


Figure 14: Full adsorption-desorption isotherm results for sample 0.81% Pd/MCM-41.

### 2.3.2.4 SEM and TEM

Figure 15 presents two scanning electron microscope (SEM) images at two magnifications for one Pd impregnated MCM-41 sample (0.12% Pd/MCM-41). Other SEM images of Pd/MCM-41 samples are included in Appendix A. At the lower magnification, the outline of an entire MCM-41 particle is visible, having the approximate dimensions of 3.8 by 1.3  $\mu\text{m}$ . These values are consistent with the particle sizes estimated for calcined MCM-41 via SEM described in Section 2.3.1.4. The density of palladium is high relative to that of the  $\text{SiO}_2$  which makes up the MCM-41 material. Therefore, areas of high Pd density should appear bright relative to the MCM-41 surface in SEM images. The arrows and dashed circle placed within the

images below indicate several such bright points visible on the MCM-41 particle surface. It is proposed that these points represent Pd centres on the surface of MCM-41. Figure 15 (B) shows the same Pd/MCM-41 sample at higher magnification and indicates that there is a range of different Pd centre diameters on the MCM-41 surface. The larger Pd centres visible in the image are approximately 15 nm in diameter. Smaller centres, such as those within the dashed circle, are too small to be reliably measured. There may also be Pd centres present which are too small to be visible in SEM images. Finally, SEM is not a penetrative technique. It is not possible to observe any Pd particles which may be located within the pores of the MCM-41 sample. Therefore, a calculation of concentration and dispersion of Pd centres within the MCM-41 samples was not attempted due to the unreliable results it would produce.

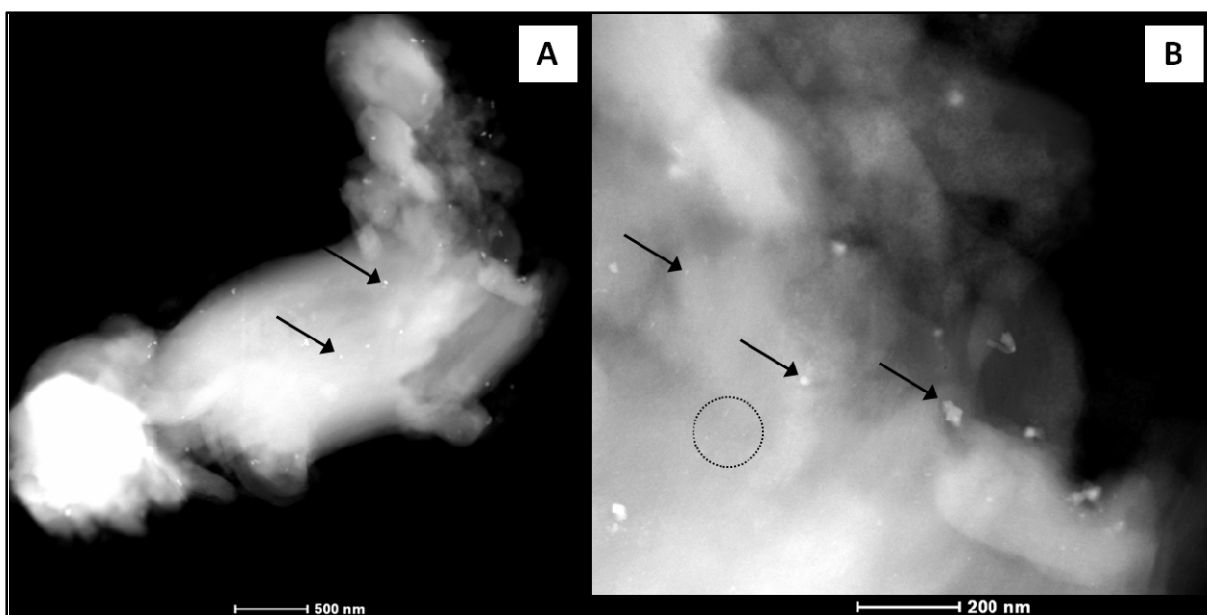


Figure 15: SEM images collected at two magnifications for Pd impregnated MCM-41 (0.12% Pd/MCM-41). (A) shows the outline of an MCM-41 particle with Pd centres visible on its surface. (B) Indicates the range of different diameter Pd centres visible on the MCM-41 surface.

An image taken via transmission electron microscopy (TEM) of the same 0.12% Pd/MCM-41 sample shown in Figure 15 is presented in Figure 16. Other TEM images taken of Pd/MCM-41 samples are included in Appendix A. A particle of MCM-41 is visible in the left half of the image. The sharp transition from the textured light and dark pattern in the left side of the image to a uniformly gray region in the right is proposed to represent an MCM-41 particle boundary. As noted above, Pd is dense relative to the  $SiO_2$  making up the MCM-41 material. This difference would result in Pd centres appearing dark relative to MCM-41 particles in TEM

images. Therefore, the rounded, oblong, relatively dark spots in Figure 16 are proposed to be Pd centres in the image. The upper arrow indicates one such Pd centre – a relatively dark spot measuring approximately 20 by 40 nm.

To the left of the lower arrow and black bar denoting the MCM-41 particle boundary are a series of alternating light and dark parallel lines. This repeating pattern likely represents MCM-41 pores viewed along their length. The distance between the middles of adjacent, lighter parallel lines would correspond to the cell parameter of the material. Ten of these pores were measured and the average cell parameter was calculated as  $3.56 \pm 0.17$  nm. This value is 7% lower than the average cell parameter value for metal impregnated materials calculated via XRD results and summarized in Table 4. Average pore diameter calculated from the TEM image assuming a pore wall thickness equal to 0.63 nm is 14% lower than the primary mesopore width calculated based on XRD results for the parent material (Combo 2). However, this difference is consistent with the difference between pore widths of the parent material relative to metal impregnated MCM-41 samples calculated based on XRD results.

The MCM-41 material itself is semi-transparent to the TEM beam. Therefore, it is not possible to determine whether the Pd centres visible in Figure 16 are located on the surfaces or within the pores of the MCM-41 sample. It is unlikely that the Pd centres visible in the TEM image are located within the pores of MCM-41 given that the dimensions of the metal centres are large compared to the calculated pore diameters. It is possible that the pores visible in Figure 16 contain Pd centres which are too small to be positively identified in the TEM image. However, reliable identification of such small diameter Pd centres is beyond the capability of TEM at these magnifications.

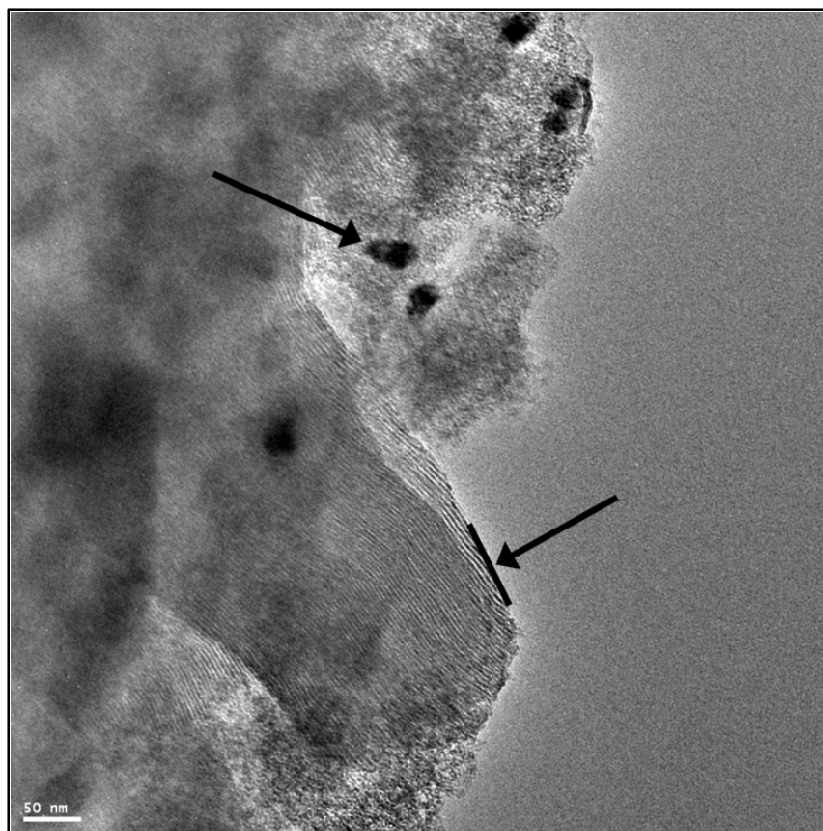


Figure 16: TEM image of Pd impregnated MCM-41 sample (0.12% Pd/MCM-41). Upper arrow indicates probable Pd centre. Lower arrow indicates proposed boundary of a particle of MCM-41. Mesoporosity of the MCM-41 particle is visible to the left of the lower arrow, parallel

### 2.3.2.5 Metal Concentrations

A set of five samples at different mass percent loadings of Pd on MCM-41 were analyzed via an energy dispersive X-ray spectrometer-equipped SEM (EDAX). Each of the five samples was imaged and analyzed at two different magnifications. Sample EDAX result summaries for one of the samples (0.81% Pd/MCM-41) are included in Figure 17. Results indicate a Pd percent by mass of 1.01% and 1.40% at each magnification. Peaks in the spectrogram at the bottom of the summaries were identified as Pd, O, and Si. The presence of Si and O is due to the  $SiO_2$  of the parent MCM-41 material. The unlabelled peak at the far left of the spectrogram represents carbon. The presence of carbon was due to sample preparation which involved sputter coating of the mounted samples with carbon. One sample (1.16% Pd/MCM-41) indicated that there may be a small mass of chlorine present. Chlorine may be present in the sample due to use of  $Pd(NH_3)_4Cl_2 \cdot H_2O$  as the Pd source. Chlorine may also result from contamination due to handling of samples, presence of sample-mounting tape, or the sample holder. Any substantial

amount of chlorine contamination due to handling is unlikely given that care was taken to never touch samples or EDAX components with un-gloved hands during analysis. The scale of the analyzed surface area is indicated in the bottom right corner of the SEM image located at the upper left of each analysis result in Figure 17. The EDAX results for the remaining four samples are summarized in Table 7 and included in detail in Appendix A. Positive average values in Table 7 indicate that a given analysis technique returned a higher metal concentration than that calculated based on mass of metal source added during synthesis. A negative average value indicates that the given analysis technique returned a lower metal concentration value than was calculated based on the mass of metal source added during synthesis.

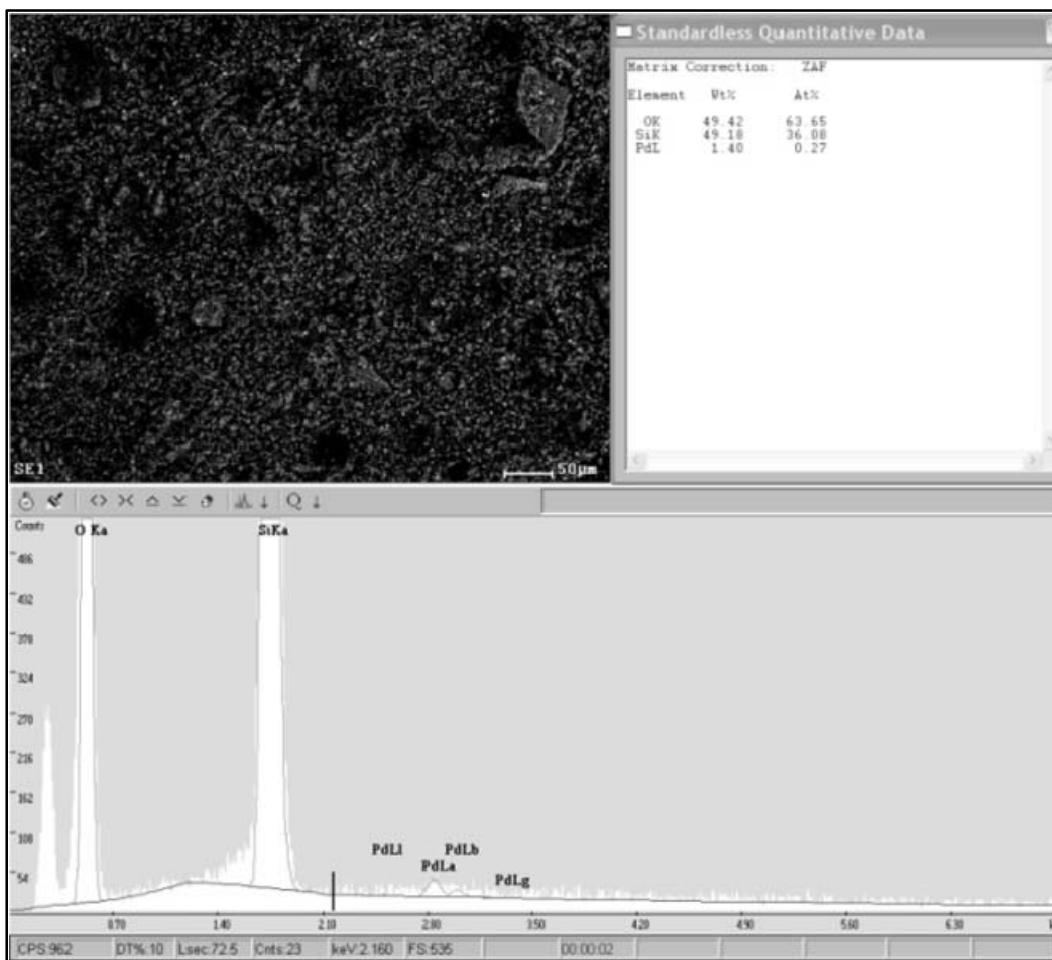


Figure 17: Results of EDAX analysis for a Pd impregnated MCM-41 sample (0.81% Pd/MCM-41). Area analyzed was the entire SEM area in the upper left panel. The unlabeled peak at the left of the spectrogram is carbon.

The summary of EDAX analysis results in Table 7 shows large deviations from calculated percent loadings of Pd on MCM-41. Pd loadings determined via EDAX analysis differed from

calculated percent by mass by an average of 46% and 43% at 200x and 1000x magnifications, respectively. EDAX indicated mass percent loadings that were higher than those calculated based on reagent metal masses in all five samples. However, a clear trend of increased Pd mass percent loading in the samples as the mass of added Pd source increased is evident in both the calculated and EDAX analysis results.

There are several limitations to the EDAX technique with respect to identifying metal impregnated MCM-41. Most importantly, EDAX is not a penetrative technique. It is only capable of identifying species present on the surfaces of the sample particles. It is not possible to determine the concentration of metal species that are present within the pores of MCM-41. Second, the scale of the SEM image in Figure 17 shows that even at lower magnification, a relatively small portion of MCM-41 particle surfaces is being analyzed. This could result in a possible ‘nugget effect’ where uneven distributions of metal across the particle surfaces may strongly influence reported metal concentration values. This type of effect may cause an under- or over-estimate of metal concentrations depending on whether areas of low or high metal concentration are included in the sample area. Relatively large Pd centres, or agglomerations of Pd centres could result in a nugget effect. This nugget effect is a potential problem in metal impregnated MCM-41, where small masses of metal (0.81% to 2.30% of final sample mass) are spread over a large surface area ( $\sim 1,000 \text{ m}^2/\text{g}$ ). Finally, the low signal-to-noise ratios in the spectrogram, which resulted from the low mass of Pd present in the Pd/MCM-41 particles, may have affected the ability of the technique to produce accurate overall mass loading values.

**Table 7: Comparison of percent loadings by mass of metal on MCM-41 determined via EDAX, ICP and AAS with calculated loadings.**

Metal	Metal Source	Percent loading results:				
		Calculated	EDAX (200x)	EDAX (1000x)	ICP (Pd)	AA (Ni)
Pd	$Pd(NH_3)_4Cl_2 \cdot H_2O$	0.12	-	-	0.08	-
		0.81	1.40	1.01	0.47	-
		0.99	-	-	0.72	-
		1.10	1.70	1.95	0.75	-
		1.16	2.22	2.24	0.85	-
		1.76	2.49	2.18	1.17	-
		2.30	3.26	3.92	1.47	-
Ni	$NiCl_2 \cdot 6H_2O$	0.14	-	-	-	0.26
		1.02	-	-	-	0.83
		1.12	-	-	-	1.07
		1.32	-	-	-	1.32
	$CNiO_3$	0.12	-	-	-	0.26
		1.12	-	-	-	1.07
Ni-Pd	$NiCl_2 \cdot 6H_2O$ & $Pd(NH_3)_4Cl_2 \cdot H_2O$	0.13	-	-	0.06	0.05
		1.01	-	-	0.32	0.46
	$Ni(NO_3)_2 \cdot 6H_2O$ & $Pd(NH_3)_4Cl_2 \cdot H_2O$	1.22	-	-	0.40	0.32

<b>Average % deviation from calculated =</b>	46	43	36	30
--	----	----	----	----

Pd impregnated samples were also analyzed for metal concentration via fire assay with inductively coupled plasma (ICP). The results of this analysis are included in Table 7. The Pd lower detection limit was 5 ppb and the upper limit was 100,000 ppb. The -36% average deviation value indicates that ICP results show lower metal concentrations than those calculated based on mass of Pd source added during sample synthesis. However, the trend of increasing calculated mass percent loadings of Pd was matched by the ICP results.

Table 7 also includes the results of  $HNO_3 - HF - HClO_4 - HCl$  digestion and atomic absorption spectroscopy analysis (AAS) for Ni concentrations in the Ni/MCM-41 and Ni-Pd/MCM-41 samples. The lower limit for Ni determination was 0.0001% and the upper limit was 80%. The average Ni concentration as indicated by AAS was in agreement with the values calculated based on the mass of Ni source added during synthesis. However, AAS results both under- and over-estimated the mass percent of Ni present by as much as 74% as compared to the

calculated percent loadings. Control samples consisting of only 50-70 mesh Ottawa silica sand did not contain any Pd or Ni. Thus, sand used to dilute metal impregnated MCM-41 sample particles did not influence the metal concentration results produced by ICP and AAS analyses.

All four of the SEM, TEM, EDAX, and ICP analyses positively identified the presence of Pd in the Pd/MCM-41 and Ni-Pd/MCM-41 samples. The AAS analysis positively identified the presence of Ni in all Ni/MCM-41 and Ni-Pd/MCM-41 samples. The different analyses were generally not in close agreement with the calculated mass percent loading of metal on the metal impregnated MCM-41 samples. The AAS analysis for Ni was in closest agreement with calculated Ni mass percent loadings. The ICP analysis was in closest agreement with calculated Pd concentrations. EDAX analysis at either magnification was in poorest agreement with calculated mass percent loadings. It is proposed that the calculated mass percent loadings of metal on MCM-41 provides the most accurate estimate of the actual concentrations of metal in the samples. The calculated mass percent loading of metal is based solely on the mass of metal source reagent and final sample masses. Metal source and final sample mass were determined using the best available balance. Therefore, sources of uncertainty in the calculated value should be minimal. Uncertainty in other analysis techniques is high relative to calculated values due to specific reasons discussed above as well as to the inherently greater complexity of the more sophisticated analysis techniques and more involved sample preparation procedures.

### **2.3.3 Metal Impregnated Silica Sand**

Two samples of Pd impregnated 50-70 mesh Ottawa silica sand (Pd/sand) were prepared for this research. Pd/sand samples were prepared and used in several experiments as a comparison with results obtained using Pd/MCM-41. Due to the limited use of Pd/sand materials in this study, these samples were not characterized with as many techniques as for the metal impregnated MCM-41 materials.

Results of the 11 point BET nitrogen adsorption surface area analysis are presented in Table 8. These surface areas are relatively low compared to those of Pd impregnated MCM-41 (Table 6) and show poor agreement between samples 1 and 2. It is expected that surface areas of the two materials should be approximately equal as both samples were prepared at similar mass percent loadings of Pd and used the same parent, silica sand material. Plots of the adsorption isotherms

for these two samples are included in Appendix A. It is clear from the relatively non-linear isotherms that the analysis was problematic. These difficulties are attributed to the relatively low surface area per unit mass of Pd/sand. The basis of the BET surface area analysis technique breaks down when the volume of  $N_2$  displaced by a sample is much greater than the volume adsorbed to the sample surface. This breakdown can occur for materials of low surface area, such as the sand used in preparing these two samples. Methods of correcting for the low sample surface area per unit mass involved adding filler materials possessing minimal surface area such as glass rods or beads to the sample tubes. Attempts to generate better agreement between BET analysis results by adding different combinations of the two filler materials to the sample tubes were unsuccessful. The BET surface area results presented in Table 8 are considered unreliable.

An estimate of the Pd/sand sample surface area can be calculated by assuming that grains of 50-70 mesh Ottawa silica sand are perfect spheres of 0.3 mm diameter. If the density of a sand particle is equal to that of silica ( $\rho = 2.65 \text{ g/cm}^3$ ), then a theoretical surface area of  $0.0075 \text{ m}^2/\text{g}$  is calculated for Pd/sand samples. This value is in closest agreement with BET results for the first Pd/sand sample, but is generally in poor agreement with either of the BET analysis results. It is assumed that the calculated surface areas of the Pd/sand materials are closer to the actual surface areas of the samples. It is clear that surface areas of Pd/sand samples are low relative to similarly prepared Pd/MCM-41 materials, regardless of the disagreement between the different surface area determinations.

The two Pd/sand samples were analyzed for Pd concentration by fire assay and inductively coupled plasma analysis (ICP). Lower and upper limits of the analysis technique are the same as those described for metal impregnated MCM-41 in Section 2.3.2.5. Calculated mass percent loading of Pd in the two samples and the results of the ICP analysis are included in Table 8. The metal concentrations determined via ICP differ substantially from the calculated values and values determined by ICP for both samples were lower than the calculated value. However, the presence of Pd in both Pd/sand samples was confirmed by the ICP analysis. As with Pd/MCM-41 materials, the calculated mass percent loading is assumed to be the most accurate estimate of the actual metal concentration. These calculated values depend only on masses of the metal source and the final sample yield during the Pd impregnation procedure. Therefore, sources of uncertainty in this determination should be minimal.

**Table 8: BET surface area, calculated surface area, and mass percent loadings of Pd on sand in Pd/sand materials.**

Sample:	Surface Area:		Metal Loading:						
	BET (m <sup>2</sup> /g)	Calculated (m <sup>2</sup> /g)	Sand (g)	Metal Source (mg)	Metal (mg)	Yield (g)	Calculated % Loading	% by ICP	% Deviation from Calculated
1.	0.00282	0.0075	1.0159	26.311	10.261	1.0242	1.00	0.32	-103
2.	0.14381	0.0075	3.7574	97.252	37.928	3.7797	1.00	0.37	-92

## 2.4 Conclusions

A series of calcined MCM-41 materials were synthesized following a procedure based on previously published methods. Samples were characterized by X-ray diffraction (XRD), BET nitrogen adsorption surface area, scanning electron microscope (SEM), and transmission electron microscope (TEM) analyses. All calcined samples produced for this research exhibited the hexagonally-arranged mesopores and high surface areas (average =  $983 \pm 50$  m<sup>2</sup>/g) characteristic of well-formed MCM-41. Results of XRD analyses performed on samples indicated an average primary mesopore diameter of  $4.31 \pm 0.08$  nm. Full adsorption-desorption isotherms collected during BET analysis of a calcined MCM-41 sample indicated a narrow distribution of pore diameters and a pore radius of 1.3 nm. Due to instrument malfunction, BET analysis was problematic and it is proposed that primary mesopore diameters calculated based on XRD results provided more accurate values. For similar reasons, surface areas determined via an 11 point BET analysis using a different instrument are also considered more accurate than the result obtained from the full adsorption-desorption isotherm. SEM images revealed the so-called ‘wormy’ MCM-41 morphology in MCM-41 samples. Particles visible in SEM images had dimensions in the range 2 to 5  $\mu$ m by 5 to 10  $\mu$ m. TEM images taken of an MCM-41 sample demonstrated the repeating pore structure of the material and indicated a cell parameter value of  $4.6 \pm 0.3$  nm, which is in good agreement with cell parameters calculated from XRD results.

Metal impregnated MCM-41 samples were prepared with different mass percent loadings of Pd, Ni, and bimetallic Ni-Pd. These samples underwent a similar suite of characterization techniques as performed for the purely siliceous, calcined MCM-41 materials. Low angle XRD results indicated a broadening and loss of intensity of the higher order diffraction peaks and a rightward shift of the (100) peak with a corresponding reduction in the cell parameter value to  $4.06 \pm 0.06$  nm as compared to as-synthesized MCM-41. Pd impregnated samples prepared at higher mass percent loadings of metal exhibited a set of diffraction peaks identified as Pd metal. All metal impregnated samples produced a diffraction peak at approximately  $80.7^\circ 2\theta$  which is

tentatively identified as an artifact of the instrument or equipment used in the analysis. The average BET surface area of metal impregnated samples was  $789 \pm 65 \text{ m}^2/\text{g}$ . Lower surface area relative to the calcined, parent MCM-41 material is attributed to partial or complete blocking of mesopores. Full adsorption-desorption isotherm results indicated a wider distribution of pore diameters. Pd centres of approximately 15 nm and smaller were identified in SEM images of Pd/MCM-41. Pd centres of 20 to 40 nm in diameter were also identified in TEM images taken of Pd/MCM-41 samples. Locations of Pd centres could not be definitively determined via TEM imaging. An average cell parameter value of  $3.56 \pm 0.17 \text{ nm}$  was calculated from the TEM image. This value is consistent with those calculated based on XRD results. Presence of Pd, Ni, or Ni-Pd was confirmed by energy dispersive X-ray spectroscopy (EDAX), inductively coupled plasma (ICP), and atomic absorption (AAS) analyses. Quantitative results from these analyses suggested metal concentrations which differed substantially from calculated values for many of the samples. It is proposed that calculated values provide the most accurate estimate of metal mass percent loadings as they were based on simple mass measurements of materials during sample preparation.

Two samples of Pd/sand were prepared at similar mass percent loadings of Pd. The calculated surface area of the two samples was  $0.0075 \text{ m}^2/\text{g}$ . BET surface area analysis results of Pd/sand materials were unreliable due to the low surface area per unit mass of the samples. Presence of Pd in both samples was confirmed by ICP analysis.

## CHAPTER 3

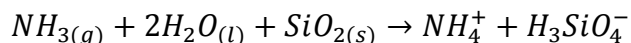
### 3. STABILITY OF MCM-41-SUPPORTED METAL AND LONG TERM STABILITY OF MCM-41

#### 3.1 Background

The utility and longevity of an MCM-41-supported transition metal system in liquid phase reactions will depend in part on the stability of the material while in contact with water. Reactive materials which are unstable and rapidly dissolve when in contact with water would be generally unsuitable for use in a water treatment technology. There has been some disagreement in the literature as to whether MCM-41 is stable in water or while in contact with ambient humidity. It has been reported that MCM-41 is intrinsically unstable when in contact with water, dissolving rapidly and trending towards a steady-state dissolved  $SiO_2$  concentration corresponding to saturation with respect to amorphous silica. However, the characteristic hexagonal structure and high surface areas of MCM-41 are maintained even after extended periods of contact with deionized water at 25°C (Guthrie & Reardon, 2008).

Since its initial description by Beck *et al.* (1992), the chemico-physical characteristics of MCM-41 have been studied and described in depth in the literature. Of interest to many researchers is the application of MCM-41 as an adsorbent or catalyst support material in aqueous or high temperature reactions in the presence of water vapour. As such, much research has examined the material's stability in water and while exposed to water vapour, over a range of different temperatures. Conflicting results concerning the stability of MCM-41 in water and when exposed to water vapour have been published in the last two decades, with some researchers concluding that the structure, porosity, and surface area of the material is resistant to exposure to water and water vapour, while others concluded that it is not. Zhao *et al.* (1998) found that MCM-41 was unstable under exposure to ambient conditions (60% relative humidity), undergoing structural collapse within three months. This finding is inconsistent with that of Hassan (2006), who noted that a sample of the material left exposed to air under ambient temperature and humidity during an extended storage period did not experience any loss of its hexagonal structure. Mori *et al.* (2002) found that MCM-41 is very sensitive to degradation when exposed to hot water or steam. Koyano *et al.* (1997) reported collapse of the hexagonal MCM-41 structure following extended

exposure to water vapour over a saturated aqueous solution of  $NH_4Cl$ . However, in this case there is reason for the instability.  $NH_{3(g)}$  would progressively exsolve from the  $NH_4Cl$  solution and dissolve in moisture films around the MCM-41 particles resulting in elevated pHs due to hydrolysis of  $NH_3^0$  to  $NH_4^+$  and causing enhanced dissolution of the MCM-41 silica:



Carrott *et al.* (1999) also reported a reduction in pore volume, size, and uniformity upon exposure to water vapour for periods of time up to 1 yr.

By contrast, in a study to mimic the effect of groundwater conditions on MCM-41, Zhao *et al.* (2000) found that characteristic aspects of the MCM-41 material were stable under a range of concentrations of  $CaCl_2$  in water. Galarneau *et al.* (2007) noted that although the solubility of MCM-41 in water is relatively high, no mass loss of initial material was observed after exposure to water, suggesting a re-deposition of silica inside the MCM-41 mesopores. This observation suggests that the stability of MCM-41 may be related to the pore size of the material. Mokaya (1999) proposed that the relatively unstable MCM-41 structure can be improved by increasing the pore wall thicknesses and encouraging silica condensation within the pore walls during the material's synthesis. Landau *et al.* (1999) indicated that MCM-41 prepared following a hydrothermal synthesis method possesses a resistance to degradation by exposure to neutral and acidic waters. However, the silica-based material is quite unstable when exposed to water at elevated pH values of between 7.8 and 8.9. Finally, although the material rapidly dissolves when in contact with deionized water, it retains its characteristic hexagonal structure and high surface areas (Guthrie & Reardon, 2008).

The stability of MCM-41 upon exposure to water or water vapour under a range of conditions may be improved via incorporation of additional substances which increase the material's hydrophobicity. For example, incorporating fluoride into the MCM-41 structure during its synthesis will increase the surface hydrophobicity (Xia *et al.*, 2000). Kim *et al.* (1995) reported that ion-exchanged Al-incorporated MCM-41 had a relatively high hydrothermal stability upon exposure to room temperature water vapour. This finding was supported by those of Mokaya (2000), who found that incorporation of small amounts of Al into the MCM-41 structure during its synthesis resulted in a marked improvement of its hydrothermal stability relative to the purely

siliceous form. Shen & Kawi (1999) also reported that incorporating small amounts of a metal such as Al rendered the material resistant to structural collapse under treatment with boiling water over several days. However, it has been reported that Al incorporated into the MCM-41 structure during its hydrothermal synthesis had no effect on its solubility in deionized water at  $25\pm 0.1^\circ\text{C}$  compared to purely siliceous MCM-41 (Guthrie & Reardon, 2008). Finally, it has been proposed that the stability of MCM-41 is improved via synthesis methods and post-synthesis procedures which thicken the pore walls. Pore wall thickening may also be achieved by depositing a metal oxide on the surfaces of MCM-41 (He *et al.*, 2001).

The purpose of the study described in this chapter was to determine the stability of MCM-41-supported Pd, Ni, and bimetallic Ni-Pd compared to as-synthesized MCM-41 at  $25\pm 0.1^\circ\text{C}$  and ambient pressure. These three materials are referred to here as Pd/MCM-41, Ni/MCM-41, and Ni-Pd/MCM-41. A preliminary attempt is made to model the dissolution kinetics of the MCM-41-supported Pd materials. Finally, results of a long-term experiment investigating changes in the physical characteristics of purely siliceous, calcined MCM-41 over 1,174 days exposure to deionized water will be presented and discussed.

## **3.2 Experimental Methods**

### **3.2.1 Solubility experiment**

The solubility experiments made use of several MCM-41, Pd/MCM-41, and Ni/MCM-41 materials at different mass percent loadings of metal. The Ni/MCM-41 materials were produced using one of two Ni sources (nickel (II) chloride or nickel carbonate). These materials are identified by the mass percent loading of metal on MCM-41. Detailed descriptions of these samples' synthesis and characterization are included in Chapter 2.

Samples were prepared in duplicate in 125 ml HDPE bottles containing solid to liquid ratios (solid sample material and deionized water) of 1/200 and 1/100 by mass. Bottles requiring only a few sampling events during the experiment were scaled down to 20 ml HDPE bottles. Scaled down experiments used similar solid to liquid ratios as experiments conducted using larger HDPE bottles. Control samples were prepared by filling bottles with deionized water. Bottles were tightly sealed with threaded screw caps and Teflon tape and then mounted in a wheel

configuration in an isotherm bath. A schematic of the wheel configuration is presented in Figure 18. Water was heated and maintained at  $25 \pm 0.1^\circ\text{C}$  by a computer-controlled aquarium heater. An aquarium pump installed in the bath ensured a constant temperature throughout the bath and kept the wheel-mounted samples in rotation about a horizontal axis. This rotation ensured that solid sample particles contacted all of the solution in the sample bottles.

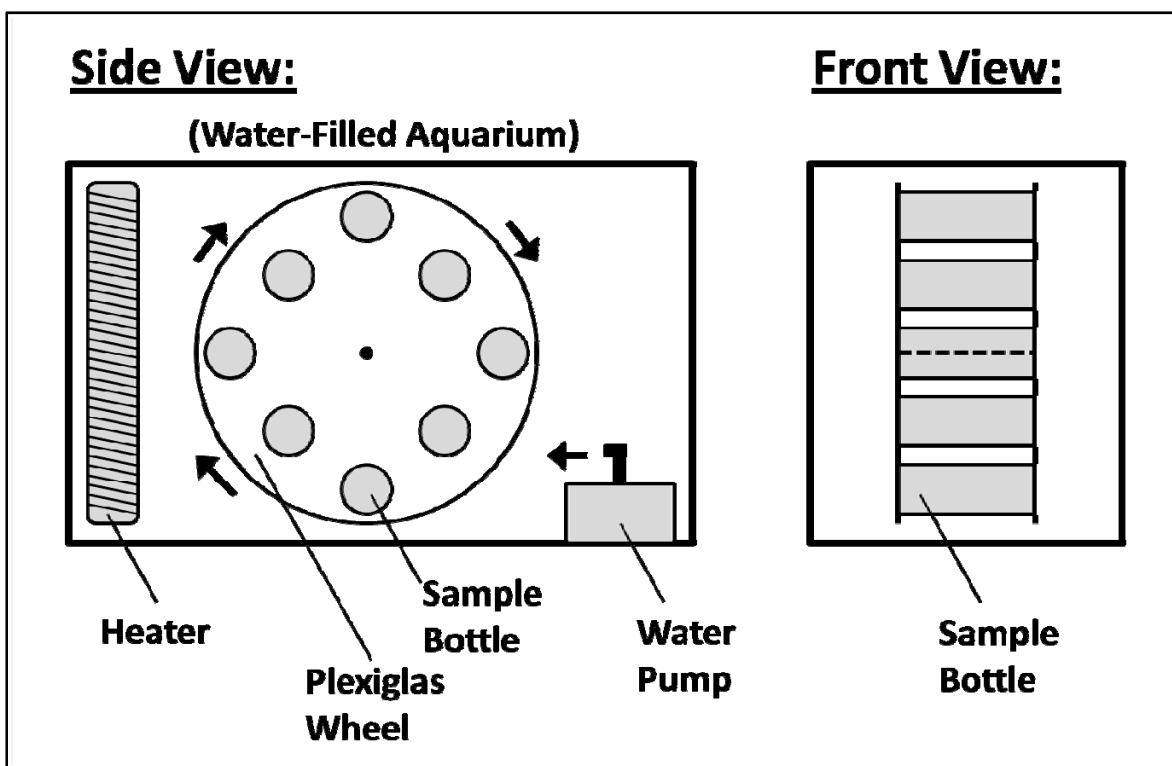


Figure 18: Schematic demonstrating the set-up of sample bottles inside an isotherm bath maintained at  $25 \pm 0.1^\circ\text{C}$ .

Samples of the supernatant solution in the bottles were taken at intervals throughout the experiment and passed through a  $0.2 \mu\text{m}$  Acrodisc® filter. Concentration of  $\text{SiO}_2$  was determined using a Pharmacia LKB Novaspec II spectrophotometer and following the molybdosilicate method (Eaton *et al.*, 1995). A brief procedure for this method is included in Appendix B. Sample pH was measured with a Fisher Scientific Accumet meter and ALpHA PHE-1411 probe. The meter was calibrated using 4.00 and 7.00 buffers. Solid materials recovered following termination of the experiment were separated from supernatant solution by centrifuge and dried under light vacuum over a saturated  $\text{KCl}$  solution (80% relative humidity). Properties of the recovered materials were examined using XRD and BET nitrogen adsorption

surface area analyses and compared to those of the freshly prepared materials. Dissolution rate kinetics for Pd/MCM-41 samples were simulated using Phreeqci (V 2.18.3.5570, USGS).

### 3.3 Results and Discussion

#### 3.3.1 Solubility Experiment

The masses of MCM-41 supported metal materials and of metal contained within each reaction bottle are included in Appendix B. Variability in masses of metal impregnated MCM-41 samples and metal between the sample bottles was low, therefore,  $SiO_2$  concentration results from the dissolution experiments were not normalized with respect to either sample or metal masses.

The method detection limit for  $SiO_2$  was determined to be  $1.33 \times 10^{-2}$  mmol/l. Error bars were calculated as the 95% confidence interval for five repeated preparations and analyses of a single sample. At least one error bar was determined for each of the following plots. However, error bars are often not visible in the plots due to the low amount of uncertainty in the analysis resulting in small error bars which are easily obscured by the data point markers. Results for all error bar calculations are included in Appendix B.

The results of the dissolution experiments comparing solubility over 50 d of contact with deionized water of 0.12% and 1.16% Pd/MCM-41 are presented below in Figure 19 and Figure 20. Detailed data collected during the experiment along with analysis results for reagent blanks are included in Appendix B. Figure 19 compares the solubility of the two mass percent loadings of Pd on Pd/MCM-41 at a solid-to-liquid ratio of 1/200. Figure 20 compares the two materials' solubility at a solid-to-liquid ratio of 1/100. The dissolution rate was relatively low and steady-state  $SiO_2$  concentration was not achieved within the 50 d experiment. However, it is expected that given adequate time, Pd/MCM-41 would dissolve until saturation with respect to amorphous silica ( $\sim 2$  mmol/l) was achieved. This result would be consistent with earlier findings for purely siliceous MCM-41 and aluminum-incorporated MCM-41 (Guthrie & Reardon, 2008). The hexagonal structure of MCM-41 is the result of the arrangement of the material's mesopores. The pore walls themselves are composed of amorphous silica, therefore it is expected that

dissolution of MCM-41 will produce a mmol/l  $SiO_2$  versus time curve trending towards saturation with respect to amorphous silica.

A comparison of the maximum  $SiO_2$  concentrations achieved in Figure 19 and Figure 20 shows that for similar materials, the rate of dissolution increases with increasing masses of material present in the reaction bottle. This result is likely due to solubility being a function of surface area: as the surface area of MCM-41 in the reaction bottles is increased, the dissolution rate will also increase. The surface areas of the 0.12% and 1.16% Pd/MCM-41 samples were  $522 \pm 3$  m<sup>2</sup>/g and  $521 \pm 6$  m<sup>2</sup>/g, respectively. In Figure 19, the sample and duplicate for 0.12% Pd/MCM-41 achieved an  $SiO_2$  concentration of 1.3 and 1.4 mmol/l by the end of the experiment, respectively. The sample and duplicate for 1.16% Pd/MCM-41 achieved an  $SiO_2$  concentration of 0.9 and 1.0 mmol/l, respectively. These results indicate that 1.16% Pd/MCM-41 dissolves at a lower rate than 0.12% Pd/MCM-41. This observation suggests that resistance to dissolution by deionized water increases with increasing quantities of Pd grafted to the surfaces and within the pores of MCM-41. In Figure 20, the sample and duplicate for 0.12% Pd/MCM-41 both achieved an  $SiO_2$  concentration of 1.7 mmol/l by the end of the experiment. The sample and duplicate for 1.16% Pd/MCM-41 achieved an  $SiO_2$  concentration of 1.4 and 1.5 mmol/l, respectively. These results are similar to those of Figure 19 in that they indicate increased resistance to dissolution by deionized water as the mass percent loading of Pd is increased.

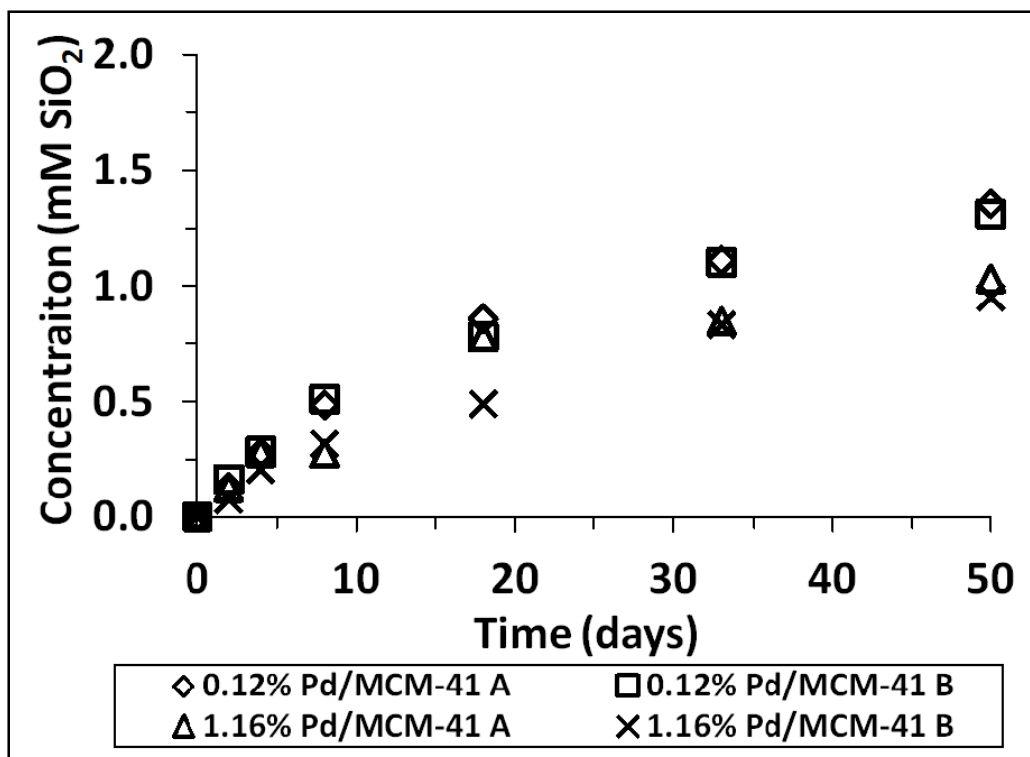


Figure 19: Results of dissolution experiments comparing solubility of Pd/MCM-41 at two different mass percent loadings. Solid-to-liquid ratios in all sample bottles was 1/200.

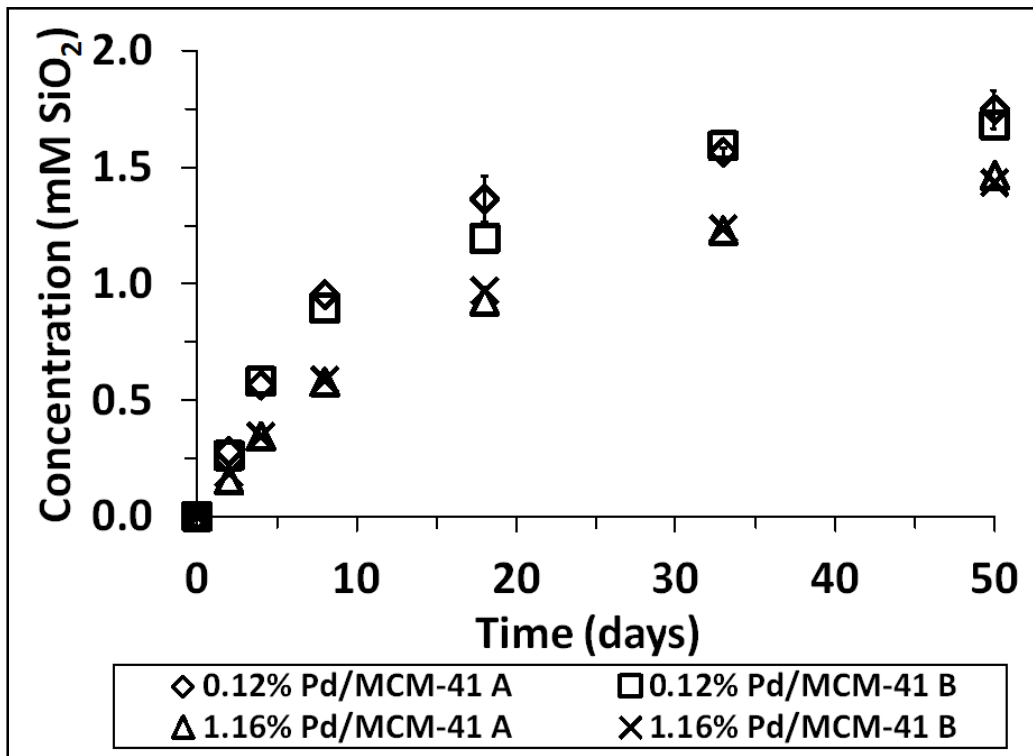


Figure 20: Results of dissolution experiments comparing solubility of Pd/MCM-41 at two different mass percent loadings. Solid-to-liquid mass ratios in all sample bottles was 1/100.

The results of a similar set of dissolution experiments undertaken using Ni/MCM-41 are presented in Figure 21 and Figure 22. The Ni/MCM-41 materials for this experiment were prepared using nickel carbonate as a source of Ni (Chapter 2). Detailed data collected during these experiments, along with uncertainty calculations and analysis results for reagent blanks are included in Appendix B. It was found that Ni/MCM-41 dissolved at a higher rate than Pd/MCM-41. Therefore, Ni/MCM-41 dissolution experiments were carried out over approximately 24 h, rather than 50 d. Figure 21 presents results from experiments using 0.12% and 1.12% Ni/MCM-41 at solid-to-liquid ratios of 1/200. Figure 22 presents results from dissolution experiments using the same two Ni/MCM-41 materials but at solid-to-liquid ratios of 1/100. In Figure 21 and Figure 22 the sample and duplicate using 0.12% Ni/MCM-41 achieved  $SiO_2$  concentrations of 1.9 and 2.0 mmol/l by the end of the experiment. The sample and duplicate for 1.12% Ni/MCM-41 achieved  $SiO_2$  concentrations of 1.8 and 1.9 mmol/l. These values are within the expected range for saturation with respect to amorphous silica ( $\sim 2$  mmol/l). Therefore, Ni/MCM-41 is less resistant to dissolution by deionized water and the dissolution rate for samples at a solid-to-liquid ratio of 1/200 are approximately equal. Interestingly, Ni/MCM-41 is also substantially less resistant to dissolution by deionized water when compared with purely siliceous MCM-41 which required 5 to 10 d to achieve an  $SiO_2$  concentration of 2 mmol/l (Guthrie & Reardon, 2008). In Figure 22, both the sample and duplicate containing 0.12% Ni/MCM-41 achieved an  $SiO_2$  concentration of 1.9 mmol/l by the end of the experiment.

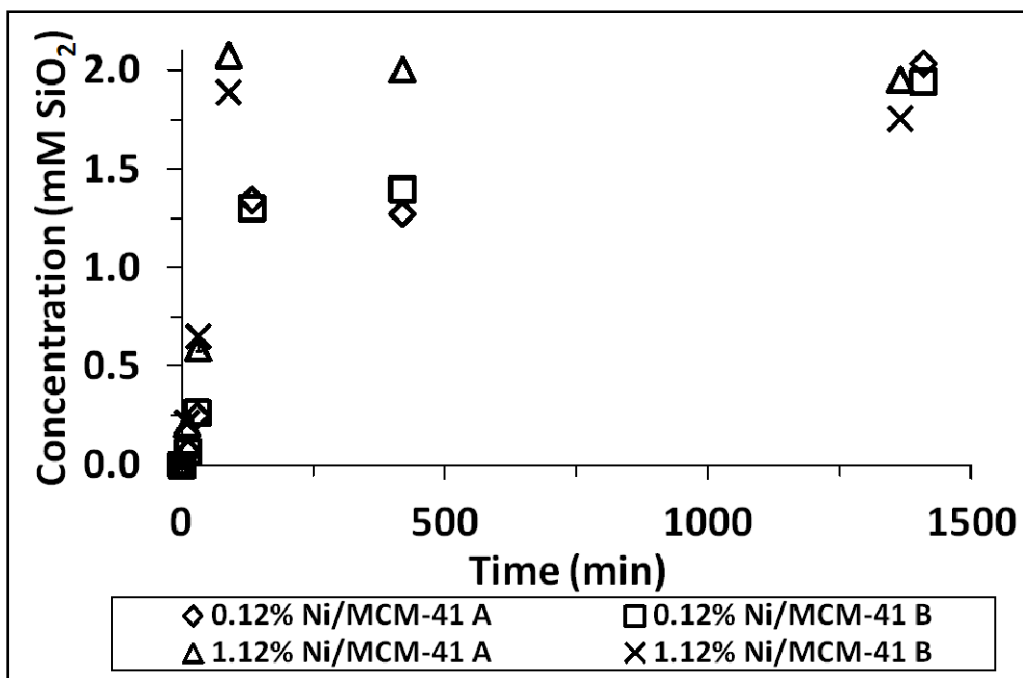


Figure 21: Results of dissolution experiments comparing solubility of Ni/MCM-41 at two different mass percent loadings. Solid-to-liquid mass ratios in all sample bottles was 1/200. Source of Ni was nickel carbonate.

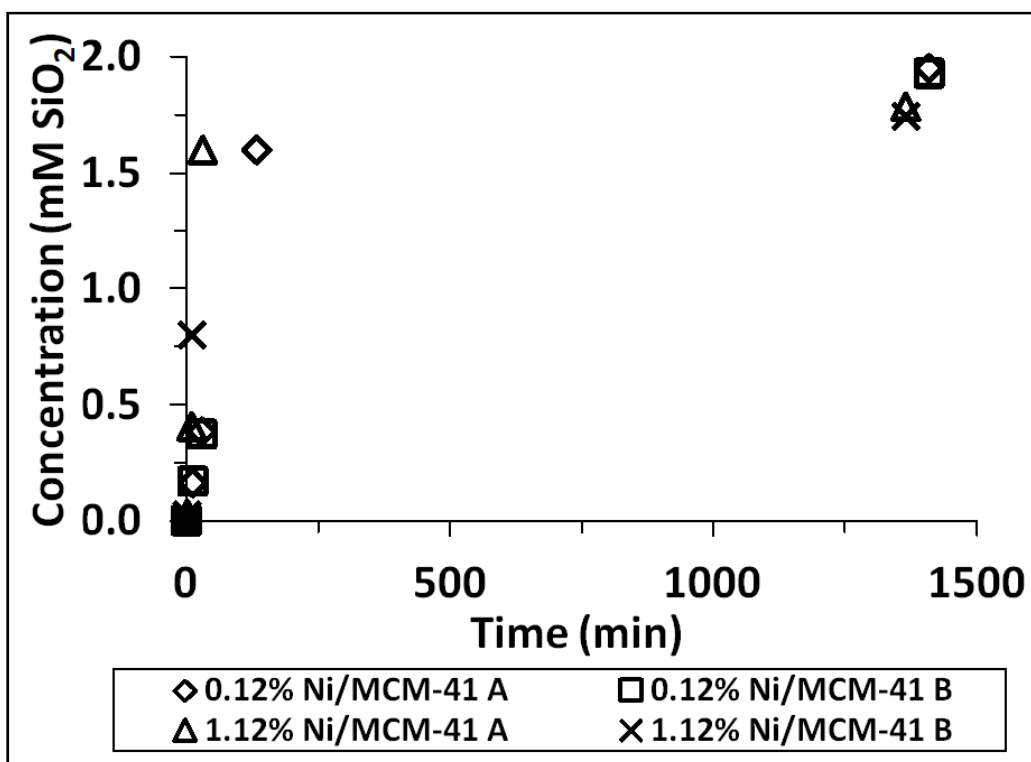


Figure 22: Results of dissolution experiments comparing solubility of Ni/MCM-41 at two different mass percent loadings. Solid-to-liquid mass ratios in all sample bottles was 1/100. Source of Ni was nickel carbonate.

A third set of dissolution experiments were undertaken using samples of Ni/MCM-41. The Ni/MCM-41 materials prepared for these experiments used nickel (II) chloride as a nickel source (Chapter 2). Nickel (II) chloride was used in preparing these materials to determine if the Ni source has any affect on the stability of Ni/MCM-41 in deionized water. The dissolution experiments were carried out over approximately 24 h. Results of analyses of reagent blanks are included in Appendix B. Figure 23 presents results from experiments using 0.14% and 1.32% Ni/MCM-41 at solid-to-liquid ratios of 1/200. Figure 24 presents results from dissolution experiments using the same two Ni/MCM-41 materials but at solid-to-liquid ratios of 1/100. In Figure 23, the sample and duplicate containing 0.14% Ni/MCM-41 achieved  $SiO_2$  concentrations of 1.8 and 1.9 mmol/l by the end of the experiment. Both the sample and duplicate for 1.32% Ni/MCM-41 achieved an  $SiO_2$  concentration equal to 1.9 mmol/l. These values are within the expected range for saturation with respect to amorphous silica. In Figure 24, the sample and duplicate using 0.14% Ni/MCM-41 each achieved  $SiO_2$  concentrations of 1.9 mmol/l. The sample and duplicate which contained 1.32% Ni/MCM-41 also attained a concentration of 1.9 mmol/l by the end of the experiment. Therefore, mass percent loading of Ni in Ni/MCM-41 did not influence the final, steady-state  $SiO_2$  concentration. Comparing the dissolution curves for all four materials presented in Figure 23 and Figure 24 suggests that the dissolution rate increases slightly when higher mass percent loadings of Ni are present. This finding is the reverse of that for Pd/MCM-41 materials, where increasing the mass percent loading of Pd on the surfaces and in the pores of MCM-41 enhanced the stability and lowered the dissolution rate of Pd/MCM-41 in deionized water relative to purely siliceous MCM-41. The presence of Ni in Ni/MCM-41 materials lowers the stability of the material in deionized water relative to both purely siliceous MCM-41 as well as Pd/MCM-41 and increasing the mass percent loading of Ni on Ni/MCM-41 increased the dissolution rate for the material.

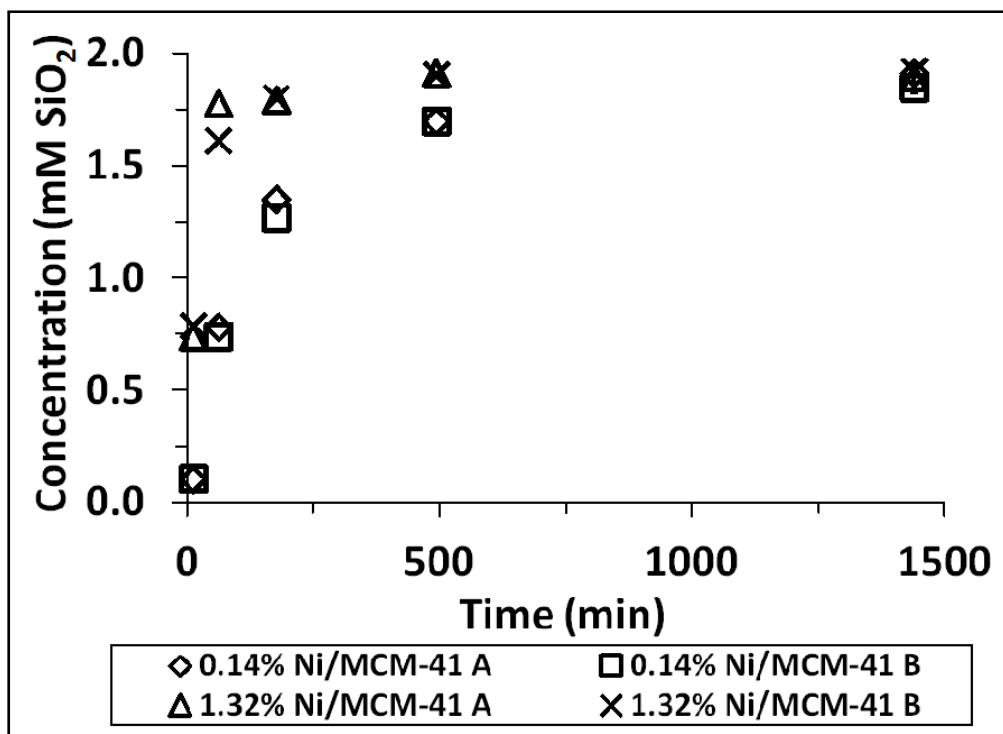


Figure 23: Results of dissolution experiments comparing solubility of Ni/MCM-41 at two different mass percent loadings. Solid-to-liquid mass ratios in all sample bottles was 1/200. Source of Ni was nickel (II) chloride.

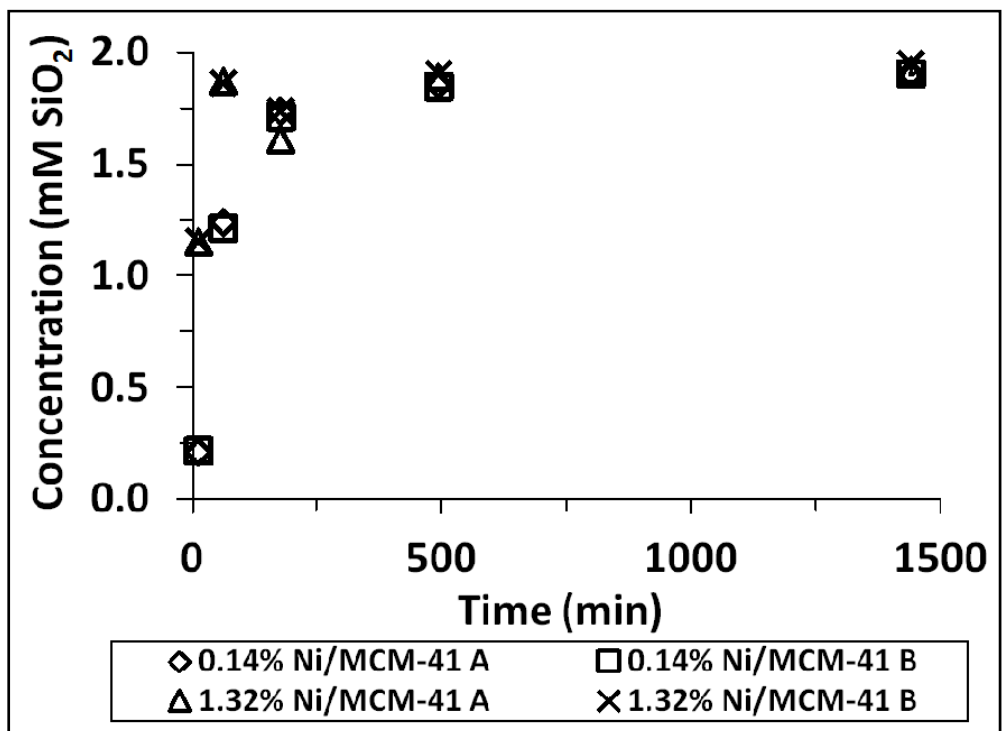


Figure 24: Results of dissolution experiments comparing solubility of Ni/MCM-41 at two different mass percent loadings. Solid-to-liquid mass ratios in all sample bottles was 1/100. Source of Ni was nickel (II) chloride.

A fourth dissolution experiment was undertaken using a sample of 1.22% Ni-Pd/MCM-41 (Chapter 2). This smaller scale experiment was performed to determine if the low Ni/MCM-41 stability in deionized water could be mitigated by including a small amount of Pd. Detailed results collected during this experiment, along with analysis results for reagent blanks are included in Appendix B. A sample and duplicate were prepared containing 1.22% Ni-Pd/MCM-41 and deionized water at a solid-to-liquid ratio of 1/200 and sampled after 1,345 min (22 h and 25 min). Both the sample and duplicate achieved an  $SiO_2$  concentration of 1.8 mmol/l. This value is within the expected range for saturation with respect to amorphous silica. Therefore, inclusion of Pd in the Ni-Pd/MCM-41 material does not appear to have any mitigating effect on the relatively low stability of Ni/MCM-41 materials in deionized water.

One possible explanation for the lower apparent stability of any MCM-41-supported metal materials which include Ni is the formation of  $Ni(OH)_2$  and increased solution pH. A series of pH measurements were made of the supernatant solution samples taken during several of the dissolution experiments. A detailed tabulation of these pH results is included in Appendix B. The average pH value of supernatant solution samples from the Pd/MCM-41 dissolution experiments was  $4.84 \pm 0.29$  for 0.12% Pd/MCM-41 and  $3.69 \pm 0.10$  for 1.16% Pd/MCM-41. Increasing the quantity of Pd present in the sample was accompanied by a decrease in pH values and increased stability of Pd/MCM-41 in contact with deionized water. The average pH value of the supernatant solution samples from the Ni/MCM-41 dissolution experiments was  $6.01 \pm 0.17$  for 0.12% Ni/MCM-41,  $5.90 \pm 0.12$  for 0.13% Ni/MCM-41,  $6.44 \pm 0.11$  for 1.12% Ni/MCM-41, and  $6.10 \pm 0.11$  for 1.17% Ni/MCM-41.

A simulation of deionized water in equilibrium with  $Ni(OH)_2$  was performed using Phreeqci and the Wateq4f database. The presence of  $Ni(OH)_2$  increased an initially neutral solution pH to a value of 8.54. A simulation containing small concentrations of  $Ni(OH)_2$  ( $1.2 \times 10^{-10}$  mol/kg) also caused a similar increase in pH to a value of 8.37. A pH value within this range only causes a small change in amorphous silica solubility (~ 1% increase). Therefore, an increase in solution pH does not explain the rapid dissolution of Ni/MCM-41 relative to Pd/MCM-41 or MCM-41.

The apparent low stability of Ni impregnated MCM-41 materials in deionized water relative to both MCM-41 and Pd/MCM-41 was investigated further. It is proposed that the rapid dissolution

of Ni/MCM-41 and Ni-Pd/MCM-41 was due to either the intrinsic instability of the Ni impregnated materials, or residual Ni salts such as  $NiSO_4$  and  $NiCO_3$  remaining on the surfaces of the Ni impregnated materials following its synthesis. Dissolution of these salts would result in increased solution ionic strength and enhanced dissolution of the MCM-41 materials in those reaction bottles during the dissolution experiment. It has been shown that silica dissolution kinetics are enhanced in electrolyte solutions relative to deionized water at 25°C (Hanton-Fong, 1992).

A summary of solution conductivity values for several samples during the dissolution experiments is presented in Table 9. Average conductivity of samples taken from bottles containing Ni/MCM-41 was higher than those containing Pd/MCM-41. Higher conductivity values indicate higher solution ionic strength which may be related to greater masses of residual salts on the Ni/MCM-41 materials. The higher ionic strength in these solutions could have caused the relatively rapid dissolution of  $SiO_2$  in the Ni/MCM-41 samples.

**Table 9: Summary of conductivity measurements taken during the various dissolution experiments described above.**

Sample	Solid:Liquid	Time (d)	uS/cm (corrected)
0.13% Ni/MCM-41	1:100	31	11
1.17% Ni/MCM-41	1:100	31	251
1.17% Ni/MCM-41	1:200	31	116
0.14% Ni/MCM-41	1:100	5	18
0.14% Ni/MCM-41	1:100	5	27
1.22% Ni-Pd/MCM-41	1:200	1	3
		287	14
1.22% Ni-Pd/MCM-41	1:200	1	3
		287	10
1.16% Pd/MCM-41	1:100	3	80
		5	21
1.16% Pd/MCM-41	1:200	3	17
		5	14
0.12% Pd/MCM-41	1:100	1	2
0.12% Pd/MCM-41	1:100	4	4
		5	4
0.12% Pd/MCM-41	1:200	2	1
		4	3
Blank	-	-	1
Blank	-	-	2

If rapid dissolution of Ni impregnated MCM-41 was a result of intrinsic instability of the material, then there would be a greater decrease in the characteristic hexagonal form and surface area of Ni/MCM-41 samples relative to Pd/MCM-41. Figure 25 presents the results of low angle XRD analyses for as-synthesized, calcined Pd/MCM-41 compared to those for materials recovered after 50 d in contact with deionized water. There is little apparent change in the XRD results for both the 0.12% and 1.16% Pd/MCM-41 samples. In both cases, the peak labeled as 100 is still evident with little loss in its intensity for the recovered samples. Therefore, there was no evidence for a loss in the hexagonal form of the Pd/MCM-41 samples after 50 d in deionized water. The cell parameter for recovered materials was calculated based on the  $2\theta$  position of the 100 peak. The cell parameter value was then used to calculate the primary mesopore diameter of the recovered material and compare to that of the freshly-synthesized material. A summary of these calculations is presented in

Table 10. The calculations indicate a 1.3% and 0.2% decrease in the primary mesopore diameter for the recovered 0.12% and 1.16% Pd/MCM-41 samples, respectively.

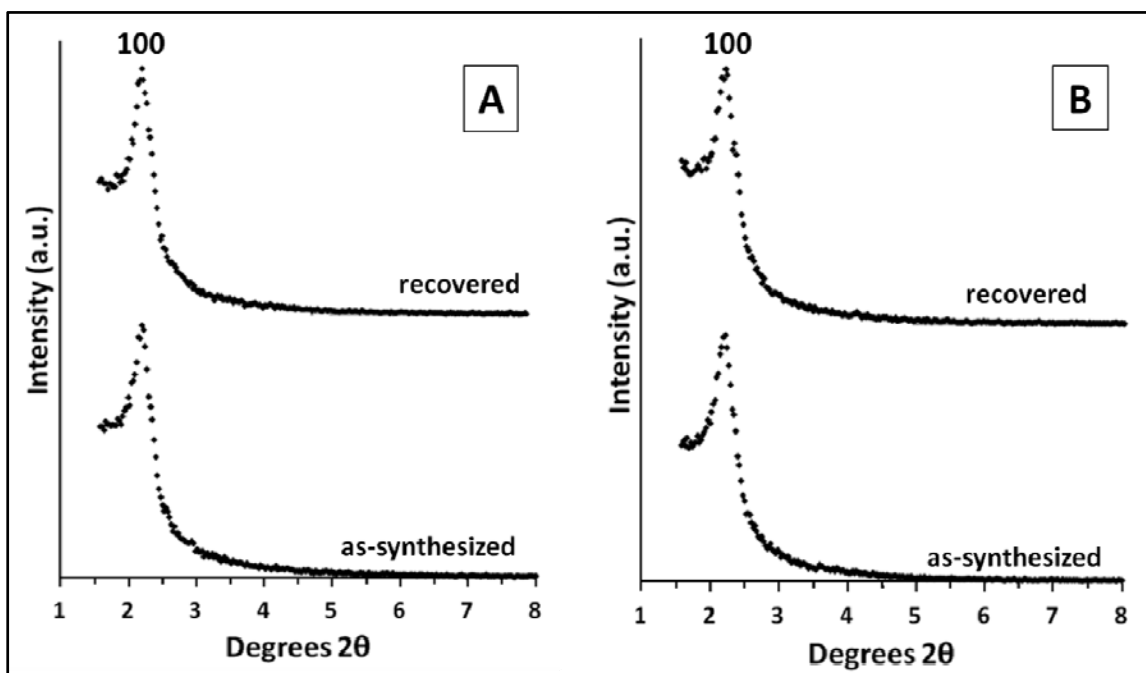


Figure 25: Comparison of as-synthesized Pd/MCM-41 and materials recovered after 50 d in deionized water. (A) 0.12% Pd/MCM-41. (B) 1.16% Pd/MCM-41.

**Table 10: Comparison of physical characteristics calculated using low angle XRD results for as-synthesized and recovered Pd/MCM-41 and Ni/MCM-41 materials.**

Material	Sample	Day	2 $\theta$ (100)	d100	a (nm)	Wd (nm)	Wt (nm)
0.12% Pd/MCM-41	as-synthesized	-	2.19	40.3	4.66	3.99	0.66
	recovered	50	2.22	39.8	4.60	3.94	0.65
	% $\Delta$ =		1.3	-1.3	-1.3	-1.3	-1.3

Material	Sample	Day	2 $\theta$ (100)	d100	a (nm)	Wd (nm)	Wt (nm)
1.16% Pd/MCM-41	as-synthesized	-	2.19	40.3	4.66	3.99	0.66
	recovered	50	2.20	40.2	4.65	3.99	0.66
	% $\Delta$ =		0.2	-0.2	-0.2	-0.2	-0.2

Material	Sample	Day	2 $\theta$ (100)	d100	a (nm)	Wd (nm)	Wt (nm)
0.12% Ni/MCM-41	as-synthesized	-	2.22	39.9	4.60	3.95	0.65
	recovered	40	2.19	40.3	4.66	4.00	0.66
	% $\Delta$ =		-1.2	1.2	1.2	1.2	1.2

Material	Sample	Day	2 $\theta$ (100)	d100	a (nm)	Wd (nm)	Wt (nm)
1.12% Ni/MCM-41	as-synthesized	-	2.22	39.9	4.60	3.95	0.65
	recovered	40	2.19	40.4	4.67	4.01	0.66
	% $\Delta$ =		-1.4	1.4	1.4	1.4	1.4

Results of an 11-point BET surface area analysis performed on recovered materials indicated that 0.12% Pd/MCM-41 possessed a surface area of 533 m<sup>2</sup>/g after 50 d in deionized water at 25°C. This result represents a 2% increase relative to the freshly prepared material and is probably insignificant given an average uncertainty of 2% for surface area analyses of Pd/MCM-41 samples. A surface area analysis using the recovered 1.16% Pd/MCM-41 sample indicated a surface area of 529 m<sup>2</sup>/g, which also represents a 2% increase in surface area relative to the freshly synthesized material. As in the case of the 0.12% Pd/MCM-41, this likely does not represent a significant change in surface area. Therefore, Pd/MCM-41 samples did not undergo any significant loss of surface area after 50 d of contact with deionized water.

Figure 26 presents the results of low angle XRD analyses performed on as-synthesized Ni/MCM-41 materials and materials recovered after 40 d in deionized water at 25°C. There is a broadening of the 100 peak and substantial decrease in intensity of the 110 and 200 peaks for each of the recovered 0.12% and 1.12% Ni/MCM-41 relative to the freshly prepared materials. The 110 and 200 peaks are not discernible in the recovered 1.12% Ni/MCM-41 sample. These results indicate that there was a decrease in the hexagonal form of Ni/MCM-41 materials after

40 d in deionized water. The decrease in order was more pronounced in the material with higher mass loadings of Ni. The cell parameter and primary mesopore diameters of the recovered materials were calculated and are presented in

Table 10. The primary mesopore diameters increased by 1.2% and 1.4% for the recovered 0.12% and 1.12% Ni/MCM-41 samples, respectively. As in the case of Pd/MCM-41 samples, these small percent changes are not significant.

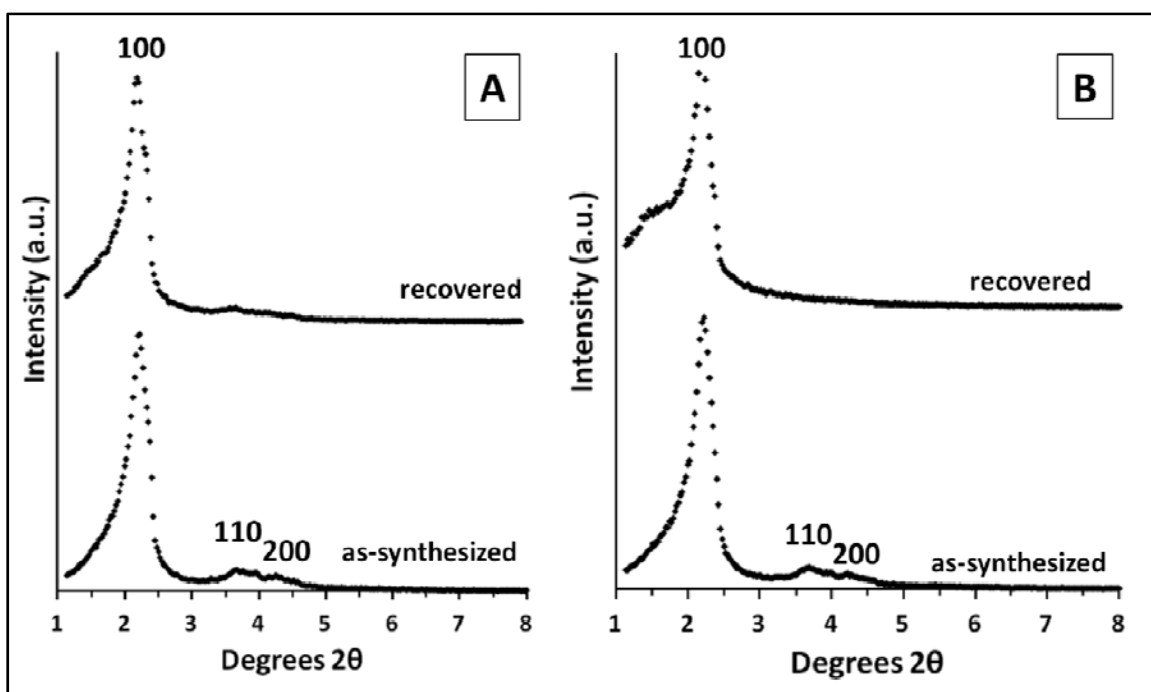


Figure 26: Comparison of as-synthesized Ni/MCM-41 and materials recovered after 40 d in deionized water. (A) 0.12% Ni/MCM-41. (B) 1.12% Ni/MCM-41.

Results of an 11-point BET surface area analysis of the 0.12% Ni/MCM-41 sample recovered after 40 d in deionized water indicated a surface area of 839 m<sup>2</sup>/g. This value represents a 10% decrease in surface area relative to the as-synthesized material. Surface area analysis of the 1.12% Ni/MCM-41 sample indicated a surface area of 657 m<sup>2</sup>/g after 40 d in deionized water. This value represents a 33% decrease in surface area relative to the as-synthesized material. The Ni/MCM-41 materials at both mass loadings of Ni exhibited a substantial loss of surface area after 40 d of contact with deionized water.

The possibility that Ni/MCM-41 dissolved more rapidly than Pd/MCM-41 due to residual salts such as NiCO<sub>3</sub> remaining on the material's surface following its synthesis was investigated

further in the following dissolution experiment. The experiment was conducted to compare the dissolution rates of purely siliceous MCM-41 (Combo 2), 0.12% Pd/MCM-41, and 0.12% Ni/MCM-41 in a 0.01 M *NaCl* solution. The 0.01 M *NaCl* solution was used to eliminate as a variable, any possible influence of residual salts on the dissolution rates for the earlier experiments described above. The conductance of the prepared 0.01 M *NaCl* solution was 1.12 mS/cm. All sample bottles were prepared using a solid/liquid ratio of 1/200 and mounted in the same isotherm bath at  $25 \pm 0.1^\circ\text{C}$  used in the earlier dissolution experiments. A detailed summary of sample bottle contents is included in Appendix B. Concentration of  $\text{SiO}_2$  in solution samples taken during the experiment were determined using a spectrophotometer and following the molybdate blue method (Appendix B).

Results of  $\text{SiO}_2$  concentration analyses for the samples taken at intervals during the experiment are presented in Figure 27. Uncertainty in the analysis was determined by analyzing five, separate samples taken from the 0.12% Ni/MCM-41 duplicate sample reaction bottle after 1405 min. The uncertainty was found to be 4% of the reported  $\text{SiO}_2$  concentration value. The reagent blank sample and duplicate did not indicate any presence of  $\text{SiO}_2$ . Sample and duplicate from the purely siliceous MCM-41 reaction bottles achieved  $\text{SiO}_2$  concentrations of 2.2 and 2.3 mM within 24 h, respectively. Both the 0.12% Pd/MCM-41 sample and duplicate achieved concentrations of 1.1 mM  $\text{SiO}_2$  within 24 h. These values were between 67% and 71% lower than those for the purely siliceous MCM-41 samples. Therefore, Pd impregnated MCM-41 was substantially more resistant to dissolution by the 0.01 M *NaCl* solution than purely siliceous MCM-41. The 0.12% Ni/MCM-41 sample and duplicate achieved concentrations of 1.9 and 2.0 mM  $\text{SiO}_2$  within 24 h, respectively. These concentrations were between 13% and 14% lower than those for purely siliceous MCM-41. Thus, the Ni impregnated MCM-41 material was slightly more resistant to dissolution by the 0.01 M *NaCl* solution, but substantially less resistant than the Pd/MCM-41 material at similar mass loadings of metal.

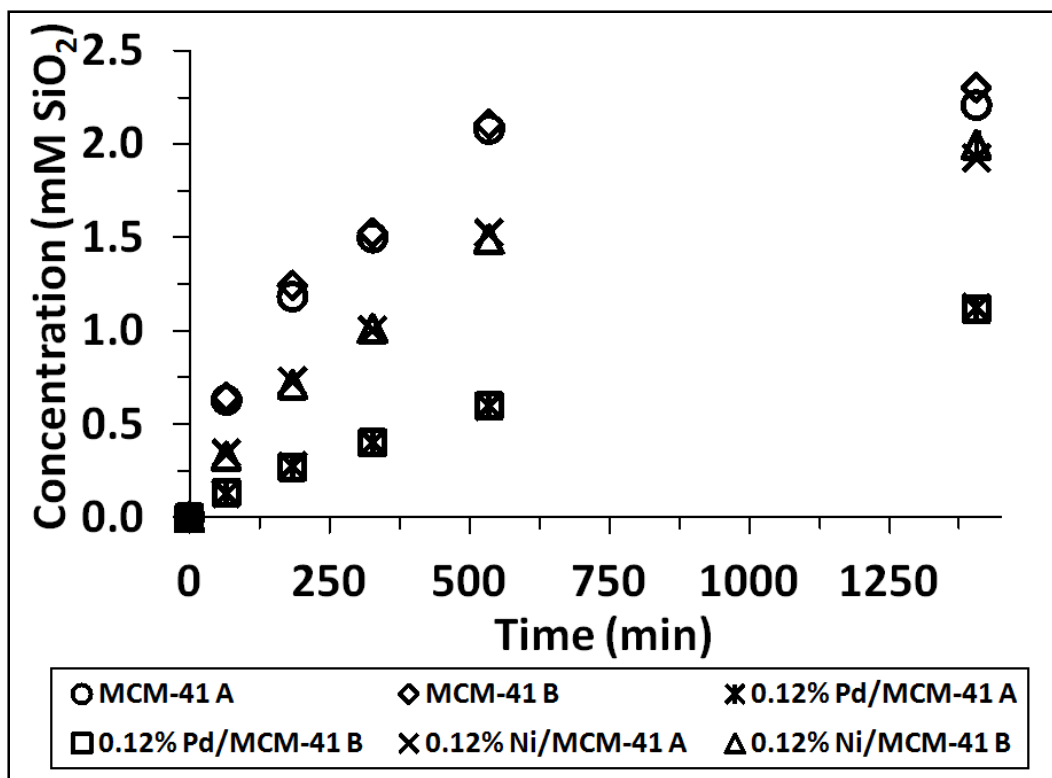


Figure 27: Results of dissolution experiments comparing purely siliceous MCM-41 (Combo 2), 0.12% Pd/MCM-41, and 0.12% Ni/MCM-41 in a 0.01 M NaCl solution.

Therefore, the rapid dissolution of Ni impregnated MCM-41 materials was likely due to a salt effect resulting from the presence of residual Ni salts such as  $NiSO_4$  and  $NiCO_3$  on the material's surfaces, and their subsequent dissolution when the material was brought into contact with deionized water. Similar dissolution rates were observed for purely siliceous MCM-41 in a NaCl salt solution. These results are consistent with the findings of Hanton-Fong (1992) who showed that the dissolution rate of silica is enhanced in neutral salt solutions compared to deionized water. However, the results of the above experiments also indicated that impregnation of MCM-41 with Pd enhances the material's resistance to dissolution by both deionized water and a 0.01 M NaCl solution. These results are promising with regards to using Pd impregnated MCM-41 materials in water treatment technologies. Conversely, results suggest that longevity of Ni impregnated MCM-41 materials may be limited in water treatment technologies.

### 3.3.2 Dissolution Rate Modeling

An attempt was made to model the  $SiO_2$  concentration results from the Pd/MCM-41 dissolution experiments using the RATES and KINETICS keyword blocks in Phreeqci. The

model was constructed using a first-order dissolution rate equation for quartz published by Rimstidt & Barnes (1980) and developed into an algorithm following a method presented in Appelo & Postma (2007). Amorphous silica ( $SiO_{2(a)}$ ) was used in place of MCM-41 in the model. The proposed first-order dissolution rate equation for MCM-41 is described by the following relation:

$$r_{MCM-41} = k_{MCM-41} \cdot \left(1 - \frac{IAP}{K}\right)$$

where  $k_{MCM-41}$  is the dissolution rate constant for the different MCM-41 materials, IAP is the ionization activity product, and K is the equilibrium constant. This equation can be integrated and solved using Phreeqci for various concentrations of  $SiO_2$  in solution as a function of time. The dissolution rate constant was determined via a linear fit to the  $SiO_2$  concentration versus time results from the dissolution experiments. The value of  $k_{MCM-41}$  was then normalized with respect to the surface area of a particular sample as determined from BET surface area analyses. These values are summarized in Table 11. Although the determination of  $k_{MCM-41}$  via a linear fit to the  $SiO_2$  concentration versus time data is mathematically simplistic, a comparison of  $R^2$  values with critical  $R^2$  values for seven pairs of observations indicated that the calculated  $k_{MCM-41}$  values may be considered as valid. The dissolution of Pd/MCM-41 materials in deionized water was then modeled using Phreeqci on the basis of the calculated  $k_{MCM-41}$  values and sample-specific parameters determined from the solid-to-liquid ratio of a given experiment. It was assumed that 1 kg of deionized water was in contact with the Pd/MCM-41 particles.

An example of the input file for one such simulation (1.16% Pd/MCM-41 at a solid-to-liquid ratio of 1/200) is presented below in Figure 28. Parm(1) and parm(2) refer to the parameters  $A_0$  and V, which represent the surface area of Pd/MCM-41 in contact with deionized water and the volume of deionized water, respectively. SR refers to the saturation ratio or index of the substance in solution. SR was assumed to be similar to that of amorphous silica ( $SiO_{2(a)}$ ). The parameter  $m_0$  represents the initial moles of  $SiO_2$  in contact with the 1 kg of water. The exponent of the parameter  $(m/m_0)^{0.67}$  accounts for changes in surface area as particles dissolve. The value 0.67 assumes a uniform distribution of spherical particles. Although MCM-41 particles are unlikely to be perfectly spherical, the value 0.67 still accounts for changes in particle geometry as dissolution proceeds. A series of simulations were run using Phreeqci while adjusting the

value of the exponent above and below a value of 0.67. It was found that changes in the value from 0.0001 to 0.999 had a negligible effect on the modeled dissolution curves. The ‘step’ parameter refers to the time step over which Pd/MCM-41 dissolution was modeled. In Figure 28, the total time was 4.32E6 s (50 d) with a time step of 1.73E5 s.

**Table 11: Summary of values calculated for dissolution rate constant calculations for Pd/MCM-41 materials.**

Material	Solid/Liquid	SA (m <sup>2</sup> /g)	A <sub>o</sub> (m <sup>2</sup> )	m <sub>o</sub> (mol/l)	# of points
0.12% Pd/MCM-41	1/200	522.4	2612	8.39E-02	7
	1/100	522.4	5224	1.67E-01	7
1.16% Pd/MCM-41	1/200	521.1	2605	8.23E-02	7
	1/100	521.1	5211	1.65E-01	7

Material	R <sup>2</sup>	Critical R <sup>2</sup>	Admissable? Y/N	Log(k <sub>MCM-41</sub> (calculated))	Log(k <sub>MCM-41</sub> (manual fit))
0.12% Pd/MCM-41	0.932	0.754	Y	-12.3	-12.7
	0.833	0.754	Y	-12.2	-12.7
1.16% Pd/MCM-41	0.948	0.754	Y	-12.4	-12.9
	0.900	0.754	Y	-12.2	-12.9

```

SOLUTION 1
  temp  25
  pH    7
  pe    4
  redox pe
  units mmol/kgw
  density 1
  -water 1 # kg

RATES
  SiO2(a)
  -start
  10 A0 = parm(1)
  20 V = parm(2)
  30 rate = 10^-12.4*(1-SR("SiO2(a))) * A0/V*(m/m0)^.67
  40 moles = rate*time
  50 save moles
  -end

KINETICS 1
  SiO2(a)
    -formula SiO2
    -m0 0.0832224
    -parms 2605.4545 1
    -step 4.32E6 in 25
INCREMENTAL_REACTIONS true

SELECTED_OUTPUT
  -file      C:\Users\Colin\Desktop\selected.xls
  -totals    Si

END

```

Figure 28: Phreeqc simulation of dissolution kinetics for 1.16% Pd/MCM-41 at a solid-to-liquid ratio of 1/200.

Results of the simulations of dissolution kinetics for the four Pd/MCM-41 dissolution experiments are presented in Figure 29. It was found that the  $k_{\text{MCM-41}}$  values obtained via linear fit to the dissolution data yielded a poor correspondence with the experimental data. It is proposed that the poor fit resulted from either the assumption of a uniform distribution of spherical particles or because the linear fit to experimental data provided a poor estimation of  $k_{\text{MCM-41}}$ . The  $k_{\text{MCM-41}}$  values used in the simulated results in Figure 29 were determined by using the linear fit  $k_{\text{MCM-41}}$  as a starting point and then adjusting the  $k_{\text{MCM-41}}$  value until a satisfactory match between simulated and experimental data was obtained. These values of  $k_{\text{MCM-41}}$  are presented above in Table 11 under the column heading ‘Log( $k_{\text{MCM-41}}$ (manual fit))’. It is proposed

that these ‘manual fit’ values of  $k_{\text{MCM-41}}$  are the more accurate when compared with those determined via a linear fit to the experimental data.

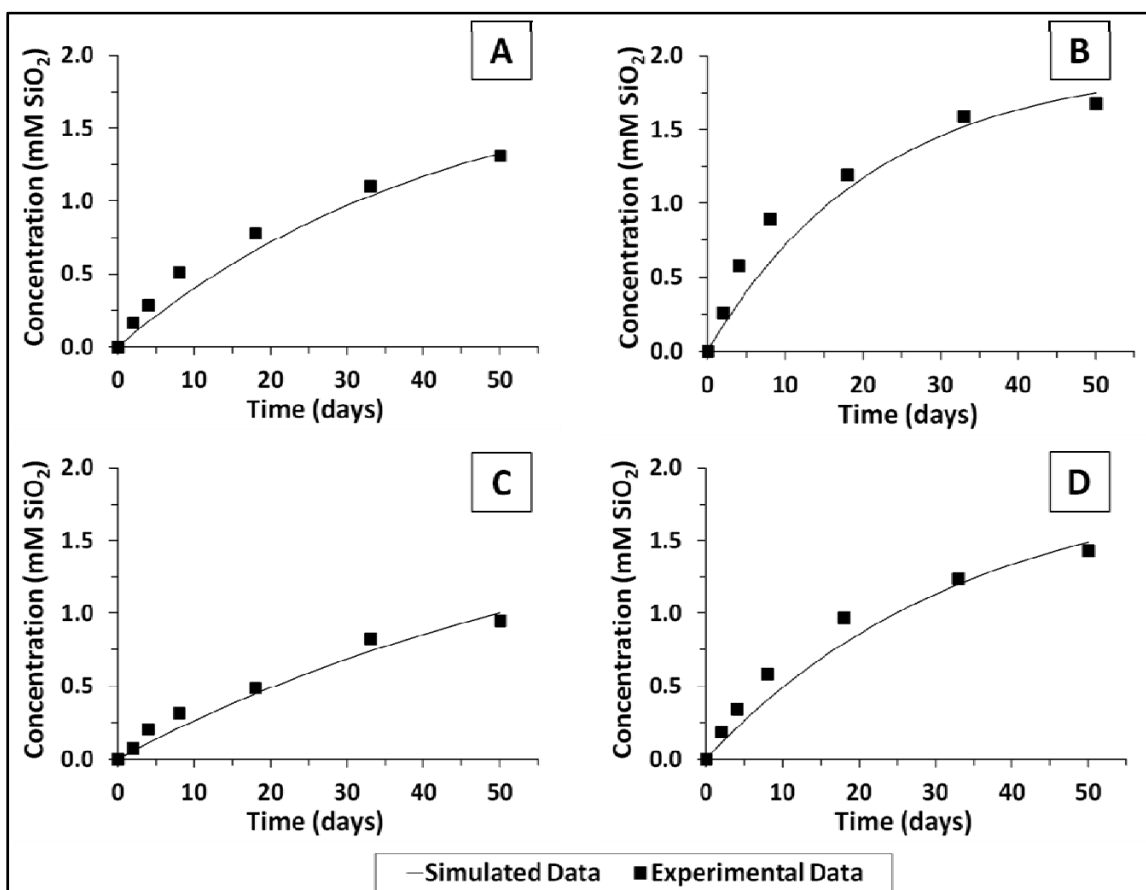


Figure 29: Comparison of simulated and experimental dissolution results for: (A) 0.12% Pd/MCM-41 at a solid to liquid ratio of 1/200, (B) 0.12% Pd/MCM-41 at a solid to liquid ratio of 1/100, (C) 1.16% Pd/MCM-41 at a solid to liquid ratio of 1/200, and (D) 1.16% Pd/MCM-41 at a solid to liquid ratio of 1/100.

### 3.3.3 Long term dissolution experiment

A sample of purely siliceous MCM-41 from an earlier experiment was allowed to continue mixing on the wheel setup for 1,174 d. Solid material was recovered from this experiment after 280 d and upon termination of the experiment. Figure 30 compares the low angle XRD results for the as-synthesized material and materials recovered after 280 and 1,174 d of contact with deionized water. The trace for the as-synthesized material exhibits a small peak (210) which is absent in the materials recovered after 280 d and 1,174 d. However, the characteristic first three peaks (100, 110, 200), which together indicate a hexagonal arrangement

of the MCM-41 mesopores, are easily identified in all three plots. Therefore, the hexagonal structure of MCM-41 was still intact after 1,174 d of contact with deionized water.

Results of a BET nitrogen adsorption surface area analysis indicated that the as-synthesized, calcined MCM-41 sample had a surface area of 874 m<sup>2</sup>/g. The MCM-41 sample recovered after 1,174 d of contact with deionized water had a surface area of 841 m<sup>2</sup>/g. The sample recovered after 280 d was not analyzed with respect to surface area. The change in surface area between the as-synthesized sample and the sample recovered after 1,174 d represents a percent decrease of 3.8%. Although the initial surface area of the as-synthesized material was relatively low for a well-formed sample of MCM-41, it is still a high surface area siliceous material possessing the characteristic hexagonal form of MCM-41. Therefore, there was no substantial loss of surface area in the MCM-41 sample after 1,174 d of contact with deionized water.

The low angle XRD and surface area results indicated that the structure and high surface area of purely siliceous MCM-41 are resistant to change while in contact with deionized water at 25±0.1°C for periods as long as 1,174 d. This conclusion is promising with regards to the longevity of MCM-41 when used in water treatment technologies.

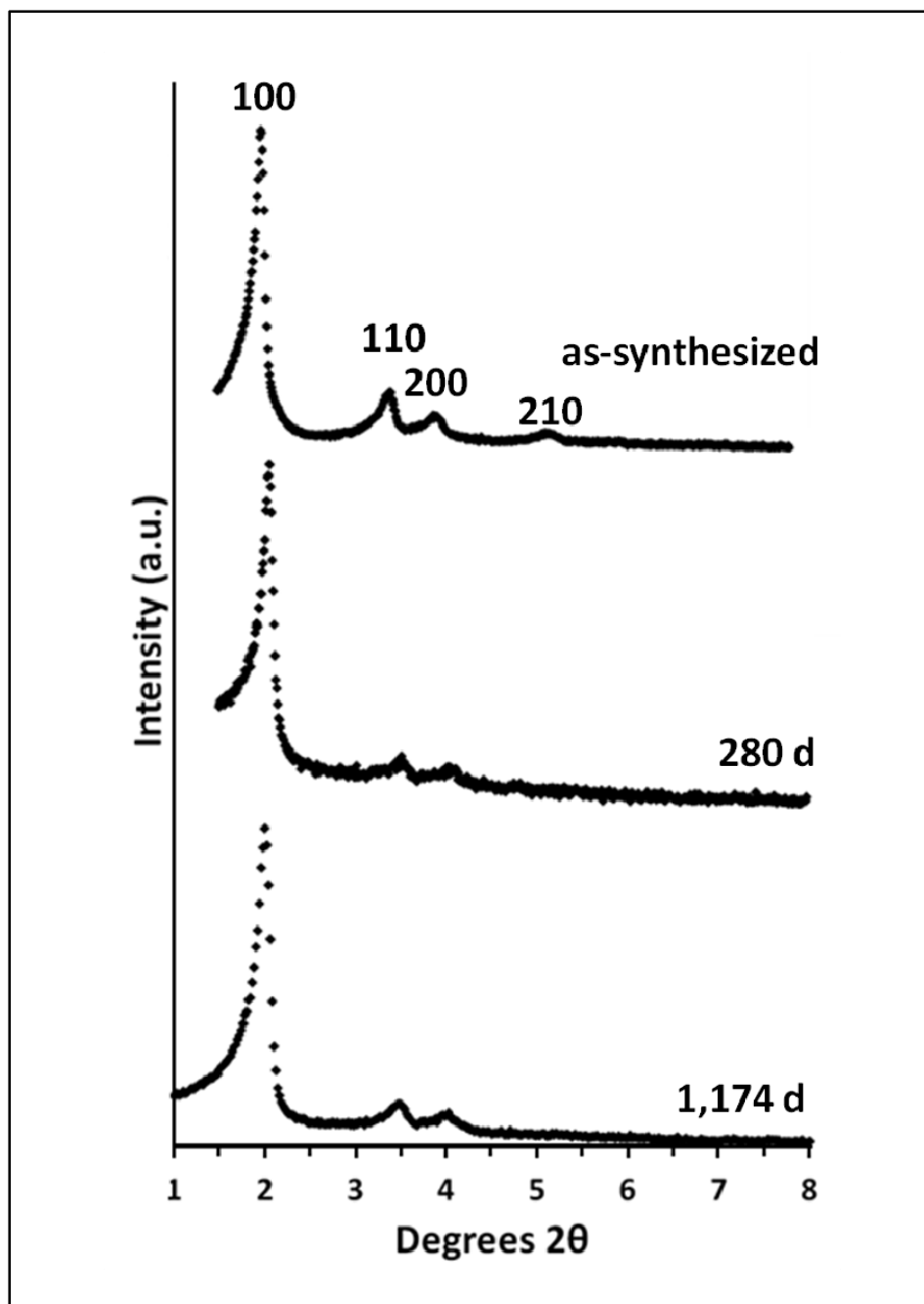


Figure 30: Comparative low angle XRD plots for as-synthesized MCM-41 as well as material recovered after 280 d and 1,174 d contact with deionized water.

Characteristics determined via low angle XRD for the calcined MCM-41 are compared to those of the recovered materials in Table 12. After 1,174 d in contact with deionized water, the values of the cell parameter “a”, primary mesopore diameter, and wall thickness all decreased by 0.10%. This very small decrease in these three characteristics indicates that there was no substantial change in the porosity of the MCM-41 material over the 1,174 d experiment.

**Table 12: Comparison of MCM-41 characteristics determined by low angle XRD after 280 and 1,174 days in deionized water.**

Sample	2 $\theta$ (100)	d100	a (nm)	Wd (nm)	Wt (nm)
as-synthesized	1.97	44.75	5.17	4.43	0.73
280 d	2.04	43.35	5.01	4.29	0.71
1,174 d	1.98	44.71	5.16	4.43	0.73

### 3.4 Conclusions

All materials tested via the above-described dissolution experiments were soluble in deionized water at  $25\pm 0.1^\circ\text{C}$ . The  $\text{SiO}_2$  of the MCM-41 support material dissolved and trended towards a steady-state concentration corresponding to saturation with respect to amorphous silica ( $\sim 2$  mmol/l). This finding was consistent with earlier findings using purely siliceous MCM-41. The presence of metals on the surfaces and within the pores of Pd/MCM-41, Ni/MCM-41, and Ni-Pd/MCM-41 influenced the dissolution rate of  $\text{SiO}_2$  in the MCM-41 samples.

The Pd/MCM-41 materials had higher stability when in contact with deionized water relative to purely siliceous MCM-41. It is proposed that the decreased surface area resulting from surface coverage and partial pore blocking by Pd in Pd/MCM-41 decreases the solubility of the material.

All samples containing Ni (Ni/MCM-41 and Ni-Pd/MCM-41) exhibited lower stability in deionized water when compared with both purely siliceous MCM-41 and Pd/MCM-41. Both Ni and Pd impregnated MCM-41 materials exhibited enhanced stability relative to purely siliceous MCM-41 in 0.01 M *NaCl* solution. The enhancement in stability was more pronounced for Pd/MCM-41.

As-synthesized, calcined MCM-41 was resistant to degradation of both the hexagonally arranged mesopores and surface area while in contact with deionized water at  $25\pm 0.1^\circ\text{C}$  for an extended period of time (1,174 d). This result is promising with regards to application of MCM-41 in water treatment technologies.

## CHAPTER 4

### 4. HYDROGEN UPTAKE BY Pd/MCM-41

#### 4.1 Background

Research into the interaction of hydrogen gas and metals has been driven by possible applications in several areas including catalysis and chemical production, fuel cell technology, and water treatment. The hydrogen-palladium system, specifically, has attracted interest due to palladium's potential use in fuel cell technology storage systems and as a high efficiency catalyst in many different reactions. Additionally, repeated pressurization and depressurization of Pd with hydrogen does not result in the hydrogen embrittlement seen in other metals such as iron (Vogel *et al.*, 2010).

When hydrogen gas is brought into contact with Pd, it dissociates into individual atoms at the surface and diffuses into the metal lattice, forming a random solid solution of palladium hydride (Iyer & Pickering, 1990; Prasanth *et al.*, 2010). In bulk Pd metal, hydrogen occupies the interstitial, octahedral sites of the metal's fcc lattice and can migrate to any available vacancies or voids in the structure (Iyer & Pickering, 1990; Flanagan & Oates, 1991; Sachs *et al.*, 2001). As hydrogen is absorbed and released by Pd, the metal undergoes a transition between the  $\alpha$  and  $\beta$ -phase (Walter & Chandler, 1965; Horner & Wagner, 1974; Flanagan & Oates, 1991). The  $\alpha$ -phase describes a solution phase with lattice constants (the distance between unit cells) similar to those of palladium metal. As hydrogen pressure increases and gas continues to enter the Pd lattice, the lattice expands, creating additional lattice sites, thus increasing the lattice constant. At a certain pressure, the  $\alpha$ -phase converts to the  $\beta$ -phase (Jewell & Davis, 2006). The  $\alpha$  to  $\beta$  phase transition indicates the formation of metal hydrides in the palladium (Flanagan *et al.*, 1980).

The use of a solid support material with a reactive metal can reduce the tendency of free metal particles to aggregate together. Thus, using a support material can aid in obtaining well-dispersed metal centers of relatively small diameter and high surface area, while avoiding coalescence of metal particles during their use as a catalyst (Koh *et al.*, 1997; Huang *et al.*, 2006; Park & Lee, 2010; Prasanth *et al.*, 2010). Support materials are often used in conjunction with highly reactive nano-sized metals for similar reasons. Certain properties of metal nanoparticles, including

solubility, reactivity, surface area, concentration of surface sites and defects, may differ markedly from their larger-sized or bulk counterparts (Wang & Zhang, 1997; Chen & Elimelech, 2006; Theng & Yuan, 2008). MCM-41 is one such support material of interest. It is a siliceous, mesoporous material possessing several interesting characteristics: exceptionally high surface areas ( $> 1000 \text{ m}^2/\text{g}$ ) and a pore size that can be adjusted between 2 and 10 nm, depending on the synthesis procedure and reagents used in its synthesis (Beck *et al.*, 1992). An in-depth discussion of the unique properties of MCM-41 may be found in Section 1.1 of Chapter 1 and Section 2.1 of Chapter 2.

Reactive metals such as Pd can be grafted to the surface and within the pores of MCM-41 (Koh *et al.*, 1997; Decyk, 2006). Metals may also be incorporated within the MCM-41 structure during its hydrothermal synthesis (Zhang *et al.*, 1996; Ziolk *et al.*, 2004). Prasanth *et al.* (2010) reported hydrogen uptake of 35.1 ml  $\text{H}_2/\text{g}$  by Pd-incorporated MCM-41 samples. In this material,  $\text{Pd}^{2+}$  was incorporated into the structure of MCM-41 during its hydrothermal synthesis. The purpose of the current research is to determine the hydrogen absorption capacity of Pd grafted to the surfaces and within the pores of MCM-41 (Pd/MCM-41) at  $298.2 \pm 0.1 \text{ K}$  up to pressures of between 50 and 100 kPa and compare it to unsupported Pd black. Comparison will also be made between results of the current research and those reported in the literature.

## **4.2 Experimental Methods**

### **4.2.1 Reagents**

Palladium black (Pd, 99.9%, CAS<sup>#</sup>7440-05-3, Phillipsburg, NJ) was obtained from Alfa Aesar. Hydrogen gas (99.995%, CAS<sup>#</sup>1333-74-0, Kitchener, ON) was obtained from Praxair.

### **4.2.2 Hydrogen Absorption**

A detailed discussion of the synthesis and characterization of all reactive materials used in the following experiments is included in Sections 2.2.2, 2.2.3 2.3.1, and 2.3.2 of Chapter 2.

$\text{H}_{2(\text{g})}$  absorption by Pd/MCM-41 was measured using two interconnected stainless steel cells of known volume equipped with computer-monitored pressure transducers (Figure 31). Cells, valves, and pressure transducer were connected by stainless steel tubing and Swagelok fittings.

All cells were filled with  $H_{2(g)}$  and tested to ensure no leakage or uptake of hydrogen by the metal components. Known masses of dry Pd/MCM-41 were placed in CELL 2. The cell apparatus was submerged in a temperature-controlled water bath at  $25\pm 0.1^\circ\text{C}$ . Both cells were evacuated using an Edwards 2-stage vacuum pump via the inlet of CELL 1. Hydrogen was added by injection from a gas-tight glass-on-glass syringe to CELL 1 and allowed to equilibrate thermally with the apparatus. Hydrogen was introduced to reactive Pd/MCM-41 in CELL 2 by opening a valve between cells after the cell pressure showed no further decrease with time. The initial and final cell pressures in kPa were recorded. This process was repeated with successive injections of hydrogen until the desired final pressure was achieved. Similarly, hydrogen was removed from CELL 2 in successive steps by lowering the pressure in CELL 1 via vacuum pump, allowing remaining hydrogen gas to equilibrate thermally, and then opening the valve between cells. Results of simplified measurements are also included in the following chapter. In these cases, only one injection of  $H_{2(g)}$  was made and the uptake recorded. Maximum uptake of  $H_{2(g)}$  measured in this fashion should not differ from that determined via isotherms generated from successive injections of  $H_{2(g)}$ .

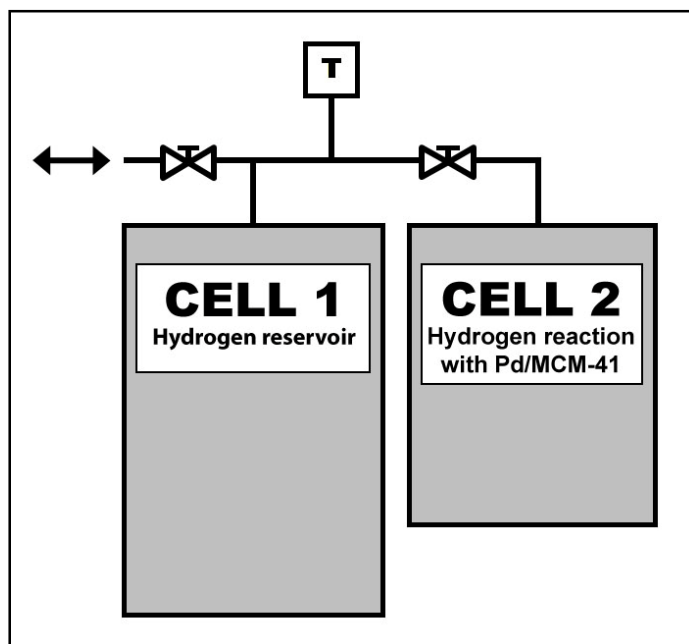


Figure 31: Schematic showing setup of pressure cells.  $H_{2(g)}$  was added and removed via CELL 1. Reactive material was contained in CELL 2. (T – Pressure transducer)

Pd/MCM-41 samples were pre-treated by pressurizing the cells with hydrogen to approximately 120 kPa and leaving them overnight. Cells were then evacuated, re-pressurized to 120 kPa with

hydrogen and left for a minimum of 2 h. Finally, cells were put under vacuum for 30 mins before starting an experimental run. Reproducible results were achievable following this pre-treatment procedure. Cycles of pressurization and de-pressurization ensured conversion of relatively unstable  $PdO$  material in the palladium clusters on Pd/MCM-41 to  $Pd^0$  (Sachs *et al.*, 2001).

$H_{2(g)}$  absorption by Pd was calculated using pressure transducer readings and the ideal gas law as the difference between calculated initial moles of  $H_{2(g)}$  gas in CELL 1 and final total moles of  $H_{2(g)}$  in both cells' headspace once the connecting valve between cells was opened.

Experiments conducted with empty cells as well as un-palladized MCM-41 confirmed hydrogen pressure differences resulted from absorption by Pd within reported experimental uncertainties. Absorption results are expressed as moles of hydrogen absorbed per mole of Pd (H/Pd) at selected pressures. A plot of the equilibrated hydrogen pressure versus H/Pd gives the pressure-composition (P-C) isotherm for each Pd/MCM-41 sample. Experiments were also conducted with palladium black (Pd, 20  $m^2/g$ ) as an analogue of bulk Pd metal. Standard deviation of transducer measurements was 0.03 kPa at 97.51 kPa. Standard error in H/Pd determinations was between 1 and 4 % of calculated H/Pd values.

## 4.3 Results and Discussion

### 4.3.1 Hydrogen Absorption Experiments

Maximum extent of hydrogen absorption was determined from the steady-state portion of the P-C isotherm, where further increases in hydrogen pressure produced no change in hydrogen uptake, i.e. constant H/Pd values. Steady state was defined as points on the curve exhibiting less than 10% change from each previous, lower pressure point. These values agreed closely with earlier identification of steady-state portions of isotherms by visual inspection. Typical results for un-palladized, calcined MCM-41 are shown in Figure 32 as a plot of 'H Discrepancy' vs. pressure. Plotted results confirm no measurable sorption of hydrogen by the MCM-41 support material.

A typical P-C isotherm from one experimental run using 2.04% Pd/MCM-41 is shown in Figure 33. Absorption occurred rapidly, with steady-state pressure generally achieved within 10 mins of introducing hydrogen to CELL 2 (See Figure 31). Hysteresis shown by H/Pd results at lower

pressures ( $< 0.1$  atm) during depressurization stage was typical for all runs and Pd/MCM-41 samples. Consistency of maximum  $H_{2(g)}$  absorption between experimental runs using the same Pd/MCM-41 sample indicated that absorbed  $H_{2(g)}$  was released when the sample was put under vacuum between runs.

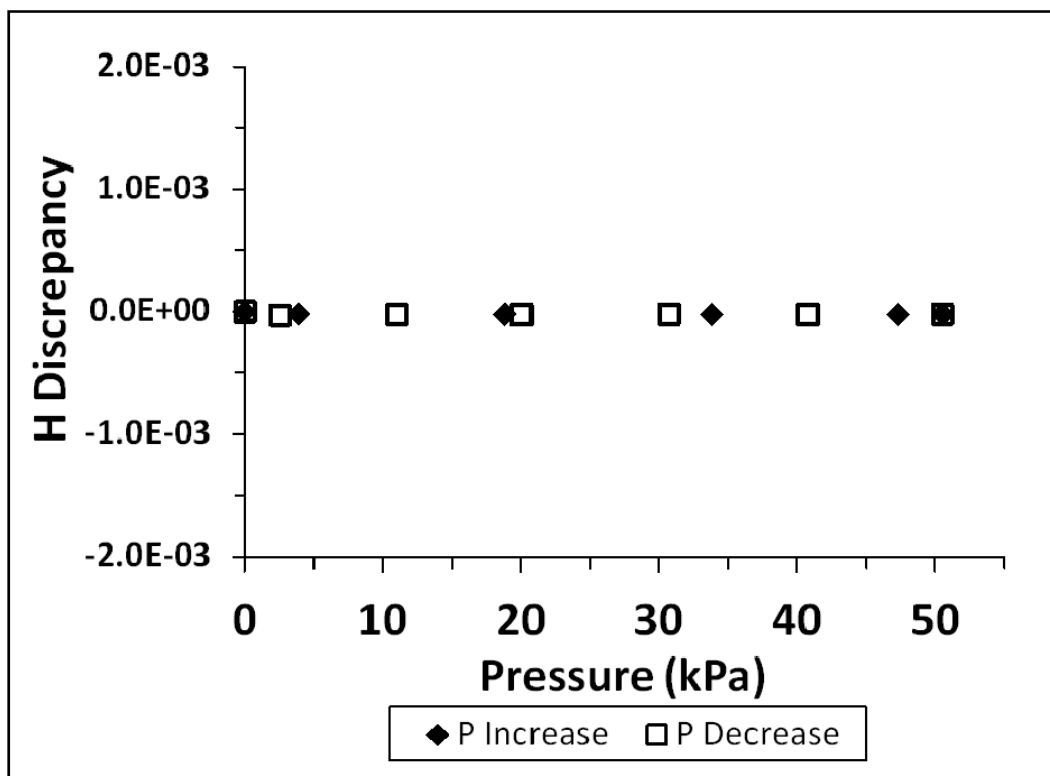


Figure 32: Typical hydrogen absorption results for pure silica MCM-41. 'H Discrepancy' refers to the difference between actual moles of H in the cell and moles calculated assuming no uptake. An H discrepancy of zero indicates no uptake of hydrogen by the sample.

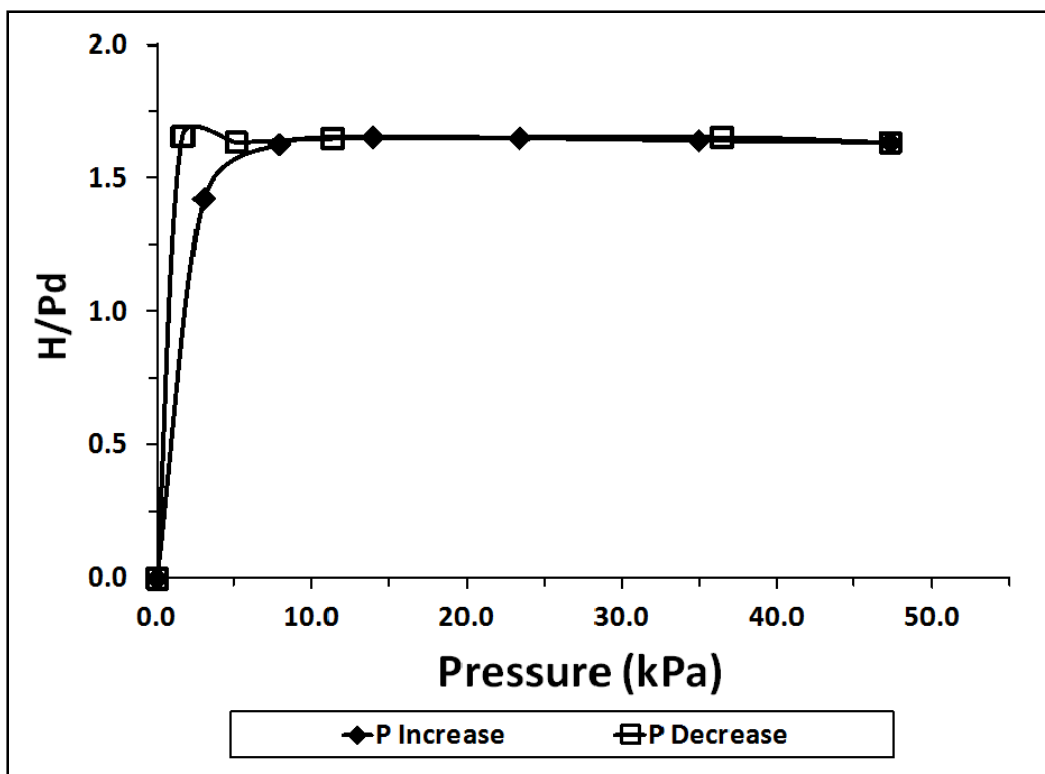


Figure 33: Typical pressure versus hydrogen absorption curve for a Pd/MCM-41 sample (2.30% Pd/MCM-41 results shown). H/Pd represents moles of hydrogen absorbed per mole of Pd present.

A set of example isotherms for increasing and decreasing hydrogen pressure with Pd black is presented in Figure 34. In this case, hydrogen was injected into the cells to achieve a steady-state pressure approaching 250 kPa. Results clearly indicate that no further uptake of hydrogen occurs above pressures of approximately 50 kPa. This result is consistent with results for uptake by Pd/MCM-41. Figure 34 also includes a point ( $\square$ ) showing the result of an experimental run to calculate hydrogen uptake based on volume difference (rather than pressure differences as in other calculations). In this experiment, hydrogen was added to CELL 1 and CELL 2 apparatus using a glass-on-glass syringe and the amount absorbed was determined from the volume markings on the syringe. The result of this experimental run agrees closely with earlier results determined from measurements taken using the pressure transducers.

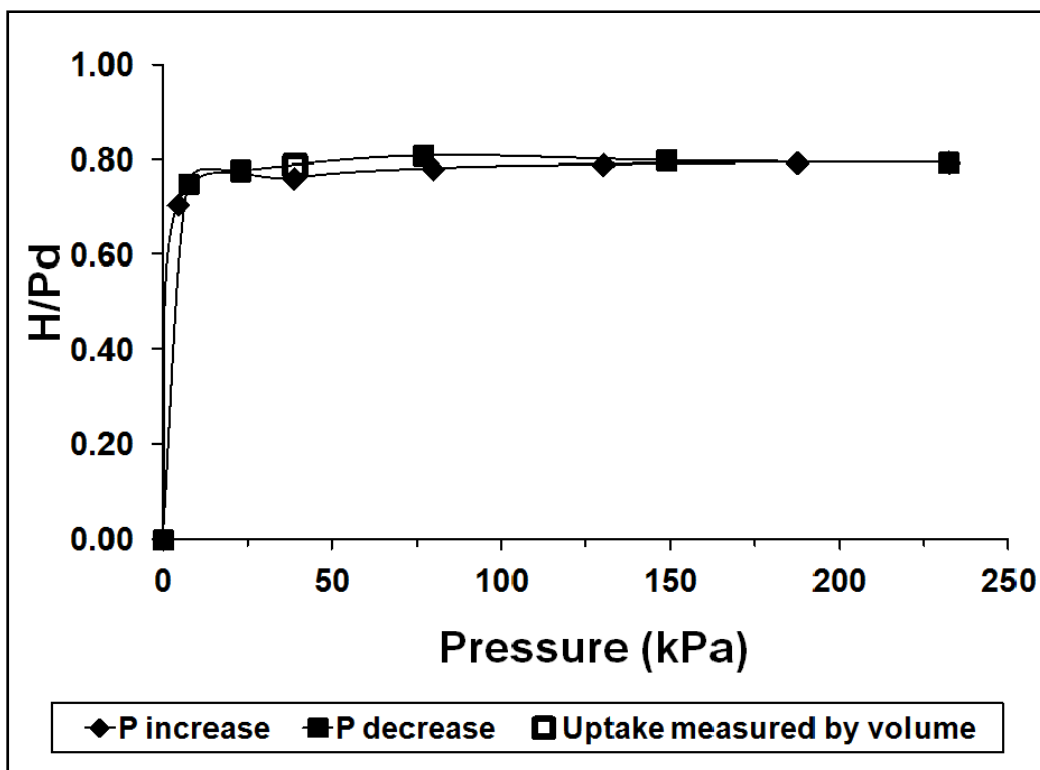


Figure 34: Typical pressure versus hydrogen absorption isotherms for Pd black. An independent experiment where uptake was determined via a volume measurement is indicated by the open square point. H/Pd represents moles of hydrogen absorbed per mole of Pd present.

The appearance of hysteresis in H/Pd results upon lowering  $P_{H_2}$  suggests a two-phase field during absorption/desorption and a phase transition in the metal (Sachs *et al.*, 2001; Pundt *et al.*, 2004). Similar hysteresis results of experiments with Pd reported by other researchers were caused by a difference in the formation pressure of the metal hydride phase relative to the decomposition pressure (Flanagan *et al.*, 1980). This phase transition results from lattice expansion and the associated tensile stress as increasing amounts of hydrogen enter the Pd lattice and metal hydride is formed with corresponding lattice contraction during dehydriding (Flanagan *et al.*, 1975; Flanagan *et al.*, 1980; Flanagan & Oates, 1991; Sachs *et al.*, 2001). Misfit dislocations of the lattice – or, disruptions to the regularity of the lattice structure – as reported in bulk Pd are not expected in particles with diameter less than 4 nm (Ichinose, 2000; Sachs *et al.*, 2001). Instead, hysteresis in smaller particles is caused by a coherency, or internal elastic stress in the metal, resulting in different chemical potentials during loading and unloading of hydrogen into Pd, thus forming a hysteresis loop (Schwarz & Khachatryan, 1995; Sachs *et al.*,

2001; Pundt *et al.*, 2004). Diameters of Pd centres in prepared Pd/MCM-41 materials may be within this range, as discussed in Section 2.3.2.4 of Chapter 2.

Hydrogen pressurization pretreatment of Pd/MCM-41 samples (described above) removes the oxide layer on Pd, leaving a reduced Pd metal. Reduced Pd on Pd/MCM-41 samples prepared following the method of Koh *et al.* (1997) should yield an average Pd particle size of 2-2.5 nm with good distribution within MCM-41 pores. Therefore, it is proposed that hysteresis in this case results from differing chemical potentials during loading and unloading of hydrogen into Pd samples, rather than creation of misfit dislocations as occurs in larger diameter Pd particles.

Hydrogen absorption experiments for each Pd/MCM-41 sample were repeated a minimum of five times to determine the degree of reproducibility of P-C isotherms. Average H/Pd values of all steady-state points on P-C isotherms for each Pd/MCM-41 sample were plotted versus the mass percent loading of Pd and are presented in Figure 35. A summary of more detailed information used in creating Figure 35 is included in Appendix C. Error bars were calculated as the standard deviation at a 95% confidence interval. The error bar for the 2.30% Pd/MCM-41 samples results is roughly equal to the height of the data point. Average absorption at all mass percent Pd loadings was  $0.85 \pm 0.18$  H/Pd with an apparent, overall trend of increasing absorption as mass percent of Pd on MCM-41 increased from 0.81 to 2.30%. Maximum hydrogen absorption was 1.07 H/Pd for 2.30% Pd/MCM-41. Minimum hydrogen absorption was 0.74 H/Pd by 1.10% Pd/MCM-41. The  $R^2$  value of a trend line applied to the H/Pd versus mass percent loading Pd plot was 0.42. The critical  $R^2$  value for five data points at a 95% confidence level is 0.71. Therefore, the apparent increase in H/Pd as the mass percent Pd loading increases is not significant. Results of similar experiments using Pd black showed absorption of  $0.79 \pm 0.09$  H/Pd, which was 30% less than uptake by 2.30 % Pd/MCM-41, but only 7% less than the average uptake by all five Pd/MCM-41 samples.

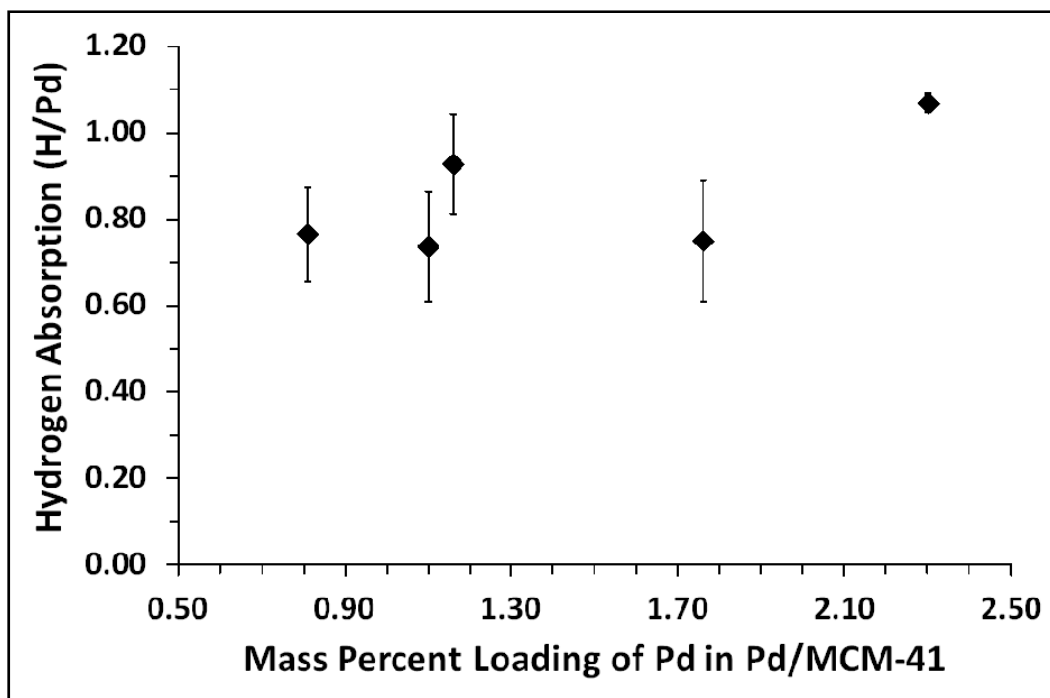


Figure 35: Results of hydrogen absorption by Pd/MCM-41 samples at different mass percent loadings of Pd.

Hydrogen solubility in bulk Pd has been calculated as  $S = 27.1 P^{0.5}$  according to Sieverts' Law, where  $S$  is in  $\text{mol/m}^3$  and  $P$  is in Pa (Sachs *et al.*, 2001). Boudart & Hwang (1975) measured hydrogen absorption of 0.50 H/Pd in small Pd particles supported on  $\text{SiO}_2$  and  $\text{Al}_2\text{O}_3$  at 303 K. Jewell & Davis (2006) reported 0.03 H/Pd in  $\alpha$  phase Pd and 0.6 H/Pd in  $\beta$  phase at room temperature. Pundt *et al.* (2004) reported that bulk Pd absorbed 0.6 H/Pd at room temperature while Pd surfaces can adsorb up to 1 H/Pd. Kuji *et al.* (2002) performed experiments with nano-sized and coarser-grained Pd at 298 K. They recorded absorption of just over 0.7 H/Pd at 100 kPa for coarse-grained samples while nano-sized Pd samples of diameter 8 nm absorbed between 0.45 and 0.50 H/Pd. Sachs *et al.* (2001) studied surfactant and polymer-stabilized nano-clusters of Pd at room temperature. They reported absorption between 0.40 and 0.65 H/Pd at 100 kPa for surfactant-stabilized clusters of diameter 2, 3 and 5 nm. Researchers have noted small Rh metal clusters less than 1 nm in diameter can absorb up to 8 atoms deuterium per metal atom; however, the maximum absorption reported for Pd was lower at 3.25 moles deuterium per mole of neutral Pd atoms and approaches unity as Pd cluster size increases (Cox *et al.*, 1990; Sachs *et al.*, 2001, Pundt *et al.*, 2004). In the only published paper on the H/Pd ratios in palladized MCM-41, Prasanth *et al.* (2010) prepared 3.7% by weight Pd-incorporated, hydrothermally synthesized

MCM-41 and recorded absorption of 0.306 H/Pd (35.1 cc H<sub>2</sub>/g) at 303 K. In their material, Pd<sup>2+</sup> was incorporated into the MCM-41 structure during synthesis rather than being deposited onto the surfaces and within pores. Additionally, their mass percent of Pd in MCM-41 samples was greater than the 2% maximum used in this current study. Both these aspects of Prasanth *et al.*'s absorption study may account for their substantially lower observed H/Pd results.

A combined comparison of all published results is difficult due to differences in reaction temperatures, support materials, mass of Pd, and sample preparation techniques. However, average absorption by Pd/MCM-41 at 25.0±0.1°C and Pd mass percent loadings between 0.81 and 2.30% was higher than results published by other researchers using different Pd preparations and support materials. Published results described above are summarized in Table 13. The enhanced deuterium absorption by metal particles as their diameter decreased below 1 nm reported by Cox *et al.* (1990) implies the possibility of similar enhancements for other small-sized transition metals. This would suggest that further enhancements to hydrogen uptake may be achieved using exceptionally small particles of Pd. Enhanced absorption by Pd/MCM-41 compared to other, previously published results using other Pd materials may be explained by a larger proportion of subsurface sites in nano-sized Pd particles in Pd/MCM-41 relative to surface and bulk sorption sites.

**Table 13: Comparison of published values for hydrogen uptake by palladium.**

Material Description	Uptake	T (K)	Reference
SiO <sub>2</sub> and Al <sub>2</sub> O <sub>3</sub> supported Pd	H/Pd = 0.50	303	Boudart & Hwang (1975)
bulk Pd	$S = (27.1)(P^{0.5})$	298	Sachs <i>et al.</i> (2001)
surfactant-stabilized Pd	H/Pd = 0.40 to 0.65	298	Sachs <i>et al.</i> (2001)
coarse-grained Pd	H/Pd = 0.7	298	Kuji <i>et al.</i> (2002)
nano-sized Pd	H/Pd = 0.45 to 0.50	298	Kuji <i>et al.</i> (2002)
bulk Pd	H/Pd = 0.6	298	Pundt <i>et al.</i> (2004)
Pd surface	H/Pd = 1.0	298	Pundt <i>et al.</i> (2004)
alpha-phase Pd	H/Pd = 0.03	298	Jewell & Davis (2006)
beta-phase Pd	H/Pd = 0.6	298	Jewell & Davis (2006)
Pd-incorporated MCM-41	H/Pd = 0.306	303	Prasanth <i>et al.</i> (2010)

#### 4.4 Conclusions

The average amount of  $H_{2(g)}$  absorbed by Pd in Pd/MCM-41 in this study was  $0.85 \pm 0.18$  H/Pd and absorption did not vary significantly as a function of mass percent loading of Pd on Pd/MCM-41. Extent of absorption exceeded that of most other published Pd-hydrogen system results. It is proposed that the relatively high uptake of hydrogen by Pd/MCM-41 may result from an enhanced proportion of near surface sites in Pd centres. The enhancement in  $H_{2(g)}$  uptake in Pd/MCM-41 relative to other supported Pd materials reported in the literature suggests that Pd/MCM-41 has potential as an  $H_{2(g)}$  reservoir for reaction catalysis or fuel cell technology applications.

## CHAPTER 5

### 5. DEGRADATION OF CONTAMINANTS BY METAL IMPREGNATED MCM-41

#### 5.1 Background

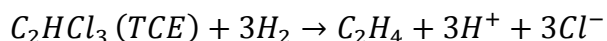
The *in situ* treatment of chlorinated volatile organic compounds (cVOC) in groundwater can involve the use of zero-valent iron (ZVI) in a permeable reactive barrier (PRB) (Gillham & O'Hannesin, 1994; O'Hannesin & Gillham, 1998; Day *et al.*, 1999; Gavaskar, 1999; Jiao *et al.*, 2009; Ruhl *et al.*, 2012). The iron causes abiotic reductive dehalogenation reactions and has been used to degrade a wide variety of chlorinated organic compounds as well as inorganic contaminants where attenuation in the subsurface can be enhanced through reductive reactions (Blowes *et al.*, 1997; McCreadie *et al.*, 2000). For some recalcitrant organic compounds, long contact times [i.e. thicker permeable reactive barriers (PRB)] between reactive media and contaminants may be necessary to achieve a desired contaminant or breakdown product concentration level (Schuth *et al.*, 2000). ZVI is also prone to loss of reactivity over time due to the accumulation of inorganic precipitates on its particle surfaces. Use of a catalyst in conjunction with zero-valent iron in a PRB or in *ex situ* treatment technologies may help circumvent these problems and may lead to a more rapid and complete degradation of contaminants. Treatment methods that completely transform chlorinated compounds into products of lesser toxicity are preferable over other techniques that produce secondary waste streams requiring further treatment (Schreier & Reinhard, 1995).

Incorporation of transition metal catalysts, such as nickel and palladium, into treatment systems shows promise for improving current treatment methods as they can induce degradation of a variety of contaminants at ambient conditions while producing relatively low amounts of reaction intermediates (Lowry & Reinhard, 1999; Xu *et al.*, 2005). Several studies have investigated directly plating transition metals onto the surfaces of the ZVI particles to improve their reactivity. Rapid deactivation of the bimetallic catalyst due to precipitation or dissolution is often reported with this approach (Zhang, 1998). An alternate approach is to use a separate support for the catalyst rather than the ZVI itself. As described in Chapter 2, a supported catalyst used in conjunction with ZVI could be used in PRB technology, pump-and-treat methods, or a combination of the two. In the envisioned field application of the technology, the actual source

of hydrogen gas for the Pd/MCM-41 support catalyst will come from the anaerobic corrosion of ZVI, an ongoing reaction whenever ZVI is in contact with groundwater. However, hydrogen was supplied in the current experiments by using hydrogen-saturated stock solutions, maintaining contact between stock solutions and a hydrogen headspace during experiments, and by adding a second stage of stock solution contact with a hydrogen headspace before it entered the columns.

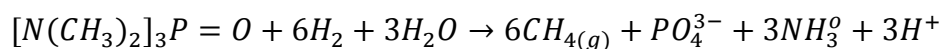
In this chapter, the experiments focused on degradation of a chlorinated volatile organic compound (cVOC) variously referred to as trichloroethylene, trichloroethene, ethinyl trichloride, or ethylene trichloride (TCE, Figure 36). TCE provides a good model cVOC with which the ability of Pd/MCM-41 to induce degradation may be ascertained before attempting treatment of other, more recalcitrant compounds. TCE is a relatively widespread groundwater contaminant. In an article by Page (1981) and later summarized by Pankow & Cherry (1996), it was reported that 388 out of 669 wells tested in New Jersey were contaminated by detectable concentrations of TCE. A different study by Soeteman *et al.* (1981), was also summarized by Pankow and Cherry (1996) and described 67% of sampled wells in the Netherlands as contaminated with detectable concentrations of TCE. In a preliminary draft of a health risk assessment, the United States Environmental Protection Agency (EPA) notes that TCE is frequently found as a groundwater contaminant and estimates that between 9% and 34% of drinking water supplies contain detectable concentrations of the compound (USEPA, 2001). Similar levels of TCE concentration can be expected in any industrial area which has seen its widespread use and improper disposal at any point in the past. The frequency with which TCE contamination is found in groundwater sources is a reflection of its extensive use in the past in applications such as degreasers and dry cleaning solvents (Newman *et al.*, 1997). Concern over TCE contamination is due to an increased risk to human health given adequate exposure to the compound over time. Similar to other toxic cVOCs, TCE-induced health risks due to exposure via drinking water can occur at ppb levels of contamination (Cothorn *et al.*, 1986; Crosta & Dotti, 1998).

In the case of TCE, the following overall degradation reaction has been proposed in which TCE reacts with hydrogen to form ethane (McNab & Ruiz, 1998):



This process may be described as a reductive dechlorination reaction as the TCE molecule is in a relatively oxidized state relative to its degradation product ethane. It has been proposed by other researchers that when Pd is present, TCE adsorbs to the Pd surface and undergoes complete dehalogenation before desorbing as ethane, essentially following the overall reaction described above (Lowry & Reinhard, 1999; Kim & Carraway, 2003; Sriwatanapongse *et al.*, 2006). Once adsorbed, TCE may react via a succession of partial degradation steps to intermediate products, desorb, re-adsorb as an intermediate product, and then finally desorb as ethane. Although it is possible that TCE follows a sequential degradation reaction in the presence of Pd under a given set of conditions, the current study focuses interest on the overall reaction and final degradation products.

A second set of batch experiments investigating the ability of Pd/MCM-41 to degrade the contaminant hexamethylphosphoramide (HMPA, Figure 36) is also described in this chapter. HMPA ( $C_6H_{18}N_3OP$ ) is an organic solvent used as a reagent in a variety of organic reactions and synthesis procedures. It is a colourless liquid at room temperature and a suspected human carcinogen. Complete HMPA degradation induced by Pd/MCM-41 in hydrogen saturated deionized water is proposed to follow the pathway:



where HMPA reacts with hydrogen and water to form methane, phosphate, and ammonia.

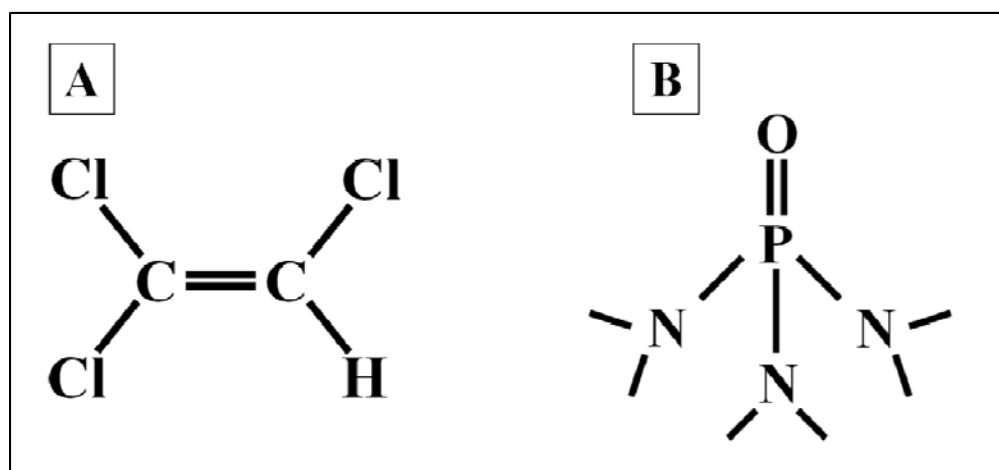


Figure 36: Representation of (A) trichloroethylene and (B) hexamethylphosphoramide molecular structures.  $CH_3$  groups on N atoms for hexamethylphosphoramide not shown.

The purpose of the experiments described in this chapter was to determine the ability of an MCM-41 supported Pd catalyst to degrade TCE and HMPA in hydrogen-saturated deionized water. Experiments were also conducted to determine the ability of Pd supported on sand (Pd/sand) to induce degradation of TCE. Pd/sand was included to determine the benefit of using MCM-41 as a metal support compared to other, less costly materials. This study constitutes an early step towards evaluating the potential and limitations of using an MCM-41-supported catalyst as an additive to ZVI to improve its ability to dechlorinate hydrocarbons in PRBs.

## 5.2 Experimental Methods

### 5.2.1 Reagents

Trichloroethylene (TCE,  $C_2HCl_3$ , 99.9%, CAS#79-01-6, Phillipsburg NJ) was obtained from J.T. Baker. Hexamethylphosphoramide (HMPA,  $C_6H_{18}N_3PO$ ,  $\geq 98\%$ , CAS#680-31-9, Phillipsburg, NJ) was obtained from Sigma-Aldrich. Hydrogen gas (99.995%, CAS#1333-74-0, Kitchener, ON) was obtained from Praxair. Deionized water was used in all experimental work, unless noted otherwise.

### 5.2.2 TCE Degradation Batch Experiment

A batch experiment was undertaken to compare the abilities of MCM-41 and sand-supported Pd (Pd/MCM-41 and Pd/sand, respectively) at inducing degradation of trichloroethylene (TCE). An evaluation of the comparative benefit of using MCM-41 in degradation reactions, relative to a readily available support material of low cost was deemed to be of interest. Ottawa silica sand was selected as a support material to be compared to MCM-41 due to its low cost and ready availability.

Materials prepared for this experiment included unpalladized, acid washed, 50-70 mesh, Ottawa silica sand as well as 1.00% Pd/sand and 1.10% Pd/MCM-41. Details regarding the synthesis and characterization of these materials are presented in Chapter 2 and Appendix A.

A hydrogen-saturated solution was prepared by bubbling hydrogen gas through a sparger into a 2 l glass carboy filled with 993.3 ml of deionized water for 30 min. At 1 atm pressure and 298 K, this produces a solution with a dissolved hydrogen concentration of 0.863 mmol/l (Randall &

Failey, 1927). After 30 min of sparging, the deionized water was spiked with TCE to obtain a desired concentration of 10 mg/l.

The carboy was sealed with a rubber stopper and the solution was stirred for 3 h using a magnetic stir bar. Meanwhile, an average mass of  $0.0506 \pm 3.17 \times 10^{-4}$  g of the appropriate sand, Pd/sand and Pd/MCM-41 materials were added to 40 ml glass reaction bottles. The average mass of Pd present in the sample bottles containing metal impregnated samples was  $5.13 \times 10^{-4} \pm 1.21 \times 10^{-5}$  g. The target solid/liquid mass ratio was 1/800. This solid/liquid mass ratio was found to be adequate to degrade similar initial concentrations of TCE in earlier work (Guthrie, 2007). As the variation in Pd present in each sample bottle was low (2.36% of the average Pd mass), it was deemed as having a negligible influence on the results. Therefore, concentration results were not normalized with respect to mass of Pd present in each sample bottle.

The reaction bottles were filled to overflowing with the hydrogen-saturated TCE solution and crimp-sealed with Teflon and rubber caps. All samples were prepared in duplicate. A representation of a typical reactive sample is shown in Figure 37. Control samples were also prepared with 40 ml of the hydrogen-saturated TCE solution and crimp sealed. The time at which the bottles were sealed was recorded as time zero ( $t_0$ ) for the experiment. The bottles were well-mixed via end-over-end rotation during the experiment to ensure that MCM-41 and Pd/MCM-41 materials were in continuous contact with all of the solution.

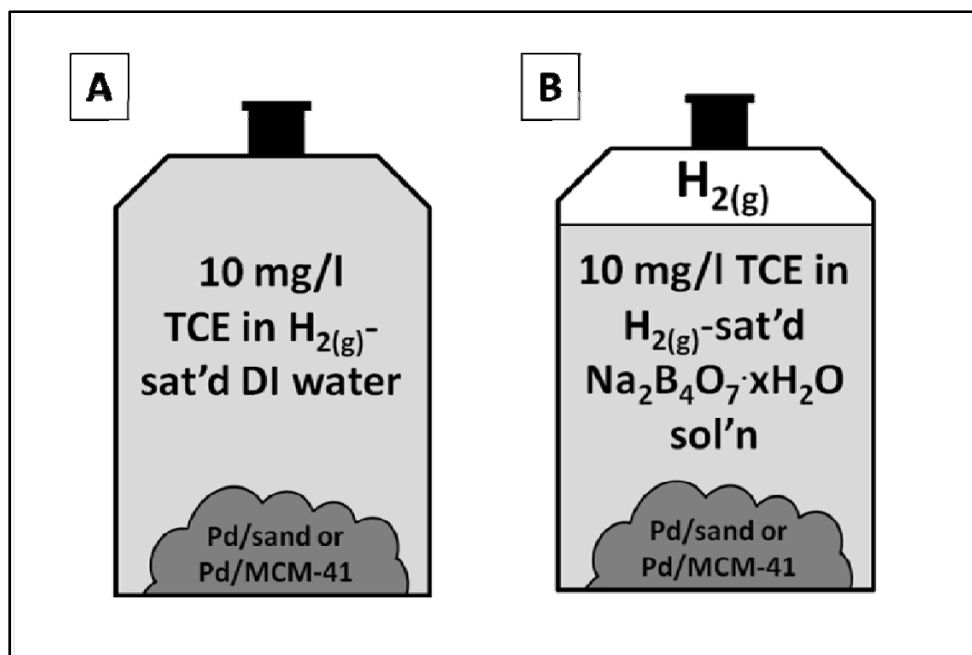


Figure 37: Schematic showing typical reactive sample setup for: (A) first phase of TCE degradation batch experiment with no headspace, and (B) second phase including 2 ml hydrogen headspace and TCE in a hydrogen-saturated,  $Na_2B_4O_7 \cdot xH_2O$  in deionized water solution.

Each reaction bottle was centrifuged at up to 4,400 rpm for 1 min prior to sampling to separate the solid particles from solution. The sample bottles were de-crimped and two, 10 ml samples of the supernatant solution were sampled by filling a 5 ml plastic syringe and passing the solution through a 0.2  $\mu\text{m}$  Supor<sup>®</sup> membrane Acrodisc<sup>®</sup> syringe filter. 10 ml glass sample bottles were filled to overflowing with the solution and crimp-sealed with Teflon and rubber caps. The sample bottles were stored under refrigeration at 278 K until they were analyzed.

The samples were analyzed for TCE concentration using a Hewlett Packard 5890 Series II gas chromatograph equipped with a Ni<sup>63</sup> ECD detector and following a liquid-liquid extraction gas chromatograph analysis technique. The detector temperature was 300°C, injection temperature was 200°C, and the column temperature was 50°C to 150°C at a rate of 15 cm<sup>3</sup>/min and then held for 1 min. The carrier gas was pre-purified helium with a total flow rate of 25 ml/min and the makeup gas was 5% methane and 95% argon. The samples were analysed for VC, 1-1 DCE, and the *cis* and *trans* isomers of DCE using a Hewlett Packard 5890 gas chromatograph equipped with an Hnu photo ionization detector using an Hnu NSW-plot capillary column and following a PID gas chromatograph analysis technique. The lamp potential was 10.2 eV. The GC had an initial temperature of 50°C with a temperature program of 20°C/min. Final temperature

was 200 °C and held for 9 min. The detector temperature was 150 °C and the injector was 100 °C. The carrier gas was ultra-pure helium with a flow rate of 20 ml/min. Finally, samples were also analyzed for methane, ethylene, and ethane using a Hewlett Packard 5790 gas chromatograph equipped with a flame ionization detector (FID) using a GS-Q plot capillary column. The GC had an initial temperature of 60°C, which was held for 3 min. The temperature was then increased at a rate of 15°C/min up to 120°C and held at 125°C for 10 min. The detector was set for 280°C with an injector temperature of 200°C. The carrier gas was ultra-pure nitrogen with a flow rate of 20 ml/min.

A follow-up batch experiment was performed using similar procedures and using the same equipment as the experiment described above. In this experiment, pH of the hydrogen-saturated TCE solution was elevated to 9.15 by addition of a 2 mmol/l  $Na_2B_4O_7 \cdot xH_2O$  solution. The pH was measured using an Omega AlpHa<sup>®</sup> PHE-1411 electrode and Fisher Scientific Accumet pH meter 50 calibrated using 7.00 and 10.00 buffers. In addition, batch reaction sample bottles in this experiment included a 2 ml headspace of  $H_{2(g)}$  to ensure that hydrogen was not a limiting reagent in TCE degradation reactions. Headspace was added to reaction bottles after they had been filled to overflowing and crimp-capped. Hydrogen was injected via a glass on glass syringe and needle inserted through the Teflon and rubber cap. Hydrogen-saturated TCE and  $Na_2B_4O_7 \cdot xH_2O$  solution displaced by the 2 ml of hydrogen passed from the sample bottles through a syringe needle inserted through the Teflon and rubber cap.

### **5.2.3 TCE Degradation Column Experiment**

#### **5.2.3.1 TCE Degradation Column Experiment - First of Two**

A TCE degradation column experiment was undertaken to confirm the ability of Pd/MCM-41 to degrade TCE over a large number of pore volumes with continuous input of TCE solution. Other columns were filled with different reactive materials including: sand supported Pd (Pd/sand), Ni/MCM-41, and Ni-Pd/MCM-41. These materials were included in the experiment to ascertain their abilities to induce degradation of TCE and compare them to that of Pd/MCM-41.

Experiments were conducted using small, glass columns connected to stainless steel tubing at the inflow and outflow points using Swagelok metal-to-glass transitions. Teflon tubing was used to connect the feed solution carboy to the stainless steel tubing connected to the column. Teflon tubing was also used between the column outflow sampling port and the effluent reservoir. The experiment was performed at ambient laboratory temperatures of approximately 293 K. Columns of relatively low internal volume were used in this experiment to both reduce the mass of reactive materials needed for the fill mixtures and to allow the experiment to proceed to a high number of pore volumes (PV) within a reasonable amount of time.

Column length was 6.0 cm and internal diameter was 1.8 cm, yielding an internal volume of 15 cm<sup>3</sup>. A schematic illustrating the typical column setup from the experiment is presented in Figure 38. Columns were loosely packed with glass wool at the inflow and outflow points to reduce the potential for migration of porous materials out of the columns. Approximately 0.1 cm<sup>3</sup> and 1.0 cm<sup>3</sup> of glass wool was added to the inflow and outflow points of the columns, respectively. A small glass vial with inflow and outflow ports was installed immediately before the inflow point of the column. During the experiment, this vial was kept filled with  $H_{2(g)}$  to ensure that saturation with respect to hydrogen was maintained in the TCE feed solution as it entered the reactive column. Two sampling ports were located at the inflow and outflow points of the column. Sampling ports consisted of a T-junction installed in the Teflon tubing between the  $H_{2(g)}$  filled vial and the column as well as between the column outflow point and the effluent reservoir. The sampling ports in the T-junctions were sealed with rubber sleeve septa. Sampling proceeded by inserting a needle-equipped 10.0 ml glass-on-glass syringe. Syringes were allowed to fill under pressure of the pump so as to not alter solution flow characteristics through the column.

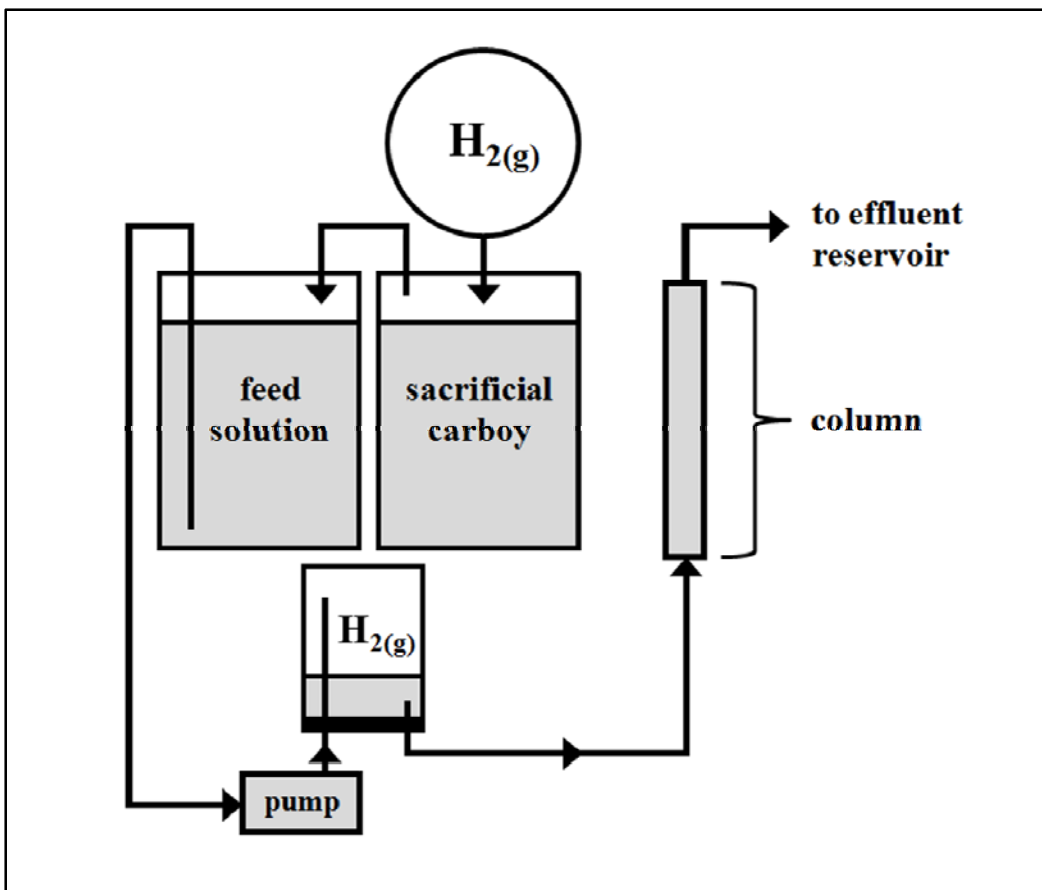


Figure 38: Schematic of TCE degradation columns. Sacrificial and feed solution carboys contain 10 mg/l TCE in hydrogen-saturated deionized water. Reactive columns contained porous materials described in Table 14. Additional  $H_{2(g)}$  reservoir is shown between the pump and column.

TCE solution flow through the column was controlled by a peristaltic pump. As the feed solution level in the reservoir decreased, hydrogen was continually replenished via a Mylar bag filled with hydrogen connected to a ‘sacrificial carboy’ containing TCE solution.

The mass of each column was recorded prior to filling with porous materials. Each reactive column was then filled with desired masses of either Pd/sand, Pd/MCM-41, Ni/MCM-41, or Ni-Pd/MCM-41. Relatively small masses of these reactive materials were used in each column. Thus, 50-70 mesh, acid washed, Ottawa silica sand was mixed with reactive materials to ensure an adequate volume of porous material to fill each column. A control column was filled using only 50-70 mesh, acid washed, Ottawa silica sand. A summary of the porous materials used to fill each column is given in Table 14.

**Table 14: Summary of column porous material properties. First set of column experiments.**

Column	Reactive Material	% Loading	Reactive material as % of total porous	Sand as % of total porous material	column (g)	Packed mass of column (g)
1	Pd/sand	1.00	1.49	98.51	203.53	219.17
2	Pd/MCM-41	0.99	1.50	98.50	205.53	222.21
3	Ni/MCM-41	1.02	1.50	98.50	203.49	219.33
4	Ni-Pd/MCM-41	1.01	1.50	98.50	205.71	221.84
5	Pd/MCM-41	0.12	1.50	98.50	207.63	224.22
6	Ni-Pd/MCM-41	0.13	1.50	98.50	205.76	221.63
7	Control	-	-	100.00	199.78	212.38

Column	Wetted mass of packed column (g)	Pore Volume (ml)	Porosity	Dry Bulk Density (g/cm <sup>3</sup> )	Wet Bulk Density (g/cm <sup>3</sup> )
1	226.08	6.91	0.45	1.0	1.5
2	229.67	7.46	0.49	1.1	1.6
3	227.08	7.75	0.51	1.0	1.5
4	230.31	8.47	0.55	1.1	1.6
5	232.60	8.38	0.55	1.1	1.6
6	231.95	10.32	0.68	1.0	1.7
7	219.52	7.14	0.47	0.8	1.3

The combined reactive materials and silica sand were mixed end-over-end for 15 min to ensure a homogeneous mixture. Differences in colour between reactive materials (gray, to grayish black) and silica sand (white) allowed the attainment of a homogeneous mixture to be determined via visual inspection. The resulting porous material was transferred in stages to the column so as to maintain a homogeneous mixture as much as was possible. The sides of each column were gently tapped periodically during filling to consolidate the fill material. This tapping was done to avoid unexpected consolidation of porous materials during flow of TCE solution through the columns during the experiment. The stainless steel Swagelok fittings were then installed at the inflow and outflow points, sealing the columns. The masses of the filled columns were recorded.

Initial flow to the columns was deionized water. The mass of each saturated column was recorded and used in calculating the pore volumes (PV). Flow rates were calculated and adjusted to desired volumes per unit time during this stage. The target flow rate was 4 ml/min. This flow rate was chosen based on observations for similar column experiments using Pd to induce degradation of cVOCs (Wayne Noble, personal communication, January 11, 2012).

The feed solution to the column was prepared by sparging deionized water with  $H_{2(g)}$  for 30 min in a glass carboy. The carboy was then spiked with the calculated volume of TCE and tightly sealed with a rubber stopper. The resulting solution was vigorously stirred with a magnetic stir bar for 3 h. Target TCE concentration was 10 mg/l. The carboy was then installed between the sacrificial carboy and the pump. The pump was then activated, initiating flow through the reactive column.

Samples were taken at intervals during the experiment and stored at 279 K in inverted glass vials with rubber and Teflon-sealed screw caps. Pore volumes of feed solution that had passed through each column at the time of sampling were calculated by dividing the total mass of effluent collected from column outlets by the pore volume of each column. Samples were analyzed for concentrations of TCE, VC, 1-1 DCE, and the *cis* and *trans* isomers of DCE.

At the end of the Pd/MCM-41 column experiment, solid Pd/MCM-41 material was recovered from the column. The material was characterized via low angle XRD and the 11 point BET nitrogen adsorption surface area analysis using the instruments described in Chapter 2. Results of these analyses were then compared to those of the freshly prepared Pd/MCM-41.

The pH measurements were made using an Omega AlpHa<sup>®</sup> PHE-1411 electrode and Fisher Scientific Accumet pH meter 50 which was calibrated using 4.00 and 7.00 buffers.

Samples taken at later times during the column degradation experiment were also measured with respect to conductance using an Orion Model 162 conductivity meter and probe. A cell constant for the probe was determined by measuring the conductance of a 0.01 mol/kg *KCl* solution. The conductance of the solution (1408  $\mu\text{S}/\text{cm}$  at 25 °C) was divided by the measured conductance to yield the cell constant. All measured values of sample conductance were multiplied by the cell constant to obtain the real conductance.

### **5.2.3.2 TCE Degradation Column Experiment - Second of Two**

A second column experiment was undertaken using larger scale columns which included multiple sampling ports along the length of each column. The purpose of this experiment was to obtain TCE degradation profiles as a function of length along the column, thus facilitating calculation of reaction rate constants and degradation half-lives. Columns were made of

Plexiglas<sup>®</sup> and contained mixtures of Pd/MCM-41 and silica sand (20-30 mesh Ottawa sand) at different proportions of reactive Pd/MCM-41 to sand and at different mass percentage loadings of Pd. The experiment was performed at ambient laboratory temperatures: approximately 293 K. Column ends were closed with Plexiglas<sup>®</sup> end caps fitted with rubber O-rings. Plastic mesh installed in the end caps inhibited loss of solid particles from within the column.

Column length was 30.0 cm and internal diameter was 2.5 cm, yielding an internal volume of 147 cm<sup>3</sup>. Sampling ports were located every 2.5 cm along the length of reactive columns. A control column had ports every 2.0 cm along its length. A Teflon Swagelok<sup>®</sup> fitting was screwed into each sampling port. A 16 ½ gauge Precision Glide<sup>®</sup> needle was packed with glass wool and tapped through each fitting and aligned with the centre of the column. When not being sampled, needles were sealed with a plastic 3 ml syringe filled with silicon sealant. Sampling proceeded by replacing the sealed syringe with a glass-on-glass syringe. Syringes were allowed to fill under pressure of the pump so as to not disturb flow of solution through the columns.

Flow of solution through columns was controlled by a solenoid-operated Teflon micro pump and three valves actuated by a computer/data acquisition system using LabVIEW software. A schematic of the pump, valve, and column setup is presented in Figure 39. As feed solution level in the reservoir decreased, hydrogen headspace was continually replenished via a Mylar bag filled with  $H_{2(g)}$  connected to the ‘sacrificial carboy’.

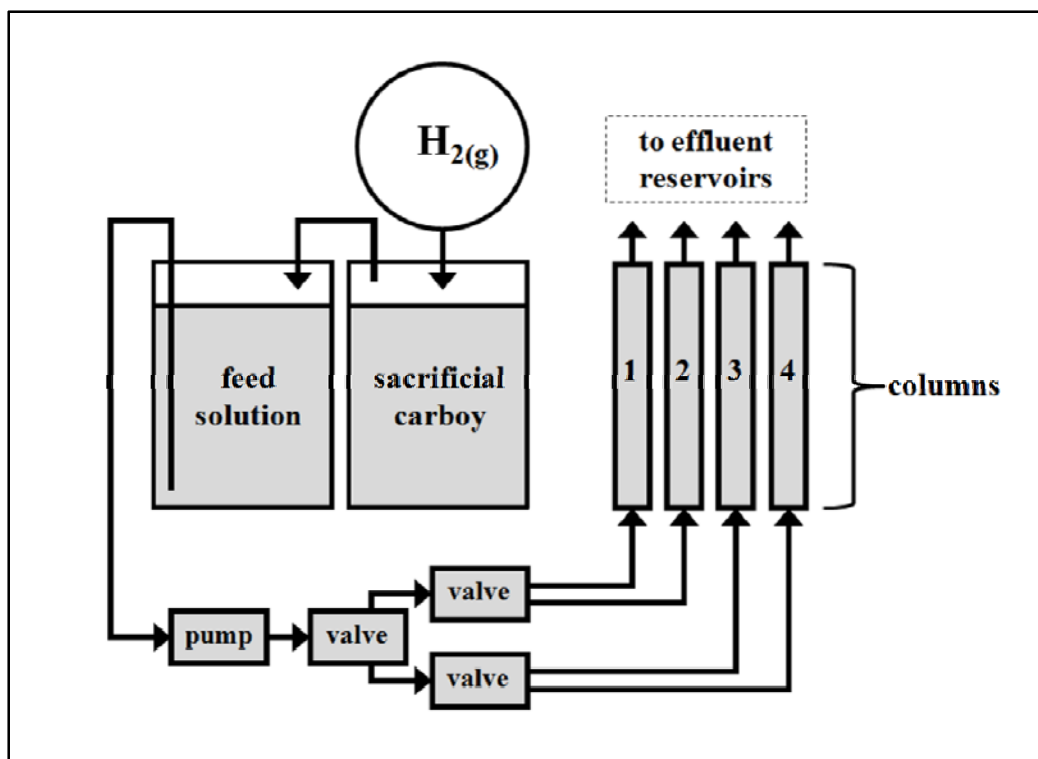


Figure 39: Schematic of columns with computer-controlled pump and valve system. Sacrificial and feed solution carboys contain 10 mg/l TCE in hydrogen-saturated deionized water. Columns 1-4 contain reactive porous materials described in Table 15.

Two Pd/MCM-41 samples were prepared for use in the column experiment following the procedures described in Chapter 2. One sample was 1.23% Pd/MCM-41 while the other was 3.47% Pd/MCM-41. Four separate columns were prepared using these materials (Table 15).

Fill materials for each column were placed in glass jars and rotated about a horizontal axis for one hour at 4 rpm to achieve a homogenous mixture. Attainment of a homogeneous mixture could be ascertained by visual inspection due to the colour differences between Pd/MCM-41 and silica sand: grayish-black and white, respectively. The different Pd/MCM-41 and sand mixtures were added in stages to each column so as to maintain a homogenous mixture as much as was possible. Column sides were tapped with a rubber mallet after each addition of the mixture to consolidate the fill material. The column end-caps were then screwed into place, sealing the columns.

The mass of each column was recorded before and after filling with sand and Pd/MCM-41 mixtures. Columns were then flushed for 30 min with beer gas (30%  $CO_2$ , 70%  $N_2$ ). Feed

solution was kept in a 10 l glass carboy. A hydrogen headspace was maintained in the feed solution carboy to avoid partitioning of dissolved hydrogen into the headspace. The ‘sacrificial carboy’ was included to allow the hydrogen headspace to equilibrate with a 10 mg/l TCE solution before entering the feed solution carboy. This carboy was added to reduce the mass of TCE that could partition into the headspace of the feed solution carboy. Feed solutions were prepared by sparging 9 l of Nanopure<sup>®</sup> deionized water with hydrogen gas for one hour. Sparging of the solution was performed to obtain a hydrogen-saturated solution (0.863 mmol H<sub>2</sub>/l; Randall & Failey, 1927). This solution would have provided a factor of 7.6 excess of hydrogen necessary to degrade the 10 mg/l TCE in the feed solution. As shown above, absorption of hydrogen by Pd/MCM-41 will not substantially lower the excess of hydrogen even if maximum hydrogen absorption were to take place.

Initial flow to columns was hydrogen-saturated deionized water. After 3 days, feed solution was changed to 9 l of hydrogen-saturated deionized water spiked with 180 µl of 506,203 mg/l TCE in methanol stock solution. The TCE spiked to the feed solution was increased to 360 µl of TCE stock per 9 l of solution after the fifth sampling. The TCE spiked feed solution was changed as necessary during the experiment.

Masses of the empty columns, columns filled with reactive porous materials, and solution-saturated columns were recorded and used in calculating the pore volume, porosity, and bulk density of fill material in the columns. These calculations are summarized in Table 15.

**Table 15: Summary of column fill properties. Second set of column experiments.**

Column	% loading Pd in Pd/MCM-41	Pd/MCM-41 as % of total fill material	Sand as % of total fill material	Column (g)	Packed mass of column (g)	Wetted mass of packed column (g)	Pore volume (ml)	Porosity	Dry Bulk Density (g/cm <sup>3</sup> )	Wet Bulk Density (g/cm <sup>3</sup> )
1	1.23	1.5	98.5	464.23	732.31	783.54	51.23	0.35	1.8	2.2
2	1.23	4.2	95.8	520.99	765.94	815.16	49.22	0.33	1.7	2.0
3	3.47	1.5	98.5	527.51	771.15	819.77	48.62	0.33	1.7	2.0
4	-	0	100	486.89	740.21	789.96	49.75	0.34	1.7	2.1

Samples were taken at intervals during the experiment and stored at 279 K in inverted glass vials with rubber and Teflon-sealed screw caps. Pore volumes of feed solution that had passed through each column at the time of sampling were calculated by dividing the total mass of effluent collected from column outlets by the pore volume of each column. Samples were analyzed for TCE, 1,1 DCE, *cis* DCE, *trans* DCE, and VC concentrations using previously described methods.

The experiment was terminated after approximately three months. Steady-state degradation profiles for all reactive columns had been achieved by that time.

#### 5.2.4 HMPA Degradation Batch Experiment

A batch test experiment was undertaken to investigate the possibility of using an MCM-41 supported palladium catalyst (Pd/MCM-41) to induce degradation of hexamethylphosphoramide (HMPA) in hydrogen-saturated deionized water with a hydrogen gas headspace present.

Given the degradation reaction proposed in Section 5.1, a progressive decrease in solution HMPA concentration over time during a batch experiment would indicate either occurrence of degradation of HMPA or its adsorption to Pd/MCM-41 surfaces. However, progressive and stoichiometric increases of dissolved phosphate and ammonia concentrations in conjunction with decreasing HMPA concentration would confirm that complete degradation of HMPA had taken place. This experiment was intended only to demonstrate whether or not Pd/MCM-41 could induce HMPA degradation in the presence of hydrogen; therefore, a determination of any degradation intermediates of HMPA and their concentrations was beyond the scope of the study.

The batch experiment used a sample of 1.01% by mass Pd/MCM-41 from a single batch (MCM-4 parent material). Detailed descriptions of the MCM-41 and Pd/MCM-41 synthesis procedures

as well as sample characterization results can be found in Chapter 2 and Appendix A. The 1.01% by mass loading of Pd was selected based on earlier work, which suggested this to be within the range of optimal catalyst loading for degradation reactions (Guthrie, 2007).

The batch experiment was undertaken in 40 ml glass sample bottles filled with hydrogen-saturated deionized water. All samples were prepared in duplicate. The hydrogen saturated solution was prepared by passing hydrogen gas through a sparger into a 4 l Erlenmeyer flask for 4 h. Dissolved hydrogen concentration at saturation at 1 atm and 298 K is 0.863 mmol/l (Randall & Failey, 1927).

HMPA was added to the hydrogen solution prior to filling the 40 ml bottles to produce an initial HMPA concentration of 30 mg/l (0.167 mmol/l). Samples of Pd/MCM-41 were carefully massed and added to batch reaction bottles prior to filling to overflowing with the hydrogen-saturated HMPA solution. Detailed descriptions of batch reaction bottle contents are included in Appendix D. The average mass of Pd metal in each bottle was  $2.86 \times 10^{-3} \pm 2.10 \times 10^{-6}$  g. As the deviation in Pd metal mass between bottles was low relative to reactive sample mass, variation in mass of Pd between bottles was ignored. Thus, the HMPA concentration results described below were not normalized with respect to Pd metal mass.

The sample bottles were crimp-sealed with Teflon and rubber caps and centrifuged for 3 min at 4,400 rpm to allow reactive particles to settle to the bottoms of the bottles. The start time of the experiment was taken as the time when reactive sample bottles were crimp-sealed. A 6 ml hydrogen headspace was then added via gas syringe inserted through the Teflon and rubber seals of the crimp caps. HMPA solution displaced by the 6 ml of hydrogen passed from the sample bottles through a syringe needle inserted through the Teflon and rubber cap. The target solid/liquid mass ratio in reactive samples was 1/120. A representation of a typical reactive sample for the batch experiment is shown in Figure 40. Control samples consisted of 40 ml sample bottles filled with 34 ml of the HMPA and hydrogen-saturated deionized water solution and a 6 ml hydrogen headspace.

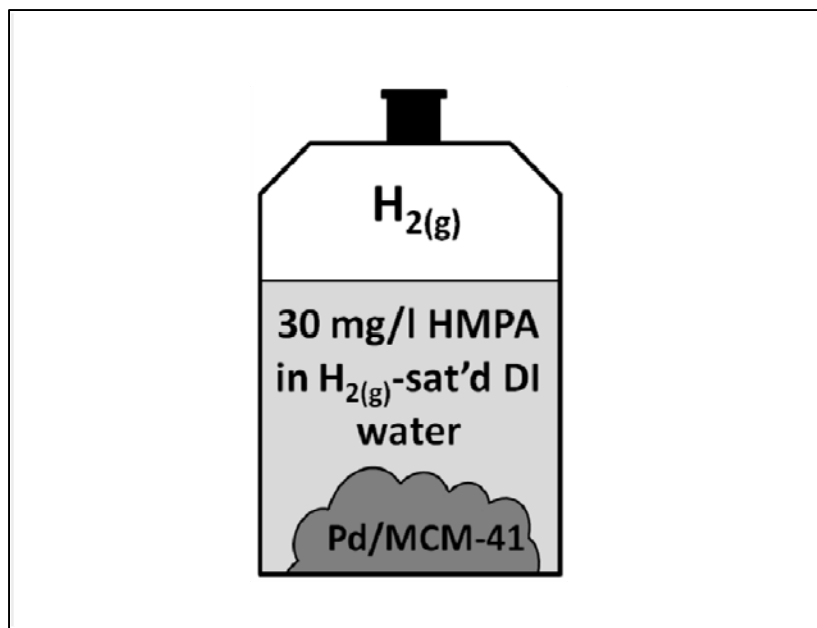


Figure 40: Representation of typical reactive sample for HMPA degradation batch experiment including a 6 ml hydrogen headspace.

Moles of HMPA that could partition into the hydrogen headspace were calculated by Henry's Law and found to be negligible. As discussed in Chapter 4, an average of 0.85 moles of H can be absorbed per mole of Pd metal ( $H/Pd = 0.85$ ). If this quantity of hydrogen absorption by palladium occurred during the experiment, there would still be a factor of 7.7 excess of H in the solution and headspace than would be required for complete degradation of the initial HMPA concentration.

Sample bottles were kept in end-over-end rotation for the duration of the experiment to ensure that the solid Pd/MCM-41 particles contacted all of the HMPA solution. Rotation also ensured that hydrogen gas from the headspace contacted all of the HMPA solution. The supernatant solution in each bottle was sampled at 4 h, 7 h, 1 d, 3 d, 5 d, 7 d, 13 d, and 15 d. The 40 ml sample bottles were centrifuged at 4,400 rpm for three to five minutes prior to sampling. Centrifugation settled the Pd/MCM-41 particles to the bottom of the bottles, avoiding transfer of reactive particles along with supernatant solution samples. Sample bottles were then de-crimped and 25 ml of supernatant solution were syringe-filtered (0.22  $\mu\text{m}$  acetate Acrodisc) into glass sample bottles. The sample bottles were filled to overflowing and sealed with rubber and Teflon caps. Samples were stored in a refrigerator at 278 K until analyzed for HMPA and phosphate concentrations.

HMPA concentrations in reactive and control samples were determined using a Hewlett Packard 5790 gas chromatograph equipped with a flame ionization detector using a Restek RTX-OPP2 (30 m x 0.53 mm ID x 0.5 mm) capillary column. Direct aqueous injection was utilized. The GC column was kept at 125°C for 7 min. The detector was set for 280°C and the injector temperature was 200°C. The carrier gas was ultra-pure nitrogen with a flow rate of 10 ml/min. The detection limit was not determined for this method, but is expected to be between 5 and 10 ppm.

Phosphate concentrations were determined via ion chromatography using a Dionex DX 500 equipped with a Dionex AS17 plus AG17 Guard Column. The eluent was a 20 mM NaOH (isocratic) solution and a flow rate of 1 ml/min was used. Samples were not analyzed for ammonia concentration. Results of phosphate concentration analyses are assumed to be adequate to confirm occurrence of degradation rather than sorption of initial HMPA.

## 5.3 Results and Discussion

### 5.3.1 TCE Degradation Batch Experiment

A concentration of TCE equal to 10 mg/l corresponds to  $4.58 \times 10^{19}$  molecules TCE/l, requiring  $1.38 \times 10^{20}$  electrons/l to be reduced to ethylene. The electron donor ( $H_2$ ) in the hydrogen-saturated solution would provide  $1.04 \times 10^{21}$  electrons/l at the above-stated solubility. Therefore, the hydrogen-saturated solution provides 7.6 times the electrons necessary to reduce the TCE in the sample bottles. It was found in Chapter 4 that 0.85 moles of H can be taken up per mole of Pd present ( $H/Pd = 0.85$ ). If this quantity of H was taken up by the average mass of Pd present in each batch reaction bottle, there would remain a 7.1 times excess of hydrogen necessary to degrade the TCE present in each sample bottle.

A plot showing results from the batch experiments comparing the abilities of Pd/sand and Pd/MCM-41 to induce degradation of TCE is shown in Figure 41. The MDL values for TCE and intermediate and final degradation products are presented in Table 16. This experiment was performed without the presence of a  $H_{2(g)}$  headspace. Detailed results from the batch experiment are presented in Appendix D. Initial TCE concentrations were determined from analysis of two sample blanks containing only TCE in hydrogen saturated deionized water. Two control samples containing only silica sand indicated an apparent decrease of 12 and 23% of initial TCE

concentrations. Degradation intermediate products including 1,1 DCE, *cis* and *trans* DCE, and VC were either below detection limits, or were one to two orders of magnitude lower in concentration than in samples containing reactive Pd supported on sand or MCM-41. In addition, final degradation products ethane (MDL = and ethene were detected at less than 1% of initial TCE concentration or below detection limits, respectively. Therefore, the small decrease in initial TCE concentration in sand control samples could not be attributed to reductive dehalogenation of the compound following the proposed reaction from Section 5.1. Therefore, any degradation of TCE recorded in reactive samples may be attributed to the presence of Pd.

**Table 16: Method detection limits (MDL) for TCE and its intermediate and final degradation products.**

Species	MDL (mmol/l)
TCE	7.6E-06
VC	2.1E-05
1,1-DCE	3.0E-05
<i>t</i> DCE	2.5E-05
<i>c</i> DCE	1.3E-05
ethane	3.7E-05
ethene	3.9E-05
methane	5.6E-05

Samples taken during the Pd/sand and Pd/MCM-41 batch experiments resulted in similar extents of TCE degradation. Samples from the Pd/sand experiment were taken at intervals over the course of the experiment, allowing construction of degradation curves. Samples from the Pd/MCM-41 experiment were only taken at 120 min and compared to results obtained from the Pd/sand experiment. The mass percent loadings of Pd/sand and Pd/MCM-41 were similar (difference of 0.1%), therefore, degradation results were not normalized with respect to quantities of metal present in each batch reaction bottle. Duplicate samples from each batch experiments, taken after 120 min indicated similar concentrations of TCE degraded as for the samples used to construct degradation curves. The Pd/sand sample and duplicate indicated 34 and 39% of initial TCE had degraded, respectively. The Pd/MCM-41 sample and duplicate indicated 38 and 42% of initial TCE had degraded, respectively. Therefore, the abilities of 0.99% Pd/sand and 1.10% Pd/MCM-41 to induce degradation of TCE during the batch experiment were similar. Due to the similar maximum extent of TCE degradation induced by both materials, it

cannot be determined if one material presents an advantage over the other with respect to TCE degradation. The attainment of a relatively high steady-state value of normalized TCE concentration indicates that some aspect of the experimental design may be limiting the extent of degradation. The possibility of the extent of TCE degradation being influenced by an aspect of the experimental design was investigated via a second batch experiment discussed in detail below.

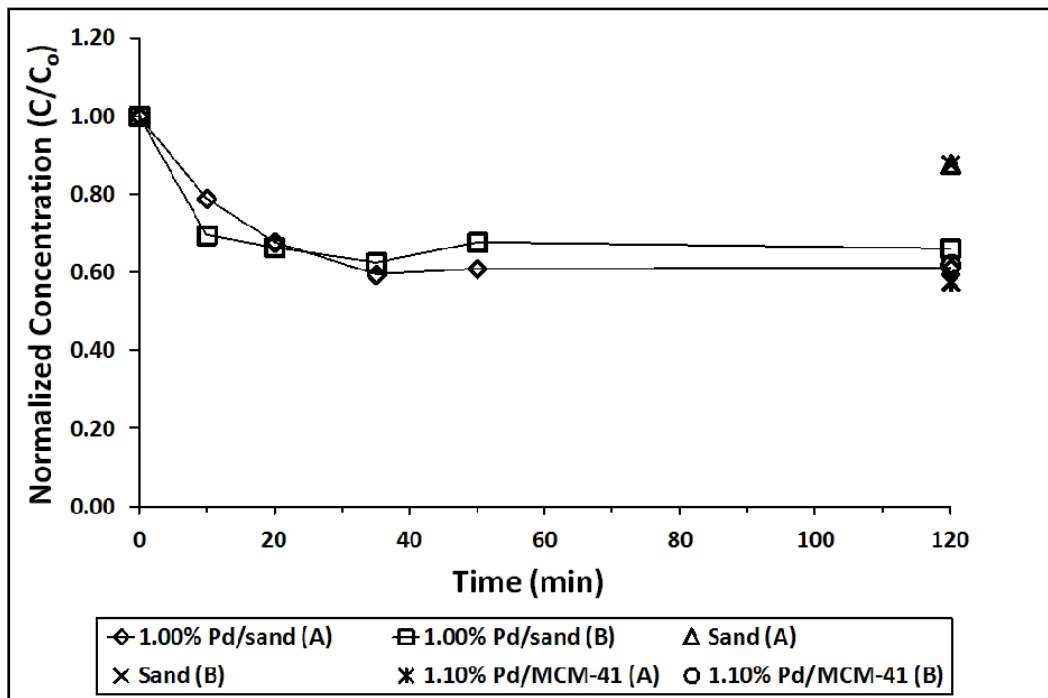


Figure 41: Results of TCE degradation batch experiment comparing sand and MCM-41 supported Pd.

As can be seen in Figure 41, adequate TCE concentration data was collected to construct degradation curves for the Pd/sand samples. It is expected that TCE degradation by Pd in the presence of hydrogen is best approximated by fitting to an integrated first-order rate equation (Lowry & Reinhard, 1999).

The integrated first-order reaction rate equation takes the form:

$$\ln C = -kt + \ln C_0$$

where  $C$  represents the concentration of TCE at time  $t$ ,  $k$  is the rate constant, and  $C_0$  is the initial concentration of TCE. For results of TCE degradation experiments, a plot of the natural

logarithm of normalized TCE concentration  $[\ln(C/C_0)]$  versus time should produce a straight line of slope  $k$ .

Results of fitting the two Pd/sand degradation curves to a first-order rate equation are summarized below in Table 17. Plots showing the various linear fits are included in Appendix D. A comparison of the  $R^2$  value of the linear fit to  $\ln(C/C_0)$  versus time data to the critical  $R^2$  value, given the number of data points, was made. Of the calculations, only the fit made to the first four points of the degradation curve for sample A of 1.00% Pd/MCM-41 had an  $R^2$  value approaching the critical value. The percent difference between the  $R^2$  value and the critical value was 0.42%.

**Table 17: First-order reaction rate calculations for first set of batch TCE degradation experiments using 1.00% Pd/sand.**

Sample	C/C <sub>0</sub> Minimum	k (min <sup>-1</sup> )	R <sup>2</sup>	# of Points	Critical R <sup>2</sup>	Admissable? (Y/N)
A	0.59	3.04E-03	0.420	6	0.811	N
	0.59	1.46E-02	0.946	first 4	0.950	~ Y
B	0.63	1.83E-03	0.217	6	0.811	N
	0.63	1.21E-02	0.724	first 4	0.950	N

In order that a carbon balance could be performed, batch reaction samples and duplicates were analyzed for TCE degradation products including: *cis* and *trans* isomers of DCE, VC, ethane, ethene, and methane. Results of the carbon balance are presented below as a plot of each degradation product as a percent of initial TCE versus time in Figure 42 and Figure 44. Separate plots are shown for the Pd/sand sample and its duplicate. Degradation products other than ethane are shown in Figure 43 and Figure 45 on an expanded y-axis. Results of the carbon balance for 1.10% Pd/MCM-41 are presented in Table 18. Samples were taken only at 120 min during the 1.10% Pd/MCM-41 batch TCE degradation experiment; therefore, results are presented in tabular rather than plotted form. Detailed data used to perform the carbon balance is included in Appendix D. Carbon balance of these products along with residual TCE in the solution accounted for between 91 and 105% of calculated total carbon in the batch reaction samples. Total carbon was based on the initial TCE concentrations. The proximity of these values to 100% indicated that all major degradation products of TCE were included in the analysis and that decreases in TCE were not a result of adsorption to Pd/sand and Pd/MCM-41 surfaces. Of the different compounds, ethane was the dominant product of TCE dehalogenation, accounting for an average of  $83 \pm 7\%$  of degraded TCE. All other products accounted for an average of  $3.4 \pm 0.4\%$

of initial TCE. Lack of detection of substantial concentrations of degradation intermediates, and the dominance of ethane as the final degradation product, suggests that TCE underwent complete degradation before desorbing as ethane during the batch experiment. This is consistent with published results regarding the degradation of TCE by Pd (Lowry & Reinhard, 1999).

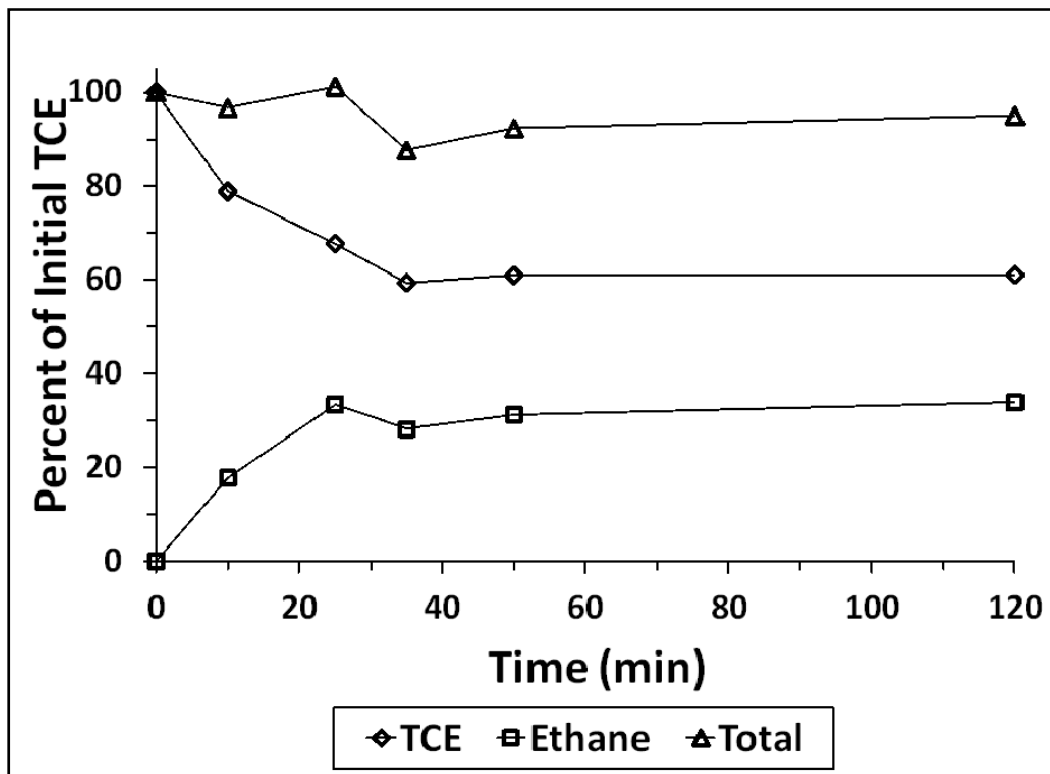


Figure 42: Results of a carbon balance performed on batch TCE degradation experiment using 1.00% Pd/sand (sample A).

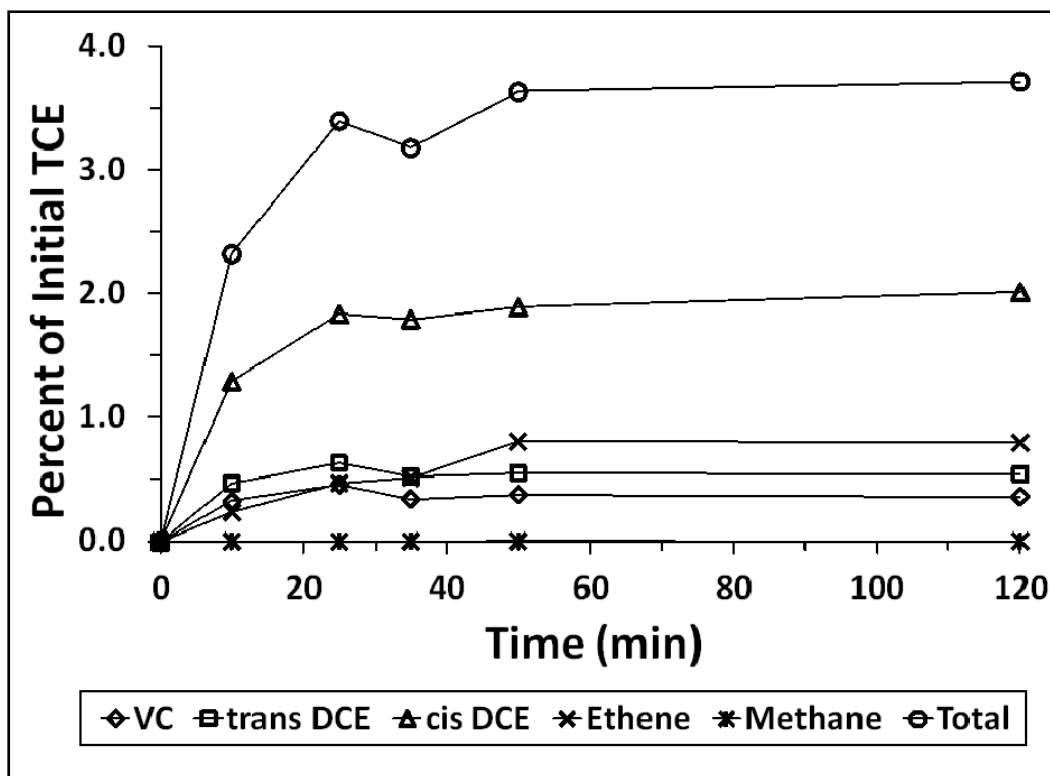


Figure 43: Results of a carbon balance on expanded y-axis performed on batch TCE degradation experiment using 1.00% Pd/sand (sample A).

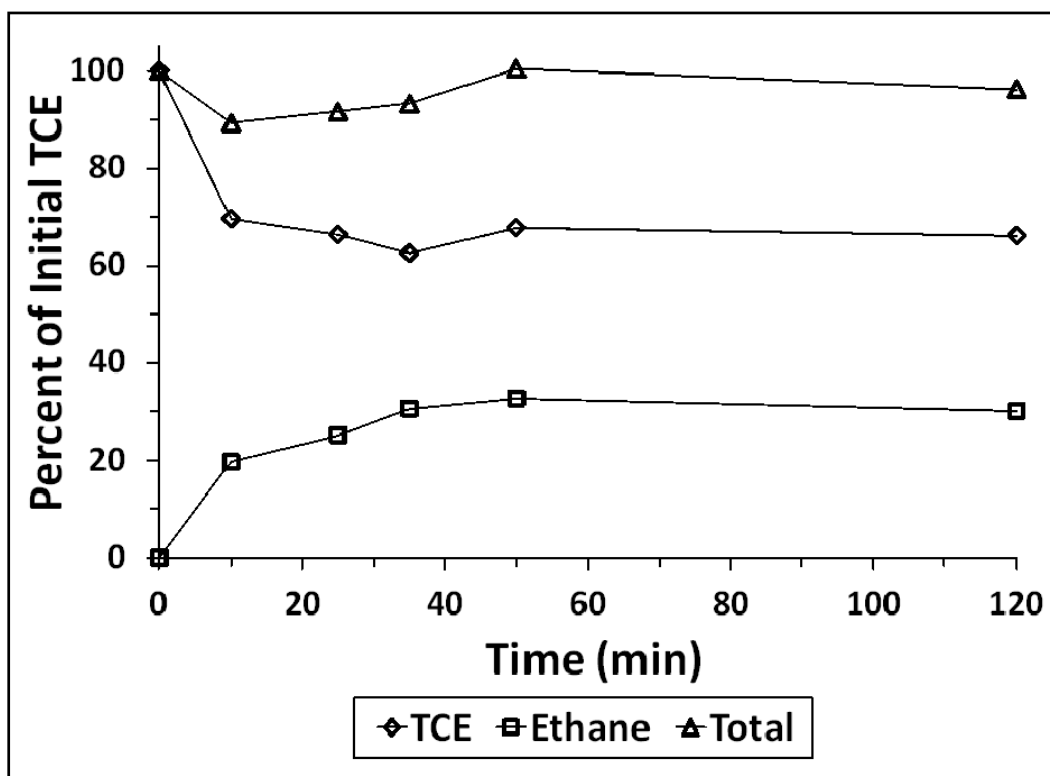


Figure 44: Results of a carbon balance performed on batch TCE degradation experiment using 1.00% Pd/sand (sample B).

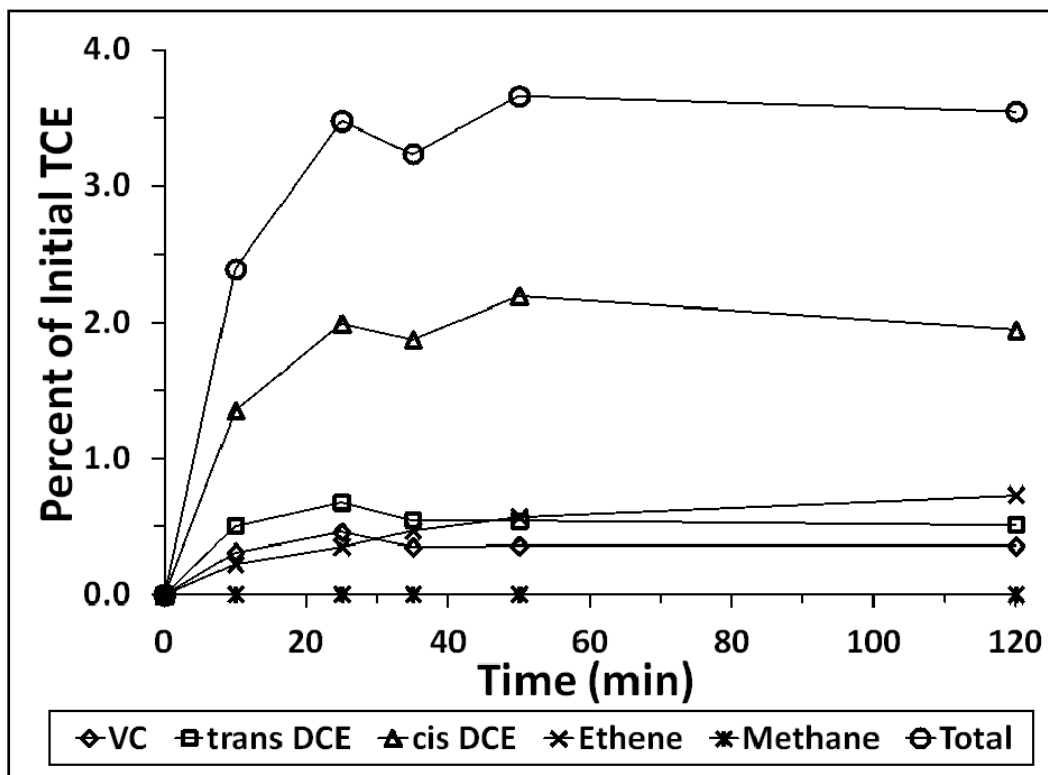


Figure 45: Results of a carbon balance on expanded y-axis performed on batch TCE degradation experiment using 1.00% Pd/sand (sample B).

**Table 18: Results of a carbon balance performed on 1.10% Pd/MCM-41 samples during the TCE degradation batch experiment.**

Compound	Sample	% Initial TCE
TCE	A	57.6
	B	62.1
VC	A	0.4
	B	0.4
tDCE	A	0.7
	B	0.7
cDCE	A	2.1
	B	2.2
Ethane	A	33.4
	B	28.8
Ethene	A	0.6
	B	1.1
Methane	A	0.0
	B	0.0
Balance	A	94.8
	B	95.2

As discussed briefly above, the TCE degradation batch experiment was repeated using a hydrogen-saturated solution with pH adjusted to a value of 9.15 using  $Na_2B_4O_7 \cdot xH_2O$ . A solution of  $Na_2B_4O_7 \cdot xH_2O$  will produce a partial pressure due to  $B_2O_{3(g)}$  formation. However, this pressure will be very low and can be ignored as a source of TCE loss from solution into the headspace within reaction bottles. Batch reaction bottles in this experiment also included a 2 ml  $H_{2(g)}$  headspace. Samples of supernatant from all batch reaction bottles were taken after 120 min of reaction time. Results of analysis for TCE concentration and a schematic showing control samples are shown in Table 19. Two sets of controls and duplicates were analyzed during this phase of the experiment. The first control sample (Control 1) and its duplicate consisted of batch reaction bottles completely filled with the  $Na_2B_4O_7 \cdot xH_2O$  in hydrogen-saturated deionized water solution. The second control sample (Control 2) and its duplicate consisted of the  $Na_2B_4O_7 \cdot xH_2O$  in hydrogen-saturated deionized water solution and included a 2 ml  $H_{2(g)}$  headspace in the batch reaction bottles. The initial TCE concentration in this experiment was assumed to be equal to the concentration in the control samples not containing the  $H_{2(g)}$  headspace. The solution and headspace in the reactive sample bottles containing either 1.00% Pd/sand or 1.10% Pd/MCM-41 was similar to that in the 'Control 2' batch reaction bottles.

Results of TCE concentration analysis for Control 2 samples indicated a slight decrease of 3 and 11% in TCE relative to Control 1 samples. This decrease may be due to either partitioning of TCE into the headspace or simply variation in analyzed TCE concentrations between different samples. No TCE was detected in samples taken from the 1.00% Pd/sand batch reaction bottles. Concentrations of TCE less than 0.004% of initial TCE were detected in samples taken from the 1.10% Pd/MCM-41 batch reaction bottles. Intermediate degradation products (*cis* and *trans* DCE, VC) were detected only in samples taken from Control 2 samples. No intermediate degradation products were detected in reactive samples containing Pd/sand or Pd/MCM-41. Intermediate degradation product concentration results are included in Appendix D. It is likely that TCE underwent complete degradation to ethane before desorbing from the Pd surface as was demonstrated above in the results from the first batch experiment. Although TCE was detected in Pd/MCM-41 batch reaction bottles, the quantity detected was below the method detection limit in both sample and duplicate (Appendix D). Therefore, a definitive conclusion as to whether sand or MCM-41 was more effective as a Pd support in the TCE degradation batch experiment is

not possible given the results shown in Table 19. Both of the Pd/sand and Pd/MCM-41 materials were roughly equal in their ability to induce degradation of TCE in the batch experiment. Therefore, a series of TCE degradation column experiments were performed to determine the benefit of MCM-41 as a Pd support relative to other materials such as silica sand. The results of those experiments are described below in Section 5.3.2.

**Table 19: Results of batch TCE degradation experiment comparing 1.00% Pd/sand and 1.10% Pd/MCM-41 in  $Na_2B_4O_7 \cdot xH_2O$  in hydrogen saturated deionized water with 2 ml  $H_{2(g)}$  headspace.**

Sample	TCE (mmol/l)	C/C <sub>o</sub>
Control 1	65.97	1.00
	65.30	1.00
Control 2	64.14	0.97
	57.90	0.89
1.00% Pd/sand	0.00	0.00
	0.00	0.00
1.10% Pd/MCM-41	0.244	3.69E-03
	0.231	3.54E-03

### 5.3.2 TCE Degradation Column Experiment

#### 5.3.2.1 TCE Degradation Column Experiment - First of Two

The results for the first three columns are shown in Figure 46 as a function of total pore volumes and in Figure 47 as a function of total time. These columns included: control, 1.00% Pd/sand, and 0.99% Pd/MCM-41 samples. Detailed TCE and degradation intermediate concentration results are included in Appendix D. Results are plotted as sample concentration of TCE normalized to initial concentration (outflow concentration/inflow concentration) versus number of pore volumes that had flowed through the column at the time of sampling. Results for all experiments were not normalized with respect to the mass percent loading of metal on MCM-41. Given that samples were prepared with roughly similar mass percent loadings (generally  $\pm 0.01\%$  variance between materials), it is expected that variance in the mass loadings would have a minimal effect on TCE degradation when compared to the effect resulting from differences between reactive metals. As reactive metal concentrations in columns were similar, reactions rates are expected to be related only to the properties of the reactive metals themselves.

The average normalized TCE concentration in control samples throughout the experiment was  $1.00 \pm 0.06$ . Intermediate TCE degradation products (1,1 DCE, *cis* and *trans* DCE, VC) were below detection limits in all samples. The average flow rate through this column during the experiment was 4.9 ml/min. Average residence time of TCE solution in the column was 1.5 min. TCE concentration did not change significantly during flow through the control column. Earlier work demonstrated that MCM-41 itself does not cause a reduction in aqueous TCE concentrations (Guthrie, 2007). Therefore, any degradation in other reactive columns can be attributed to the presence of the reactive metals in those columns.

The 1.00% Pd/sand material degraded a maximum of 48% of inflow TCE at early time and then approached a steady-state  $C/C_0$  value by 660 PV, degrading 11% of inflow TCE. There were  $2.37 \times 10^{-3}$  g of Pd present in the Pd/sand column. The intermediate degradation products VC and 1,1 DCE were below detection limits in all samples. Small concentrations of *trans* DCE were detected in four early time samples. Concentration of *trans* DCE was less than 0.5% of inflow TCE concentration. An average concentration of *cis* DCE equal to  $0.5 \pm 0.3\%$  of inflow TCE concentration was detected in 12 samples. Detection of intermediate degradation products indicates that degradation of TCE is taking place rather than adsorption to Pd/sand surfaces. The major degradation product of TCE is expected to be ethane, as shown in the batch experiment described in Section 5.3.1. Column samples were not analyzed for ethane. Average flow rate through this column during the experiment was 5.8 ml/min. Average residence time in the column was 1.2 min. Therefore, the 1.00% Pd/sand material shows some degree of ability in inducing degradation of TCE, however, there was a progressive loss of this ability over 660 pore volumes. Loss of degradation ability may be due to loss of Pd from sand surfaces and subsequent flushing from the column or from passivation of the limited available Pd surface areas on the Pd/sand material relative to Pd/MCM-41.

The 0.99% Pd/MCM-41 material degraded a maximum of 98% of inflow TCE concentration over a similar range of pore volumes (up to PV = 671) as the Pd/sand column. The Pd/MCM-41 column degraded a minimum of 81% of inflow TCE concentration during the experiment. The mass of TCE degraded by Pd/MCM-41 was relatively constant over the range of PV. Pd/MCM-41 degraded an average of  $94 \pm 9\%$  of inflow TCE. There were  $2.49 \times 10^{-3}$  g of Pd present in this column. One sample at early time during the experiment indicated a VC concentration of 0.02%

of inflow TCE concentration. VC was not above detection limits in any of the remaining samples. Concentration of 1,1 DCE was below detection limits throughout the experiment. Two samples indicated *trans* DCE concentrations above detection limits at values of 0.07% and 0.04% of inflow TCE concentration. Five samples taken during the experiment indicated an average *cis* DCE concentration of  $0.09 \pm 0.13\%$  of inflow TCE concentration. The average flow rate through the Pd/MCM-41 column during this stage of the experiment was 4.8 ml/min. Average residence time in the column was 1.6 min. It is clear from these results that Pd supported on MCM-41 is substantially more effective than a similar mass of Pd supported on silica sand at inducing degradation of TCE. It is proposed that the greater effectiveness of Pd/MCM-41 is due to there being a larger surface area of Pd exposed to the dissolved TCE. The larger surface area of the Pd/MCM-41 relative to that of Pd/sand materials (Chapter 2) results in comparatively high surface areas of Pd metal being exposed to TCE during flow through the column.

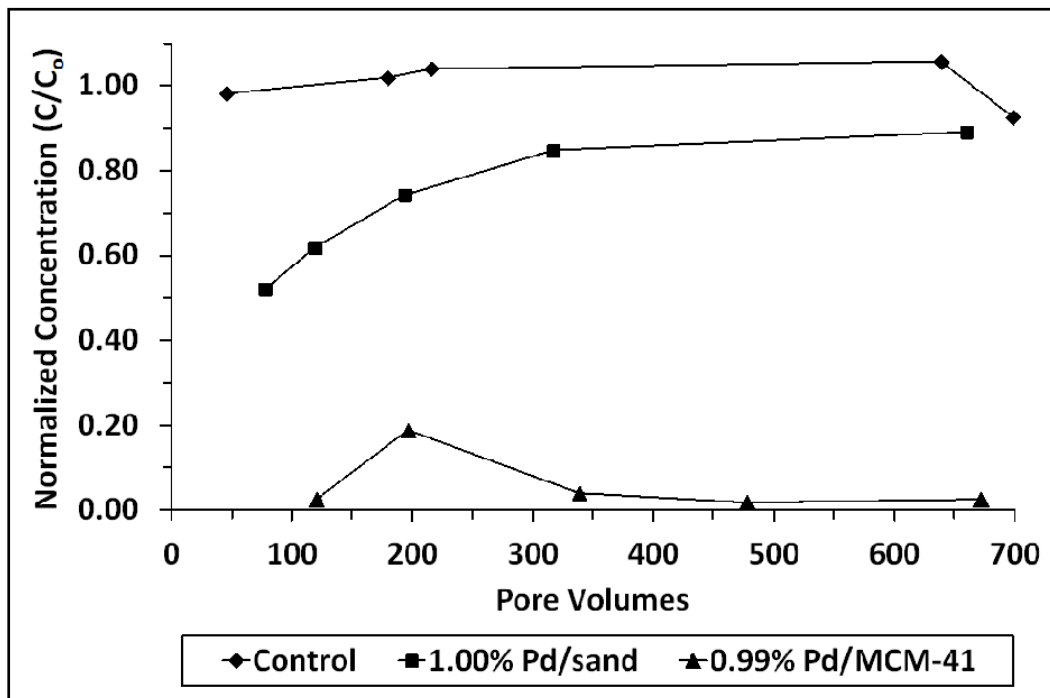


Figure 46: Results from TCE degradation columns including control, Pd/sand, and Pd/MCM-41 samples plotted as a function of total pore volumes.

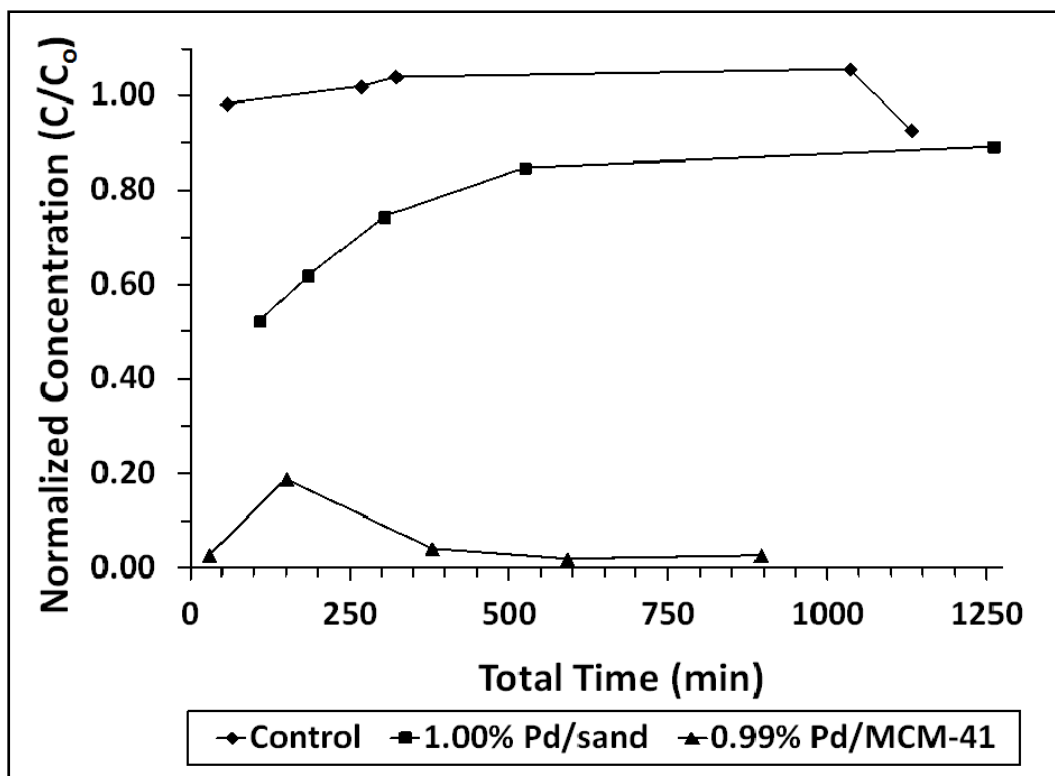


Figure 47: Results from TCE degradation columns including control, Pd/sand, and Pd/MCM-41 samples plotted as a function of total time.

Results shown in Figure 46 demonstrate the potential longevity of a Pd/MCM-41-filled column used in treating TCE. Flow through the 0.99% Pd/MCM-41 column was continued beyond 671 PV to determine if the material would demonstrate any lessening of its ability to degrade TCE in hydrogen-saturated deionized water over time. Degradation results over 5,036 PV are shown in Figure 48. Results of the same experiment are shown as a function of total time in Figure 49. The degradation profile for the Pd/MCM-41 column over this period indicates that Pd/MCM-41 is both effective and long-lived in TCE treatment. The Pd/MCM-41 material degraded a maximum of 98% and a minimum of 68% of inflow TCE during the experiment. On average, over 90% of the inflow TCE concentration was degraded during the experiment. Tabulated concentration results for TCE degradation intermediates can be found in Appendix D. Generally, concentrations of intermediate products were below detection limits in analyzed samples. The most commonly identified intermediate above detection limits was *cis* DCE. Concentrations were generally below 1% of inflow TCE concentration for any intermediate products identified as having concentrations above detection limits. The fluctuations in normalized TCE concentration during the experiment coincide with brief stoppages of flow as the feed solution

carboy was changed. Carboy changes occurred at PV equal to 712, 1520, 2036, 2912, and 3685. With the exception of PV = 2036, all of these instances of carboy changes coincided with an upward step in normalized TCE concentration. Subsequent column experiments (such as the 1.01% Ni-Pd/MCM-41 results shown in Figure 52) made use of a larger feed solution carboy, minimizing the number of flow stoppages required during the experiment. In these cases, the upward fluctuations in normalized TCE concentrations were not observed, indicating that those seen in Figure 48 are a result of the experimental design and not due to any aspect of Pd/MCM-41-induced TCE degradation. Average flow rate and residence time during the experiment were 4.6 ml/min and 1.6 min, respectively. Results shown in Figure 48 do not indicate a progressive loss in effectiveness of Pd/MCM-41 in treating TCE. Therefore, Pd/MCM-41 may be able to treat TCE in hydrogen-saturated deionized water for extended periods of time, or until re-precipitation of MCM-41 as amorphous silica blocks the Pd centres (Guthrie & Reardon, 2008), or until reactive Pd/MCM-41 particles are removed from the column by flow.

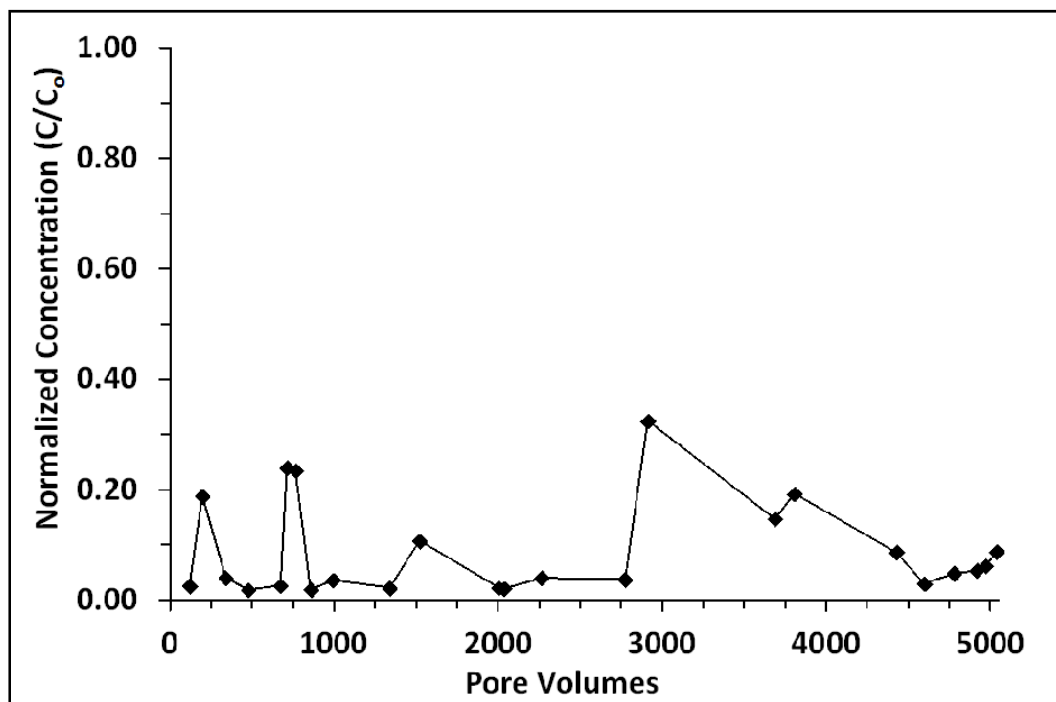


Figure 48: Long term normalized TCE concentration results versus pore volumes for 0.99% Pd/MCM-41 column.

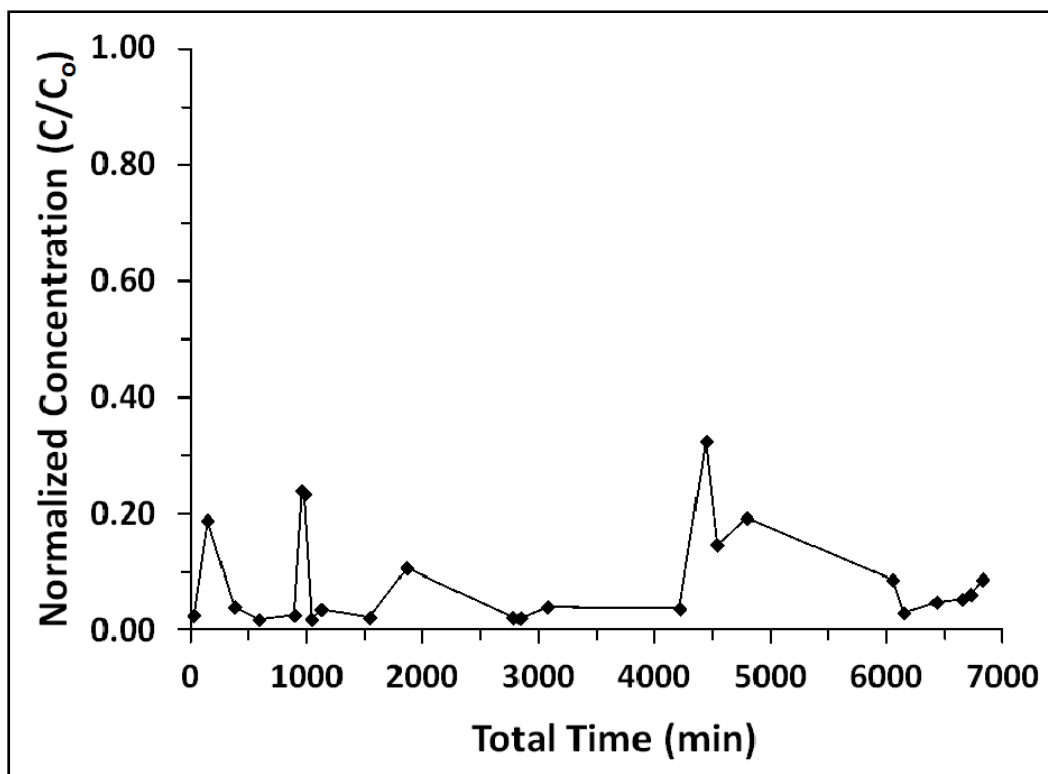


Figure 49: Long term normalized TCE concentration results versus total time for 0.99% Pd/MCM-41 column.

Determination of whether or not TCE degradation is occurring via pH and conductivity measurements is of great value due to the low cost of these analyses versus analyses for the aqueous concentrations of TCE and its degradation products. In addition, the changes in pH and conductivity between the inflow and outflow samples were used to back-calculate the mass of TCE degraded in the column. Successfully calculating changes in TCE concentration via these means presents a rapid and low cost method of monitoring the extent of degradation in the reactive columns. Indeed, successful correlation of pH and conductivity measurements with the changes in TCE concentration suggests the potential for achieving continuous, ‘real time’ measurement of the extent of TCE degradation during column experiments.

Examination of the TCE degradation reaction described above in Section 5.1 shows that complete degradation of TCE generates  $\text{Cl}^-$  which is charge balanced by  $\text{H}^+$ . This process will increase the acidity of the solution as TCE is degraded, corresponding with a decrease in solution pH. With the exception of some samples taken at early times during the experiment, pH measurements of inflow and outflow samples were taken at the same time as the above-described

aqueous samples. Of interest was the change in pH between inflow and outflow to the column. A decrease in pH during flow through the column would indicate TCE degradation is taking place within the column.

Results of pH measurements taken for the control column and reactive column containing 0.99% Pd/MCM-41 are presented in Table 20. A pH measurement was repeated five times for six, separate samples during the course of the column experiments to determine the uncertainty in the measurement. Average uncertainty in the pH value for five of the six samplings was between 0.76 and 2.47% of the measured value. One uncertainty was substantially higher, at 19.6% of the measured pH. If the 19.6% uncertainty result is ignored, the average uncertainty in the pH measurements is  $1.77 \pm 0.83\%$ . If the 19.6% value is included, the average uncertainty in the pH measurements would be  $4.75 \pm 7.66\%$ . Therefore, the 19.6% uncertainty value was ignored and  $1.77 \pm 0.83\%$  is assumed to be the more representative estimate of uncertainty in the pH measurement. The average decrease in outflow relative to inflow pH values for the control column was  $0.28 \pm 0.44$ . Average decrease in outflow relative to inflow pH values for the reactive 0.99% Pd/MCM-41 column was  $0.97 \pm 0.39$ . Comparing the confidence intervals for inflow and outflow pH measurements for the control column indicates that no significant change in pH occurred during flow through the column. The average percent difference between inflow and outflow pH values for the control and 0.99% Pd/MCM-41 columns were  $7.52 \pm 6.81\%$  and  $22.67 \pm 5.82\%$ , respectively. These results are consistent with the proposed TCE degradation reaction in Section 5.1 which generates acidity as it proceeds from left to right. There is no obvious correlation between the percent difference of inflow versus outflow pH in the 0.99% Pd/MCM-41 column and changes in the normalized TCE concentration in Figure 48. Therefore comparison of inflow versus outflow pH values can serve to identify when degradation of TCE is taking place. However, the difference in outflow and inflow pH would likely not provide a reliable quantification of mass of degraded TCE.

**Table 20: Results of pH measurements taken during control and 0.99% Pd/MCM-41 column experiments.**

Control				0.99% Pd/MCM-41			
PV	pH inflow	pH outflow	%Δ pH	PV	pH inflow	pH outflow	%Δ pH
46	4.87	4.34	11.51	2001	5.18	3.59	36.3
180	5.08	4.58	10.35	2036	5.08	3.46	37.9
216	4.65	4.10	12.57	2263	4.29	3.76	13.2
639	4.41	4.46	1.13	2771	4.48	3.58	22.3
698	4.36	4.45	2.04	2912	5.94	4.16	35.2
				3685	4.99	4.30	14.9
<b>average =</b>	4.67	4.39	7.52	3805	4.07	3.57	13.1
<b>±</b>	0.38	0.22	6.81	4427	4.03	3.34	18.7
				4597	5.39	3.79	34.9
				4778	4.27	3.63	16.2
				4917	4.24	3.6	16.3
				4969	4.39	3.65	18.4
				5036	4.266	3.586	17.3
				<b>average =</b>	4.66	3.69	22.67
				<b>±</b>	0.36	0.16	5.82

The production of  $H^+$  and  $Cl^-$  by the TCE degradation reaction presented above in Section 5.1 should also result in increased conductance in the outflow relative to the inflow point of the column. These conductivity values can then be used to calculate the theoretical mass of TCE which degraded using the Onsager equation. A detailed discussion of the Onsager equation and an algorithm developed to calculate theoretical masses of degraded TCE are included in Appendix E.

Reproducibility or uncertainty in the conductivity measurements was calculated by taking five repeated conductance measurements on one sample. Uncertainty tended to be relatively high in the conductance measurements and was especially high for samples with conductance values lower than  $1 \mu S/cm$ . One sample measured five times indicated an average conductivity of  $0.47 \pm 0.09 \mu S/cm$ , suggesting an uncertainty of 19.0% of the measurement at low conductivity. The four other samples on which repeated measurements were made had average conductivities of  $2.78 \pm 0.04 \mu S/cm$ ,  $7.92 \pm 0.40 \mu S/cm$ ,  $10.9 \pm 1.1 \mu S/cm$ , and  $73.0 \pm 4.8 \mu S/cm$ . These four repeated measurements suggest an uncertainty of between 1.27% and 10.5% in the conductivity measurements.

Results of conductivity measurements made on samples taken during the 0.99% Pd/MCM-41 column experiment are presented in Table 21. A comparison of the inflow and outflow conductivities shows that there is a large increase in the conductivity value when the TCE in hydrogen-saturated deionized water solution flows through the reactive column. This value is in agreement with the proposed TCE degradation reaction presented in Section 5.1. Due to this reaction producing  $H^+$  and  $Cl^-$  as it proceeds from left to right, it is expected that successful degradation of TCE to ethylene and ethane will cause an increase in solution conductivity. Calculated, theoretical concentration of TCE degraded was calculated based on the outflow sample conductivity measurements using the algorithm presented in Appendix E. As may be seen in Table 21, the percent difference between actual mg/l of TCE degraded and the calculated mg/l of TCE degraded ranges between 3 and 29%. A plot of actual versus calculated mass of TCE degraded was made and a linear fit applied to it. The  $R^2$  value for the linear fit was 0.65 which may be compared to a critical  $R^2$  value for five observations of 0.88. Although the criterion of the critical  $R^2$  value for a linear relationship between the variables was not met, the calculated mass of TCE degraded is useful in that it provides evidence that degradation did occur. This can be seen by comparing the relatively large calculated masses of TCE degraded in Table 21 with the relatively low values for 1.02% Ni/MCM-41 in Table 24, where no significant quantity of TCE was degraded. Therefore, although the conductivity measurements did not provide a reliable method of quantifying the actual mass of TCE degraded, the measurement was still valuable in identifying when degradation had taken place during flow through the column. This information would be useful in deciding if a given treatment technology is functional and whether further analysis of samples is warranted. The monetary and time cost associated with performing conductivity analyses is low compared to quantitative concentration analyses for cVOCs in aqueous samples.

**Table 21: Conductivity results for 0.99% Pd/MCM-41 column.**

0.99% Pd/MCM-41							
Pore Volumes	Conductivity in ( $\mu S/cm$ )	Conductivity out ( $\mu S/cm$ )	TCE in (mg/l)	TCE out (mg/l)	$\Delta$ TCE actual (mg/l)	$\Delta$ TCE calc'd (mg/l)	% Difference (Actual-Calc'd)
4597	2.00	43.88	4.81	0.14	4.67	4.52	3
4778	2.25	44.60	4.41	0.22	4.19	4.59	9
4917	2.74	46.74	4.68	0.25	4.43	4.81	8
4969	1.86	42.50	3.64	0.23	3.42	4.37	25
5036	2.43	41.15	3.45	0.30	3.15	4.23	29

Upon termination of the TCE degradation column experiment using the 0.99% Pd/MCM-41 material, the material was recovered from the porous material filling the column. Recovery was accomplished by wet sieving of the Pd/MCM-41 and sand mixture which had filled the column. Recovered Pd/MCM-41 was analyzed by low angle XRD (Figure 50). The XRD trace of the recovered Pd/MCM-41 material shows an increased noise-to-signal ratio as compared to that of the as-prepared material. It is proposed that this may be the result of loss of some degree of the hexagonal order of the mesoporosity of MCM-41 and recrystallization to amorphous silica of the Pd/MCM-41 material during the experiment, or incomplete separation of Ottawa silica sand from the Pd/MCM-41 material following the experiment. Although the 100 peak of the recovered Pd/MCM-41 is broader compared to the as-prepared material, the peak is still distinct.

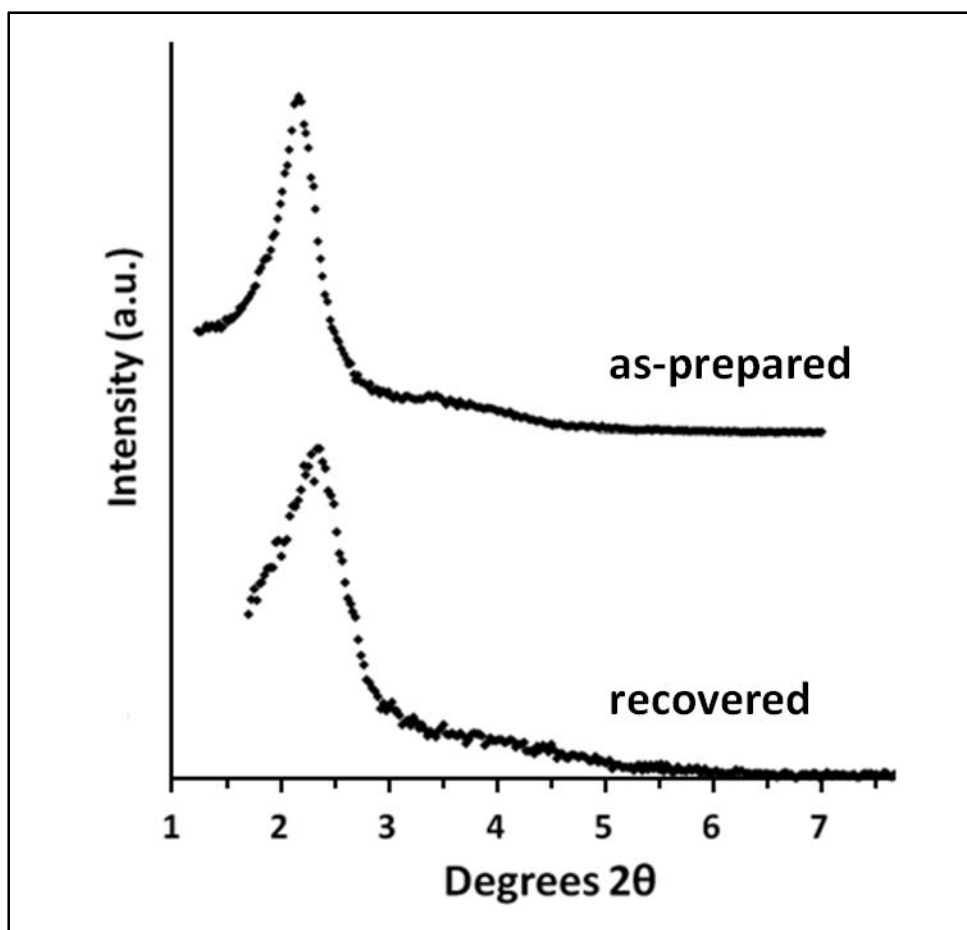


Figure 50: Comparison of low angle XRD results for 0.99% Pd/MCM-41 when freshly synthesized and recovered from column following termination of TCE degradation column experiment.

Calculated cell parameters, primary mesopore diameters, and pore wall thicknesses for as-prepared and recovered 0.99% Pd/MCM-41 are summarized below in Table 22. Results indicate a 3.6% decrease in the three parameters. It has been found that Pd/MCM-41 is resistant to degradation by deionized water (Chapter 3). Therefore, as discussed above, the decrease in value of the various material properties as determined by low angle XRD is most likely the result of some degree of contamination of the Pd/MCM-41 material by the silica sand in the column, rather than indicating a loss in the porosity of the material itself.

**Table 22: Comparison of low angle XRD characterization results for as-prepared and recovered 0.99% Pd/MCM-41.**

Sample	2 $\theta$ (100)	d100	a (nm)	Wd (nm)	Wt (nm)
as-prepared	2.36	37.43	4.32	3.71	0.61
recovered	2.28	38.80	4.48	3.84	0.64

BET nitrogen adsorption surface area analysis of the recovered material indicated a surface area of 545 m<sup>2</sup>/g. This represents a 37% decrease from the 791 m<sup>2</sup>/g surface area of the as-prepared 0.99% Pd/MCM-41 material (Chapter 2). This change would represent a significant decrease in surface area over the course of the TCE degradation column experiment. However, it is likely that much of this apparent decrease is due to incomplete separation of recovered Pd/MCM-41 material from the Ottawa silica sand. Inclusion of any of the low surface area silica sand along with Pd/MCM-4 during the BET surface area analysis would result in a large apparent decrease in surface area. Given that the XRD results presented in Figure 50 showed little change in the structure of Pd/MCM-41 during the column experiment, it is unlikely that there would be a large decrease in surface area unless substantial pore blocking had occurred. In addition, there was no substantial loss in ability of the material to degrade TCE during the experiment. These two factors suggest that the apparent loss of surface area is most likely the result of including sand with the recovered Pd/MCM-41 during the BET surface area analysis.

The apparent decrease in quality of the physical characteristics of Pd/MCM-41 materials recovered following the column experiment being caused by inclusion of silica sand in the recovered sample was confirmed by XRD analysis. Results of the analysis between 25.0 and 29.5°2 $\theta$  are shown in Figure 51. The peak centred at 27.1° 2 $\theta$  was positively identified as quartz using Eva software. Therefore, apparent decreases in the hexagonal form and surface area of

reactive porous materials recovered following the column experiment was result of imperfect separation of Pd/MCM-41 from Ottawa silica sand filling materials.

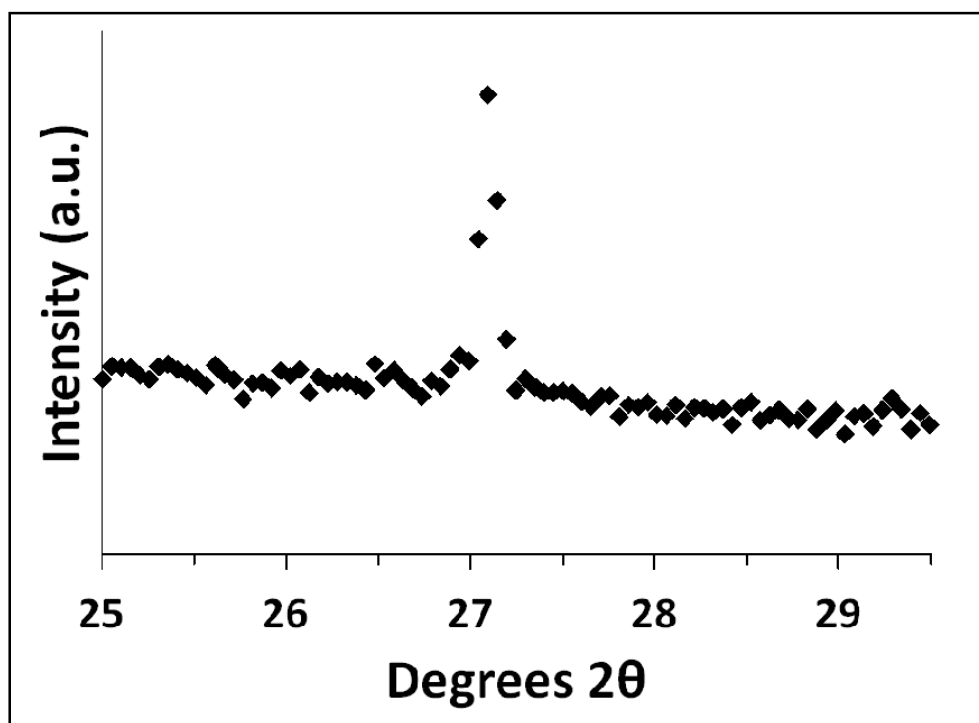


Figure 51: High angle XRD analysis of 0.99% Pd/MCM-41 recovered from column experiment. Peak at 27.1° 2θ was identified as quartz using Eva software.

Results from the column containing 1.02% Ni/MCM-41 are presented in Figure 52. The 1.02% Ni/MCM-41 results can be compared to those of the control column in Figure 46 where there was little change in normalized concentration of TCE between inflow and outflow sampling ports. Maximum decrease of TCE during flow through this column was 3.2% while the minimum was 0.1%. These values do not include samples where the normalized concentration was greater than 1.0. The average normalized TCE concentration for all five samples over 1,043 PV was  $0.99 \pm 0.02$ . No degradation intermediates were detected during the experiment. There were  $2.42 \times 10^{-3}$  g of Ni present in this column. Therefore, Ni/MCM-41 did not induce any substantial amount of TCE degradation during flow through the column. Average flow rate through this column was 5.5 ml/min. The average residence time was 1.4 min.

Results from the column containing 1.01% Ni-Pd/MCM-41 are also presented in Figure 52. A comparison of the two degradation profiles in Figure 52 clearly demonstrates the benefit of replacing approximately half of the mass of Ni with Pd in the MCM-41-supported material. The

Ni-Pd/MCM-41 column degraded a maximum of 99.9% and minimum of 98.4% of inflow TCE concentration. Average decrease in inflow TCE concentration during the experiment was  $99.5 \pm 0.8\%$ . Intermediate degradation products of TCE were below detection limits throughout the experiment. There were  $1.22 \times 10^{-3}$  g of Ni and  $1.22 \times 10^{-3}$  g of Pd present in the column. Average flow rate through the column was 4.5 ml/min, and the average residence time was 1.9 min. The Ni-Pd/MCM-41 results did not indicate any loss in effectiveness at degrading TCE over the 1,502 PV of the experiment. Therefore, 1.01% Ni-Pd/MCM-41 appears to be at least as effective as 0.99% Pd/MCM-41 in inducing degradation of TCE.

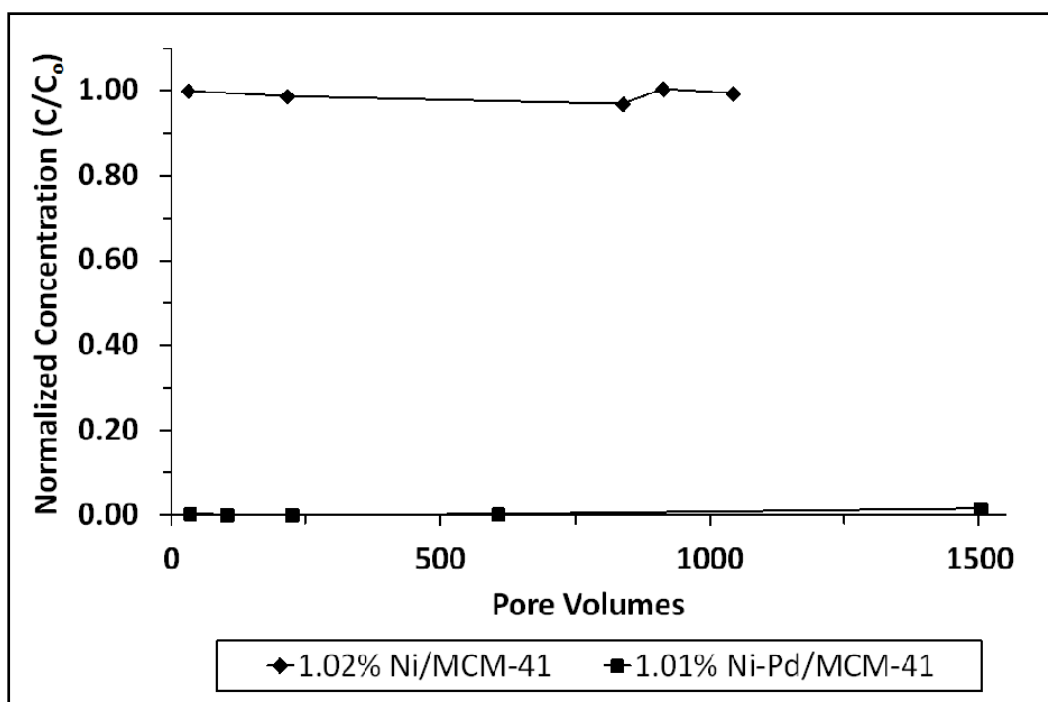


Figure 52: Normalized TCE concentration versus pore volume results for Ni/MCM-41 and Ni-Pd/MCM-41 samples.

Results of pH measurements taken on inflow and outflow samples during the 1.02% Ni/MCM-41 and 1.01% Ni-Pd/MCM-41 column experiments are presented in Table 23. Results are similar to those described above for the control and 0.99% Pd/MCM-41 columns. In the 1.02% Ni/MCM-41 column, there was no significant difference between the average pH values in the inflow and outflow samples. This lack of difference corresponds with no decrease in TCE concentrations during flow through the column. In the column containing 1.01% Ni-Pd/MCM-41, where a decrease in TCE concentration during flow through the column was recorded, there is a significant difference between inflow and outflow sample pH values. The average pH value

decreased by  $0.65 \pm 0.26$  during flow through the 1.01% Ni-Pd/MCM-41 column. This difference is reflected in the relatively large percent difference in pH between the inflow and outflow samples.

**Table 23: Results of pH measurements taken during 1.02% Ni/MCM-41 and 1.01% Ni-Pd/MCM-41 column experiments.**

1.02% Ni/MCM-41				1.01% Ni-Pd/MCM-41			
PV	pH inflow	pH outflow	%Δ pH	PV	pH inflow	pH outflow	%Δ pH
31	5.30	5.27	0.57	35	4.11	3.53	15.18
215	5.24	5.56	5.93	103	3.89	3.53	9.70
838	5.39	5.43	0.74	224	4.35	3.55	20.25
913	5.33	5.07	5.00	606	4.39	3.51	22.28
1043	5.17	5.38	3.94	1502	4.27	3.65	15.71
<b>average =</b>	5.29	5.34	3.24	<b>average =</b>	4.20	3.55	16.63
<b>±</b>	0.10	0.23	3.05	<b>±</b>	0.25	0.07	6.08

Conductivity results for the 1.02% Ni/MCM-41 column are presented in Table 24. In this column, no significant amount of TCE was degraded. This result is reflected in the similarity between measured inflow and outflow conductivities. In this case, the percent differences between actual and calculated masses of TCE degraded were relatively large, indicating the poor agreement between actual and calculated masses of degraded TCE. A linear fit to a plot of actual versus calculated masses of degraded TCE yields an  $R^2$  value of 0.29, substantially lower than the critical value of 0.88 for 5 observations. This result indicates that there was no reliable linear relationship between the two variables. Conductivity results for the 1.01% Ni-Pd/MCM-41 column are also presented in Table 24. The large mass of TCE degraded during flow through this column is reflected in the relatively large differences between inflow and outflow conductivities compared to those for the 1.02% Ni/MCM-41 column. The  $R^2$  value of a linear fit to a plot of the calculated versus actual mg/l of TCE degraded was 0.052. This value may be compared to the critical  $R^2$  value of 0.88. As the  $R^2$  is substantially lower than the critical value for five observations, there is no linear relationship between actual and calculated mg/l of TCE degraded.

**Table 24: Conductivity results for 1.02% Ni/MCM-41 and 1.01% Pd/MCM-41 columns.**

1.02% Ni/MCM-41							
Pore Volumes	Conductivity in (μS/cm)	Conductivity out (μS/cm)	TCE in (mg/l)	TCE out (mg/l)	Δ TCE actual (mg/l)	Δ TCE calc'd (mg/l)	% Difference (Actual-Calc'd)
31	3.83	3.62	7.05	7.04	4.00E-06	0.37	196
215	2.95	3.00	7.00	6.90	9.60E-05	0.31	105
838	2.74	3.42	6.68	6.47	2.10E-04	0.35	50
913	2.43	4.56	5.23	5.25	-1.90E-05	0.47	217
1043	2.78	3.22	6.04	6.00	4.40E-05	0.33	153

1.01% Ni-Pd/MCM-41							
Pore Volumes	Conductivity in (μS/cm)	Conductivity out (μS/cm)	TCE in (mg/l)	TCE out (mg/l)	Δ TCE actual (mg/l)	Δ TCE calc'd (mg/l)	% Difference (Actual-Calc'd)
35	5.30	74.82	6.14	2.76E-02	6.11	7.70	23
103	16.68	83.91	6.46	5.90E-03	6.45	8.64	29
224	3.79	81.52	7.01	4.60E-03	7.01	8.39	18
606	3.64	80.90	7.31	2.40E-02	7.29	8.33	13
1502	2.40	73.01	7.01	1.11E-01	6.90	7.52	9

Results shown in Figure 52 raised the question of whether Ni in the Ni-Pd/MCM-41 contributed to the degradation of TCE or whether degradation was solely a result of the presence of Pd in the material. This issue was investigated by repeating the column experiment with two MCM-41 samples containing low mass percent loadings of Pd and Ni-Pd while maintaining similar mass percent loadings of metal. The results of these two column experiments are presented in Table 25. The first column contained 0.12% Pd/MCM-41 with  $2.99 \times 10^{-4}$  g of Pd present in the column. The second column contained 0.13% Ni-Pd/MCM-41 with  $1.49 \times 10^{-4}$  g of Ni and  $1.50 \times 10^{-4}$  g of Pd present in the column. Results of the experiment comparing abilities of Pd/MCM-41 and Ni-Pd/MCM-41 are presented in Table 25. The table also includes concentrations for TCE degradation intermediates as percents of inflow TCE concentration. These intermediates were detected in all analyzed samples.

Initially, duplicate samples of column inflow and outflow were analyzed and compared after approximately 700 PV. However, duplicate samples for the 0.12% Pd/MCM-41 column experiment showed poor agreement. Therefore, samples from the 0.12% Pd/MCM-41 column taken at earlier times were also analyzed for TCE concentrations. If the final normalized TCE concentration versus PV result from the Pd/MCM-41 column is ignored, the degradation profile indicated a progressive loss in ability to induce degradation of TCE after the first 200 PV. However, the final point suggests that the Pd/MCM-41 column was still able to degrade 71.0%

of inflow TCE concentration. Normalized TCE concentration results for this column indicate a minimum of 20% and maximum of 96% of inflow TCE having been degraded. The average loss in initial TCE concentration was 53%. Sample and duplicate from the Ni-Pd/MCM-41 column after 730 and 734 PV indicated that 6% to 7% of inflow TCE had been degraded, also suggesting some loss of ability to induce degradation. Comparison of TCE concentration decreases induced by 0.13% Ni-Pd/MCM-41 with those induced by the 0.12% Pd/MCM-41 after similar PV (PV = 550-950) indicates that 0.12% Pd/MCM-41 degraded between 14 and 19% more of the inflow TCE than did 0.13% Ni-Pd/MCM-41. This comparison suggests that Pd cannot be replaced by a 50% Ni and 50% Pd metal of the same total percent mass loading of metal while still achieving the same result with regard to degradation of TCE. Therefore, while a Ni-Pd/MCM-41 sample can induce degradation of TCE in hydrogen-saturated deionized water, it is not as effective as an equivalent mass percent loading of Pd on Pd/MCM-41.

**Table 25: Comparison of normalized TCE concentration results for column experiments containing 0.12% Pd/MCM-41 or 0.13% Ni-Pd/MCM-41.**

<b>0.12% Pd/MCM-41</b>					
PV	TCE (C/C <sub>o</sub> )	VC (% C/C <sub>o</sub> )	1,1 DCE (% C/C <sub>o</sub> )	<i>trans</i> DCE (% C/C <sub>o</sub> )	<i>cis</i> DCE (% C/C <sub>o</sub> )
138	0.04	-	-	-	-
572	0.75	-	-	-	-
917	0.80	0.33	0.49	0.33	1.14
949	0.29	0.17	0.34	0.15	0.64

<b>0.13% Ni-Pd/MCM-41</b>					
PV	TCE (C/C <sub>o</sub> )	VC (% C/C <sub>o</sub> )	1,1 DCE (% C/C <sub>o</sub> )	<i>trans</i> DCE (% C/C <sub>o</sub> )	<i>cis</i> DCE (% C/C <sub>o</sub> )
730	0.94	0.10	0.08	0.13	0.29
734	0.93	0.10	0.08	0.07	0.27

Results of pH measurements for inflow and outflow samples taken during the 0.12% Pd/MCM-41 and 0.13% Ni-Pd/MCM-41 column experiments are presented in Table 26. As discussed above, the relatively large percent differences between inflow and outflow pH values are indicative of the TCE degradation that was taking place in both of the reactive columns. The average pH value for outflow samples in the 0.12% Pd/MCM-41 column decreased by  $0.91 \pm 0.74$  relative to the average inflow pH value. In the 0.13% Ni-Pd/MCM-41 column, average pH decreased by  $0.98 \pm 0.72$ . Average percent difference between inflow and outflow pH values for

the 0.12% Pd/MCM-41 and 0.13% Ni-Pd/MCM-41 columns were  $21.10 \pm 11.37\%$  and  $19.61 \pm 14.62\%$ , respectively.

**Table 26: Results of pH measurements taken during 0.12% Pd/MCM-41 and 0.13% Ni-Pd/MCM-41 column experiments.**

0.12% Pd/MCM-41				0.13% Ni-Pd/MCM-41			
PV	pH inflow	pH outflow	%Δ pH	PV	pH inflow	pH outflow	%Δ pH
138	4.48	3.63	20.96	79	5.37	4.79	11.42
572	4.25	3.63	15.74	172	5.54	4.76	15.15
917	4.80	4.07	16.46	531	5.64	3.76	40.00
949	5.21	3.80	31.25	730	6.03	4.98	19.07
				734	5.13	4.53	12.42
<b>average =</b>	4.69	3.78	21.10	<b>average =</b>	5.54	4.56	19.61
<b>±</b>	0.66	0.33	11.37	<b>±</b>	0.42	0.59	14.62

Conductivity results for samples taken during the 0.12% Pd/MCM-41 column experiment are presented in Table 27. As with other conductivity measurements and calculations taken during the column experiments, there is poor agreement between the actual masses of TCE degraded and those calculated based on conductivity measurements. This poor agreement is reflected in the large percent difference between actual and calculated mass of TCE that degraded. One exception is the sample taken after 917 PV which showed a very close agreement between actual and calculated masses of TCE degraded. Linear fit to a plot of actual versus calculated masses of degraded TCE yielded an  $R^2$  value of 0.74. This value is lower than the critical  $R^2$  value of 0.95 for four pairs of observations, indicating there is no linear relationship between actual and calculated masses of TCE degraded. However, similar to the results from the other columns discussed above, the large difference between measured inflow and outflow conductivities indicates that degradation of inflow TCE is taking place within the column.

The results of conductivity measurements made during the 0.13% Ni-Pd/MCM-41 column experiment are also presented in Table 27. Only two samples, taken after 730 and 734 PV were analyzed for TCE concentrations. Therefore, no attempt is made to correlate calculated and actual masses of degraded TCE for this experiment. The percent differences of 76% and 52% between actual and calculated mg/l of degraded TCE suggest that there likely is not a strong correlation between measured conductivity and mass of TCE degraded for this reactive column.

However, the relatively large difference between measured inflow and outflow conductivity values is indicative of the fact that TCE degradation is taking place during flow through the column. This process was confirmed by quantitative analyses for TCE concentrations in the two inflow and outflow samples taken at later times.

**Table 27: Conductivity results for 0.12% Pd/MCM-41 and 0.13% Ni-Pd/MCM-41 columns.**

0.12% Pd/MCM-41							
Pore Volumes	Conductivity in (µS/cm)	Conductivity out (µS/cm)	TCE in (mg/l)	TCE out (mg/l)	Δ TCE actual (mg/l)	Δ TCE calc'd (mg/l)	% Difference (Actual-Calc'd)
138	1.85	70.40	10.55	0.38	10.16	7.25	33
572	2.55	40.99	10.10	7.55	2.55	4.22	49
917	3.20	18.65	9.44	7.54	1.91	1.92	1
949	2.56	34.80	8.91	2.59	6.32	3.58	55
0.13% Ni-Pd/MCM-41							
Pore Volumes	Conductivity in (µS/cm)	Conductivity out (µS/cm)	TCE in (mg/l)	TCE out (mg/l)	Δ TCE actual (mg/l)	Δ TCE calc'd (mg/l)	% Difference (Actual-Calc'd)
79	2.34	20.36	-	-	-	2.09	-
172	2.03	5.91	-	-	-	0.61	-
531	1.88	26.28	-	-	-	2.70	-
730	2.84	10.85	8.11	7.61	0.50	1.12	76
734	2.54	3.50	8.32	7.71	0.62	0.36	52

### 5.3.2.2 TCE Degradation Column Experiment – Second of Two

Difficulties were encountered in trying to achieve the target TCE concentration of 10 mg/l in the column inflow. It was found that TCE concentration in the feed solution was consistently lower than calculated assuming concentration in the stock solution was 506,200 mg/l. On average, a TCE spike to the carboy calculated to produce a 10 mg/l concentration resulted in a feed solution concentration of 3.41 mg/l. Average feed solution concentration increased to 6.85 mg/l upon a doubling of the TCE spike calculated to achieve a 10 mg/l concentration. Three possible reasons for this discrepancy are:

1. Partitioning of TCE into the vapour phase within feed solution reservoir.
2. TCE concentration in stock solution being lower than the assumed value of 506,200 mg/l.
3. Incomplete dissolution of TCE spike added to the carboy.

Care was taken to reduce the mass of TCE that could partition into the vapour phase of the solution reservoir by including a sacrificial TCE solution before the feed solution reservoir. Hydrogen gas used as headspace in the feed solution reservoir would first equilibrate with TCE-

spiked solution in the sacrificial carboy. This addition to the experimental design effectively minimized the mass of TCE in the feed solution carboy that could partition into the hydrogen headspace. As an increase in TCE concentrations over time at the inflow point of the column was not observed, it is unlikely that the spiked TCE is gradually dissolving into the feed solution. Therefore, explanation #3 was rejected. Thus, it is proposed that low TCE concentrations in the feed solution resulted from TCE stock solution concentration being lower than the expected 506,200 mg/l. This proposal could be confirmed through a careful analysis of the stock solution. Confirmation of this process having taken place was not undertaken as target TCE concentrations of 10 mg/l could still be achieved by adjusting the volume of TCE stock solution added to the carboy. As degradation results are compared via normalized masses of TCE as well as pseudo first-order rate constants and degradation half-lives, the unexpectedly low inflow TCE concentrations at early stages of this experiment does not impact the interpretation of the results.

Early time samplings of reactive columns showed similar masses of degraded TCE in each column. The extent of TCE degradation was independent of the mass of Pd present in the reactive columns. This observation indicated that there was a limiting reagent in the TCE degradation proposed in Section 5.1. The most likely candidate for limiting the extent of reaction in this case is  $H_{2(g)}$ . Therefore, the column experiment was shut down temporarily to re-evaluate the experimental design. It is because of this that early time results discussed below are for samples taken after relatively high PV of feed solution had passed through the reactive columns.

Prior to shutdown, deionized water was flushed through the columns for 3 d. The shutdown period lasted 50 d. A glass vial of approximately 20 ml was installed between the valves and the inflow points of the columns. Similar to the column setup described in Section 5.2.3.1, this vial was kept filled with  $H_{2(g)}$  and intended to provide an additional stage of hydrogen contact with the feed solution before entering the column. This addition to the experimental design was included to maintain saturation with respect to hydrogen in inflow TCE solution and thereby eliminate the possibility that hydrogen was the limiting reactant in the TCE degradation reaction taking place in the columns. Upon re-initiating flow through the columns it was found that reactive column #2 had become irreparably blocked, completely stopping flow. Blockage is likely the result of migration and settling of smaller particles including Pd/MCM-41, in the porous material within column #2. Column #2 was omitted from the experiment following the

shutdown period. Settling may have been exacerbated by lack of flow of solution through the column during the shutdown period. It was noted in later experiments that reactive Pd/MCM-41 particles were able to migrate between particles of silica sand in the porous material. Colour differences between the Pd/MCM-41 and sand particles made it possible to observe this migration via visual inspection.

Average normalized mass of TCE at all sampling points in the control column during the experiment was  $1.01 \pm 0.02$ . Therefore, any decrease in TCE concentration in the reactive columns may be attributed to the presence of Pd/MCM-41. A detailed summary of control data is included in Appendix D.

Results of TCE degradation upon adding the additional stage of  $H_{2(g)}$  contact with inflow solution in column #1 are shown in Figure 53. Reaction time on the horizontal axis refers to the residence time of TCE stock solution within the column before it reached a given sampling port. The values were calculated on the basis of flow rate determined during each sampling event. Samples at later times were taken over a larger range of sampling ports to determine if degradation was taking place further along the column. Examining the degradation curves in Figure 53 shows that extent of degradation increases as PV increases between 240 and 305. Between PV 305 and 338, the extent of degradation decreases and eventually attains a steady-state value approaching a normalized concentration of 1.00. This trend indicates that the ability of Pd/MCM-41 to induce degradation of TCE decreases over time. As the Pd/MCM-41 reactive column in Section 5.3.2.1 showed no loss in ability to degrade TCE over time, it is proposed that the apparent loss of ability to induce TCE degradation in this case may be attributed to the experimental design. Aspects of the design that may have resulted in the apparent loss in degradation ability include: dissolution and re-precipitation of  $SiO_2$ , creating preferred pathways through the column; migration of reactive materials resulting in a heterogeneous distribution of reactive materials within the column; or, flushing of reactive Pd entirely from the column.

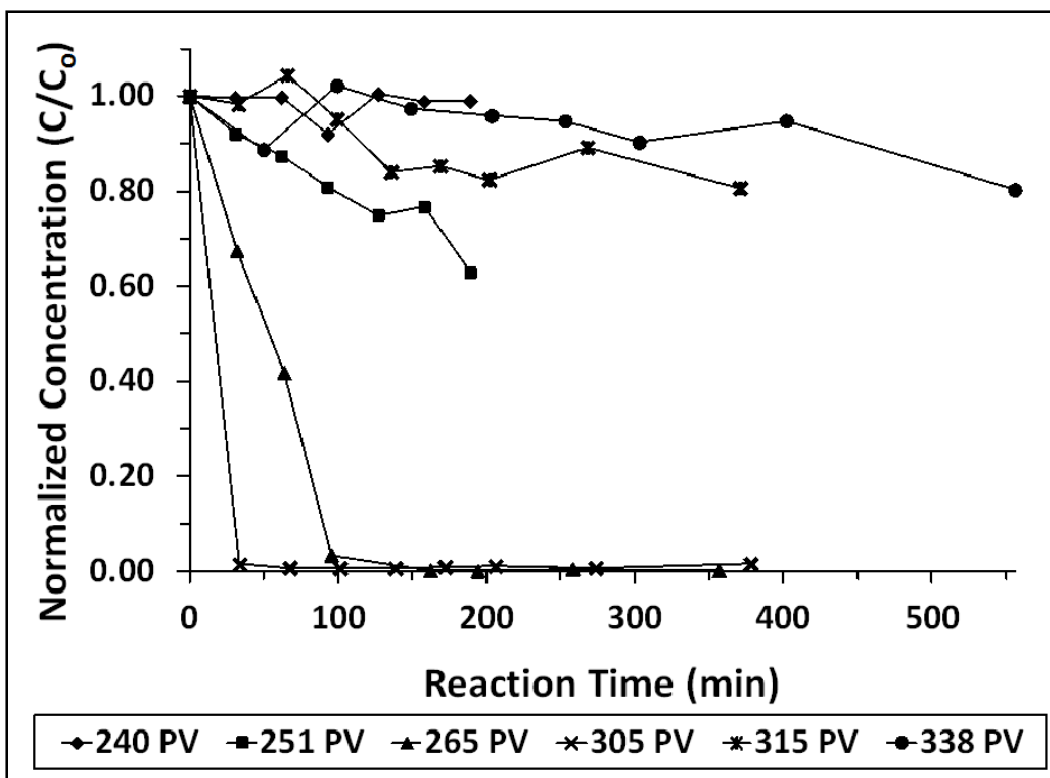


Figure 53: Normalized TCE concentration ( $C/C_0$ ) versus time profile for column #1.

Results for column #3 following the shutdown period and addition of the extra  $H_{2(g)}$  contact stage are presented in Figure 54. The difference in maximum extents of degradation between column #1 and #3 is negligible. Both columns degraded similar masses of TCE. Both columns approached a similar steady-state mass of degraded TCE at 338 and 364 PVs for column #1 and #3, respectively.

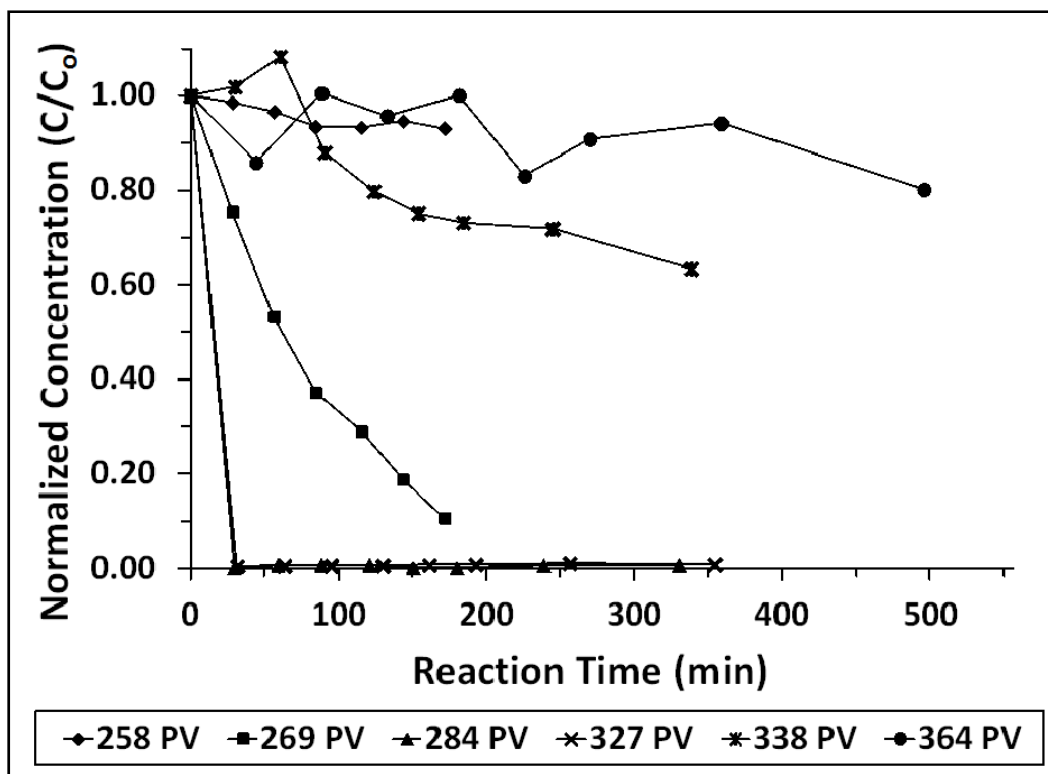


Figure 54: Normalized TCE concentration ( $C/C_0$ ) versus time profile for column #3.

Degradation results from column #1 and #3 were fit to either pseudo first-order reaction rate or zero-order reaction rate depending on whether a plot of  $\ln(C/C_0)$  or  $C$  as a function of time produced a straight line. Although an effort was made to fit certain curves – generally the early time portions of curves where rapid degradation took place – to a zero-order rate law, degradation of TCE induced by Pd in the presence of  $H_{2(g)}$  should best be approximated by a first-order rate equation (Lowry & Reinhard, 1999). Therefore, reaction rate constants and degradation half-lives calculated below using a first-order rate equation are assumed to be the more accurate estimation of the actual values. Integrated first-order rate equations used in the calculations presented below are discussed in greater detail in Section 5.3.1. The integrated zero-order reaction rate equation takes the form:

$$C = -kt + C_0$$

where  $C$  is concentration at time  $t$ ,  $k$  is the reaction rate constant, and  $C_0$  is the initial

concentration. The degradation half-life for a zero-order reaction is calculated via:

$$t_{1/2} = \frac{[C_o]}{k}$$

Plotting  $C$  with respect to  $t$  produces a straight line of slope equal to  $k$ .

In cases where degradation occurred rapidly, the degradation plot of  $C/C_o$  versus time approached a straight line and an attempt was made to fit these portions of the curve to a zero-order reaction rate. When degradation occurred relatively slowly over the length of the column, a plot of  $C/C_o$  versus time produced a curve and the data was fit to the first-order reaction rate equation. As discussed above, it is expected that the degradation curves in Figure 53 and Figure 54 should be best approximated by pseudo first-order reaction kinetics. With a few exceptions, linear fit to zero and pseudo first-order reaction rate equations was generally poor as indicated by the  $R^2$  values in Table 28. Plots showing the linear fit to the degradation data are included in Appendix D. The  $R^2$  values which were less than the critical value, given the number of data points, were considered inadmissible. Calculations based on only two data points were also inadmissible as the  $R^2$  value is meaningless in this case. In column #1, degradation curves constructed for PVs 251 and 265 were successfully fit to a first-order integrated reaction rate equation. Early time data from the degradation curve after 265 PV was successfully fitted to a zero-order integrated rate equation. In column #3, degradation curves constructed after 258, 269, and 338 PV were successfully fitted to a first-order integrated reaction rate equation. Early time data for the degradation curve after 258 PV was fitted to a zero-order integrated reaction rate equation. In addition, the degradation curve constructed using data collected after 269 PVs was successfully fitted to a zero-order integrated reaction rate equation.

**Table 28: Summary of first and zero-order rate laws fit to degradation profiles of columns #1 and #3.**

Column 1								
PV	C/C <sub>o</sub> Minimum	Rate Order	k (min <sup>-1</sup> )	t <sub>1/2</sub> (min)	R <sup>2</sup>	# of points	Critical R <sup>2</sup>	Admissable? (Y/N)
240	9.20E-01	1 <sup>st</sup>	4.55E-05	15227	0.313	6	0.811	N
251	6.29E-01	1 <sup>st</sup>	2.14E-03	324	0.932	7	0.754	Y
265	1.32E-03	0 <sup>th</sup>	2.98E-07	50	0.994	first 4	0.950	Y
		1 <sup>st</sup>	1.97E-02	35	0.720	8	0.707	Y
305	6.58E-03	0 <sup>th</sup>	7.05E-07	17	1.000	first 2	-	N
		1 <sup>st</sup>	5.47E-03	127	0.171	9	0.666	N
315	8.06E-01	0 <sup>th</sup>	2.96E-08	989	0.670	8	0.707	N
		1 <sup>st</sup>	6.39E-04	1085	0.642	9	0.666	N
338	8.03E-01	0 <sup>th</sup>	1.07E-08	1955	0.471	9	0.666	N
		1 <sup>st</sup>	2.83E-04	2448	0.476	9	0.666	N
Column 3								
PV	C/C <sub>o</sub> Minimum	Rate Order	k (min <sup>-1</sup> )	t <sub>1/2</sub> (min)	R <sup>2</sup>	# of points	Critical R <sup>2</sup>	Admissable? (Y/N)
258	9.31E-01	0 <sup>th</sup>	2.14E-08	643	0.967	first 4	0.950	Y
		1 <sup>st</sup>	4.11E-04	1689	0.776	7	0.754	Y
269	1.07E-01	0 <sup>th</sup>	1.27E-07	100	0.946	7	0.754	Y
		1 <sup>st</sup>	1.25E-02	55	0.986	7	0.754	Y
284	1.66E-03	0 <sup>th</sup>	9.75E-07	15	1.000	first 2	-	N
		1 <sup>st</sup>	6.95E-03	100	0.142	9	0.666	N
327	5.51E-03	0 <sup>th</sup>	7.74E-07	16	1.000	first 2	-	N
		1 <sup>st</sup>	5.19E-03	134	0.126	9	0.666	N
338	6.34E-01	1 <sup>st</sup>	1.58E-03	438	0.859	9	0.666	Y
364	8.01E-01	1 <sup>st</sup>	3.06E-04	2269	0.317	9	0.666	N

### 5.3.3 HMPA Degradation Batch Experiment

Figure 55 summarizes the concentration results from analyses of batch test samples, including control samples, as a plot of normalized mass versus time. Detailed data collected during the batch experiment are included in Appendix D.

Initial HMPA concentration for reactive sample set A was equal to the HMPA concentration of a non-reactive sample taken at time zero (0.233 mmol/l). Initial HMPA concentration for the control samples was also assumed equal to 0.233 mmol/l. In the case of reactive sample set B, the initial concentration of HMPA was equal to the concentration of a second, non-reactive sample taken at time zero (0.316 mmol/l). Normalized concentrations were calculated by dividing a sample's concentration at a given time by the initial HMPA concentration value. Normalized masses for reactive sample set A, set B, and control samples at time zero were assumed equal to one.

Normalized concentration results for the control samples show a slight decrease of approximately 5% in initial concentration and then attain relatively constant normalized mass

with an average value of 1.12. Lack of substantial deviation from a normalized mass of one in control samples suggests no spontaneous degradation of HMPA took place. Thus, any change in HMPA concentrations in reactive samples can be attributed to the presence of the reactive Pd/MCM-41 material. Results for reactive sample set A show an overall decrease in HMPA concentration of approximately 30% relative to the initial concentration in 15 d. The decrease in HMPA concentration for this sample set had stabilized by 7 d. Results for reactive sample set B show a rapid decrease in initial HMPA concentration within 1 d. HMPA concentration after 1 d was relatively constant, attaining an overall decrease of approximately 32% relative to the initial concentration in 15 d. Of the two reactive sample sets, set A appears to present better quality results with the suggestion of a degradation curve between 0 and 7 d. However, as will be discussed below, it was concluded that no degradation of HMPA occurred. Therefore, no attempt was made to simulate HMPA degradation results using pseudo first-order kinetic rate laws. If a pseudo first-order rate law were applied to results of set A, a rate constant of  $0.022 \text{ d}^{-1}$  and a degradation half-life of 32 d could be calculated ( $R^2 = 0.760$ , Appendix D).

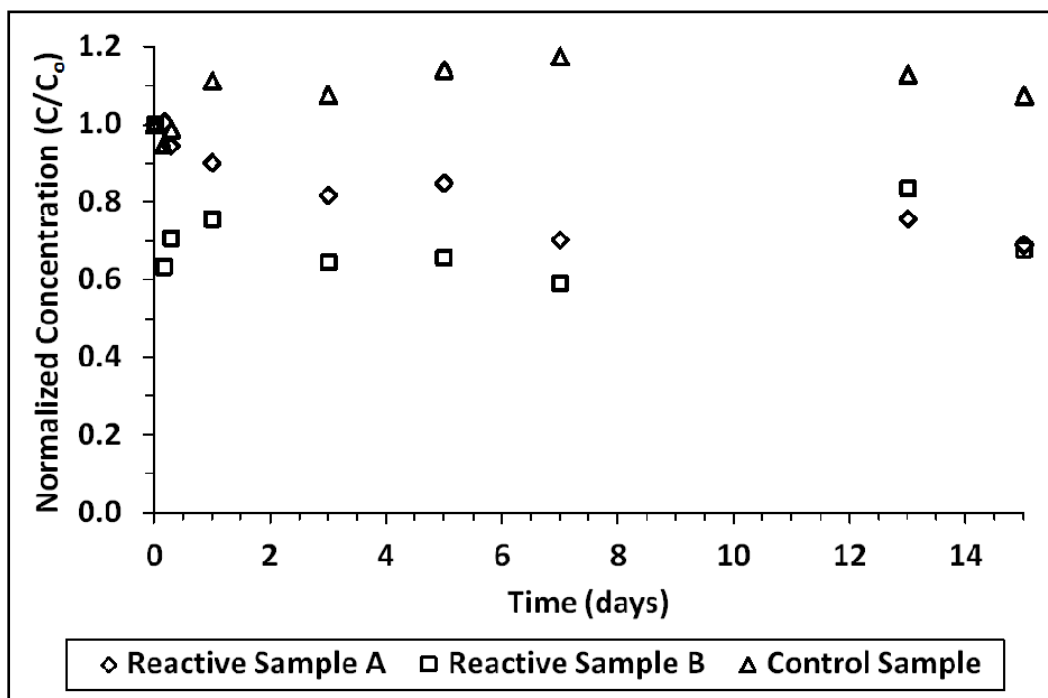


Figure 55: Normalized HMPA concentration versus time results for degradation batch experiments.

Concentration results for phosphate were below detection limits ( $6.56 \times 10^{-4} \text{ mmol/l}$ ) for all control and reactive samples for the duration of the experiment. Since phosphate (V) (and thus

phosphate species) is the stable valence form of phosphorus at the redox conditions of a hydrogen gas - water system, the absence of dissolved phosphate in the batch experiments samples suggests that degradation of initial HMPA cannot explain the decrease in concentration shown in Figure 55. Three possible explanations for the observed decrease in HMPA concentration are proposed:

1. Adsorption of HMPA molecules onto the surfaces of Pd/MCM-41.
2. Incomplete HMPA degradation, producing unknown (and unanalyzed) intermediate products containing phosphate.
3. A combination of 1 and 2.

Given the trend towards a steady normalized mass concentration value, and that phosphate was not detected in samples over time, it is proposed that explanation #1 is the most likely explanation for the observed HMPA degradation results. While Pd/MCM-41 did induce an apparent decrease of around 30% of initial HMPA concentrations, it was concluded that Pd/MCM-41 is likely not a viable material for use in HMPA treatment technologies. Therefore, a definitive determination of which of the three proposed explanations for the observed decrease in concentration was considered beyond the scope of the study at this time.

## **5.4 Conclusions**

A series of batch and column experiments were performed to determine the ability of Pd/MCM-41 to induce degradation of TCE in the presence of hydrogen. A column experiment also included Ni/MCM-41 and Ni-Pd/MCM-41 and compared the ability of those materials to induce degradation of TCE to that of Pd/MCM-41. Some batch and column experiments included Pd supported on sand (Pd/sand) to determine the benefit of using MCM-41 as a metal support material. A batch test was also performed to determine if Pd/MCM-41 could induce degradation of hexamethylphosphoramide (HMPA).

A batch experiment comparing the abilities of Pd/sand and Pd/MCM-41 to induce degradation of TCE in hydrogen-saturated deionized water indicated similar degradation abilities for both materials. However, both materials only degraded between 34 and 42% of initial TCE, suggesting that an aspect of the experimental design was limiting the degradation reaction.

Analysis of the intermediate degradation products *cis* and *trans* dichloroethylene (DCE) and vinyl chloride (VC) as well as the breakdown products ethene, ethane, and methane, indicated that ethane was the dominant product of TCE degradation in the presence of Pd/MCM-41 and hydrogen. This result suggests that TCE undergoes complete degradation to ethane, before desorbing from the Pd/sand or Pd/MCM-41 surfaces. Results of a TCE degradation batch experiment at elevated pH and including a hydrogen headspace were inconclusive as to the benefit of using MCM-41 as a Pd support compared to silica sand as a less costly alternative. Both Pd/sand and Pd/MCM-41 degraded initial TCE concentrations to below method detection limits within 120 min. No intermediate TCE degradation products were detected in batch reaction samples, suggesting that TCE underwent complete degradation before desorbing from the Pd/sand and Pd/MCM-41 surfaces as ethane.

A series of column experiments was performed to compare the abilities of Pd/sand, Pd/MCM-41, Ni/MCM-41, and Ni-Pd/MCM-41 to induce degradation of TCE in hydrogen-saturated deionized water. Results showed that Pd/MCM-41 was more effective and had greater longevity than Pd/sand when used to degrade TCE. No degradation of inflow TCE occurred in the column containing Ni/MCM-41. Comparison between results obtained from columns containing Pd/MCM-41 and Ni-Pd/MCM-41 indicated that while some Pd may be substituted for Ni and still retain the ability to induce TCE degradation, Ni-Pd was not equal in its effectiveness as Pd alone in inducing TCE degradation.

A set of experiments was performed using columns of larger internal volumes than the above-described column experiment. These experiments were performed in an effort to obtain TCE degradation profiles which could be fit to integrated first-order reaction rate equations. Fit to first-order reaction rate equations was generally poor while indicating reaction rate constants of between  $4.55 \times 10^{-5}$  and  $1.97 \times 10^{-2} \text{ min}^{-1}$ .

Pd/MCM-41 induced a small decrease of around 30% in initial HMPA concentrations in a batch experiment in hydrogen-saturated deionized water in the presence of a headspace of  $H_{2(g)}$ . Relatively small masses of HMPA degraded and there was no detection of proposed degradation products during the experiment. These two factors indicate that Pd/MCM-41 was not effective at

inducing degradation of HMPA. The small decrease in HMPA is proposed to be the result of some degree of adsorption of the compound to the Pd surfaces in the Pd/MCM-41 material.

## CHAPTER 6

### 6. SUMMARY OF CONCLUSIONS AND FUTURE WORK RECOMMENDATIONS

#### 6.1 Summary of Conclusions

The purpose of the current research was to investigate the feasibility of using MCM-41 for the purposes of treating groundwater contaminated with chlorinated volatile organic compounds. This potential feasibility was investigated by performing a series of detailed analyses to characterize the MCM-41, Pd/MCM-41, Ni/MCM-41, Ni-Pd/MCM-41, and Pd/sand materials used in the experimental work described in Chapters 3 through 5. Successful synthesis of purely siliceous MCM-41 materials was confirmed by low angle XRD and BET nitrogen adsorption surface area analyses. The presence of the three characteristic peaks (100, 110, 200), indicating a hexagonal arrangement of mesopores was identified in all MCM-41 samples prepared for this work. Results of BET surface area analyses indicated that all samples possessed the characteristic high surface areas of well-formed samples of MCM-41 ( $\sim 1,000 \text{ m}^2/\text{g}$ ). Presence and mass of metals in metal impregnated MCM-41 materials were determined via XRD, SEM, TEM, EDAX, ICP, and AA analyses. Presence of the appropriate metals was confirmed by all six techniques, but the concentrations identified by the different techniques varied widely. It is proposed that calculated mass percent loading of metal on MCM-41 provides the most accurate determination of the actual mass of metal present in the various materials.

The stability of Pd/MCM-41 in deionized water was appraised in a dissolution experiment carried out at  $25 \pm 0.1^\circ\text{C}$  and at different solid/liquid ratios and mass percent loadings of Pd. It was found that Pd/MCM-41 was more stable than purely siliceous MCM-41 in deionized water and that stability increased with increased mass percent loadings of Pd. It was concluded that increased stability of Pd/MCM-41 compared to MCM-41 was due to the reduction in the material's surface area as a result of surface coverage and partial or complete blocking of pores by Pd centres. Both Ni/MCM-41 and Ni-Pd/MCM-41 exhibited lower stability than MCM-41 and Pd/MCM-41. The Ni and Pd impregnated MCM-41 materials both exhibited enhanced stability in 0.01 M *NaCl* solution. The stability was enhanced to a greater extent in the case of the Pd/MCM-41 material.

Physical characterization of MCM-41 recovered after 1,174 d of contact with deionized water did not indicate any substantial decrease in its hexagonal structure or surface area. The stability of both Pd/MCM-41 and MCM-41 in contact with deionized water shows promise with respect to their potential application in water treatment technologies.

The ability of Pd in Pd/MCM-41 to absorb and release  $H_{2(g)}$  was investigated through a series of experiments in pressure cells at  $25 \pm 0.1^\circ\text{C}$  and up to approximately 101.3 kPa. It was found that Pd in Pd/MCM-41 at mass percent loadings between 0.81% and 2.30% could absorb an average of  $0.85 \pm 0.18$  moles of H for every mole of Pd present in the sample. This result was similar to the moles of hydrogen absorbed by a sample of bulk Pd (Pd black). Uptake by Pd/MCM-41 exceeded that of most other published Pd-hydrogen systems, suggesting that uptake by Pd may be enhanced when supported on MCM-41. This observation is tentatively attributed to a higher proportion of surface and subsurface sites in the samples relative to other, supported Pd materials.

Batch and column degradation experiments were conducted to investigate the ability and longevity of Pd/MCM-41, Ni-MCM-41, Ni-Pd/MCM-41 and Pd/sand materials to induce degradation of trichloroethylene (TCE) in the presence of hydrogen. Comparison of results obtained using Pd/sand and Pd/MCM-41 clearly demonstrated the advantage of using MCM-41 as a Pd support relative to the low cost Pd/sand material. Batch and column experiments using Pd/MCM-41 indicated that TCE was completely degraded in the presence of the material before desorbing as ethane. Minimal concentrations of intermediate degradation products were detected, if at all. Results of a column experiment using Ni/MCM-41 showed that the material does not induce degradation of TCE in the presence of hydrogen. Column experiments using Ni-Pd/MCM-41 materials indicated that while the material does induce degradation of TCE, the Pd cannot be substituted for Ni on a 1:1 basis while maintaining comparable degradation abilities.

A batch experiment showed that Pd/MCM-41 did not induce substantial degradation of hexamethylphosphoramide (HMPA). Lack of detection of phosphate (a proposed product of HMPA degradation) suggested that the small reduction in initial HMPA concentrations observed during the experiment was most likely the result of adsorption of the contaminant to the Pd/MCM-41 surfaces.

## 6.2 Future Work Recommendations

The long term stability of both MCM-41 and Pd/MCM-41 in deionized water, the ability of Pd/MCM-41 to absorb greater quantities of hydrogen than most other published Pd-hydrogen systems, and the demonstrated ability of Pd/MCM-41 to degrade trichloroethylene in column experiments running over 5,000 PV suggests that MCM-41 has great potential for applications in the treatment of water contaminated by chlorinated volatile organic compounds. It is strongly recommended that study of the material continues towards a pilot-scale or physical model-scale demonstration of its ability to induce degradation of TCE in the presence of hydrogen.

Progress towards this application would benefit from future work focusing on several key areas:

- Determining the long-term stability of Pd/MCM-41 in deionized water. The work described in the current document investigated dissolution of the material over 50 d. It would be beneficial to perform a similar study lasting one or more years.
- Collecting data of hydrogen absorption by Pd/MCM-41 over a larger range of mass percent loadings of Pd.
- Investigating hydrogen uptake by Ni/MCM-41 and Ni-Pd/MCM-41.
- Determining why Pd/MCM-41 exhibits enhanced hydrogen uptake compared to most other published Pd-hydrogen systems.
- Conducting a column experiment using Pd/MCM-41 to induce degradation of trichloroethylene where the hydrogen is furnished by corrosion of zero-valent iron particles. Later column experiments could also use simulated groundwaters containing different concentrations of major and minor ionic species.
- Investigation of Pd/MCM-41's ability to induce degradation of other organic compounds, such as: tetrachloroethylene, polychlorinated biphenyls, and chlorinated benzenes.

## REFERENCES

- Algarra, M., Jiménez, M. V., Rodríguez-Castellón, E., Jiménez-López, A., & Jiménez-Jiménez, J. (2005). Heavy metals removal from electroplating wastewater by aminopropyl-Si MCM-41. *Chemosphere*, 59(6), 779-786.
- Appelo, C.A.J. & Postma, D. (2007). *Geochemistry, Groundwater and Pollution*, 2<sup>nd</sup> Edition. Balkema, Leiden, the Netherlands, 649 pp.
- Araújo, A. S., Souza, M. J. B., Silva, A. O. S., Pedrosa, A. M. G., Aquino, J. M. F. B., & Coutinho, A. C. S. L. S. (2005). Study of the adsorption properties of MCM-41 molecular sieves prepared at different synthesis times. *Adsorption*, 11(2 SPEC. ISS.), 181-186.
- Azaïs, T., Tourné-Péteilh, C., Aussenac, F., Baccile, N., Coelho, C., Devoisselle, J. M., & Babbonneau, F. (2006). Solid-state NMR study of ibuprofen confined in MCM-41 material. *Chemistry of Materials*, 18(26), 6382-6390.
- Beck, J. S., Vartuli, J. C., Roth, W. J., Leonowicz, M. E., Kresge, C. T., Schmitt, K. D., et al. (1992). A new family of mesoporous molecular sieves prepared with liquid crystal templates. *Journal of the American Chemical Society*, 114(27), 10834-10843.
- Blin, J. L., Otjacques, C., Herrier, G., & Su, B. -. (2001). Kinetic study of MCM-41 synthesis. *International Journal of Inorganic Materials*, 3(1), 75-86.
- Blowes, D. W., Ptacek, C. J., & Jambor, J. L. (1997). In-situ remediation of Cr(VI)-contaminated groundwater using permeable reactive walls: Laboratory studies. *Environmental Science and Technology*, 31(12), 3348-3357.
- Boudart, M., & Hwang, H. S. (1975). Solubility of hydrogen in small particles of palladium. *Journal of Catalysis*, 39(1), 44-52.
- Brunauer, S., Emmett, P. H., & Teller, E. (1938). Adsorption of gases in multimolecular layers. *Journal of the American Chemical Society*, 60(2), 309-319.

- Chen, K. L., & Elimelech, M. (2006). Aggregation and deposition kinetics of fullerene (C60) nanoparticles. *Langmuir*, 22(26), 10994-11001.
- Cheng, C. F., Park, D. H., & Klinowski, J. (1997). Optimal parameters for the synthesis of the mesoporous molecular sieve [Si]-MCM-41. *Journal of the Chemical Society - Faraday Transactions*, 93(1), 193-197.
- Corma, A., Kan, Q., Navarro, M. T., Pérez-Pariente, J., & Rey, F. (1997). Synthesis of MCM-41 with different pore diameters without addition of auxiliary organics. *Chemistry of Materials*, 9(10), 2123-2126.
- Cox, D. M., Fayet, P., Brickman, R., Hahn, M. Y., & Kaldor, A. (1990). Abnormally large deuterium uptake on small transition metal clusters. *Catalysis Letters*, 4(4-6), 271-278.
- Crosta, G. F., & Dotti, M. (1998). Volatile halocarbons in a drinking water supply system: Forecasting contamination values and estimating health risk. *Chemosphere*, 37(14-15), 2873-2884.
- Day, S. R., O'Hannesin, S. F., & Marsden, L. (1999). Geotechnical techniques for the construction of reactive barriers. *Journal of Hazardous Materials*, 67(3), 285-297.
- Decyk, P. (2006). States of transition metal ions in modified mesoporous MCM-41 and in microporous ZSM-5 studied by ESR spectroscopy. *Catalysis Today*, 114(2-3), 142-153.
- Eaton, A. D., Clesceri, L. S., & Greenberg, A. E., Eds. (1995). Standard Methods for the Examination of Water and Wastewater, 19<sup>th</sup> Edition. American Public Health Association, American Water Works Association, Water Environment Federation, Washington, DC, USA. 1325 pp.
- Flanagan, T. B., Clewley, J. D., & Lynch, J. F. (1975). The effect of dislocations on the hydride phase transition in the palladium/ hydrogen system. *Journal of the Less-Common Metals*, 41(2), 343-346.
- Flanagan, T. B., Bowerman, B. S., & Biehl, G. E. (1980). Hysteresis in metal/hydrogen systems. *Scripta Metallurgica*, 14(4), 443-447.

- Flanagan, T. B., & Oates, W. A. (1991). The palladium-hydrogen system. *Annual Review of Materials Science*, 21(1), 269-304.
- Galarneau, A., Nader, M., Guenneau, F., Di Renzo, F., & Gedeon, A. (2007). Understanding the stability in water of mesoporous SBA-15 and MCM-41. *Journal of Physical Chemistry C*, 111(23), 8268-8277.
- Gavaskar, A. R. (1999). Design and construction techniques for permeable reactive barriers. *Journal of Hazardous Materials*, 68(1-2), 41-71.
- Gaydhankar, T. R., Taralkar, U. S., Jha, R. K., Joshi, P. N., & Kumar, R. (2005). Textural/structural, stability and morphological properties of mesostructured silicas (MCM-41 and MCM-48) prepared using different silica sources. *Catalysis Communications*, 6(5), 361-366.
- Ghiaci, M., Abbaspur, A., Kia, R., & Seyedeyn-Azad, F. (2004). Equilibrium isotherm studies for the sorption of benzene, toluene, and phenol onto organo-zeolites and as-synthesized MCM-41. *Separation and Purification Technology*, 40(3), 217-229.
- Gillham, R. W., & Ohannesin, S. F. (1994). Enhanced degradation of halogenated aliphatics by zero valent iron. *Ground Water*, 32(6), 958-967.
- Guthrie, C.P. (2007). Potential and Limitations of MCM-41 in Dechlorination Reactions. Masters Thesis. Department of Earth Sciences, University of Waterloo, Waterloo, Canada. 98 pp.
- Guthrie, C. P., & Reardon, E. J. (2008). Metastability of MCM-41 and Al-MCM-41. *Journal of Physical Chemistry A*, 112(15), 3386-3390.
- Haber, J., Block J.H., & Delmon, B. (1995). Manual of Methods and Procedures for Catalyst Characterization. *Pure and Applied Chemistry*, 67, Nos 8/9, 1257-1306.
- Hanton-Fong, C. J. (1992). The Solubility and Dissolution Kinetics of Amorphous Silica in Electrolyte Solutions at 25°C. M.Sc. Thesis, Department of Earth Sciences, University of Waterloo, Waterloo, Canada.

- Hassan, J. (2006). NMR Study of Exchange and Hydration Site Identification in MCM-41. Doctoral Thesis. Department of Physics and Astronomy, University of Waterloo, Waterloo, Canada. 141 pp.
- He, J., Duan, X., & Li, C. (2001). Improving the stability of MCM-41 by monolayer dispersion of a metal oxide. *Materials Chemistry and Physics*, 71(3), 221-225.
- Horner, H., & Wagner, H. (1974). A model calculation for the  $\alpha$ - $\alpha'$  phase transition in metal-hydrogen systems. *Journal of Physics C: Solid State Physics*, 7(18), 3305-3325.
- Huang, S. Y., Huang, C. D., Chang, B. T., & Yeh, C. T. (2006). Chemical activity of palladium clusters: Sorption of hydrogen. *Journal of Physical Chemistry B*, 110(43), 21783-21787.
- Ichinose, H. (2000). Crystal interface and high-resolution electron microscopy - the best partner. *Science and Technology of Advanced Materials*, 1(1), 11-20.
- Idris, S. A., Davidson, C. M., McManamon, C., Morris, M. A., Anderson, P., & Gibson, L. T. (2011). Large pore diameter MCM-41 and its application for lead removal from aqueous media. *Journal of Hazardous Materials*, 185(2-3), 898-904.
- Iyer, R. N., & Pickering, H. W. (1990). Mechanism and kinetics of electrochemical hydrogen entry and degradation of metallic systems. *Annual Review of Materials Science*, 20(1), 299-338.
- Jana, S. K., Nishida, R., Shindo, K., Kugita, T., & Namba, S. (2004). Pore size control of mesoporous molecular sieves using different organic auxiliary chemicals. *Microporous and Mesoporous Materials*, 68(1-3), 133-142.
- Jewell, L. L., & Davis, B. H. (2006). Review of absorption and adsorption in the hydrogen-palladium system. *Applied Catalysis A: General*, 310(1-2), 1-15.
- Jiao, Y., Qiu, C., Huang, L., Wu, K., Ma, H., Chen, S., et al. (2009). Reductive dechlorination of carbon tetrachloride by zero-valent iron and related iron corrosion. *Applied Catalysis B: Environmental*, 91(1-2), 434-440.

- Jutidamrongphan, W., Park, K. Y., Dockko, S., Choi, J. W., & Lee, S. H. (2012). High removal of phosphate from wastewater using silica sulfate. *Environmental Chemistry Letters*, *10*(1), 21-28.
- Kao, C. M., & Lei, S. E. (2000). Using a peat biobarrier to remediate PCE/TCE contaminated aquifers. *Water Research*, *34*(3), 835-845.
- Kim, J. M., Kwak, J. H., Jun, S., & Ryoo, R. (1995). Ion exchange and thermal stability of MCM-41. *Journal of Physical Chemistry*, *99*(45), 16742-16747.
- Kim, Y. H., & Carraway, E. R. (2003). Dechlorination of chlorinated ethenes and acetylenes by palladized iron. *Environmental Technology*, *24*(7), 809-819.
- Koh, C. A., Nooney, R., & Tahir, S. (1997). Characterisation and catalytic properties of MCM-41 and Pd/MCM-41 materials. *Catalysis Letters*, *47*(1-2), 199-203.
- Koyano, K. A., Tatsumi, T., Tanaka, Y., & Nakata, S. (1997). Stabilization of mesoporous molecular sieves by trimethylsilylation. *Journal of Physical Chemistry B*, *101*(46), 9436-9440.
- Kruk, M., Jaroniec, M., Sakamoto, Y., Terasaki, O., Ryoo, R., & Ko, C. H. (2000). Determination of pore size and pore wall structure of MCM-41 by using nitrogen adsorption, transmission electron microscopy, and X-ray diffraction. *Journal of Physical Chemistry B*, *104*(2), 292-301.
- Kruk, M., Jaroniec, M., & Sayari, A. (1997). Adsorption study of surface and structural properties of MCM-41 materials of different pore sizes. *Journal of Physical Chemistry B*, *101*(4), 583-589.
- Kruk, M., Jaroniec, M., & Sayari, A. (1999). A unified interpretation of high-temperature pore size expansion processes in MCM-41 mesoporous silicas. *Journal of Physical Chemistry B*, *103*(22), 4590-4598.
- Kuji, T., Matsumura, Y., Uchida, H., & Aizawa, T. (2002). Hydrogen absorption of nanocrystalline palladium. *Journal of Alloys and Compounds*, *330-332*, 718-722.

- Kumar, D., Schumacher, K., Du Fresne von Hohenesche, C., Grün, M., & Unger, K. K. (2001). MCM-41, MCM-48 and related mesoporous adsorbents: Their synthesis and characterisation. *Colloids and Surfaces A: Physicochemical and Engineering Aspects*, 187-188, 109-116.
- Landau, M. V., Varkey, S. P., Herskowitz, M., Regev, O., Pevzner, S., Sen, T., et al. (1999). Wetting stability of Si-MCM-41 mesoporous material in neutral, acidic and basic aqueous solutions. *Microporous and Mesoporous Materials*, 33(1-3), 149-163.
- Landmesser, H., Kosslick, H., Storek, W., & Fricke, R. (1997). Interior surface hydroxyl groups in ordered mesoporous silicates. *Solid State Ionics*, 101-103(PART 1), 271-277.
- Lensveld, D. J., Gerbrand Mesu, J., Jos van Dillen, A., & De Jong, K. P. (2001). Synthesis and characterization of MCM-41 supported nickel oxide catalysts. *Microporous and Mesoporous Materials*, 44-45, 401-407.
- Lim, S., Ciuparu, D., Pak, C., Dobek, F., Chen, Y., Harding, D., Pfefferle, L., Haller, G. (2003). Synthesis and characterization of highly ordered Co-MCM-41 for production of aligned single walled carbon nanotubes (SWNT). *Journal of Physical Chemistry B*, 107(40), 11048-11056.
- Lowry, G. V., & Reinhard, M. (1999). Hydrodehalogenation of 1- to 3-carbon halogenated organic compounds in water using a palladium catalyst and hydrogen gas. *Environmental Science and Technology*, 33(11), 1905-1910.
- Mackay, D. M., & Cherry, J. A. (1989). Groundwater contamination: Pump-and-treat remediation. Second of a five-part series. *Environmental Science and Technology*, 23(6), 630-636.
- Mansour, F., Dimeo, R. M., & Peemoeller, H. (2002). High-resolution inelastic neutron scattering from water in mesoporous silica. *Physical Review E - Statistical, Nonlinear, and Soft Matter Physics*, 66(4), 041307/1-041307/7.

- Mastalir, A., Rác, B., Király, Z., & Molnár, A. (2007). In situ generation of Pd nanoparticles in MCM-41 and catalytic applications in liquid-phase alkyne hydrogenations. *Journal of Molecular Catalysis A: Chemical*, 264(1-2), 170-178.
- Matsumoto, A., Chen, H., Tsutsumi, K., Grün, M., & Unger, K. (1999). Novel route in the synthesis of MCM-41 containing framework aluminum and its characterization. *Microporous and Mesoporous Materials*, 32(1-2), 55-62.
- McNab Jr., W. W., & Ruiz, R. (1998). Palladium-catalyzed reductive dehalogenation of dissolved chlorinated aliphatics using electrolytically-generated hydrogen. *Chemosphere*, 37(5), 925-936.
- Mokaya, R. (1999). Improving the stability of mesoporous MCM-41 silica via thicker more highly condensed pore walls. *Journal of Physical Chemistry B*, 103(46), 10204-10208.
- Mokaya, R. (2000). Al content dependent hydrothermal stability of directly synthesized aluminosilicate MCM-41. *Journal of Physical Chemistry B*, 104(34), 8279-8286.
- Mokaya, R. (2002). On the extended recrystallisation of mesoporous silica: Characterisation of restructured pure silica MCM-41. *Journal of Materials Chemistry*, 12(10), 3027-3033.
- Moreno, B., Nogales, R., MacCi, C., Masciandaro, G., & Benitez, E. (2011). Microbial eco-physiological profiles to estimate the biological restoration of a trichloroethylene-contaminated soil. *Ecological Indicators*, 11(6), 1563-1571.
- Mori, T., Kuroda, Y., Yoshikawa, Y., Nagao, M., & Kittaka, S. (2002). Preparation of a water-resistant siliceous MCM-41 sample, through improvement of crystallinity, and its prominent adsorption features. *Langmuir*, 18(5), 1595-1603.
- Newman, L. A., Strand, S. E., Choe, N., Duffy, J., Ekuan, G., Ruszaj, M., et al. (1997). Uptake and biotransformation of trichloroethylene by hybrid poplars. *Environmental Science and Technology*, 31(4), 1062-1067.
- O'Hannesin, S. F., & Gillham, R. W. (1998). Long-term performance of an in situ 'iron wall' for remediation of VOCs. *Ground Water*, 36(1), 164-170.

- Okumara, K., Tokai, H., & Niwa M. (2003). Structural analysis of Pd loaded MCM-41 catalysts for hydrogenation of benzene by means of XAFS. *Photon Factory Activity Report*, 20(B).
- Pankow, J.F., & Cherry, J.A. (1996). Dense Chlorinated Solvents and other DNAPLs in Groundwater. *Waterloo Press*. Portland, Oregon.
- Park, S. J., & Lee, S. Y. (2010). A study on hydrogen-storage behaviors of nickel-loaded mesoporous MCM-41. *Journal of Colloid and Interface Science*, 346(1), 194-198.
- Prasanth, K. P., Raj, M. C., Bajaj, H. C., Kim, T. H., & Jasra, R. V. (2010). Hydrogen sorption in transition metal modified mesoporous materials. *International Journal of Hydrogen Energy*, 35(6), 2351-2360.
- Pundt, A., Suleiman, M., Bähz, C., Reetz, M. T., Kirchheim, R., & Jisrawi, N. M. (2004). Hydrogen and Pd-clusters. *Materials Science and Engineering B: Solid-State Materials for Advanced Technology*, 108(1-2), 19-23.
- Randall, M., & Failey, C.F. (1927). The activity coefficient of gases in aqueous salt solution. *Chemical Reviews*, 4(3), 271-284.
- Reardon, E.J. (2004). Laboratory Manual for Earth 421. Department of Earth Sciences, University of Waterloo, Waterloo, Canada. 41 pp.
- Ribeiro Carrott, M. M. L., Candeias, A. J. E., Carrott, P. J. M., & Unger, K. K. (1999). Evaluation of the stability of pure silica MCM-41 toward water vapor. *Langmuir*, 15(26), 8895-8901.
- Richard Cothorn, C., Coniglio, W. A., & Marcus, W. L. (1986). Estimating risk to human health: Trichloroethylene in drinking water is used as the example. *Environmental Science and Technology*, 20(2), 111-116.
- Rimstidt, J. D., & Barnes, H. L. (1980). The kinetics of silica-water reactions. *Geochimica Et Cosmochimica Acta*, 44(11), 1683-1699.

- Rouquerol, J., Avnir, D., Everett, D. H., Fairbridge, C., Haynes, M., Pernicone, N., Ramsay, J. D. F., Sing, K. S. W., & Unger, K. K. (1994). Guidelines for the characterization of porous solids. *Studies in Surface Science and Catalysis*.87, pp. 10.
- Ruhl, A. S., Weber, A., & Jekel, M. (2012). Influence of dissolved inorganic carbon and calcium on gas formation and accumulation in iron permeable reactive barriers. *Journal of Contaminant Hydrology*, 142-143, 22-32.
- Saad, R., Hamoudi, S., & Belkacemi, K. (2008). Adsorption of phosphate and nitrate anions on ammonium-functionnalized mesoporous silicas. *Journal of Porous Materials*, 15(3), 315-323.
- Sachs, C., Pundt, A., Kirchheim, R., Winter, M., Reetz, M. T., & Fritsch, D. (2001). Solubility of hydrogen in single-sized palladium clusters. *Physical Review B - Condensed Matter and Materials Physics*, 64(7), 754081-7540810.
- Sayari, A. (1996). Catalysis by crystalline mesoporous molecular sieves. *Chemistry of Materials*, 8(8), 1840-1852.
- Sayari, A., Hamoudi, S., & Yang, Y. (2005). Applications of pore-expanded mesoporous silica. 1. removal of heavy metal cations and organic pollutants from wastewater. *Chemistry of Materials*, 17(1), 212-216.
- Schreier, C. G., & Reinhard, M. (1995). Catalytic hydrodehalogenation of chlorinated ethylenes using palladium and hydrogen for the treatment of contaminated water. *Chemosphere*, 31(6), 3475-3487.
- Schüth, C., Disser, S., Schüth, F., & Reinhard, M. (2000). Tailoring catalysts for hydrodechlorinating chlorinated hydrocarbon contaminants in groundwater. *Applied Catalysis B: Environmental*, 28(3-4), 147-152.
- Schwarz, R. B., & Khachaturyan, A. G. (1995). Thermodynamics of open two-phase systems with coherent interfaces. *Physical Review Letters*, 74(13), 2523-2526.

- Sener, C., Dogu, T., & Dogu, G. (2006). Effects of synthesis conditions on the structure of Pd incorporated MCM-41 type mesoporous nanocomposite catalytic materials with high Pd/Si ratios. *Microporous and Mesoporous Materials*, 94(1-3), 89-98.
- Serna-Guerrero, R., & Sayari, A. (2007). Applications of pore-expanded mesoporous silica. 7. adsorption of volatile organic compounds. *Environmental Science and Technology*, 41(13), 4761-4766.
- Shen, S. C., & Kawi, S. (2002). MCM-41 with improved hydrothermal stability: Formation and prevention of Al content dependent structural defects. *Langmuir*, 18(12), 4720-4728.
- Shen, S. C., & Kawi, S. (1999). Understanding of the effect of Al substitution on the hydrothermal stability of MCM-41. *Journal of Physical Chemistry B*, 103(42), 8870-8876.
- Shevchenko, N., Zaitsev, V., & Walcarius, A. (2008). Bifunctionalized mesoporous silicas for Cr(VI) reduction and concomitant Cr(III) immobilization. *Environmental Science and Technology*, 42(18), 6922-6928.
- Soeteman, S.C.J., De Greef, E., & Brinkmann, F.J.J. (1981). Persistency of organic contaminants in groundwater, lessons from soil pollution incidents in the Netherlands. *The Science of the Total Environment*, 21, 187-202.
- Sriwatanapongse, W., Reinhard, M., & Klug, C. A. (2006). Reductive hydrodechlorination of trichloroethylene by palladium-on-alumina catalyst: <sup>13</sup>C solid-state NMR study of surface reaction precursors. *Langmuir*, 22(9), 4158-4164.
- Theng, B. K. G., & Yuan, G. (2008). Nanoparticles in the soil environment. *Elements*, 4(6), 395-399.
- Trébosc, J., Wiench, J. W., Huh, S., Lin, V. S. Y., & Pruski, M. (2005). Solid-state MMR study of MCM-41-type mesoporous silica nanoparticles. *Journal of the American Chemical Society*, 127(9), 3057-3068.

- Trouvé, A., Batonneau-Gener, I., Valange, S., Bonne, M., & Mignard, S. (2012). Tuning the hydrophobicity of mesoporous silica materials for the adsorption of organic pollutant in aqueous solution. *Journal of Hazardous Materials*, 201-202, 107-114.
- Tun, Z., Mason, P. C., Mansour, F. K., & Peemoeller, H. (2002). Observation of adsorption of water in MCM-41 with neutron diffraction. *Langmuir*, 18(4), 975-977.
- United States Environmental Protection Agency. (2001). Trichloroethylene Health Risk Assessment: Synthesis and Characterization. External Review Draft. EPA/600/P-01/002A. 153 pp.
- Vogel, W., He, W., Huang, Q. H., Zou, Z., Zhang, X. G., & Yang, H. (2010). Palladium nanoparticles "breathe" hydrogen; a surgical view with X-ray diffraction. *International Journal of Hydrogen Energy*, 35(16), 8609-8620.
- Walter, R. J., & Chandler, W.T. (1965). The Columbian-hydrogen constitution diagram. *Transactions of the Metallurgical Society of AIME*. 233, 762-765.
- Wang, C. B., & Zhang, W. X. (1997). Synthesizing nanoscale iron particles for rapid and complete dechlorination of TCE and PCBs. *Environmental Science and Technology*, 31(7), 2154-2156.
- William Page, G. (1981). Comparison of groundwater and surface water for patterns and levels of contamination by toxic substances. *Environmental Science and Technology*, 15(12), 1475-1481.
- Xia, Q. H., Hidajat, K., & Kawi, S. (2000). Improvement of the hydrothermal stability of fluorinated MCM-41 material. *Materials Letters*, 42(1), 102-107.
- Xu, J., Dozier, A., & Bhattacharyya, D. (2005). Synthesis of nanoscale bimetallic particles in polyelectrolyte membrane matrix for reductive transformation of halogenated organic compounds. *Journal of Nanoparticle Research*, 7(4-5), 449-467.
- Zanjanchi, M. A., Sajjadi, H., Arvand, M., Mohammad-Khah, A., & Ghalami-Choobar, B. (2011). Modification of MCM-41 with anionic surfactant: a convenient design for

- efficient removal of cationic dyes from wastewater. *Clean - Soil, Air, Water*, 39(11), 1007-1013.
- Zhang, W., Wang, J., Tanev, P. T., & Pinnavaia, T. J. (1996). Catalytic hydroxylation of benzene over transition-metal substituted hexagonal mesoporous silicas. *Chemical Communications*, (8), 979-980.
- Zhang, W. X., Wang, C. B., & Lien, H. L. (1998). Treatment of chlorinated organic contaminants with nanoscale bimetallic particles. *Catalysis Today*, 40(4), 387-395.
- Zhao, H., Nagy, K. L., Waples, J. S., & Vance, G. F. (2000). Surfactant-templated mesoporous silicate materials as sorbents for organic pollutants in water. *Environmental Science and Technology*, 34(22), 4822-4827.
- Zhao, X. S., Audsley, F., & Lu, G. Q. (1998). Irreversible change of pore structure of MCM-41 upon hydration at room temperature. *Journal of Physical Chemistry B*, 102(21), 4143-4146.
- Zhao, X. S., Lu, G. Q., Whittaker, A. K., Millar, G. J., & Zhu, H. Y. (1997). Comprehensive study of surface chemistry of MCM-41 using  $^{29}\text{Si}$  CP/MAS NMR, FTIR, pyridine-TPD, and TGA. *Journal of Physical Chemistry B*, 101(33), 6525-6531.
- Ziolek, M., Nowak, I., Kilos, B., Sobczak, I., Decyk, P., Trejda, M., et al. (2004). Template synthesis and characterisation of MCM-41 mesoporous molecular sieves containing various transition metal elements - TME (Cu, Fe, Nb, V, Mo). *Journal of Physics and Chemistry of Solids*, 65(2-3), 571-581.

## APPENDIX A

Synthesis and characterization results of calcined MCM-41 and metal impregnated materials not included in Chapter 2.

---

### X-ray Diffraction Results for Calcined MCM-41 and Metal Impregnated Samples

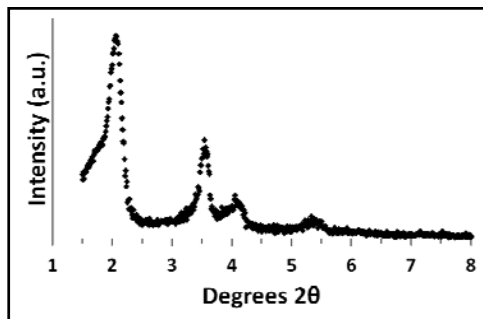


Figure 56: Low angle XRD results for sample MCM-1A.

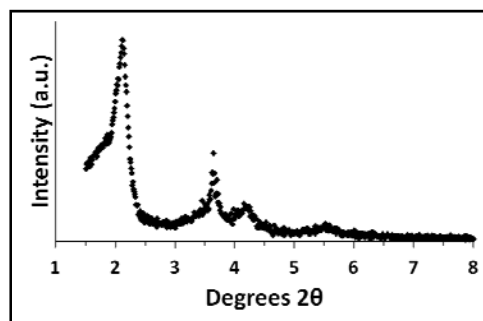


Figure 57: Low angle XRD results for sample MCM-1B.

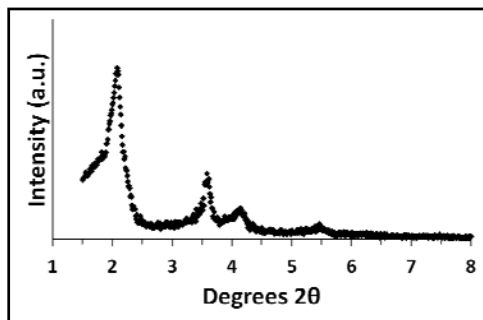


Figure 58: Low angle XRD results for sample MCM-1C.

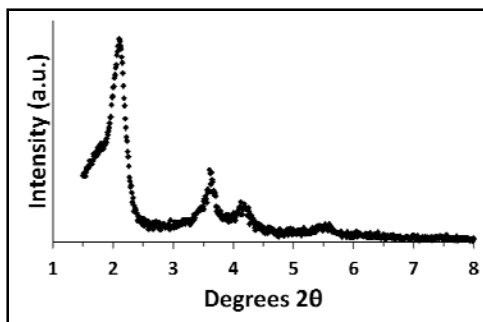


Figure 59: Low angle XRD results for sample Combo 1.

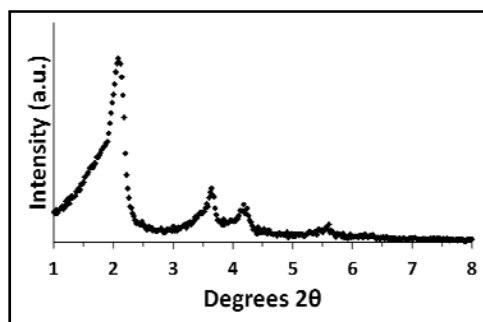


Figure 60: Low angle XRD results for sample MCM-2A.

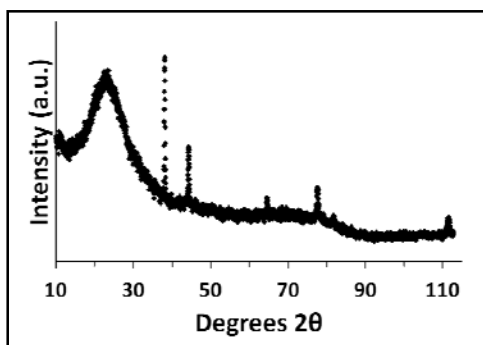


Figure 61: High angle XRD results for sample MCM-2A.

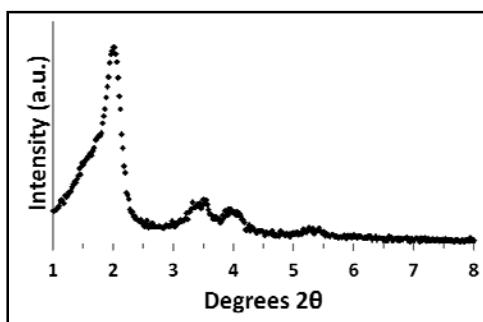


Figure 62: Low angle XRD results for sample MCM-2B.

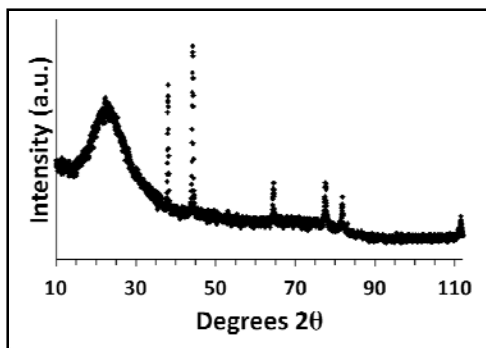


Figure 63: High angle XRD results for sample MCM-2B.

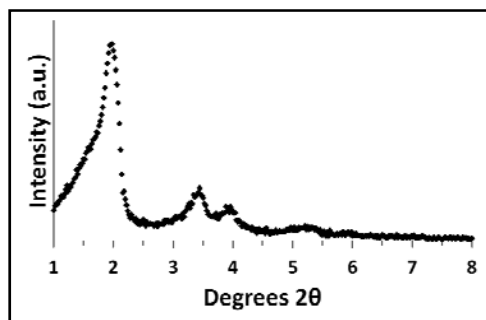


Figure 64: Low angle XRD results for sample MCM-2C.

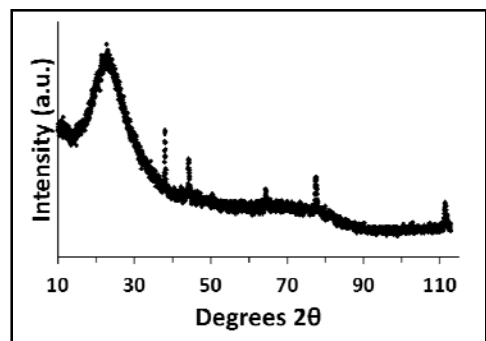


Figure 65: High angle XRD results for sample MCM-2C.

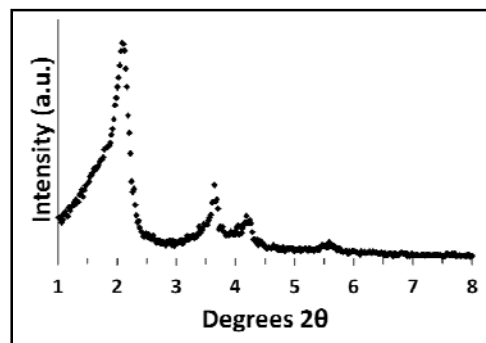


Figure 66: Low angle XRD results for sample MCM-2D.

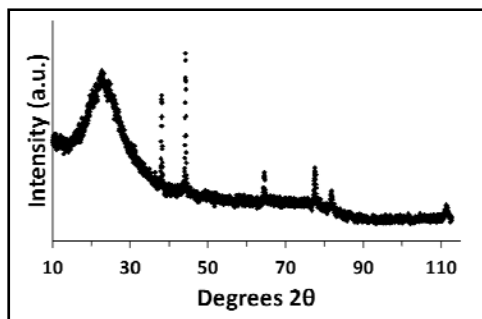


Figure 67: High angle XRD results for sample MCM-2D.

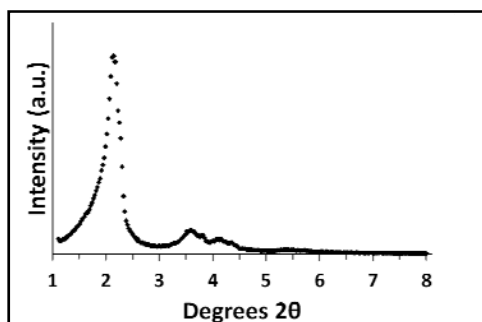


Figure 68: Low angle XRD results for sample Combo 2.

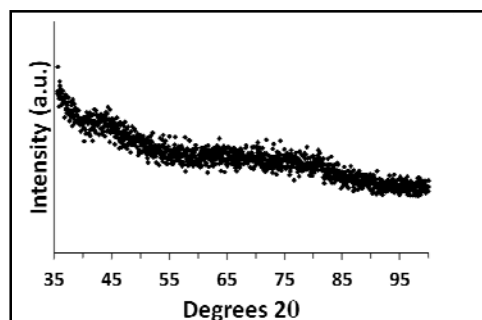


Figure 69: High angle XRD results for sample Combo 2.

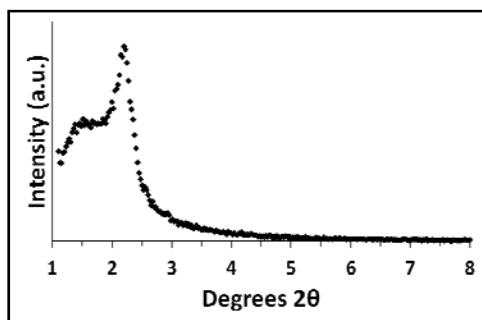


Figure 70: Low angle XRD results for sample 0.12% Pd/MCM-41.

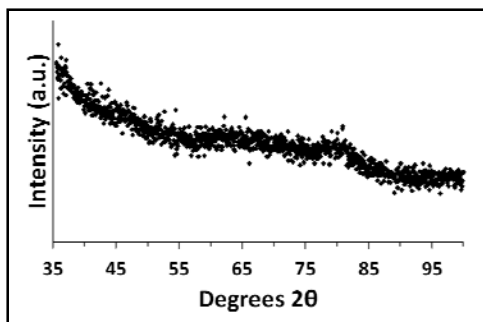


Figure 71: High angle XRD results for sample 0.12% Pd/MCM-41.

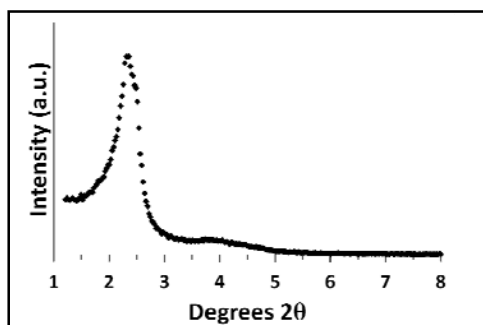


Figure 72: Low angle XRD results for sample 0.81% Pd/MCM-41

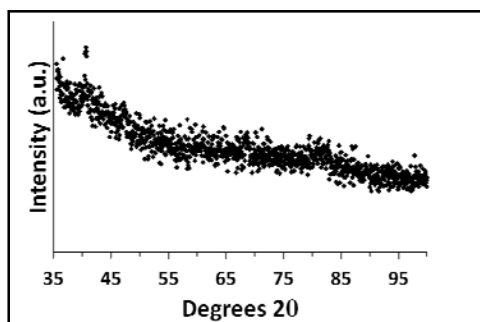


Figure 73: High angle XRD results for sample 0.81% Pd/MCM-41.

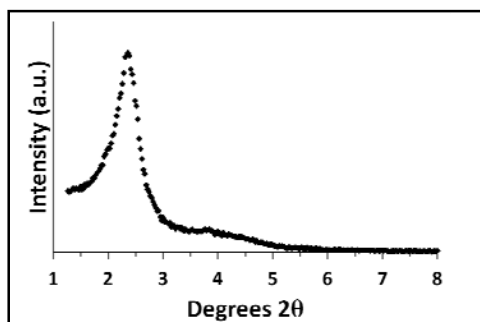


Figure 74: Low angle XRD results for sample 0.99% Pd/MCM-41

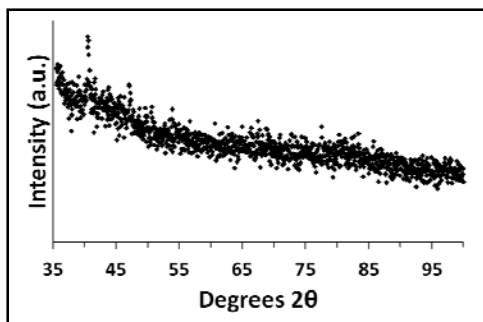


Figure 75: High angle XRD results for sample 0.99% Pd/MCM-41.

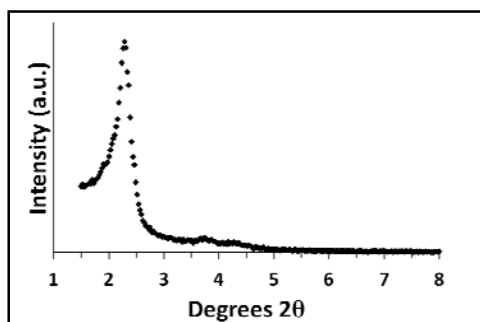


Figure 76: Low angle XRD results for sample 1.10% Pd/MCM-41

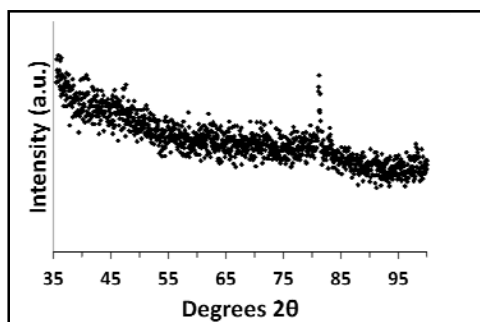


Figure 77: High angle XRD results for sample 1.10% Pd/MCM-41.

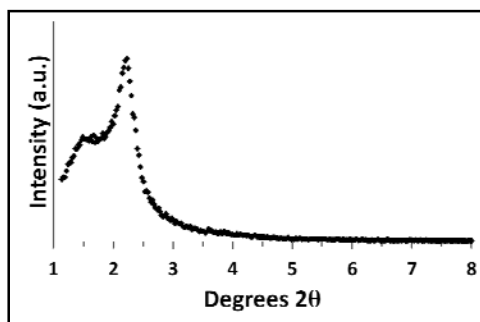


Figure 78: Low angle XRD results for sample 1.16% Pd/MCM-41

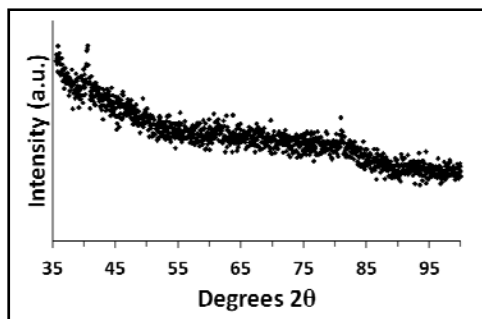


Figure 79: High angle XRD results for sample 1.16% Pd/MCM-41.

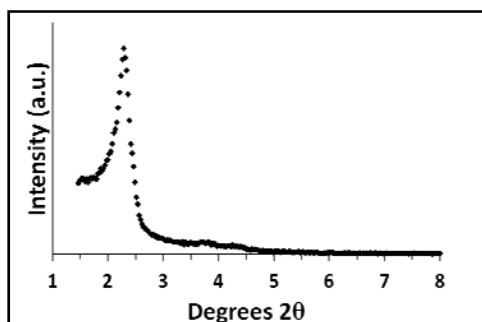


Figure 80: Low angle XRD results for sample 1.76% Pd/MCM-41

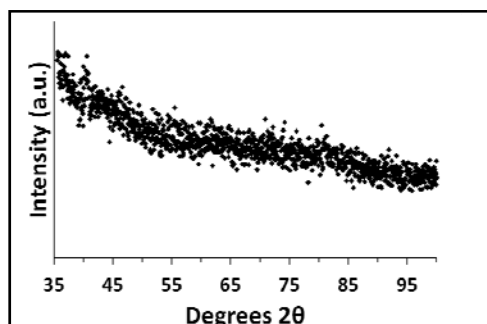


Figure 81: High angle XRD results for sample 1.76% Pd/MCM-41.

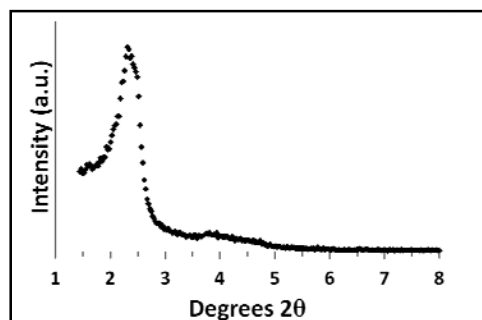


Figure 82: Low angle XRD results for sample 2.30% Pd/MCM-41

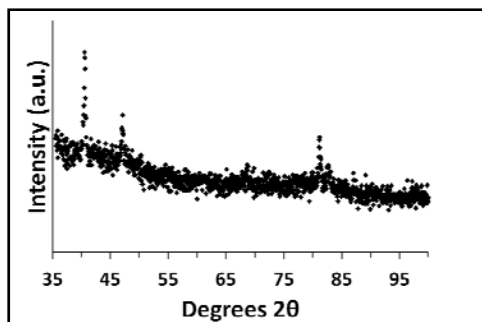


Figure 83: High angle XRD results for sample 2.30% Pd/MCM-41.

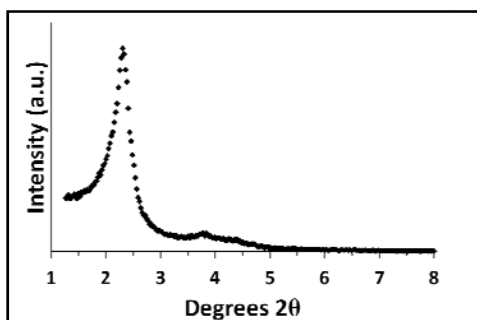


Figure 84: Low angle XRD results for sample 0.14% Ni/MCM-41.

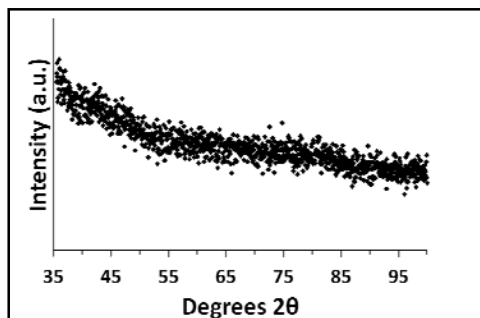


Figure 85: High angle XRD results for sample 0.14% Ni/MCM-41.

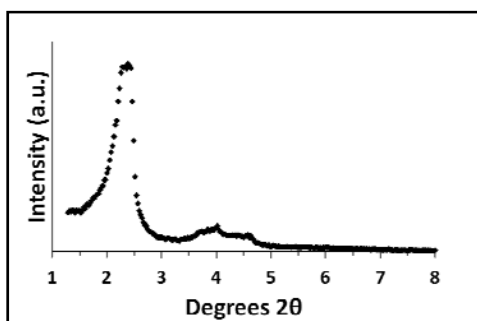


Figure 86: Low angle XRD results for sample 1.02% Ni/MCM-41.

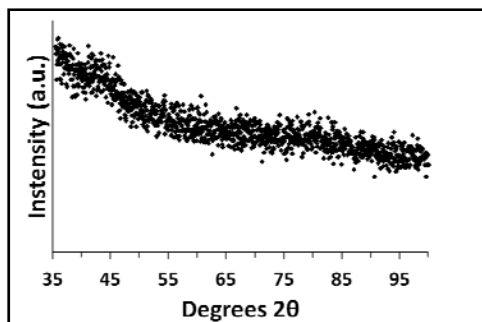


Figure 87: High angle XRD results for sample 1.02% Ni/MCM-41.

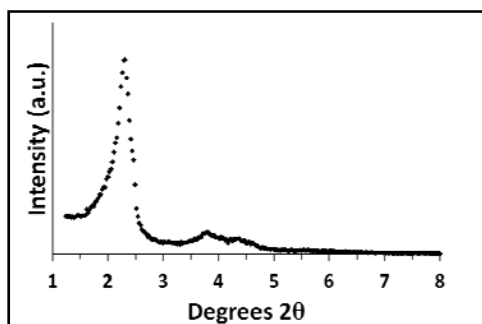


Figure 88: Low angle XRD results for sample 1.12% Ni/MCM-41 [nickel (II) chloride source].

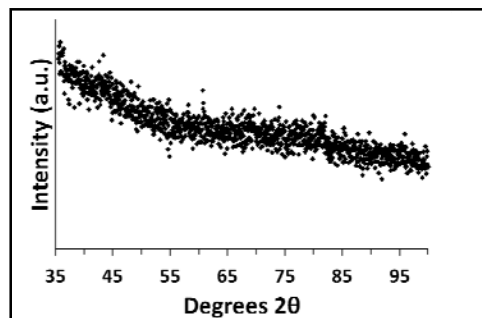


Figure 89: High angle XRD results for sample 1.12% Ni/MCM-41 [nickel (II) chloride source].

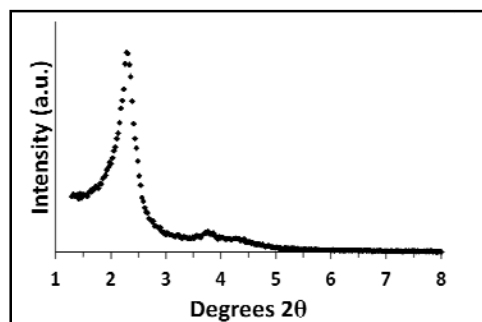


Figure 90: Low angle XRD results for sample 1.32% Ni/MCM-41.

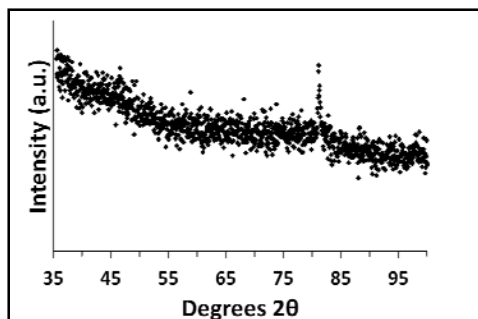


Figure 91: High angle XRD results for sample 1.32% Ni/MCM-41.

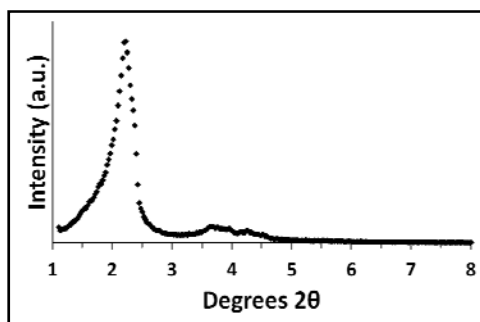


Figure 92: Low angle XRD results for sample 0.12% Ni/MCM-41 (nickel carbonate source).

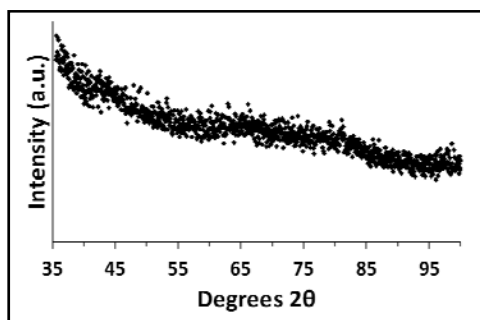


Figure 93: High angle XRD results for sample 0.12% Ni/MCM-41 (nickel carbonate source).

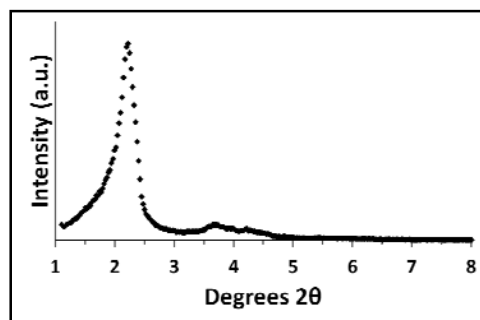


Figure 94: Low angle XRD results for sample 1.12% Ni/MCM-41 (nickel carbonate source).

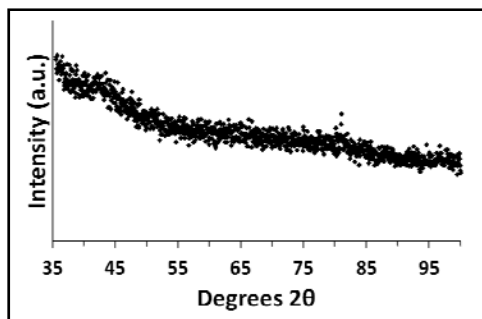


Figure 95: High angle XRD results for sample 1.12% Ni/MCM-41 (nickel carbonate source).

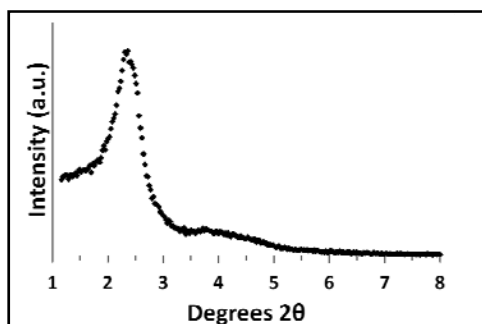


Figure 96: Low angle XRD results for sample 0.13% Ni-Pd/MCM-41.

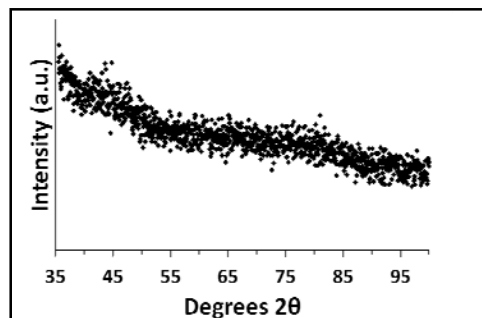


Figure 97: High angle XRD results for sample 0.13% Ni-Pd/MCM-41.

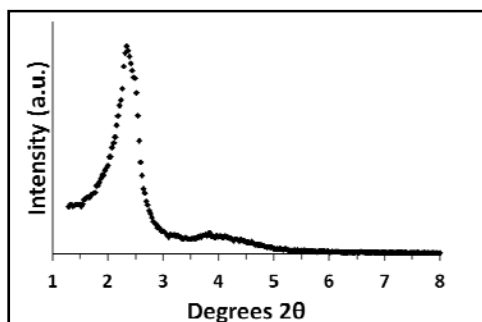


Figure 98: Low angle XRD results for sample 1.01% Ni-Pd/MCM-41.

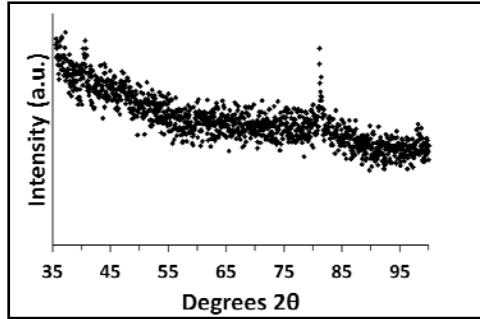


Figure 99: High angle XRD results for sample 1.01% Ni-Pd/MCM-41.

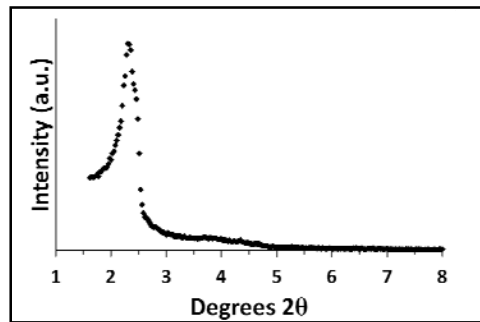


Figure 100: Low angle XRD results for sample 1.22% Ni-Pd/MCM-41.

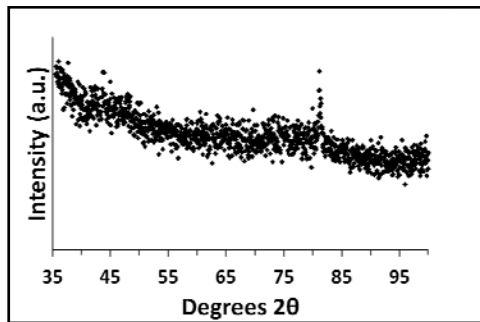


Figure 101: High angle XRD results for sample 1.22% Ni-Pd/MCM-41.

**BET Nitrogen Adsorption Surface Area Results for Calcined MCM-41 and Metal Impregnated Samples**

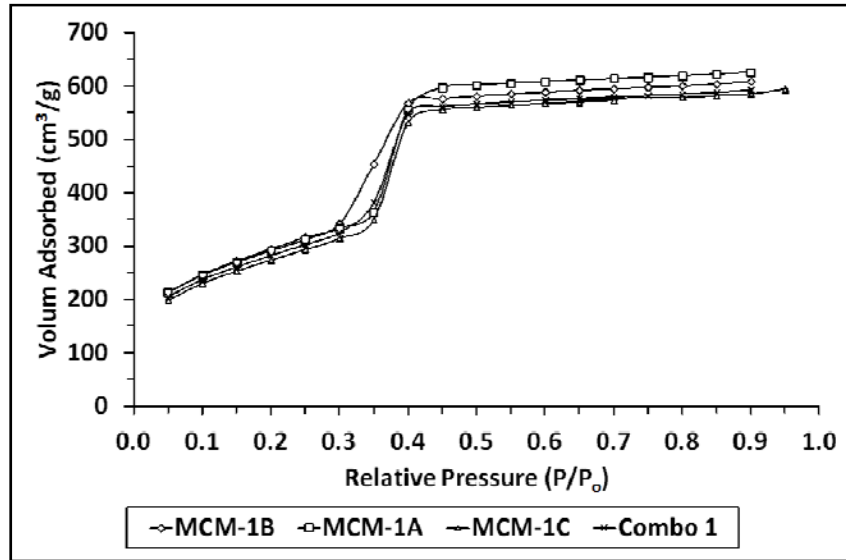


Figure 102: Full adsorption isotherms for 'Combo 1' MCM-41 material and its three constituent batches.

**Table 1: Isotherm data for 'Combo 1' MCM-41 and its three constituent batches.**

MCM-1A		MCM-1B		MCM-1C		Combo 1	
P/P <sub>0</sub>	cc/g						
0.0500	212.780	0.0500	213.527	0.0499	199.334	0.0499	205.743
0.1000	245.310	0.1000	247.245	0.1000	230.568	0.1000	237.870
0.1501	269.471	0.1500	272.451	0.1500	253.748	0.1500	261.724
0.2000	290.814	0.2001	294.886	0.2000	274.136	0.2001	282.806
0.2501	311.548	0.2501	316.998	0.2500	293.828	0.2501	303.339
0.3001	333.524	0.3000	342.094	0.3000	314.764	0.3000	325.866
0.3500	363.816	0.3500	453.749	0.3499	349.092	0.3500	381.918
0.4000	555.356	0.3999	567.601	0.3999	531.269	0.3999	547.878
0.4499	596.763	0.4499	575.919	0.4499	555.148	0.4499	561.825
0.5000	601.292	0.4999	580.871	0.4999	560.111	0.4999	566.461
0.5500	604.801	0.5500	585.055	0.5499	563.912	0.5500	570.255
0.6000	607.951	0.6001	588.690	0.6000	567.146	0.6000	573.572
0.6500	610.822	0.6499	591.826	0.6499	570.136	0.6500	576.448
0.7000	613.508	0.7000	594.714	0.7000	572.998	0.7000	579.248
0.7499	616.064	0.7499	597.447	0.6499	575.626	0.7500	582.021
0.7999	618.700	0.7999	600.183	0.8002	578.384	0.7999	584.813
0.8499	621.570	0.8499	603.359	0.8498	581.444	0.8499	588.023
				0.8998	585.330		
				0.9498	594.175		

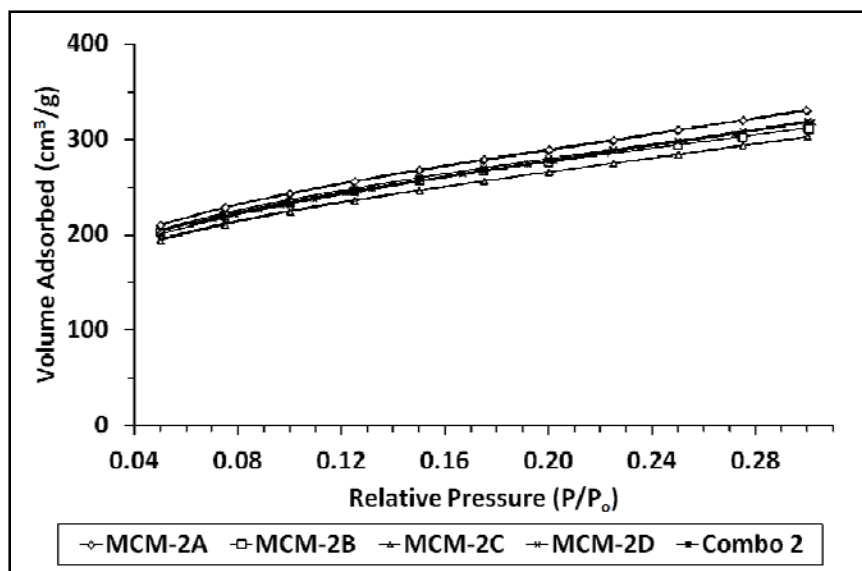


Figure 103: BET adsorption isotherms for 'Combo 2' MCM-41 and its four constituent batches.

Table 2: Isotherm data for 'Combo 2' MCM-41 and its four constituent batches.

MCM-2A		MCM-2B		MCM-2C		MCM-2D		Combo 2	
P/P <sub>0</sub>	cc/g								
0.0498	209.78	0.0498	203.0442	0.04981	195.2904	0.04982	204.8437	0.06171	211.2277
0.07483	228.02860	0.07482	220.38260	0.07481	211.72410	0.07483	222.42060	0.07035	217.08198
0.09979	242.72020	0.09987	234.32750	0.09985	225.09420	0.09983	236.48450	0.07884	222.37712
0.12478	255.49070	0.12478	246.30680	0.12483	236.43510	0.12479	248.60510	0.08777	227.56093
0.14985	267.10300	0.14985	256.99930	0.14980	246.80170	0.14985	259.71050	0.09653	232.27658
0.17476	277.85900	0.17484	266.95540	0.17483	256.54760	0.17476	269.95000	0.10902	238.74099
0.19981	288.23620	0.19978	276.34180	0.19976	265.83290	0.19981	279.89080	0.12160	244.87859
0.22472	298.37750	0.24982	294.35280	0.22478	275.05840	0.22477	289.51390	0.12662	247.27494
0.24984	309.44630	0.27476	303.19510	0.24978	284.15040	0.24974	299.06850	0.13165	249.59805
0.27477	319.60400	0.29995	312.32580	0.27476	293.42270	0.27480	309.01570	0.14934	257.11056
0.29976	330.05800	0.30041	310.71280	0.29979	302.90880	0.29972	319.49220	0.16671	264.65309
0.29943	331.29310	0.27506	298.28450	0.29992	303.48300	0.30003	319.88500	0.17417	267.55142
0.27505	320.43280	0.24996	285.53630	0.27500	294.13060	0.27506	308.59240	0.18300	271.12176
0.25001	310.35750	0.22505	274.50440	0.25003	284.67140	0.25000	297.66730	0.19177	274.89034
0.22501	299.89240	0.20001	263.52360	0.22504	275.31240	0.22503	289.29050	0.20178	278.89277
0.20007	289.64140	0.17952	253.47020	0.20020	265.94010	0.20007	276.97600	0.22172	286.54326
0.17502	279.14890	0.12340	251.29310	0.17504	256.40770	0.17500	266.63660	0.24174	294.40432
0.15011	268.25570	0.12494	251.29470	0.15006	246.42150	0.15008	255.92990	0.27166	306.16432
0.12504	256.51160	0.10008	236.60070	0.12506	235.71460	0.12503	244.56280	0.30189	318.90566
0.10006	243.70270	0.07507	222.39330	0.10009	224.16670	0.10007	231.98130		
0.07510	228.91780	0.05007	204.70920	0.07508	210.52960	0.07510	217.92360		
0.05007	210.64180			0.05007	193.92910	0.05007	200.28450		

**Table 3: Data for full adsorption-desorption isotherm, Combo 2.**

Adsorption		Desorption	
P/P <sub>0</sub>	cc/g	P/P <sub>0</sub>	cc/g
0.0504	343.849	0.9439	1040.650
0.1007	394.443	0.8984	1027.900
0.1515	431.333	0.8484	1018.510
0.2004	465.512	0.7983	1010.300
0.2514	497.356	0.7485	1000.500
0.3009	529.232	0.6930	1003.620
0.3498	579.034	0.6478	996.121
0.3997	826.463	0.5981	987.510
0.4523	920.335	0.5480	978.653
0.5026	938.648	0.4983	969.304
0.5502	945.168	0.4378	982.263
0.5998	951.926	0.3982	905.122
0.6500	957.734	0.3501	642.987
0.7006	962.590	0.3008	586.423
0.7507	966.547	0.2471	550.777
0.7999	971.636	0.1982	515.334
0.8500	991.481	0.1482	478.073
0.9027	1000.040	0.0984	436.277
0.9516	1012.320	0.0494	381.379
0.9946	1341.350		

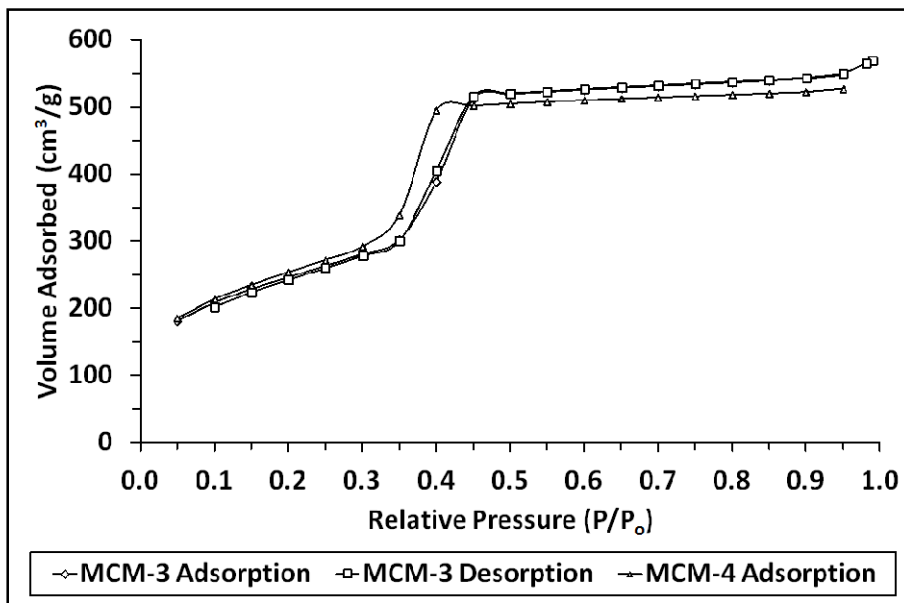


Figure 104: Adsorption isotherms for individual MCM-41 synthesis batches (MCM-3 and MCM-4).

**Table 4: Isotherm data for individual MCM-41 synthesis batches MCM-3 and MCM-4.**

MCM-3				MCM-4	
Adsorption		Desorption		P/P <sub>0</sub>	cc/g
P/P <sub>0</sub>	cc/g	P/P <sub>0</sub>	cc/g		
0.0500	180.967	0.9898	568.808	0.0500	185.228
0.1000	208.250	0.9811	564.609	0.1000	213.636
0.1500	228.372	0.9501	549.968	0.1500	234.818
0.2001	246.026	0.9001	543.341	0.2000	253.648
0.2501	262.968	0.8501	539.641	0.2500	272.085
0.3000	280.502	0.8001	536.723	0.3001	291.973
0.3500	301.746	0.7502	534.128	0.3500	338.549
0.4000	388.439	0.7003	531.464	0.4000	494.850
0.4500	511.813	0.6503	528.751	0.4500	501.665
0.4999	518.618	0.6003	525.921	0.5000	504.798
0.5499	522.248	0.5502	522.772	0.5500	507.538
0.6000	525.367	0.5002	519.280	0.5999	509.949
0.6500	528.238	0.4502	515.060	0.6499	512.124
0.7000	530.871	0.4002	405.150	0.6999	514.099
0.7500	533.431	0.3502	300.097	0.7499	516.020
0.7999	536.006	0.3003	278.365	0.7999	517.926
0.8499	538.882	0.2503	260.168	0.8499	519.857
0.8999	542.301	0.2004	242.679	0.8998	522.206
0.9499	547.553	0.1503	224.401	0.9498	527.018
		0.1002	202.430		

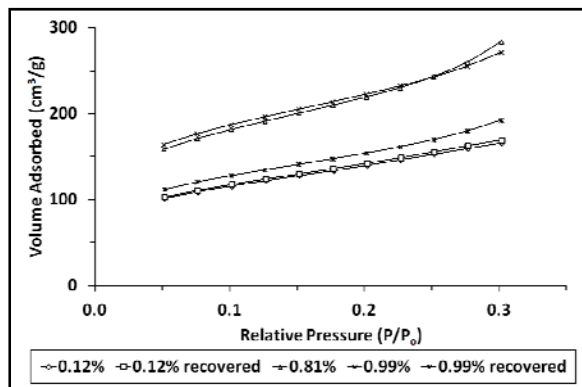


Figure 105: BET adsorption isotherm for Pd/MCM-41 samples (1 of 2).

**Table 5: BET isotherm data for Pd/MCM-41 samples (1 of 2).**

0.12%		0.12% Recovered in dissolution experiment		0.81%		0.99%		0.99% Recovered in column experiment	
P/Po	cc/g	P/Po	cc/g	P/Po	cc/g	P/Po	cc/g	P/Po	cc/g
0.0515	101.3627	0.0516	103.0577	0.0511	158.8028	0.0510	164.1568	0.0516	112.1753
0.0764	109.2515	0.0763	111.0325	0.0759	171.3116	0.0758	176.7564	0.0758	120.8526
0.1015	115.9764	0.1015	117.9512	0.1010	181.8228	0.1009	187.2622	0.1010	128.2780
0.1266	122.0751	0.1266	124.1139	0.1261	191.5142	0.1260	196.4553	0.1261	134.9163
0.1516	128.0014	0.1516	130.1657	0.1512	200.6187	0.1511	205.2857	0.1512	141.2738
0.1770	133.9457	0.1769	136.2722	0.1763	209.9700	0.1761	213.9411	0.1762	147.6597
0.2019	139.9978	0.2018	142.6470	0.2013	219.5484	0.2013	222.9622	0.2013	154.3147
0.2268	146.5267	0.2269	148.9786	0.2263	230.1947	0.2262	232.2974	0.2263	161.6161
0.2517	152.9983	0.2518	155.9587	0.2512	243.2459	0.2511	242.8130	0.2513	169.9437
0.2767	159.7996	0.2767	162.8057	0.2764	260.0161	0.2761	255.2971	0.2762	179.9059
0.3019	166.2703	0.3019	169.5597	0.3015	283.7074	0.3014	271.6431	0.3014	192.5767

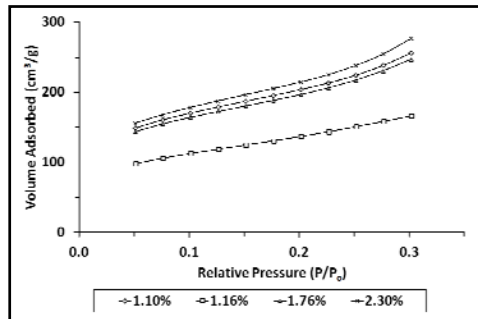


Figure 106: BET adsorption isotherms for Pd/MCM-41 samples (2 of 2).

**Table 6: BET isotherm data for Pd/MCM-41 samples (2 of 2).**

1.10%		1.16%		1.76%		2.30%	
P/Po	cc/g	P/Po	cc/g	P/Po	cc/g	P/Po	cc/g
0.0510	148.9710	0.0515	98.2430	0.0509	143.5423	0.0509	155.5225
0.0758	160.7547	0.0763	106.0403	0.0758	154.8214	0.0757	167.7375
0.1009	170.3043	0.1015	112.7027	0.1009	164.0491	0.1008	178.0081
0.1262	179.0345	0.1266	118.8192	0.1261	172.3382	0.1259	187.4669
0.1511	187.2394	0.1516	124.7160	0.1511	180.2188	0.1510	196.4677
0.1761	195.3771	0.1767	130.7065	0.1762	188.2344	0.1762	205.1874
0.2012	203.9668	0.2017	136.9742	0.2013	196.5127	0.2011	214.5060
0.2262	213.2814	0.2268	143.5280	0.2262	206.0442	0.2262	224.9623
0.2511	224.3149	0.2516	150.8134	0.2511	217.0419	0.2511	238.1817
0.2762	238.4260	0.2767	158.2916	0.2761	230.4172	0.2761	254.7232
0.3014	256.1635	0.3018	165.8888	0.3015	246.6831	0.3014	276.7791

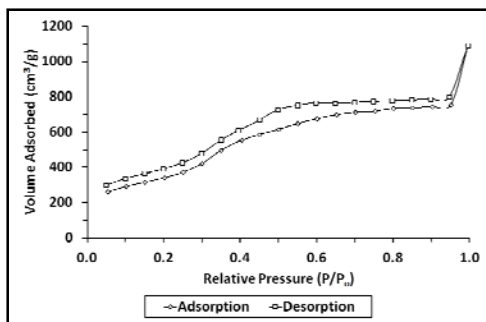


Figure 107: Full adsorption-desorption isotherm for 1.10% Pd/MCM-41 sample.

**Table 7: Full adsorption-desorption isotherm data for 1.10% Pd/MCM-41.**

Adsorption		Desorption	
P/P <sub>0</sub>	cc/g	P/P <sub>0</sub>	cc/g
0.0537	262.0352	0.9955	1091.4381
0.1021	293.8362	0.9453	797.7943
0.1499	317.5000	0.8980	787.1971
0.2019	342.7943	0.8479	781.8829
0.2508	373.0733	0.7974	777.7829
0.2997	421.2133	0.7480	773.5419
0.3497	496.5886	0.6982	768.0781
0.4036	554.7238	0.6482	762.2009
0.4497	586.4343	0.5973	765.7515
0.5000	615.6733	0.5498	750.8895
0.5494	649.4086	0.4991	726.2581
0.6004	674.5771	0.4505	669.3905
0.6518	697.2238	0.3947	609.4800
0.7006	711.6896	0.3505	556.0581
0.7526	718.3124	0.2979	478.5324
0.7998	733.8171	0.2488	425.7953
0.8496	736.8410	0.1984	391.0286
0.9024	742.9838	0.1496	365.7486
0.9503	754.1686	0.1003	338.9248
0.9955	1091.4381	0.0484	300.4743

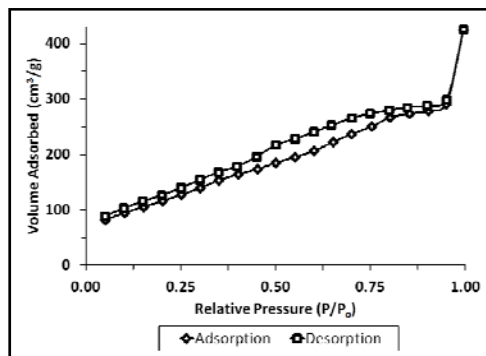


Figure 108: Full BET adsorption-desorption isotherms for 1.16% Pd/MCM-41.

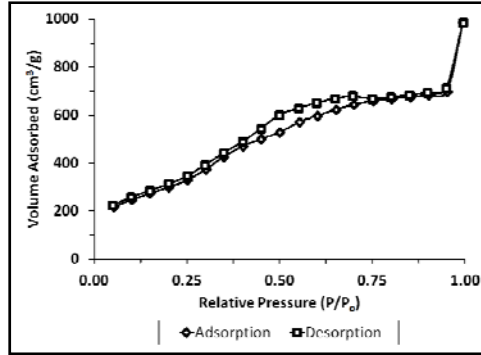


Figure 109: Full BET adsorption and desorption isotherm for 1.76% Pd/MCM-41.

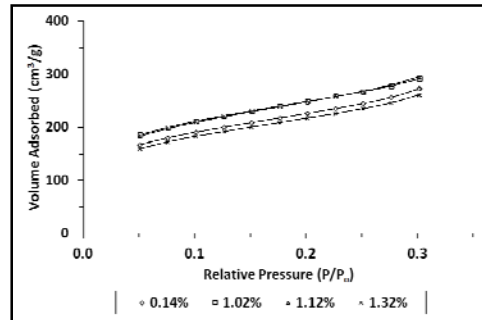


Figure 110: BET adsorption isotherms for Ni/MCM-41 samples [nickel (II) chloride source].

**Table 8: BET isotherm data for Ni/MCM-41 samples [nickel (II) chloride source].**

0.14%		1.02%		1.12%		1.32%	
P/P <sub>0</sub>	cc/g						
0.0508	167.2559	0.0512	185.5830	0.0508	182.9807	0.0508	160.2722
0.0756	179.9582	0.0760	199.8110	0.0756	197.2096	0.0756	172.7024
0.1010	190.6202	0.1012	211.4490	0.1008	209.0812	0.1007	182.9746
0.1261	200.0192	0.1264	221.7292	0.1259	219.5274	0.1263	191.9292
0.1509	208.8074	0.1514	231.2485	0.1509	229.3151	0.1509	200.5736
0.1761	217.5672	0.1763	240.3696	0.1761	238.5887	0.1760	208.9136
0.2011	226.4037	0.2015	249.3388	0.2010	248.1544	0.2010	217.4220
0.2262	235.5315	0.2264	258.3236	0.2260	257.8029	0.2260	226.0209
0.2510	245.2883	0.2513	267.9683	0.2509	267.7020	0.2509	235.4688
0.2761	256.8931	0.2763	278.2854	0.2761	279.4140	0.2760	246.3724
0.3012	272.8421	0.3015	291.2949	0.3012	294.1333	0.3013	261.5686

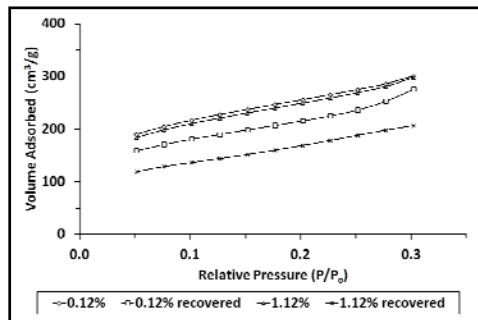


Figure 111: BET adsorption isotherms for Ni/MCM-41 samples (nickel carbonate source).

**Table 9: BET isotherm data for Ni/MCM-41 samples (nickel carbonate source).**

0.12%		0.12% Recovered in dissolution experiment		1.12%		1.12% Recovered in dissolution experiment	
P/Po	cc/g	P/Po	cc/g	P/Po	cc/g	P/Po	cc/g
0.0514	189.9715	0.0515	158.7882	0.0513	184.0451	0.0518	119.2395
0.0763	204.6370	0.0764	171.1111	0.0762	198.5236	0.0764	128.8788
0.1014	216.7549	0.1015	181.2539	0.1013	210.4767	0.1015	136.5152
0.1265	227.4386	0.1268	190.3767	0.1265	220.9332	0.1266	144.0739
0.1517	237.2738	0.1517	198.8914	0.1514	230.6972	0.1517	151.8509
0.1766	246.7468	0.1768	207.4435	0.1765	240.1831	0.1767	160.0590
0.2019	256.0342	0.2018	216.0166	0.2015	249.6086	0.2018	168.9372
0.2268	265.4136	0.2268	225.2958	0.2267	259.2341	0.2268	178.5222
0.2515	275.1719	0.2517	236.6869	0.2514	269.4581	0.2516	188.3777
0.2766	285.7852	0.2767	253.1442	0.2765	281.0777	0.2767	198.0164
0.3017	299.9886	0.3019	275.8284	0.3017	297.4308	0.3019	206.8494

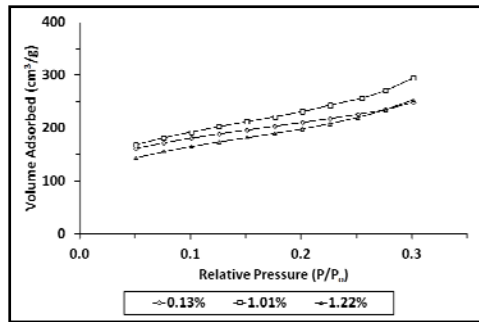


Figure 112: BET adsorption isotherm for Ni-Pd/MCM-41 samples.

**Table 10: BET isotherm data for Ni-Pd/MCM-41 samples.**

0.13%		1.01%		1.22%	
P/Po	cc/g	P/Po	cc/g	P/Po	cc/g
0.0509	160.9695	0.0509	168.0576	0.0507	144.0609
0.0757	172.0040	0.0757	181.4541	0.0756	155.4963
0.1009	181.0132	0.1009	192.5097	0.1007	165.2356
0.1260	189.1016	0.1260	202.6792	0.1258	173.8737
0.1511	196.4901	0.1510	212.2108	0.1510	181.9610
0.1760	203.8260	0.1764	221.6174	0.1759	190.1084
0.2012	210.9572	0.2012	231.5174	0.2010	198.6206
0.2261	218.3190	0.2263	242.8600	0.2260	208.5453
0.2511	226.3183	0.2547	256.3888	0.2509	220.1810
0.2760	235.4604	0.2761	270.9079	0.2761	234.7117
0.3013	248.0091	0.3013	294.7151	0.3011	252.1873

**Table 11: BET adsorption isotherm results for Pd impregnated sand samples.**

0.99%		1.01%					
		with fill rod		with glass beads		with fill rod + glass beads	
P/P <sub>0</sub>	cc/g	P/P <sub>0</sub>	cc/g	P/P <sub>0</sub>	cc/g	P/P <sub>0</sub>	cc/g
0.0510	0.0236	0.0510	0.0268	0.0510	0.0012	0.0509	0.0013
0.0764	0.0263	0.0757	0.0246	0.0757	0.0011	0.0757	0.0009
0.1015	0.0300	0.1011	0.0239	0.1011	0.0011	0.1010	0.0009
0.1267	0.0324	0.1262	0.0247	0.1262	0.0011	0.1260	0.0008
0.1514	0.0341	0.1515	0.0267	0.1515	0.0012	0.1511	0.0007
0.1768	0.0367	0.1763	0.0303	0.1763	0.0014	0.1763	0.0007
0.2018	0.0398	0.2014	0.0307	0.2014	0.0014	0.2015	0.0008
0.2268	0.0410	0.2266	0.0320	0.2266	0.0014	0.2264	0.0011
0.2518	0.0433	0.2511	0.0310	0.2511	0.0014	0.2512	0.0013
0.2768	0.0447	0.2766	0.0285	0.2766	0.0013	0.2762	0.0012
0.3022	0.0458	0.3015	0.0283	0.3015	0.0013	0.3015	0.0012

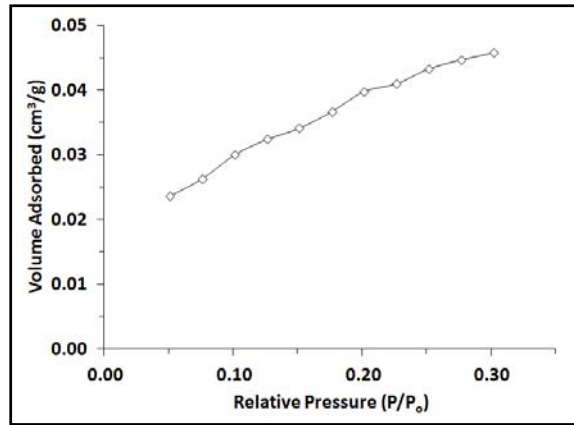


Figure 113: BET adsorption isotherm for 0.99% Pd/sand sample.

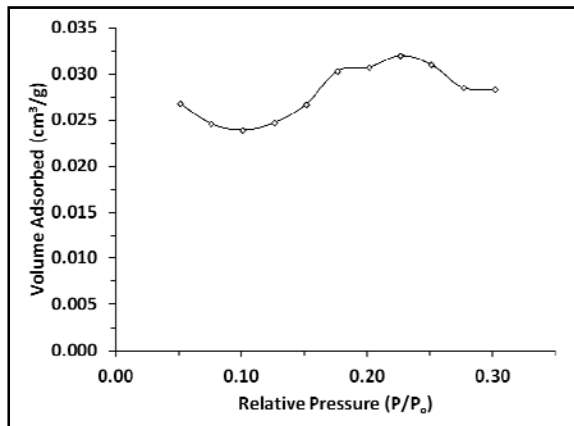


Figure 114: BET adsorption isotherm for 1.01% Pd/sand sample analyzed with filler rod.

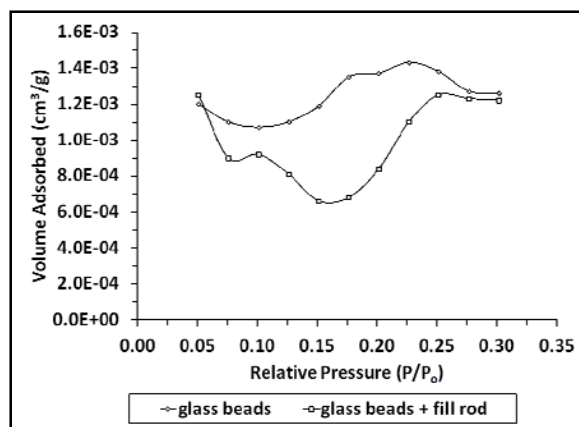


Figure 115: BET adsorption isotherm for 1.01% Pd/sand sample analyzed with glass beads as well as glass beads with a filler rod.

### SEM and TEM Images of Pd/MCM-41 Samples

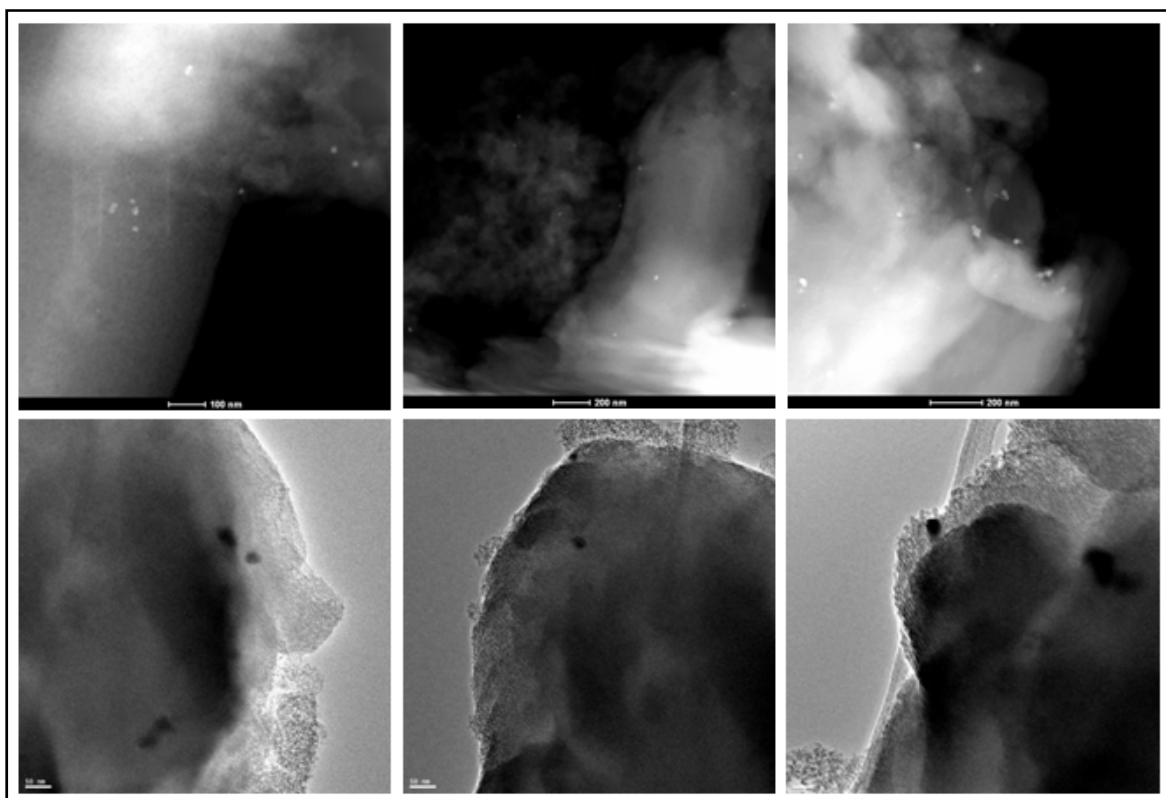


Figure 116: SEM images (top row) and TEM images (bottom row) of 0.12% Pd/MCM-41.

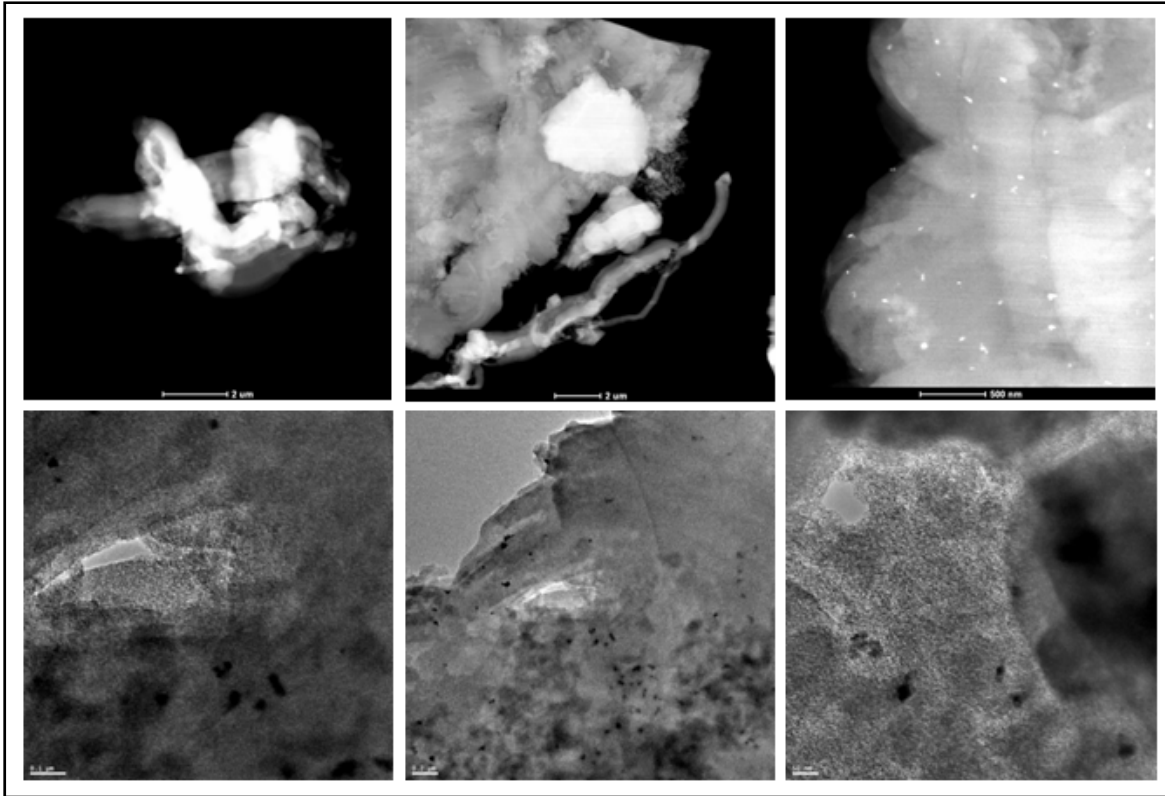


Figure 117: SEM (top row) and TEM (bottom row) images of 1.16% Pd/MCM-41.

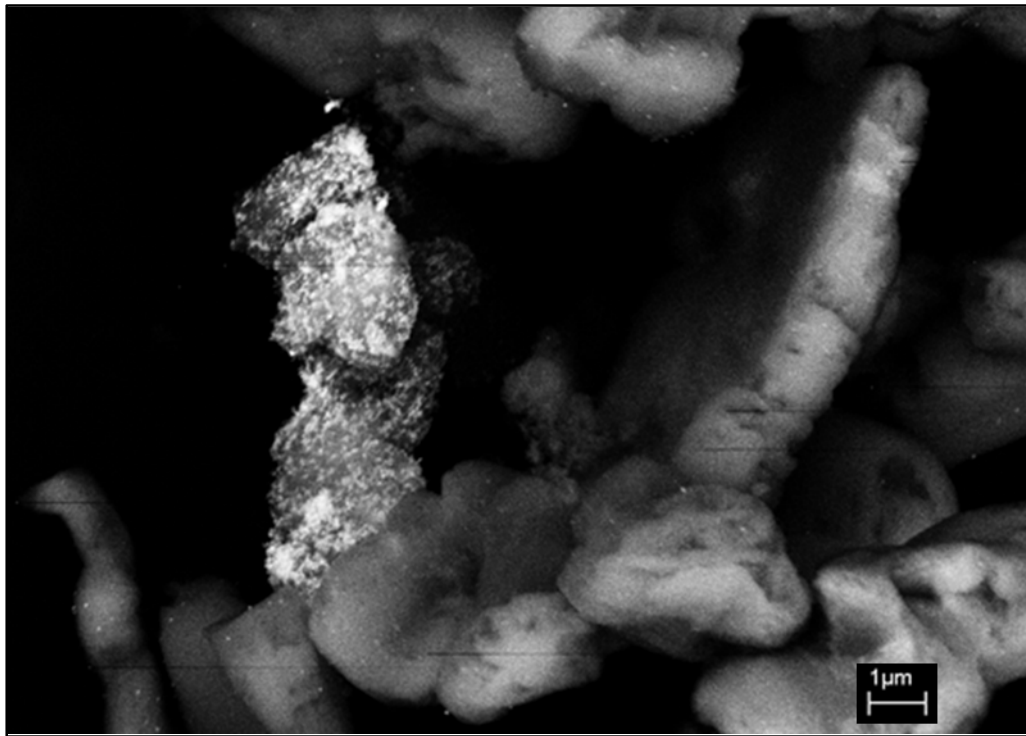


Figure 118: SEM Image of 1.01% Pd/MCM-41 sample.

## EDAX Analysis for Pd Concentration in Pd/MCM-41 Samples

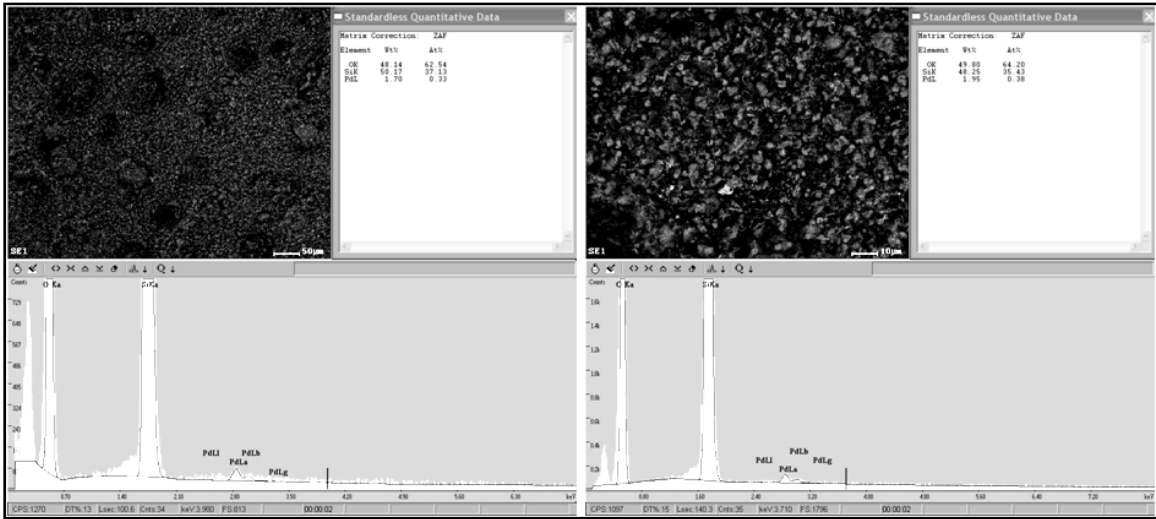


Figure 119: EDAX analysis results for sample 1.10% Pd/MCM-41 at two magnifications.

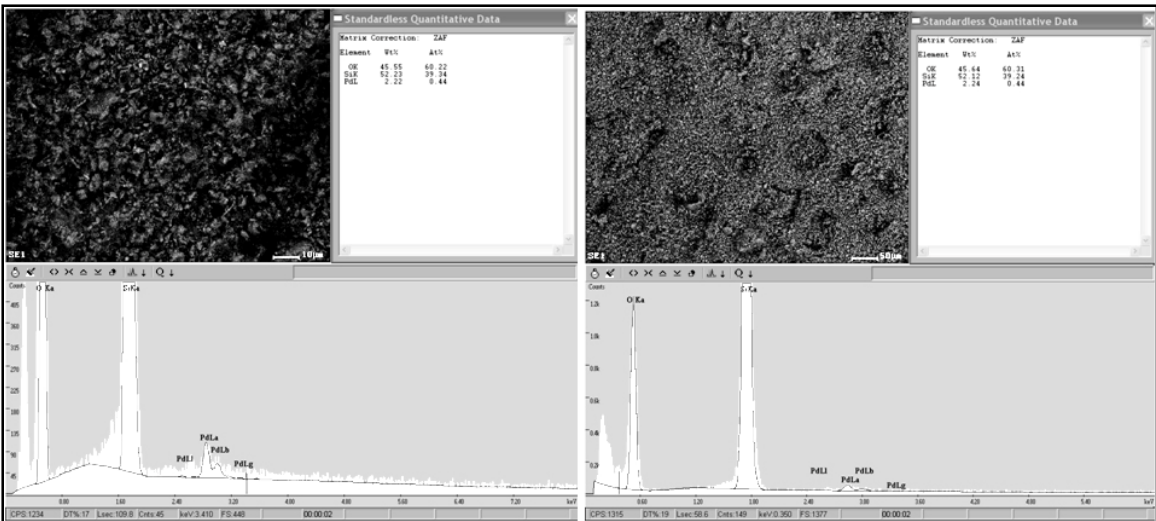


Figure 120: EDAX analysis results for sample 1.16% Pd/MCM-41 at two magnifications

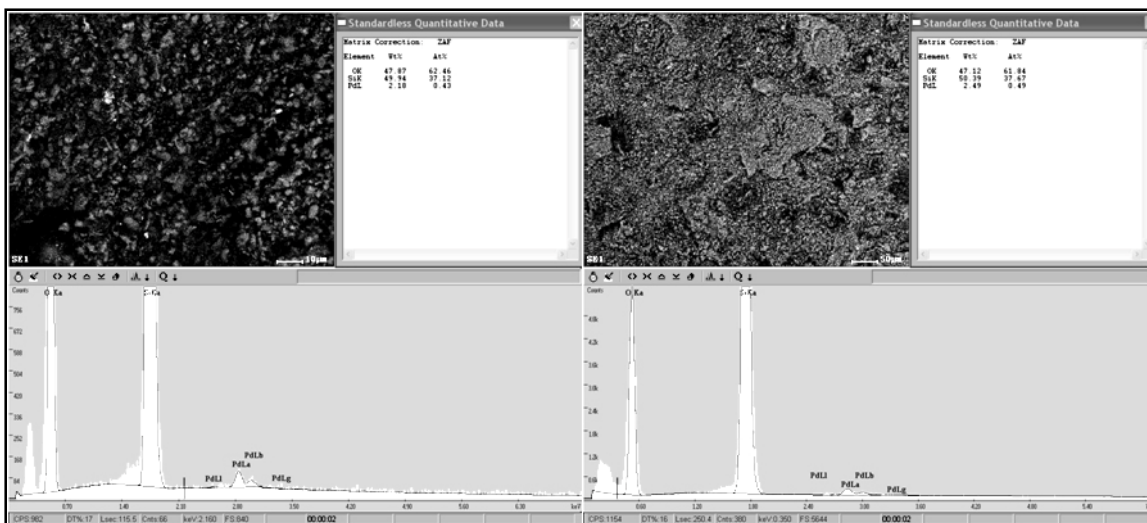


Figure 121: EDAX analysis results for sample 1.76% at two magnifications.

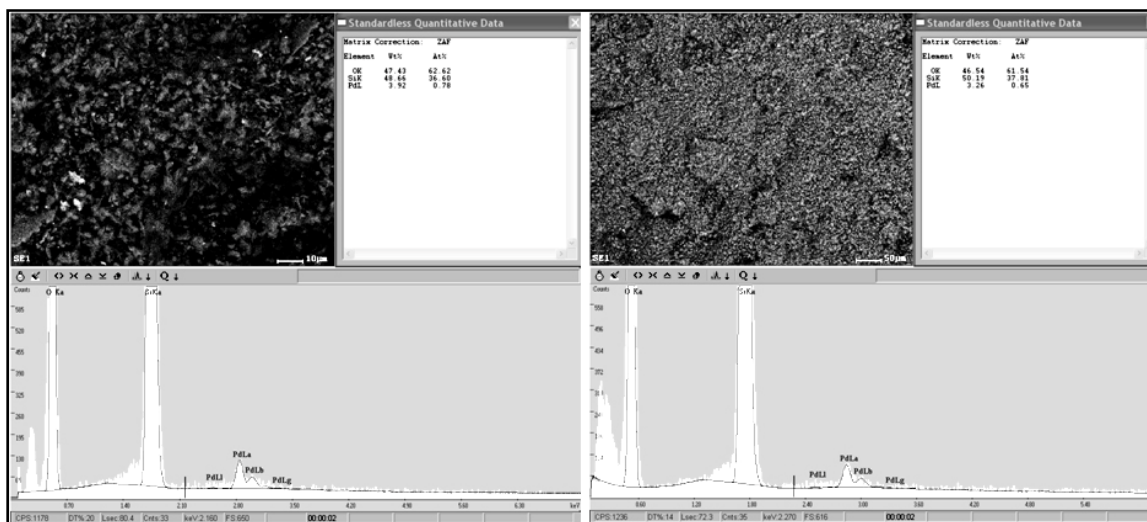


Figure 122: EDAX analysis results for sample 2.30% Pd/MCM-41 at two magnifications.

## APPENDIX B

### Procedures and detailed data not included in Chapter 3.

---

#### Molybdate Method for Spectrophotometric Analysis of $SiO_2$ Concentration

Concentration of  $SiO_2$  in samples was determined using a spectrophotometer and following a method described in Eaton *et al.* (1995). The spectrophotometer was switched on at least 30 min before use to allow the lamp time to warm up.

An ammonium molybdate solution was prepared by dissolving 10 g of  $(NH_4)_6Mo_7O_{24} \cdot 4H_2O$  in deionized water with stirring and gentle warming and diluted to 100 ml. Solution pH was adjusted to 7-8 using granular  $NaOH$ . An  $HCl$  solution was prepared by diluting concentrated  $HCl$  in equal parts deionized water (1:1 solution).

Samples were prepared by adding ammonium molybdate solution and  $HCl$  in the ratio: 100 : 2 : 4 = sample :  $HCl$  : ammonium molybdate (by volume). Sample bottles were capped, shaken, and allowed to react for 5 to 10 min. Sample solution was then transferred to a cuvette and analyzed using a spectrophotometer. Absorbance values were recorded and converted to concentrations using a 5 point calibration curve prepared using a standard solution of  $SiO_2$ . Samples were analyzed diluted or undiluted depending on expected  $SiO_2$  concentrations. Resulting concentrations were then multiplied by the appropriate dilution factor to obtain real concentrations.

## Contents of reaction bottles

**Table 12: Contents of reaction bottles for 0.12% and 1.16% Pd/MCM-41.**

0.12% and 1.16% Pd/MCM-41					
Material	Sample ID	MCM-41 (g)	Pd (g)	Water (g)	Liquid/Solid
1.16	111	0.9018	1.05E-02	90.0160	100
	112	0.9014	1.05E-02	90.0422	100
	121	0.4530	5.25E-03	90.0130	199
	122	0.4507	5.23E-03	90.0409	200
0.12	211	0.9027	1.08E-03	90.1040	100
	212	0.9055	1.09E-03	90.0977	100
	221	0.4511	5.41E-04	90.3813	200
	222	0.4547	5.46E-04	90.0786	198
-	blank	-	-	-	-
-	blank	-	-	-	-

**Table 13: pH results for dissolution experiment using 0.12% and 1.16% Pd/MCM-41.**

Materials		Sample 1 1.8 days		Sample 2 2.2 days		Sample 3 7.7 days		Sample 4 18 days		Sample 5 33 days		Sample 6 50 days	
% Pd	ID	pH	±	pH	±	pH	±	pH	±	pH	±	pH	±
-	blank	7.34	-	4.58	-	-	-	-	-	-	-	-	-
	blank	6.26	-	5.24	-	-	-	-	-	-	-	-	-
1.16	111	3.65	-	3.68	0.10	3.67	-	3.43	-	3.38	-	-	-
	112	3.66	-	3.62	-	3.45	-	3.42	-	3.48	-	-	-
	121	3.93	-	4.19	-	3.67	-	3.66	-	3.72	-	-	-
	122	4.08	-	3.94	-	3.69	-	3.70	-	3.81	-	-	-
0.12	211	4.95	-	4.69	-	4.58	-	-	-	3.62	-	-	-
	212	4.79	-	4.74	-	4.53	0.08	4.57	-	4.42	-	-	-
	221	4.80	-	4.73	-	4.68	-	4.98	-	4.73	-	-	-
	222	5.02	-	5.98	-	4.67	-	6.55	0.25	4.87	0.19	-	-

**Table 14: Contents of reaction bottles for 0.12% and 1.12% Ni/MCM-41 prepared using nickel carbonate.**

0.12% and 1.12% Ni/MCM-41 (nickel carbonate source)					
Material	Sample ID	MCM-41 (g)	Ni (g)	Water (g)	Liquid/Solid
0.12	111	0.2047	2.46E-04	20.5591	100
	112	0.2051	2.46E-04	20.5684	100
	121	0.1008	1.21E-04	20.2125	201
	122	0.1011	1.21E-04	20.2528	200
1.12	211	0.2023	2.27E-03	20.2702	100
	212	0.2108	2.36E-03	21.0796	100
	221	0.1066	1.19E-03	21.8317	205
	222	0.1041	1.17E-03	20.8856	201
-	blank	-	-	-	-
-	blank	-	-	-	-
0.12	511	0.1057	1.27E-04	10.6368	101
	512	0.1018	1.22E-04	10.2460	101
	521	0.0559	6.71E-05	11.2382	201
	522	0.0508	6.10E-05	10.2667	202
1.12	611	0.1058	1.18E-03	10.6106	100
	612	0.1079	1.21E-03	10.7927	100
	621	0.0533	5.97E-04	10.7540	202
	622	0.0515	5.77E-04	10.5016	204
-	blank	-	-	-	-
-	blank	-	-	-	-

**Table 15: pH results for dissolution experiment using 0.12% and 1.12% Ni/MCM-41.**

Materials		Sample 1 1 days		Sample 2 4 days		Sample 3 11 days		Sample 4 21 days		Sample 5 40 days	
% Ni	ID	pH	±	pH	±	pH	±	pH	±	pH	±
-	blank	-	-	-	-	-	-	-	-	4.89	-
-	blank	-	-	-	-	-	-	-	-	5.58	-
1.12	411	-	-	6.19	-	6.59	-	6.57	0.08	6.61	-
	412	-	-	6.11	-	6.29	-	6.68	-	6.62	-
	421	-	-	6.18	-	6.45	0.10	6.39	-	6.70	0.09
	422	-	-	6.30	-	6.23	-	6.47	-	6.63	-
0.12	311	-	-	5.66	-	6.58	-	5.79	-	6.25	-
	312	-	-	5.40	-	5.84	-	6.03	-	6.17	-
	321	-	-	5.74	-	-	-	6.09	-	6.28	-
	322	-	-	6.41	-	5.86	-	5.89	-	6.23	-

**Table 16: Contents of reaction bottles for a second experiment using 0.12% and 1.12% Ni/MCM-41 prepared using a nickel carbonate source.**

<b>0.12% and 1.12% Ni/MCM-41 (nickel carbonate source)</b>					
<b>Material</b>	<b>Sample ID</b>	<b>MCM-41 (g)</b>	<b>Ni (g)</b>	<b>Water (g)</b>	<b>Liquid/Solid</b>
0.12	311	0.9033	1.08E-03	90.1874	100
	312	0.9017	1.08E-03	90.1722	100
	321	0.4517	5.42E-04	90.3639	200
	322	0.4502	5.40E-04	90.0156	200
1.12	411	0.9003	1.01E-02	90.0257	100
	412	0.8965	1.00E-02	90.2600	101
	421	0.4517	5.06E-03	90.3800	200
	422	0.4522	5.06E-03	90.4950	200

**Table 17: Contents of reaction bottles for 0.14% and 1.32% Ni/MCM-41 prepared using nickel (II) chloride.**

<b>0.14% and 1.32% Ni/MCM-41 (nickel (II) chloride source)</b>					
<b>Material</b>	<b>Sample ID</b>	<b>MCM-41 (g)</b>	<b>Ni (g)</b>	<b>Water (g)</b>	<b>Liquid/Solid</b>
0.14	911	0.1811	2.54E-04	18.1136	100
	912	0.1812	2.54E-04	18.1270	100
	921	0.0907	1.27E-04	18.1532	200
	922	0.0909	1.27E-04	18.2097	200
1.32	1011	0.1814	2.39E-03	18.2000	100
	1012	0.1800	2.38E-03	18.0368	100
	1021	0.0919	1.21E-03	18.3939	200
	1022	0.0910	1.20E-03	18.2277	200
-	blank	-	-	-	-
-	blank	-	-	-	-

**Table 18: Contents of reaction bottles for an experiment using 0.13% and 1.17% Ni/MCM-41 prepared using nickel (II) chloride.**

<b>0.13% and 1.17% Ni/MCM-41 (nickel (II) chloride source)</b>					
<b>Material</b>	<b>Sample ID</b>	<b>MCM-41 (g)</b>	<b>Ni (g)</b>	<b>Water (g)</b>	<b>Liquid/Solid</b>
0.13	711	0.8994	1.17E-03	89.9595	100
	712	0.8939	1.16E-03	89.6210	100
	721	0.4548	5.91E-04	90.9960	200
	722	0.4515	5.87E-04	90.3038	200
1.17	811	0.8962	1.05E-02	89.7677	100
	812	0.9047	1.06E-02	90.5010	100
	821	0.4545	5.32E-03	90.9019	200
	822	0.4514	5.28E-03	90.3907	200
-	blank	-	-	-	-
-	blank	-	-	-	-

**Table 19: pH results from the experiment using 0.13% and 1.17% Ni/MCM-41 prepared using nickel (II) chloride.**

Materials		Sample 1 1.9 days		Sample 2 8 days	
% Ni	ID	pH	±	pH	±
-	blank	-	-	-	-
-	blank	-	-	-	-
1.17	811	5.98	-	5.99	-
	812	6.22	-	6.20	-
	821	-	-	6.04	-
	822	6.15	0.10	-	-
0.13	711	5.94	-	5.89	0.16
	712	5.79	-	5.75	-
	721	6.20	-	5.76	-
	722	5.99	-	5.88	-

**Table 20: Contents of reaction bottles from an experiment using 1.22% Ni-Pd/MCM-41.**

1.22% Ni-Pd/MCM-41					
Material	Sample ID	MCM-41 (g)	Ni + Pd (g)	Water (g)	Liquid/Solid
1.22	1121	0.3748	4.57E-03	74.9807	200
	1122	0.3750	4.58E-03	75.0559	200
-	blank	-	-	-	-
-	blank	-	-	-	-

MCM-41			0.12% Pd/MCM-41			0.12% Ni/MCM-41			
Time (min)	C (mM)	C (mM)	Time (min)	C (mM)	C (mM)	Time (min)	C (mM)	C (mM)	+/-
0	0	0	0	0.0	0.0	0	0	0	-
66	0.6	0.6	66	0.1	0.1	66	0.34	0.33	-
184	1.2	1.2	184	0.3	0.3	184	0.73	0.71	-
327	1.5	1.5	327	0.4	0.4	327	1.0	1.0	-
535	2.1	2.1	535	0.6	0.6	535	1.5	1.5	-
1405	2.2	2.3	1405	1.1	1.1	1405	1.93	2.00	0.07

**Table 21: Contents of reaction bottles for a dissolution experiment using purely siliceous MCM-41 (Combo 2), 0.12% Pd/MCM-41, and 0.12% Ni/MCM-41 in a 0.01 M NaCl solution.**

Material	MCM-41 (g)	Metal (g)	NaCl Sol <sup>n</sup> (g)	Liquid/Solid
MCM-41	0.2429	-	48.7354	201
MCM-41	0.2463	-	49.3693	200
0.12% Pd/MCM-41	0.2564	3.08E-04	51.3348	200
0.12% Pd/MCM-41	0.2589	3.11E-04	52.559	203
0.12% Ni/MCM-41	0.2535	3.04E-04	50.746	200
0.12% Ni/MCM-41	0.2554	3.06E-04	51.1686	200
Blank 1	-	-	50	-
Blank 2	-	-	50	-

## APPENDIX C

Detailed hydrogen uptake and release data, including full isotherm data not included in Chapter 4.

---

**Table 22: Isotherm data for 1.10% Pd/MCM-41 material.**

1.10% Pd/MCM-41 - Summary (1.41E-5 moles Pd in cell)	
# plateau points	H/Pd average
4	0.76
5	0.87
5	0.59
6	0.75
5	0.72

average =	0.74
±	0.13

**Table 23: Detailed isotherm data for 1.10% Pd/MCM-41 material.**

P H <sub>2(g)</sub> Injected (kPa)	P steady state (kPa)	H/Pd	% change from previous
0.00	0.00	0.00	-
4.54	3.20	0.63	200.0
9.05	7.94	0.73	14.1
18.63	16.70	0.76	4.6
28.24	26.18	0.78	2.0
41.80	39.03	0.78	0.4
0.00	0.00	0.00	-
4.90	3.45	0.80	200.0
10.64	9.31	0.86	7.7
25.49	22.60	0.89	3.0
40.95	37.68	0.90	1.5
52.85	50.15	0.91	1.0

(Continued)

P H <sub>2(g)</sub> Injected (kPa)	P steady state (kPa)	H/Pd	% change from previous
0.00	0.00	0.00	-
6.64	5.09	0.50	200.0
11.30	10.16	0.56	10.2
22.33	20.14	0.59	6.5
32.58	30.36	0.61	1.9
41.92	39.88	0.59	2.3
53.83	51.36	0.58	2.2
0.00	0.00	0.00	-
5.42	3.95	0.70	200.0
11.27	9.92	0.76	8.3
23.72	21.28	0.75	1.5
34.63	32.24	0.77	3.0
44.98	42.73	0.76	1.4
53.36	51.48	0.75	1.1
0.00	0.00	0.00	-
3.52	2.48	0.57	200.0
7.45	6.46	0.72	23.2
18.57	16.40	0.74	3.2
30.43	27.94	0.73	2.0
41.40	39.03	0.70	3.9
51.90	49.62	0.69	1.7

**Table 24: Summary of isotherm data for 1.16% Pd/MCM-41 material.**

1.16% Pd/MCM-41 -Summary (1.41E-5 moles Pd in cell)	
# plateau points	H/Pd average
3	0.90
3	0.98
5	1.06
1	0.85
5	0.85

average =	0.93
±	0.11

**Table 25: Detailed isotherm data for 1.16% Pd/MCM-41 material.**

P H <sub>2(g)</sub> Injected (kPa)	P steady state (kPa)	H/Pd	% change from previous
0.00	0.00	0	-
13.13	10.12	0.91	200.0
24.21	21.69	0.90	0.5
36.76	34.09	0.89	2.1
<del>58.11</del>	<del>54.84</del>	<del>-0.50</del>	<del>724.7</del>
0.00	0.00	0	-
11.77	8.96	0.97	200.0
25.31	22.37	0.99	2.5
37.74	35.00	0.98	0.7
0.00	0.00	0.00	-
11.79	8.91	1.07	200.0
22.40	19.98	1.08	1.5
34.45	31.87	1.07	0.9
45.30	42.92	1.05	2.0
54.01	52.04	1.04	1.7
0.00	0.00	0	-
15.08	11.78	0.83	200.0
27.00	24.27	0.86	3.3
37.23	34.90	0.87	1.4
45.12	43.31	0.85	2.4
54.55	52.56	0.84	1.9
0.00	0.00	0	-
19.08	15.05	0.9	-

**Table 26: Summary of isotherm data for 1.76% Pd/MCM-41 material.**

<b>1.76% Pd/MCM-41 - Summary</b>	
(2.00E-5 moles Pd in cell)	
# plateau points	H/Pd average
5	0.77
6	0.91
6	0.60
6	0.74
5	0.73
<b>average =</b>	0.75
<b>±</b>	0.14

**Table 27: Detailed isotherm data for 1.76% Pd/MCM-41 material.**

P H <sub>2(g)</sub> Injected (kPa)	P steady state (kPa)	H/Pd	% change from previous
0.00	0.00	0.00	-
7.59	5.56	0.75	200.0
11.91	10.75	0.78	3.4
30.91	27.32	0.77	0.2
66.67	59.69	0.75	3.6
85.67	81.12	0.80	6.5
158.88	145.56	0.67	17.5
0.00	0.00	0.00	-
7.89	5.59	0.86	200.0
17.26	15.13	0.92	5.8
25.18	23.38	0.93	1.1
36.23	33.93	0.94	1.1
44.26	42.43	0.93	1.0
52.26	50.51	0.92	0.6
82.49	76.64	1.06	14.4
0.00	0.00	0.00	-
6.95	5.11	0.59	200.0
13.51	12.00	0.60	2.4
22.96	21.01	0.60	0.3
29.21	27.74	0.61	0.9
40.90	38.56	0.60	0.4
50.83	48.64	0.60	0.0

P H <sub>2(g)</sub> Injected (kPa)	P steady state (kPa)	H/Pd	% change from previous
0.00	0.00	0.00	-
5.16	3.58	0.64	200.0
12.96	11.21	0.72	11.7
20.06	18.47	0.73	1.9
28.89	27.04	0.72	1.2
42.80	39.99	0.73	0.7
54.44	51.87	0.73	0.1
23.85	28.76	0.80	10.1
0.00	0.00	0.00	-
4.86	3.32	0.65	200.0
8.70	7.67	0.72	10.7
18.62	16.67	0.72	0.3
27.93	25.92	0.73	0.7
37.60	35.51	0.74	1.5
54.56	51.18	0.73	0.7

**Table 28: Summary of isotherm data for Pd-black material.**

Pd Black - Summary	
# plateau points	H/Pd average
5	0.76
5	0.69
6	0.76
8	0.68
average =	0.72
±	0.07

**Table 29: Detailed isotherm data for Pd-black material.**

<i>(1.01E-3 moles Pd in cell)</i>		
<b>P steady state (kPa)</b>	<b>H/Pd</b>	<b>% change from previous</b>
0.00	0.00	
36.27	0.74	200.0
81.50	0.76	2.5
133.47	0.76	0.7
191.14	0.77	0.9
219.06	0.77	0.2
150.67	0.78	-
87.34	0.77	-
25.67	0.74	-
0.00	0.00	-

<i>(1.01E-3 moles Pd in cell)</i>			
<b>P H<sub>2(g)</sub> Injected (kPa)</b>	<b>P steady state (kPa)</b>	<b>H/Pd</b>	<b>% change from previous</b>
0.00	0.00	0.00	-
21.35	2.62	0.24	200.0
26.84	3.06	0.55	79.9
31.06	16.98	0.66	19.1
44.10	35.53	0.68	2.9
61.32	54.52	0.68	0.9
199.05	157.98	0.70	3.0
283.25	248.28	0.70	0.9
0.40	69.34	0.70	-
0.07	20.80	0.67	-
0.04	7.09	0.64	-
0.03	3.14	0.62	-
0.30	1.83	0.61	-
0.00	0.00	0	-

(Cont'd)

<i>(1.83E-3 moles Pd in cell)</i>			
<b>P H<sub>2(g)</sub> Injected (kPa)</b>	<b>P steady state (kPa)</b>	<b>H/Pd</b>	<b>% change from previous</b>
0.00	0.00	0.00	-
17.48	2.30	0.13	200.0
26.07	3.22	0.32	87.1
28.29	6.40	0.51	44.2
56.91	26.94	0.73	35.7
48.46	43.48	0.74	1.6
92.06	81.41	0.76	2.7
153.63	139.30	0.77	1.9
207.17	194.12	0.78	1.2
213.79	210.00	0.78	0.4
153.59	163.98	0.78	-
85.10	100.19	0.77	-
57.98	66.42	0.76	-
0.33	15.91	0.72	-
0.13	6.38	0.69	-
0.15	3.65	0.66	-
0.00	0.00	0.00	-

<i>(1.83E-3 moles Pd in cell)</i>			
<b>P H<sub>2(g)</sub> Injected (kPa)</b>	<b>P steady state (kPa)</b>	<b>H/Pd</b>	<b>% change from previous</b>
0.00	0.00	0.00	-
21.11	1.85	0.16	200.0
23.83	2.21	0.35	12.1
24.03	2.56	0.53	0.9
29.02	14.16	0.64	18.8
40.94	34.14	0.66	34.1
64.45	57.76	0.67	44.6
82.18	77.18	0.68	24.2
101.45	96.59	0.69	21.0
143.74	134.62	0.69	34.5
180.47	171.75	0.70	22.7
240.22	227.37	0.70	28.4
149.84	164.23	0.70	-
105.82	116.91	0.69	-
75.83	83.82	0.69	-
15.88	30.47	0.66	-
0.12	8.28	0.63	-
0.00	0.00	0.00	-

**Table 30: Summary of one point hydrogen uptake measurements for 0.81% Pd/MCM-41 material.**

0.81% Pd/MCM-41		
P H <sub>2(g)</sub> Injected (kPa)	P steady state (kPa)	H/Pd
133.07	109.44	0.76
127.00	104.30	1.10
132.90	109.33	0.69
131.74	108.30	0.86
127.71	105.02	0.74

average =	0.77
±	0.11

**Table 31: Summary of one point hydrogen uptake measurements for 2.30% Pd/MCM-41 material.**

2.30% Pd/MCM-41		
P H <sub>2(g)</sub> Injected (kPa)	P steady state (kPa)	H/Pd
130.94	107.15	1.07
130.83	107.05	1.07
132.44	108.39	1.07
133.56	109.30	1.09
155.14	127.22	1.04

average =	1.07
±	0.02

## APPENDIX D

Detailed experimental setup and results not included in Chapter 5.

### TCE DEGRADATION BATCH EXPERIMENTS

**Table 32: Setup for first of two experiments (10 mg/l TCE in hydrogen saturated deionized water).**

Material	Sample ID	sample (g)	Pd (g)
sand	211	0.0508	-
	221	0.0522	-
1.00% Pd/sand	111	0.0506	5.06E-04
	121	0.0503	5.03E-04
	112	0.0506	5.06E-04
	122	0.0508	5.08E-04
	113	0.0506	5.06E-04
	123	0.0503	5.03E-04
	114	0.0506	5.06E-04
	124	0.0507	5.07E-04
	115	0.0499	4.99E-04
	125	0.0501	5.01E-04
1.10% Pd/MCM-41	511	0.0505	5.56E-04
	521	0.0500	5.50E-04

average =	0.0506	5.13E-04
±	3.17E-04	1.21E-05

TCE		MDL = 0.96 All concentrations in ug/l							
Time	Sand	1.00% Pd/sand		1.10% Pd/MCM-41		Reagent Blank		Blank	
0	-	-	-	-	-	9580	9200	0	0
10		7556	6400						
20		6484	6104						
35		5692	5756						
50		5840	4562	6232	6100				
120	7416	8072	5852	6084		5516	5718		

VC		MDL = 0.91 All concentrations in ug/l							
Time	Sand	1.00% Pd/sand		1.10% Pd/MCM-41		Reagent Blank		Blank	
0	-	-	-	-	-	3	3	0	0
10		15	14						
20		21	20						
35		16	15						
50		17	18	16	16				
120	2	1	16	16		17	16		

trans DCE		MDL = 0.85 All concentrations in ug/l							
Time	Sand	1.00% Pd/sand		1.10% Pd/MCM-41		Reagent Blank		Blank	
0	-	-	-	-	-	7	7	0	0
10		33	34						
20		45	46						
35		37	37						
50		39	41	37	40				
120	3	2	38	35		51	48		

cis DCE		MDL = 1.1		All concentrations in ug/l					
Time	Sand	1.00% Pd/sand		1.10% Pd/MCM-41		Reagent Blank		Blank	
0	-	-	-	-	-	19	20	0	0
10	-	91	92	-	-	-	-	-	-
20	-	130	135	-	-	-	-	-	-
35	-	127	127	-	-	-	-	-	-
50	-	134	142	149	148	-	-	-	-
120	4	4	142	132	150	148	-	-	-

Ethane		MDL = 0.8		All concentrations in ug/l					
Time	Sand	1.00% Pd/sand		1.10% Pd/MCM-41		Reagent Blank		Blank	
0	-	-	-	-	-	4	35	0	0
10	-	5349	5913	-	-	-	-	-	-
20	-	10067	7583	-	-	-	-	-	-
35	-	8476	9212	-	-	-	-	-	-
50	-	9409	9826	-	-	-	-	-	-
120	115	271	10190	9054	10053	9012	-	-	-

Ethene		MDL = 1.1		All concentrations in ug/l					
Time	Sand	1.00% Pd/sand		1.10% Pd/MCM-41		Reagent Blank		Blank	
0	-	-	-	-	-	0	0	0	0
10	-	2.35E-03	2.24E-03	-	-	-	-	-	-
20	-	4.69E-03	3.51E-03	-	-	-	-	-	-
35	-	5.13E-03	4.68E-03	-	-	-	-	-	-
50	-	8.07E-03	5.70E-03	-	-	-	-	-	-
120	0	0	7.97E-03	7.33E-03	5.97E-03	1.06E-02	-	-	-

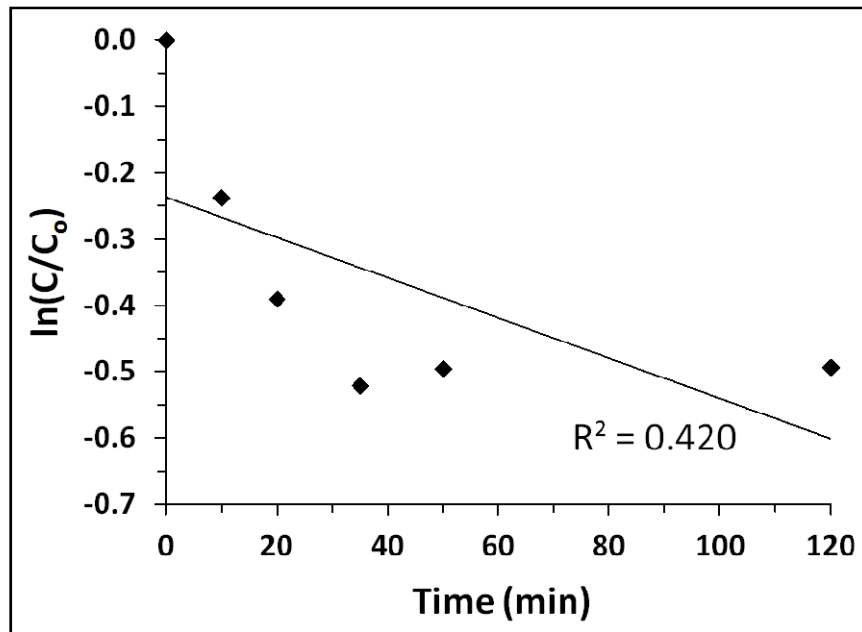


Figure 123: Linear fit to Pd/Sand batch degradation data from Section 5.3.1, including all 6 points for sample A.

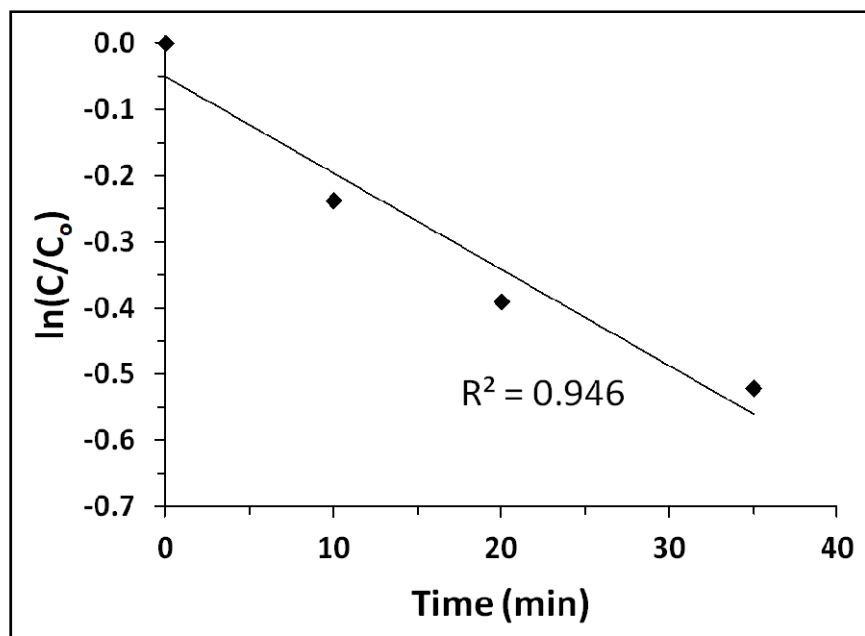


Figure 124: Linear fit to Pd/Sand batch degradation data from Section 5.3.1, including first 4 points for sample A.

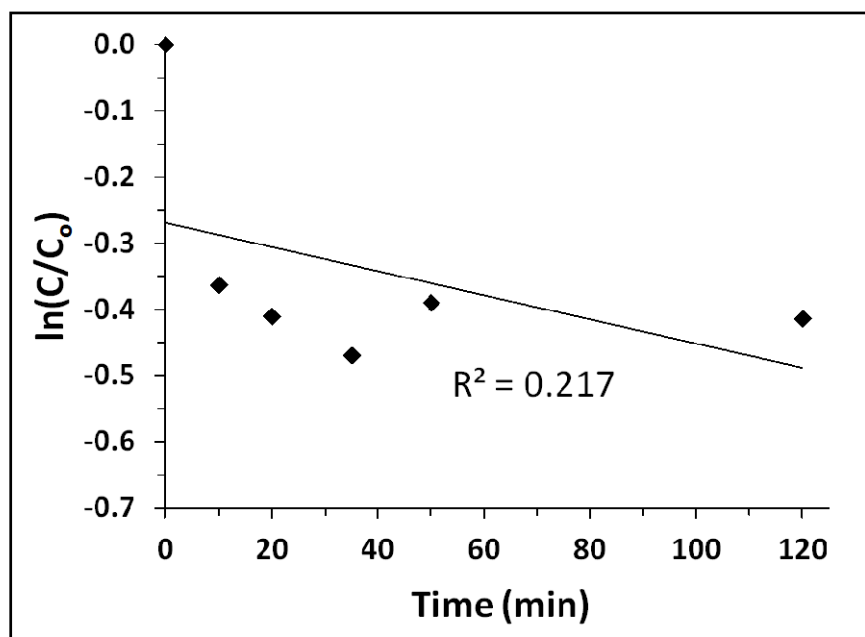


Figure 125: Linear fit to Pd/Sand batch degradation data from Section 5.3.1, including all 6 points for sample B.

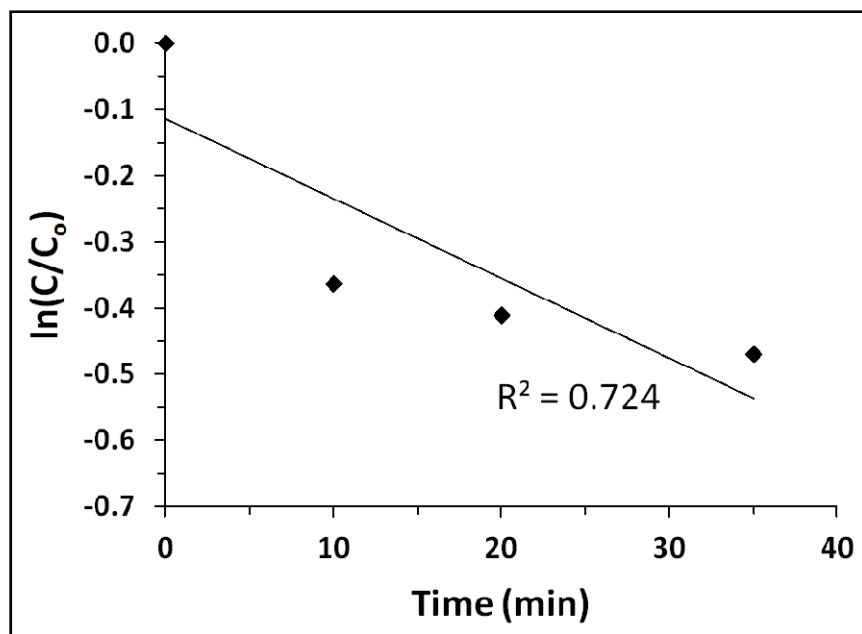


Figure 126: Linear fit to Pd/Sand batch degradation data from Section 5.3.1, including first 4 points for sample B

**Table 33: Setup for second of two experiments (10 mg/l TCE in 2mmol/l sodium borate in hydrogen saturated deionized water).**

Sample	Sample (g)	Pd (g)	TCE (ug/l)	VC (ug/l)	trans DCE (ug/l)	cis DCE (ug/l)
Control 1	-	-	8668	0	0	0
	-	-	8580	0	0	0
Control 2	-	-	8428	28	36	114
	-	-	7608	12	16	45
1.00% Pd/sand	0.05050	5.05E-04	0	0	0	0
	0.05050	5.05E-04	0	0	0	0
1.10% Pd/MCM-41	0.05000	5.50E-04	32	0	0	0
	0.05000	5.50E-04	30	0	0	0
<b>MDL =</b>			0.96	0.91	0.85	1.10

## TCE DEGRADATION COLUMN EXPERIMENTS

### Column Experiment Using Lower Internal Volume Columns:

#### Column Fill Materials

Control - sand only		0.99% Pd/MCM-41 with sand		0.13% Ni-Pd/MCM-41 with sand	
column (g)	199.78	column (g)	205.53	column (g)	205.76
column + fill (g)	212.38	column + fill (g)	222.21	column + fill (g)	221.63
fill (g)	12.60	fill (g)	16.68	fill (g)	15.87
column + fill + saturated (g)	219.52	column + fill + saturated (g)	229.67	column + fill + saturated (g)	231.95
PV (ml)	7.14	PV (ml)	7.46	PV (ml)	10.32

1.00% Pd/sand with sand		1.02% Ni/MCM-41 with sand	
column (g)	203.53	column (g)	203.49
column + fill (g)	219.17	column + fill (g)	219.33
fill (g)	15.64	fill (g)	15.84
column + fill + saturated (g)	226.08	column + fill + saturated (g)	227.08
PV (ml)	6.91	PV (ml)	7.75

1.01% Ni-Pd/MCM-41 with sand		0.12% Pd/MCM-41 with sand	
column (g)	205.71	column (g)	207.63
column + fill (g)	221.84	column + fill (g)	224.22
fill (g)	16.13	fill (g)	16.59
column + fill + saturated (g)	230.31	column + fill + saturated (g)	232.6
PV (ml)	8.47	PV (ml)	8.38

#### TCE and Degradation Intermediate Product Results

Control - sand only								
Sample ID	Port	PV	TCE (ug/l)	VC (ug/l)	11DCE (ug/l)	tDCE (ug/l)	cDCE (ug/l)	pH
111	inflow	46	3977	0	0	0	0	4.87
112	outflow		3905	0	0	0	0	4.34
121	inflow	180	3881	0	0	0	0	5.08
122	outflow		3953	0	0	0	0	4.58
131	inflow	216	3683	0	0	0	0	4.65
132	outflow		3828	0	0	0	0	4.10
141	inflow	639	3328	0	0	0	0	4.41
142	outflow		3514	0	0	0	0	4.46
151	inflow	698	3415	0	0	0	0	4.36
152	outflow		3161	0	0	0	0	4.45
blank	-	-	0	-	-	-	-	-
blank	-	-	0	-	-	-	-	-

1.00% Pd/sand with sand							
Sample ID	Port	PV	TCE (ug/l)	VC (ug/l)	11DCE (ug/l)	tDCE (ug/l)	cDCE (ug/l)
11	inflow	78	9306	0	0	0	14
12	outflow		4854	0	0	7.2	108.8
21	inflow	119	9314	0	0	12.96	0
22	outflow		5762	0	0	5.2	99.2
31	inflow	194	8857	0	0	0	12.4
32	outflow		6577	0	0	4	91.6
41	inflow	317	6373	0	0	0	75.2
42	outflow		7526	0	0	0	12.8
51	inflow	660	6627	0	0	0	13.04
52	outflow		5903	0	0	0	60.44
blank	-	-	0	0	0	0	0
blank	-	-	0	0	0	0	0

1.02% Ni/MCM-41 with sand											
Sample ID	Port	PV	TCE (ug/l)	VC (ug/l)	11DCE (ug/l)	tDCE (ug/l)	cDCE (ug/l)	pH	pH ±	Conductivity (µS/cm)	Conductivity ±
301	inflow	31	7046	0	0	0	0	5.3	-	3.83	-
302	outflow		7042	0	0	0	0	5.27	-	3.62	-
311	inflow	215	6995	0	0	0	0	5.24	-	2.95	-
312	outflow		6899	0	0	0	0	5.56	-	3.00	-
321	inflow	838	6676	0	0	0	0	5.39	-	2.74	-
322	outflow		6466	0	0	0	0	5.43	-	3.42	-
331	inflow	913	5232	0	0	0	0	5.33	-	2.43	-
332	outflow		5251	0	0	0	0	5.07	-	4.56	-
341	inflow	1043	6042	0	0	0	0	5.17	0.08	2.78	0.04
342	outflow		5998	0	0	0	0	5.38	-	3.22	-
blank	-	-	0	0	0	0	0	-	-	-	-
blank	-	-	0	0	0	0	0	-	-	-	-

1.01% Ni-Pd/MCM-41 with sand											
Sample ID	Port	PV	TCE (ug/l)	VC (ug/l)	11DCE (ug/l)	tDCE (ug/l)	cDCE (ug/l)	pH	pH ±	Conductivity (µS/cm)	Conductivity ±
351	inflow	35	6140	0	0	0	0	4.11	-	5.30	-
352	outflow		27.6	0	0	0	0	3.53	-	74.82	-
361	inflow	103	6458	0	0	0	0	3.89	-	16.68	-
362	outflow		5.9	0	0	0	0	3.53	-	83.91	-
371	inflow	224	7011	0	0	0	0	4.35	-	3.79	-
372	outflow		4.6	0	0	0	0	3.55	-	81.52	-
381	inflow	606	7314	0	0	0	0	4.39	-	3.64	-
382	outflow		24	0	0	0	0	3.51	-	80.90	-
391	inflow	1502	7010	0	0	0	0	4.27	-	2.40	-
392	outflow		111	0	0	0	0	3.65	0.08	73.01	4.80
blank	-	-	0	0	0	0	0	-	-	-	-
blank	-	-	0	0	0	0	0	-	-	-	-

0.12% Pd/MCM-41 with sand											
Sample ID	Port	PV	TCE (ug/l)	VC (ug/l)	11DCE (ug/l)	tDCE (ug/l)	cDCE (ug/l)	pH	pH ±	Conductivity (µS/cm)	Conductivity ±
401	inflow	138	10546	-	-	-	-	4.48	-	1.85	-
402	outflow		384	-	-	-	-	3.63	-	70.40	-
411	inflow	572	10104	-	-	-	-	4.25	-	2.55	-
412	outflow		7554	-	-	-	-	3.63	-	40.99	-
421	inflow	917	9444	0	0	0	0	4.8	-	3.20	-
422	outflow		7538	30.8	46.4	30.8	107.6	4.07	-	18.65	-
431	inflow	949	8912	0	0	0	0	5.21	-	2.56	-
432	outflow		2588	14.8	30.4	13.2	56.8	3.80	0.1	34.80	0.67
blank	-	-	0	0	0	0	0	-	-	-	-
blank	-	-	0	0	0	0	0	-	-	-	-

0.13% Pd/MCM-41 with sand											
Sample ID	Port	PV	TCE (ug/l)	VC (ug/l)	11DCE (ug/l)	tDCE (ug/l)	cDCE (ug/l)	pH	pH ±	Conductivity (µS/cm)	Conductivity ±
451	inflow	79	-	-	-	-	-	5.37	-	2.34	-
452	outflow		-	-	-	-	-	4.79	-	20.36	-
461	inflow	172	-	-	-	-	-	5.54	-	2.03	-
462	outflow		-	-	-	-	-	4.76	-	5.91	-
471	inflow	531	-	-	-	-	-	5.64	-	1.88	-
472	outflow		-	-	-	-	-	3.76	-	26.28	-
481	inflow	730	8112	0	0	0	0	6.03	-	2.84	-
482	outflow		7612	8.4	6.8	10.4	23.2	4.98	1	10.85	1.14
491	inflow	734	8324	0	0	0	0	5.13	-	2.54	-
492	outflow		7708	8.4	6.4	5.6	22.4	4.53	-	3.50	-

0.99% Pd/MCM-41											
Sample ID	Port	PV	TCE (ug/l)	VC (ug/l)	11DCE (ug/l)	TDCE (ug/l)	cDCE (ug/l)	pH	pH ±	Conductivity (µS/cm)	Conductivity ±
61	inflow	120	7533	0	0	5.4	5.3	-	-	-	-
62	outflow		194	0	0	0	0	-	-	-	-
71	inflow	197	6335	0	0	0	0	-	-	-	-
72	outflow		1195	1	0	2.5	17.1	-	-	-	-
81	inflow	339	7020	0	0	0	0	-	-	-	-
82	outflow		284	0	0	0	3.4	-	-	-	-
91	inflow	478	6433	0	0	0	0	-	-	-	-
92	outflow		119	0	0	0	1.5	-	-	-	-
101	inflow	671	6106	0	0	0	0	-	-	-	-
102	outflow		158	0	0	0	2	-	-	-	-
blank		-	0	-	-	-	-	-	-	-	-
blank		-	0	-	-	-	-	-	-	-	-
11	inflow	712	8227	-	-	-	-	-	-	-	-
12	outflow		1973	-	-	-	-	-	-	-	-
21	inflow	766	8037	-	-	-	-	-	-	-	-
22	outflow		1887	-	-	-	-	-	-	-	-
31	inflow	858	7632	-	-	-	-	-	-	-	-
32	outflow		145	-	-	-	-	-	-	-	-
41	inflow	993	6905	-	-	-	-	-	-	-	-
42	outflow		249	-	-	-	-	-	-	-	-
51	inflow	1337	7188	-	-	-	-	-	-	-	-
52	outflow		156	-	-	-	-	-	-	-	-
blank		-	0	-	-	-	-	-	-	-	-
blank		-	0	-	-	-	-	-	-	-	-

0.99% Pd/MCM-41 (Cont'd)											
Sample ID	Port	PV	TCE (ug/l)	VC (ug/l)	11DCE (ug/l)	TDCE (ug/l)	cDCE (ug/l)	pH	pH ±	Conductivity (µS/cm)	Conductivity ±
31	inflow	182	8465	0	0	0	0	-	-	-	-
32	outflow		907	0	0	0	12.8	-	-	-	-
51	inflow	664	7116	0	0	0	0	5.18	-	-	-
52	outflow		156	0	0	0	6.4	3.59	-	-	-
61	inflow	699	6022	0	0	0	0	5.08	-	-	-
62	outflow		124	0	0	0	6.8	3.46	-	-	-
81	inflow	926	5553	0	0	0	0	4.29	-	-	-
82	outflow		226	0	0	0	3.6	3.76	-	-	-
101	inflow	1434	5183	0	0	0	0	4.48	-	-	-
102	outflow		194	0	0	0	13.6	3.58	-	-	-
blank		-	0	-	-	-	-	-	-	-	-
blank		-	0	-	-	-	-	-	-	-	-
171	inflow	141	9513	0	0	0	0	5.94	-	-	-
172	outflow		3088	0	0	0	64.5	4.16	-	-	-
191	inflow	538	233	0	0	0	0	4.29	-	-	-
192	outflow		314	0	0	0	0	3.5	-	-	-
211	inflow	914	7859	0	0	0	0	4.99	-	-	-
212	outflow		1157	0	0	0	11.6	4.3	-	-	-
221	inflow	1034	7122	0	0	0	0	4.07	0.09	-	-
222	outflow		1372	0	0	0	0	3.57	-	-	-
251	inflow	1656	6537	0	0	0	0	4.03	-	-	-
252	outflow		570	0	0	0	0	3.34	-	-	-
blank		-	0	-	-	-	-	-	-	-	-
blank		-	0	-	-	-	-	-	-	-	-

0.99% Pd/MCM-41 (Cont'd)											
Sample ID	Port	PV	TCE (ug/l)	VC (ug/l)	11DCE (ug/l)	TDCE (ug/l)	cDCE (ug/l)	pH	pH ±	Conductivity (µS/cm)	Conductivity ±
261	inflow	4597	4809	0	0	0	3.5	5.39	-	2.00	-
262	outflow		144	0	0	0	13.1	3.79	-	43.9	-
271	inflow	4778	4408	0	0	0	3.4	4.27	-	2.25	-
272	outflow		215	0	0	0	15.5	3.63	-	44.6	-
281	inflow	4917	4681	0	0	0	3.9	4.24	-	2.74	-
282	outflow		252	0	0	0	20.1	3.60	-	46.7	-
291	inflow	4969	3642	0	0	0	5.8	4.39	-	1.86	-
292	outflow		226	0	0	0	19.2	3.65	-	42.5	-
301	inflow	5036	3450	0	0	0	3.6	0.00	0.11	2.43	0.09
302	outflow		302	0	0	0	25	0.00	0.03	41.1	0.40
blank		-	0	0	0	0	0	-	-	-	-
blank		-	0	0	0	0	0	-	-	-	-

## Column Experiment Using Larger Internal Volume Columns:

### Column Fill Material

Column	Reactive Material	Column (g)	Column + Fill (g)	Fill (g)	Reactive Material (g)	Pd (g)	Column + Fill + Saturated (g)	PV (ml)
1	1.23% Pd/MCM-41	464.23	732.31	268.08	4.02	4.95E-02	783.54	51.23
3	3.46% Pd/MCM-41	520.99	771.15	250.16	3.75	1.30E-01	819.77	48.62
Control	-	486.89	740.21	253.32	-	-	789.96	49.75

### TCE and Degradation Intermediate Product Results

Sampling #1							Sampling #2						
Column	PV	Sample ID	TCE (ug/l)	(C/C <sub>0</sub> )	ln(C/C <sub>0</sub> )	Residence Time (mins)	Column	PV	Sample ID	TCE (ug/l)	(C/C <sub>0</sub> )	ln(C/C <sub>0</sub> )	Residence Time (mins)
-	-	blank	5	-	-	-	-	-	blank	4	-	-	-
-	-	blank	5	-	-	-	-	-	blank	6	-	-	-
-	-	C <sub>0</sub>	4247	-	-	-	-	-	C <sub>0</sub>	3439	-	-	-
1	240	1o	3592	1.000	0.000	0	1	244	1o	3230	1.088	0.084	0
		1A	3578	0.996	-0.004	31			1A	2969	1.000	0.000	31
		1B	3581	0.997	-0.003	62			1B	2820	0.950	-0.052	62
		1C	3303	0.920	-0.084	93			1C	2612	0.880	-0.128	93
		1D	3606	1.004	0.004	127			1D	2420	0.815	-0.204	127
		1E	3549	0.988	-0.012	158			1E	2479	0.835	-0.180	158
		1F	3554	0.990	-0.011	189			1F	2033	0.685	-0.378	189
3	258	3o	3623	1.000	0.000	0	3	262	3o	3326	1.327	0.283	0
		3A	3569	0.985	-0.015	28			3A	2507	1.000	0.000	28
		3B	3499	0.966	-0.035	56			3B	1770	0.706	-0.348	56
		3C	3382	0.934	-0.069	84			3C	1237	0.494	-0.706	84
		3D	3380	0.933	-0.069	115			3D	969	0.387	-0.951	115
		3E	3427	0.946	-0.056	144			3E	625	0.249	-1.390	144
		3F	3372	0.931	-0.072	172			3F	355	0.142	-1.955	172
Control	258	Co	3565	1.000	-	0	Control	262	Co	3240	1.064	-	0
		CA	3472	0.974	-	27			CA	3044	1.000	-	27
		CB	3487	0.978	-	53			CB	3187	1.047	-	53
		CC	3087	0.866	-	83			CC	3173	1.042	-	83
		CD	3585	1.006	-	110			CD	3063	1.006	-	110
		CE	3405	0.955	-	133			CE	3157	1.037	-	133
		CF	3430	0.962	-	163			CF	2999	0.985	-	163

Sampling #3							Sampling #4						
Column	PV	Sample ID	TCE (ug/l)	(C/C <sub>0</sub> )	ln(C/C <sub>0</sub> )	Residence Time (mins)	Column	PV	Sample ID	ug/l	C/C <sub>0</sub>	ln(C/C <sub>0</sub> )	Residence Time (mins)
-	-	blank	3	-	-	-	-	-	blank	6	-	-	-
-	-	blank	6	-	-	-	-	-	C <sub>0</sub>	3559	-	-	-
-	-	C <sub>0</sub>	4576	-	-	-	-	-	C <sub>0</sub>	3173	-	-	-
1	265	1o	3955	1.000	0.000	0	1	305	1A	49	0.015	-4.170	34
		1A	2667	0.674	-0.394	32			1B	24	0.008	-4.890	68
		1B	1653	0.418	-0.872	64			1C	21	0.007	-5.024	101
		1C	136	0.034	-3.371	96			1D	21	0.007	-5.023	138
		1D	-	-	-	131			1E	29	0.009	-4.696	172
		1E	8	0.002	-6.173	162			1F	35	0.011	-4.508	206
		1F	5	0.001	-6.630	194			1H	23	0.007	-4.931	273
		1H	21	0.005	-5.253	258			1K	50	0.016	-4.150	378
		1K	9	0.002	-6.118	357							
3	284	3o	3779	1.000	0.000	0	3	327	3o	3234	1.000	0.000	0
		3A	6	0.002	-6.401	29			3A	18	0.006	-5.201	32
		3B	31	0.008	-4.789	59			3B	20	0.006	-5.105	63
		3C	28	0.007	-4.900	88			3C	20	0.006	-5.083	95
		3D	27	0.007	-4.945	121			3D	20	0.006	-5.067	130
		3E	7	0.002	-6.246	150			3E	26	0.008	-4.816	161
		3F	7	0.002	-6.340	180			3F	27	0.008	-4.801	193
		3H	24	0.006	-5.052	239			3H	38	0.012	-4.455	256
		3K	28	0.007	-4.922	330			3K	31	0.010	-4.655	354
Control	281	Co	3689	1.000	-	0	Control	319	Co	3118	1.000	-	0
		CA	3895	1.056	-	27			CA	3258	1.045	-	29
		CB	4247	1.151	-	54			CB	3229	1.036	-	58
		CC	3869	1.049	-	84			CC	3265	1.047	-	90
		CD	4118	1.116	-	111			CD	3205	1.028	-	119
		CE	3733	1.012	-	134			CE	3059	0.981	-	145
		CF	3747	1.016	-	164			CF	3262	1.046	-	177
		CI	3966	1.075	-	241			CI	3234	1.037	-	260
		CN	3823	1.036	-	376			CN	3131	1.004	-	405

Sampling #5							Sampling #6						
Column	PV	Sample ID	TCE (ug/l)	(C/C <sub>0</sub> )	ln(C/C <sub>0</sub> )	Residence Time (mins)	Column	PV	Sample ID	TCE (ug/l)	(C/C <sub>0</sub> )	ln(C/C <sub>0</sub> )	Residence Time (mins)
-	-	blank	4.465	-	-	-	-	-	blank	6	-	-	-
-	-	blank	7	-	-	-	-	-	blank	7	-	-	-
-	-	C <sub>0</sub>	11975	-	-	-	-	-	BP	6104	-	-	-
1	315	1o	7688	1.000	0.000	0	1	338	1o	5476	1.000	0.000	0
		1A	7554	0.983	-0.018	33			1A	4858	0.887	-0.120	50
		1B	8024	1.044	0.043	66			1B	5596	1.022	0.022	99
		1C	7313	0.951	-0.050	99			1C	5333	0.974	-0.027	149
		1D	6459	0.840	-0.174	136			1D	5248	0.958	-0.043	203
		1E	6560	0.853	-0.159	169			1E	5188	0.947	-0.054	253
		1F	6337	0.824	-0.193	202			1F	4942	0.903	-0.103	303
		1H	6855	0.892	-0.115	268			1H	5189	0.948	-0.054	402
		1K	6195	0.806	-0.216	371			1K	4397	0.803	-0.219	556
3	338	3o	7247	1.000	0.000	0	3	364	3o	5409	1.000	0.000	0
		3A	7381	1.018	0.018	30			3A	4643	0.858	-0.153	44
		3B	7844	1.082	0.079	60			3B	5437	1.005	0.005	89
		3C	6368	0.879	-0.129	91			3C	5177	0.957	-0.044	133
		3D	5771	0.796	-0.228	124			3D	5412	1.001	0.001	182
		3E	5439	0.750	-0.287	154			3E	4488	0.830	-0.187	226
		3F	5298	0.731	-0.313	184			3F	4910	0.908	-0.097	270
		3H	5207	0.718	-0.331	245			3H	5090	0.941	-0.061	359
		3K	4594	0.634	-0.456	338			3K	4332	0.801	-0.222	496
Control	329	Co	7605	1.000	-	0	Control	351	Co	5085	1.000	-	0
		CA	7944	1.045	-	28			CA	5245	1.031	-	41
		CB	8058	1.060	-	56			CB	5442	1.070	-	82
		CC	7853	1.033	-	87			CC	5535	1.088	-	128
		CD	6491	0.854	-	115			CD	4691	0.923	-	169
		CE	7426	0.976	-	140			CE	5253	1.033	-	205
		CF	7653	1.006	-	171			CF	5475	1.077	-	252
		CI	7830	1.030	-	251			CI	5448	1.071	-	370
		CN	7683	1.010	-	391			CN	5381	1.058	-	575

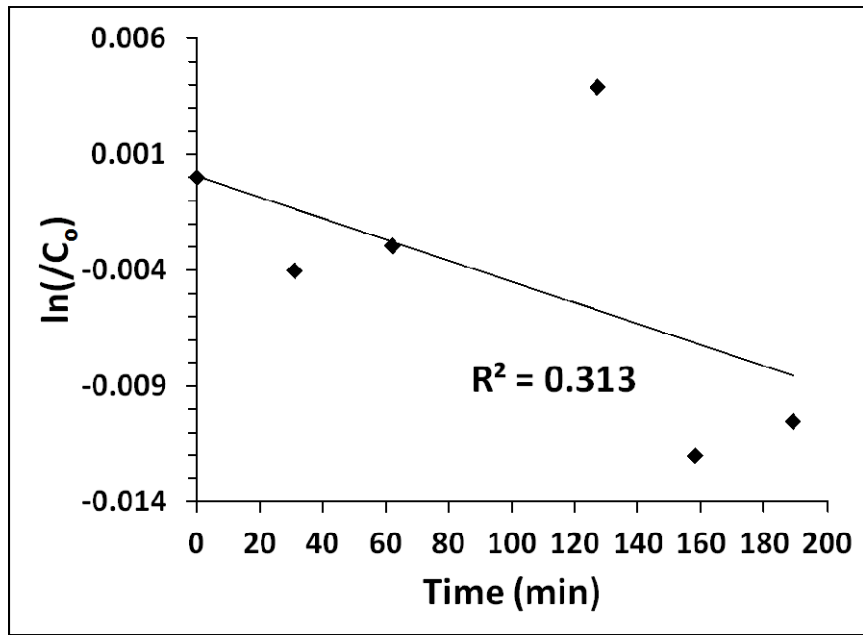


Figure 127: Column 1 after 240 PV, first order data.

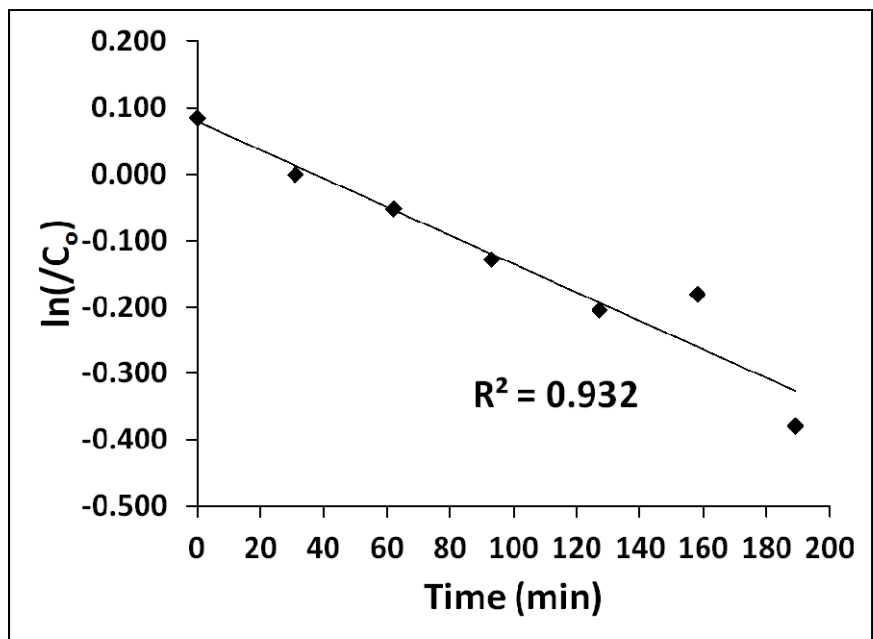


Figure 128: Column 1 after 251 PV, first order data.

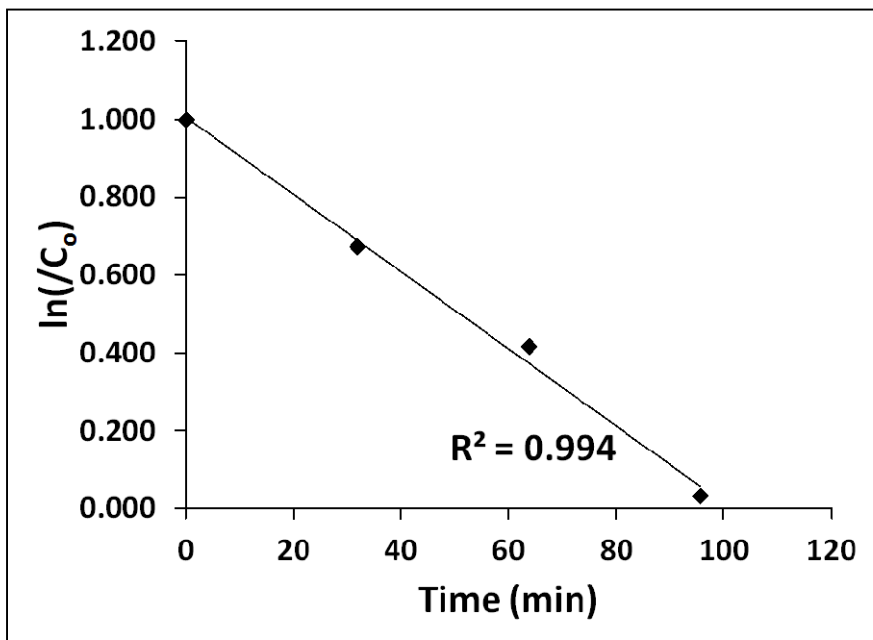


Figure 129: Column 1 after 265 PV, zero order data.

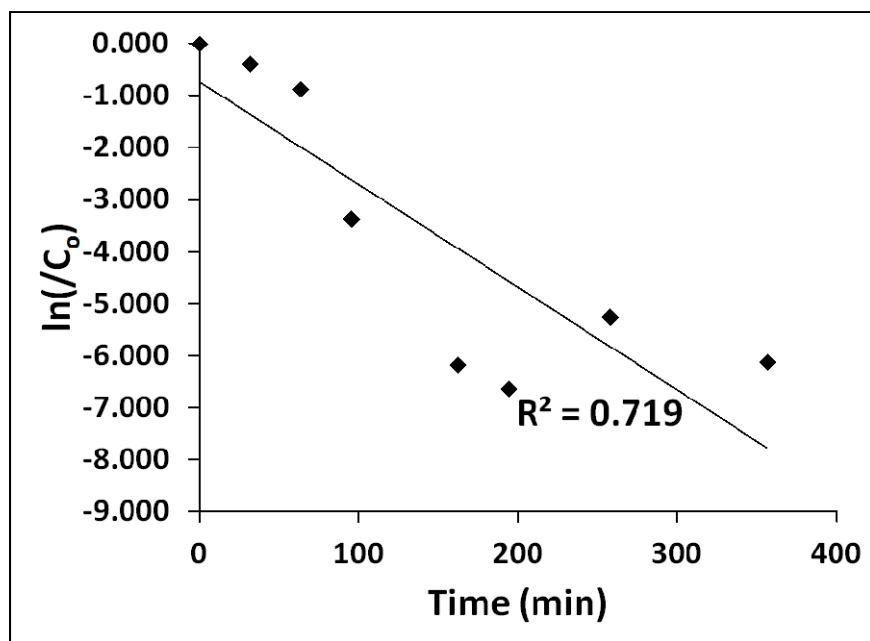


Figure 130: Column 1 after 265 PV, first order data.

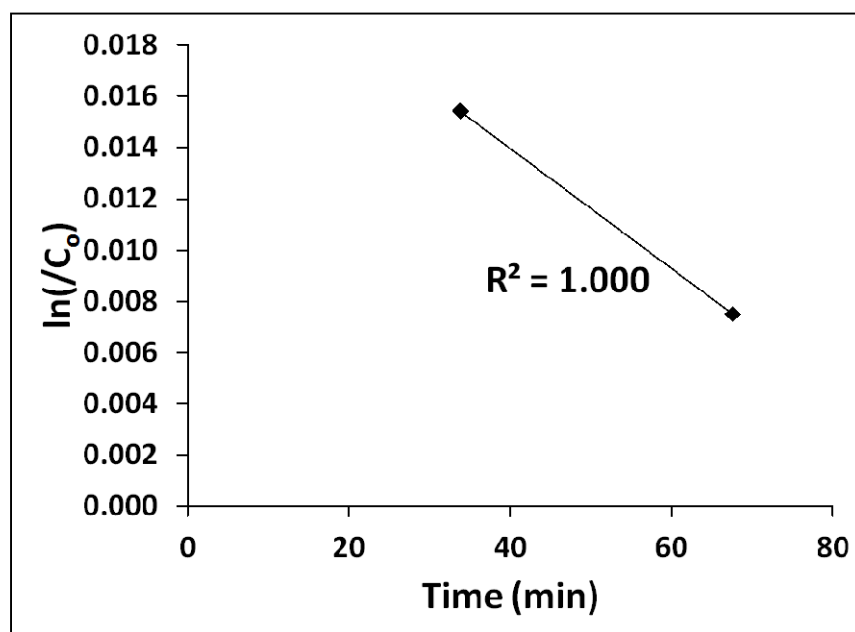


Figure 131: Column 1 after 305 PV, zero order data.

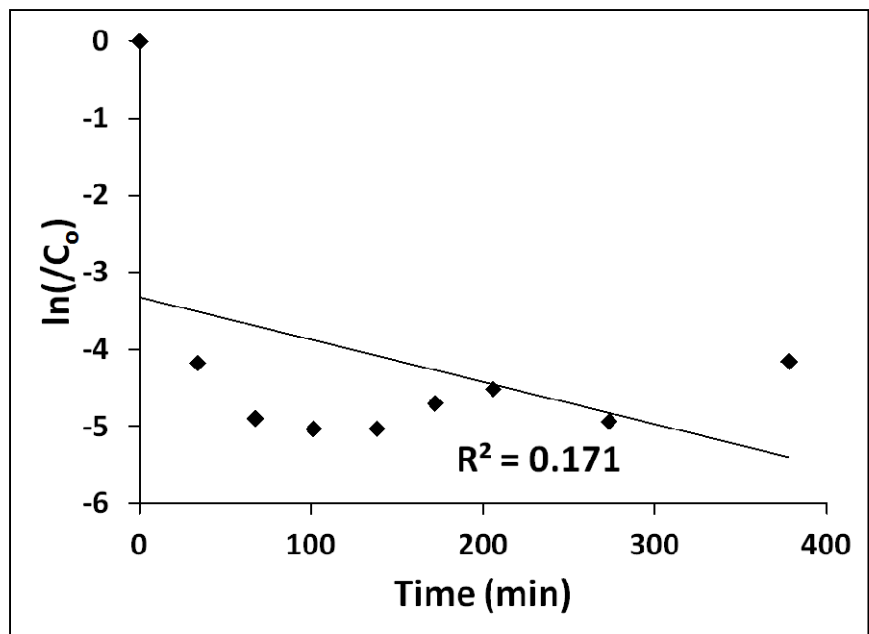


Figure 132: Column 1 after 305 PV, first order data.

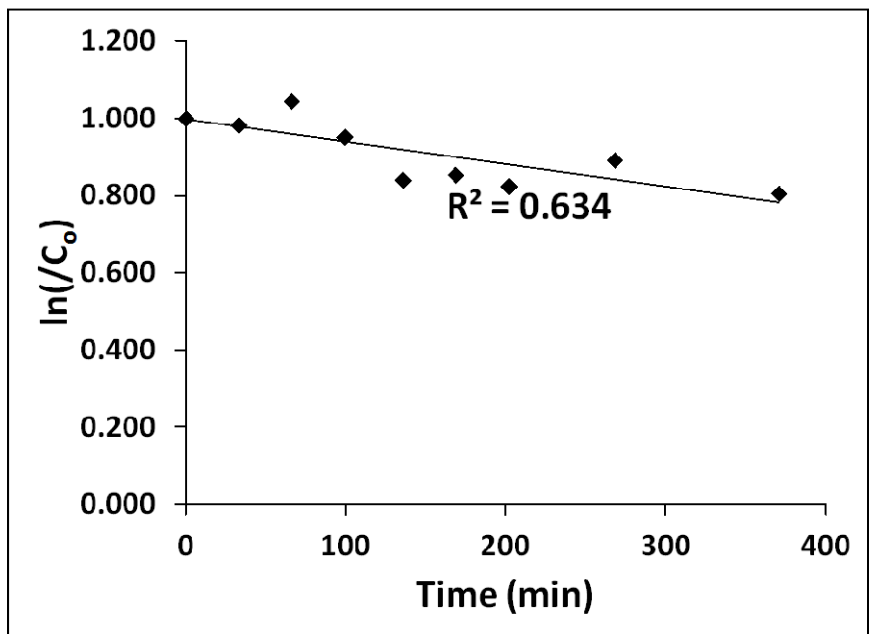


Figure 133: Column 1 after 315 PV, zero order data.

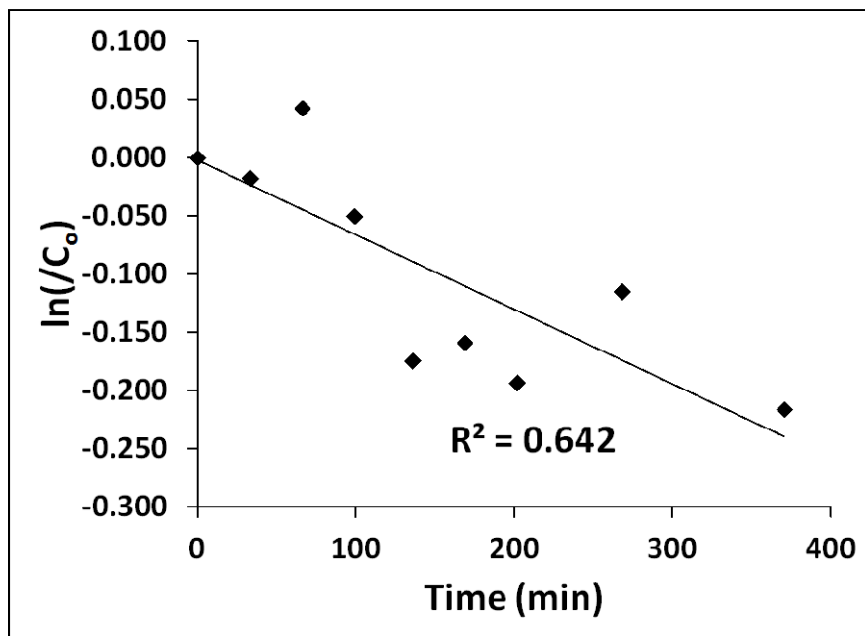


Figure 134: Column 1 after 315 PV, first order data.

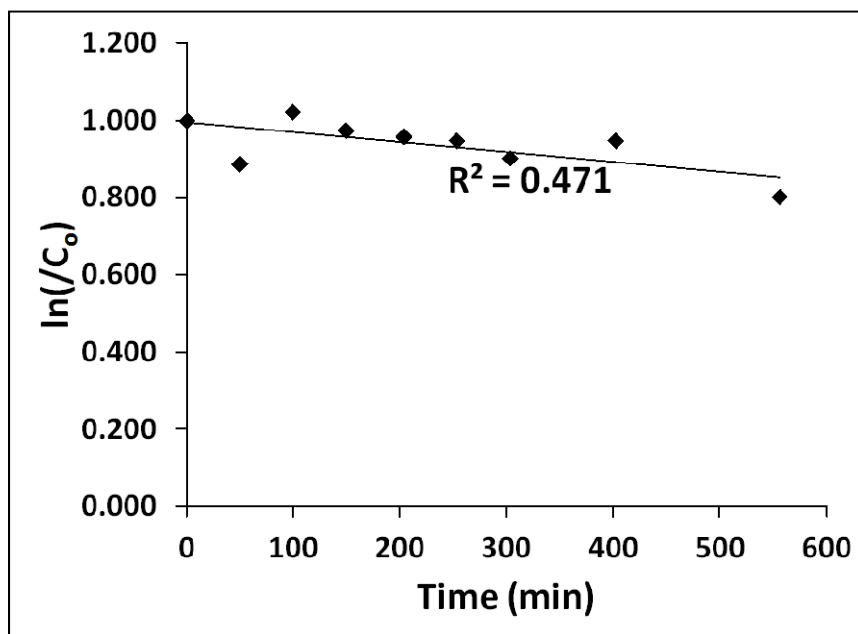


Figure 135: Column 1 after 338 PV, zero order data.

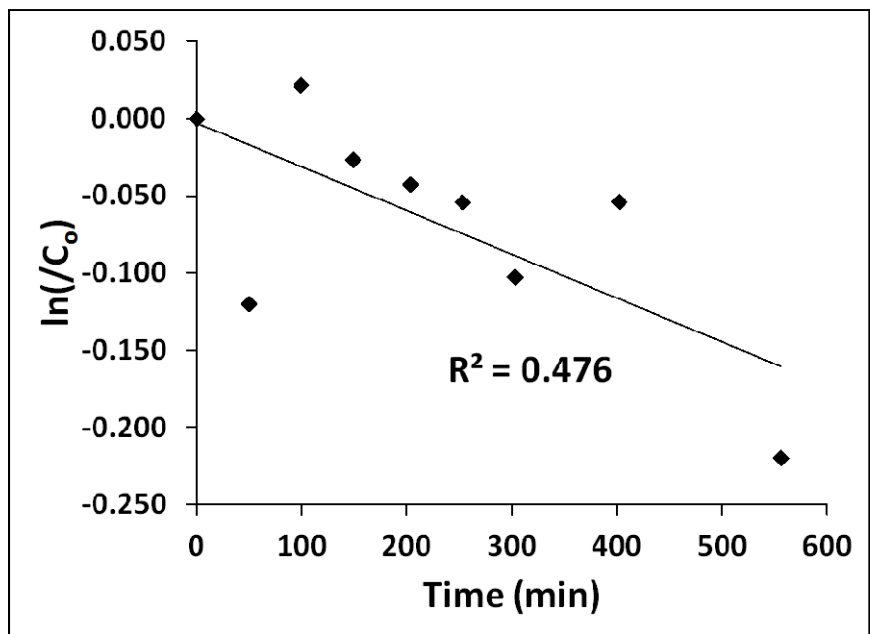


Figure 136: Column 1 after 338 PV, first order data.

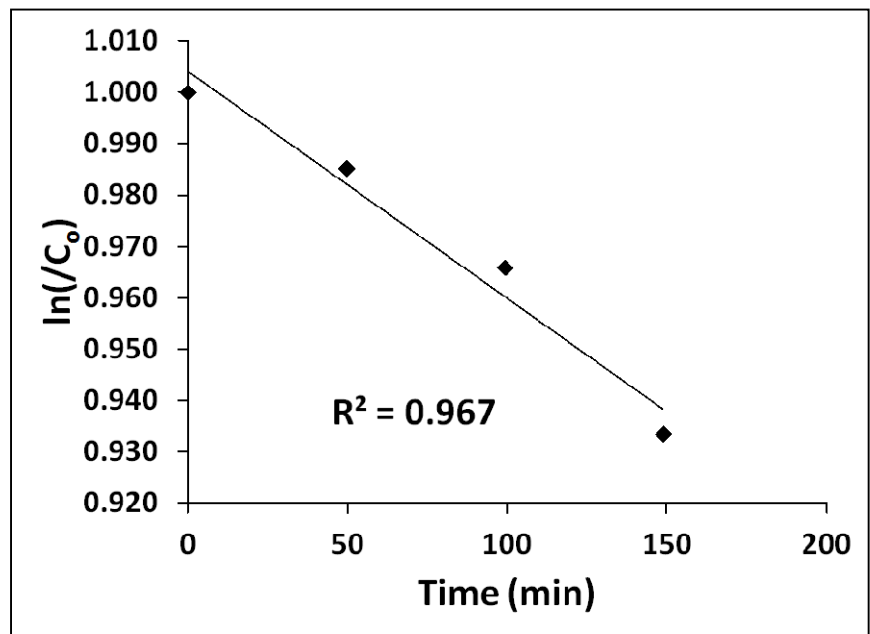


Figure 137: Column 3 after 258 PV, zero order data.

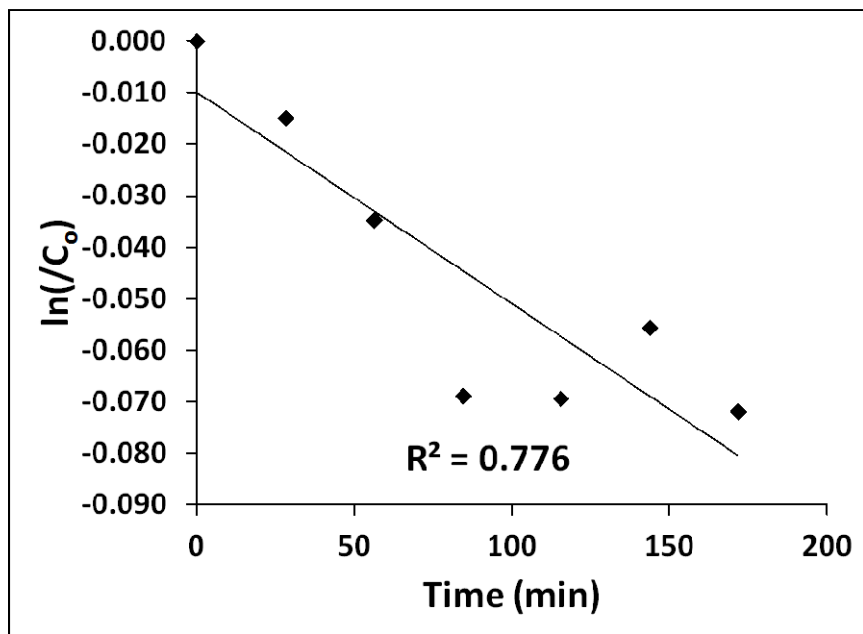


Figure 138: Column 3 after 258 PV, first order data.

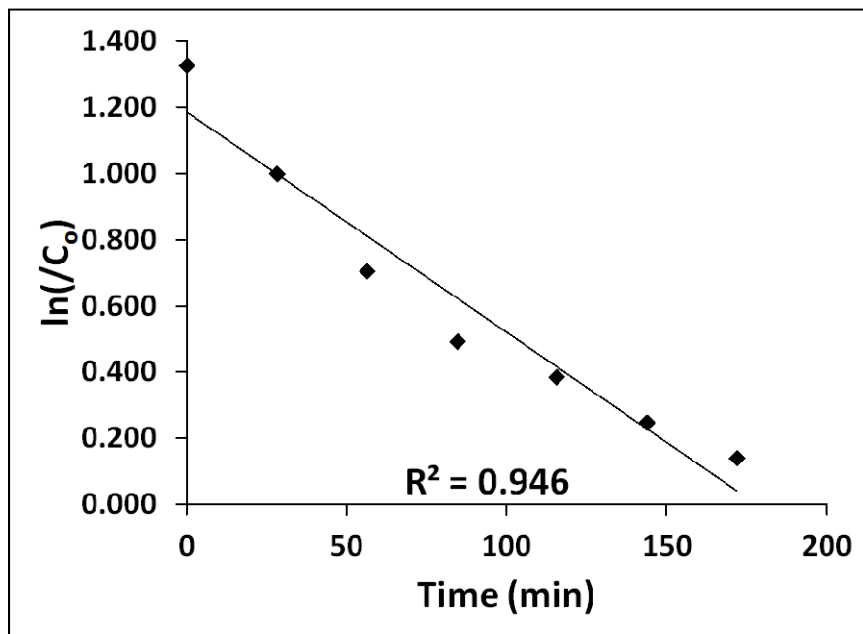


Figure 139: Column 3 after 269 PV, zero order data.

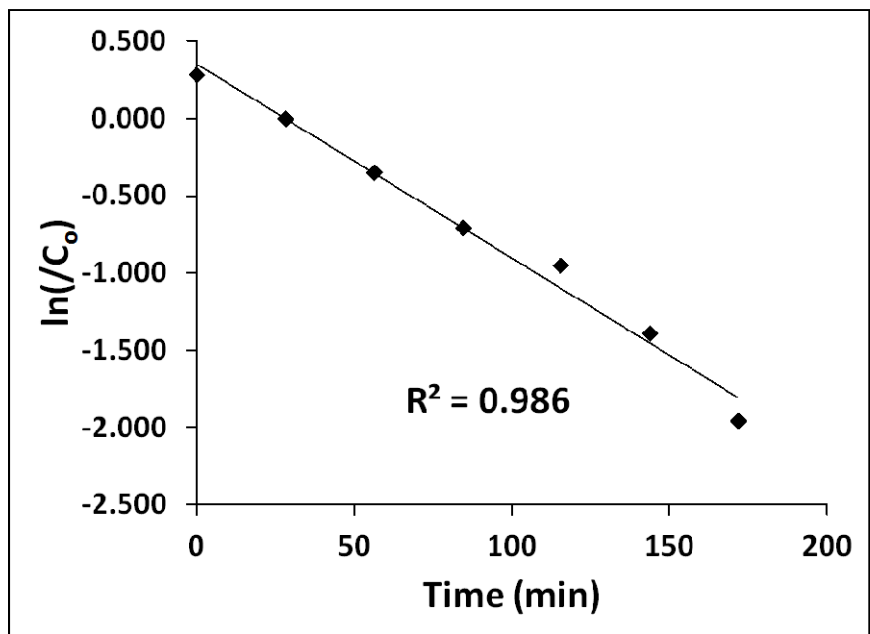


Figure 140: Column 3 after 269 PV, first order data.

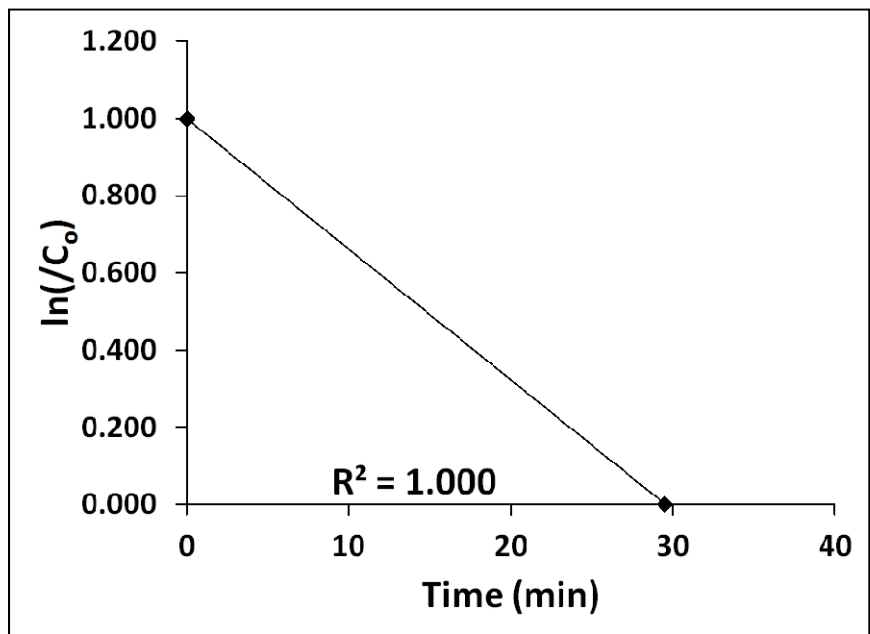


Figure 141: Column 3 after 284 PV, zero order data.

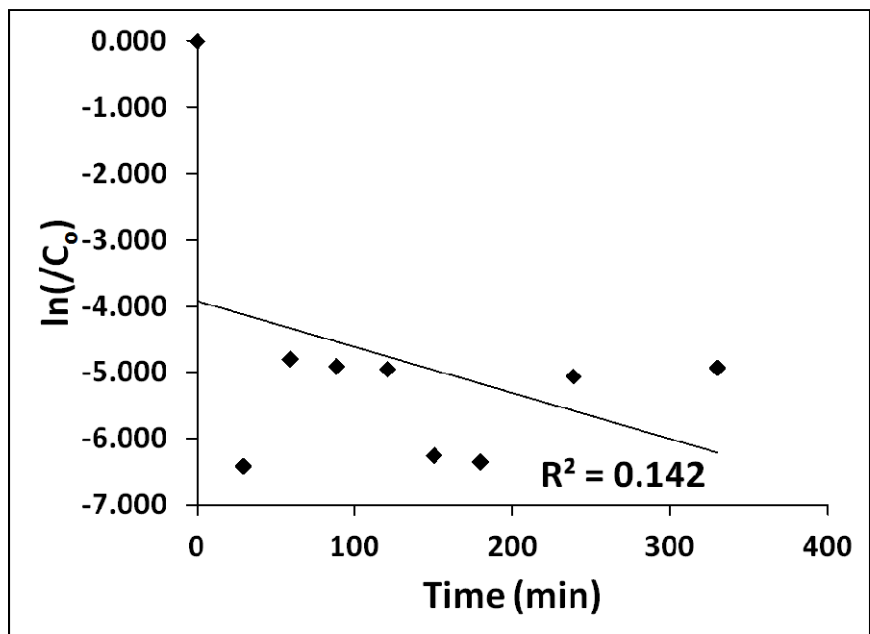


Figure 142: Column 3 after 284 PV, first order data.

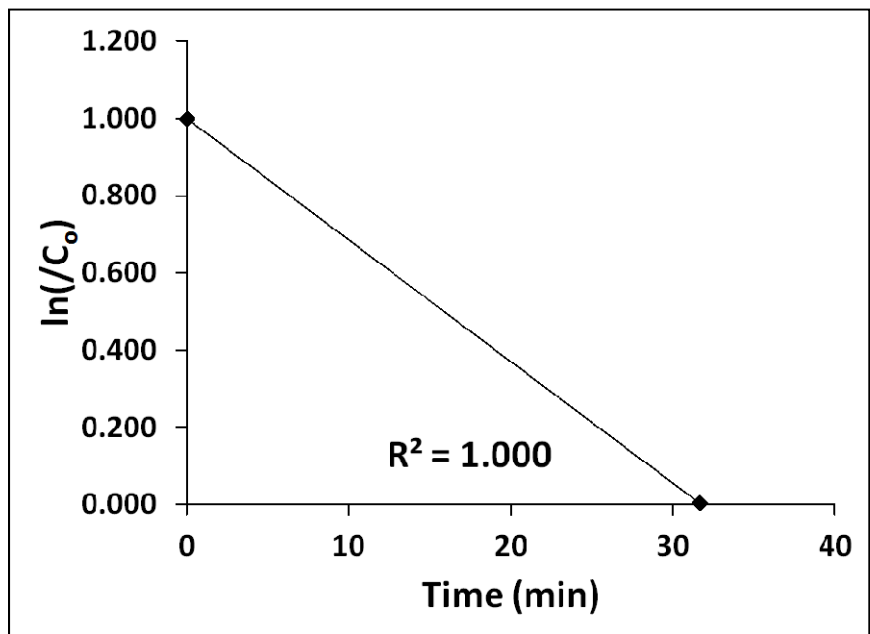


Figure 143: Column 3 after 327 PV, zero order data.

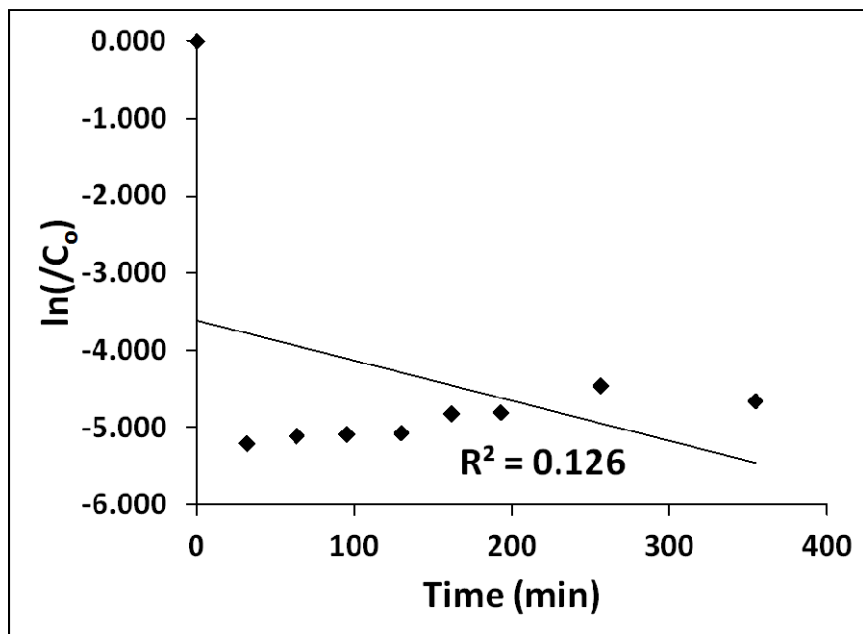


Figure 144: Column 3 after 327 PV, first order data.

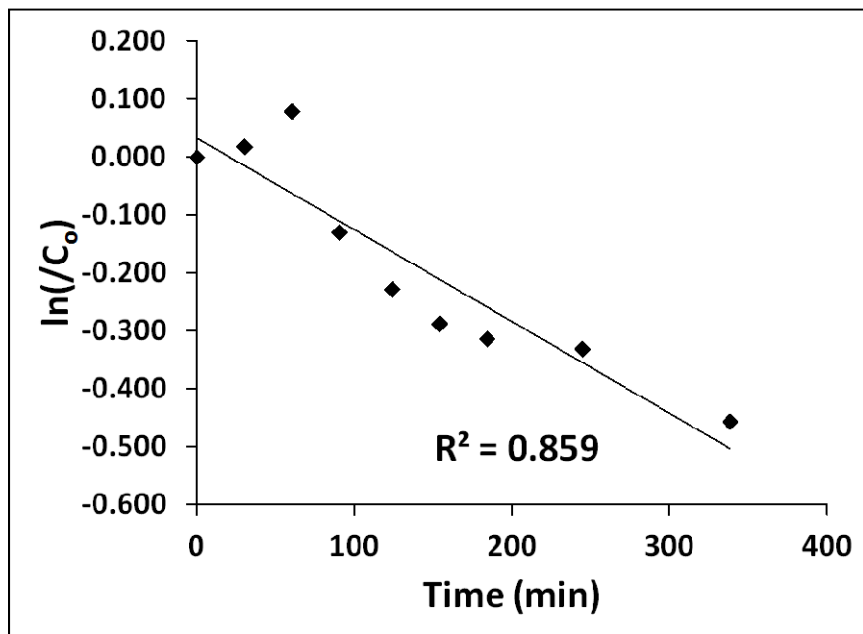


Figure 145: Column 3 after 338 PV, first order data.

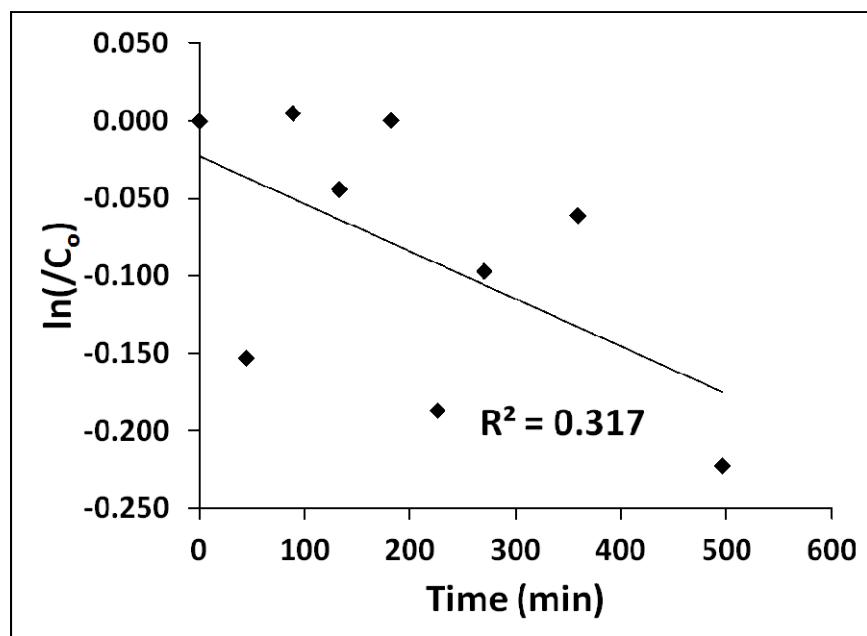


Figure 146: Column 3 after 364 PV, first order data.

### HMPA Degradation Batch Experiment

#### *Reaction Bottle Fill Material*

Sample ID	Sample (g)	Pd (g)	Sample ID	Sample (g)	Pd (g)
A1	0.283	0.002858	B1	0.283	0.002858
A2	0.283	0.002858	B2	0.283	0.002858
A3	0.283	0.002858	B3	0.283	0.002858
A4	0.283	0.002858	B4	0.283	0.002858
A5	0.283	0.002858	B5	0.283	0.002858
A6	0.284	0.002868	B6	0.283	0.002858
A7	0.283	0.002858	B7	0.284	0.002868
A8	0.284	0.002868	B8	0.283	0.002858

average =	0.283	2.86E-03	-	0.283	2.86E-03
±	0.0004	3.91E-06	-	0.0003	2.99E-06

### Concentration Results

Time (days)	Control, HMPA (mg/l)	Reactive Sample A, HMPA (mg/l)	Reactive Sample B, HMPA (mg/l)
0	-	-	-
0.17	39.5	42.0	35.9
0.29	41.2	39.4	40.1
1	46.4	37.6	42.9
3	44.9	34.1	36.6
5	47.6	35.4	37.2
7	49.0	29.3	33.5
13	47.1	31.6	47.3
15	44.8	28.8	38.4

Initial Concentration	
Sample	HMPA (mg/l)
A	41.7
B	56.6

## APPENDIX E

### Conductivity study to determine theoretical masses of TCE degraded during column experiments

---

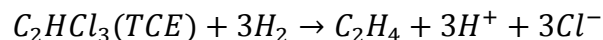
#### METHODS

During later stages of the degradation column experiment, conductivity measurements were made on a series of samples taken at timed intervals. These samples were taken at the same time as those taken for trichloroethylene (TCE) concentration analysis.

Samples of 15 ml were taken through the rubber septa-sealed inflow and outflow sampling ports on the column using a glass-on-glass syringe fitted with a needle. Samples were transferred to 20 ml HDPE sample bottles and analyzed immediately.

The cell constant for the conductivity probe and meter was calculated by measuring the conductivity of a 0.01 mol/kg KCl standard. The ratio of the theoretical conductance of this standard (1408 uS/cm) to its measured value is referred to as the cell constant. All measured conductivities of samples taken during the column experiment were multiplied by the cell constant to determine the real conductance of the samples.

The proposed degradation reaction taking place in the reactive columns is described by the following reaction:



Thus, for every mole of TCE degraded to form one mole of ethane, three moles of  $Cl^-$  are produced. The charge imbalance in solution caused by increased  $Cl^-$  is balanced by  $H^+$ . A solution containing adequate concentrations of  $Cl^-$  and  $H^+$  will have a measurable conductance. The contribution of the  $Cl^-$  and  $H^+$  to the conductance of the solution is described by their equivalent conductance values ( $\Lambda^0$ ) of 76.4 and 349.8, respectively. Therefore, samples in which degradation of TCE has occurred should exhibit elevated conductivity relative to samples where

no degradation has taken place. The following derivation of an algorithm to calculate moles of TCE degraded is based on a description of the Onsager limiting law in Reardon (2004).

The theoretical electrical conductance of a solution containing a dissolved salt can be determined via the following equation:

$$\text{Conductance} \left( \text{units: } \frac{\mu\text{S}}{\text{cm}} \right) = \Lambda \cdot C \cdot 1000$$

Where C is the concentration of the dissolved salt in eq/l and  $\Lambda$  is given by the Onsager limiting law relationship:

$$\Lambda = \Lambda^{\circ} - \left[ \frac{4.043 \times 10^3 |z_c z_a| q \Lambda^{\circ}}{T^{1.5} (1 + q^{0.5})} + \frac{5.236 \times 10^2 (|z_c| + |z_a|)}{T^{0.5}} \right] I^{0.5}$$

where:

$$\Lambda^{\circ} = \lambda_c^{\circ} + \lambda_a^{\circ}$$

The subscripts ‘a’ and ‘c’ refer to the anion and cation of the salt, respectively. Standard values for an *HCl* solution were used ( $\lambda_c^{\circ} = 349.8$ ;  $\lambda_a^{\circ} = 76.4$ ). T is temperature in Kelvin and ‘I’ is the solution ionic strength, calculated via:

$$I = \frac{1}{2} \sum m_i z_i^2$$

where ‘m’ is the concentration of the ion in molality. The value of ‘q’ is calculated using the relation:

$$q = \frac{|z_c z_a|}{(|z_c| + |z_a|)} \cdot \frac{\lambda_c^{\circ} + \lambda_a^{\circ}}{|z_a| \lambda_c^{\circ} + |z_c| \lambda_a^{\circ}}$$

In the presence of Pd, the major breakdown products of TCE degradation is ethane along with chloride. In degradation experiments, only trace concentrations of intermediate degradation products were detected, if at all (Chapter 5). Therefore, intermediate breakdown products were ignored for the purposes of conductivity calculations. It is assumed that only the  $\text{Cl}^-$  and  $\text{H}^+$  contributed to measured conductivity in the samples. Therefore, the absolute values of  $z_c$  and  $z_a$

are equal to 1. Substitution and simplification of the above equations yields the following function:

$$f(m) = 1000\Lambda^{\circ}m - \left[ 1000 \left( \frac{4.043 \times 10^3 |z_c z_a| q \Lambda^{\circ}}{T^{1.5} (1 + q^{0.5})} + \frac{5.236 \times 10^2 (|z_c| + |z_a|)}{T^{0.5}} \right) m^{1.5} \right] - c$$

where conductance is denoted by the lowercase ‘c’. Substitution of a measured conductance value allows the above equation to be solved for ‘m’, which corresponds to the theoretical molarity (m) of Cl<sup>-</sup> in solution. The value for Cl<sup>-</sup> molarity can then be used to calculate the moles of TCE that were degraded by referring the above-proposed TCE degradation reaction.

The equation denoted above as f(m) can be solved for ‘m’ by taking its derivative with respect to ‘m’:

$$f'(m) = 1000\Lambda^{\circ} - 1.5 \times 10^3 \left[ \frac{4.043 \times 10^3 |z_c z_a| q \Lambda^{\circ}}{T^{1.5} (1 + q^{0.5})} + \frac{5.236 \times 10^2 (|z_c| + |z_a|)}{T^{0.5}} \right] m^{0.5}$$

and using an iterative calculation technique such as the Newton-Raphson method. The algorithm presented below was programmed in the Visual Basic editor in Microsoft Excel and used to calculate the theoretical moles of TCE degraded given a measured conductance value. All calculations were convergent when an initial guess of 0.0001 mol/l was used for the Cl<sup>-</sup> concentration.

```

' calculate the 'bracket', a constant value based on temperature , charge, and equivalent
conductivities of the anion and cation
bracket = ((4043 * Abs(charge_cation * charge_anion) * q * lamda_naught) /
(temperature ^ 1.5 * (1 + q ^ 0.5))) + ((523.6 * (Abs(charge_cation) +
Abs(charge_anion))) / temperature ^ 0.5)

' set initial guess for concentration
m_new = 0.0001

' initialize the error
error = 1

Do While error > 0.000001

    m_old = m_new

    function_m = (1000 * lamda_naught * m_old) - (1000 * bracket * m_old ^ 1.5) - in_cond
function_primed_m = (1000 * lamda_naught) - (1.5 * 1000 * bracket * m_old ^ 0.5)

    delta = -1 * (function_m / function_primed_m)

    m_new = m_old + delta

    error = Abs(m_old - m_new) / m_new

Loop

' calculate theoretical moles of TCE that were degraded
M_TCE = m_new / 3 * 131.39 * 1000

```

Figure 147: Algorithm to calculate theoretical moles of TCE degraded based on conductivity measurements. Programmed using the Visual Basic editor in Microsoft Excel.